Operando Spectroscopy and DFT Modeling of Gold/Ceria Catalysts for CO Oxidation and Water-Gas Shift Reaction

Operando-Spektroskopie und DFT-Modellierung von Gold/Ceroxid-Katalysatoren für die CO-Oxidation und Wassergas-Shift-Reaktion
vom Fachbereich Chemie der Technischen Universität Darmstadt zur Erlangung des Grades
Doctor rerum naturalium (Dr. rer. nat.)
Dissertation von Christian Michael Schilling, M.Sc.
1. Gutachten: Prof. Dr. Christian Hess
2. Gutachten: Prof. Dr. Rolf Schäfer
3. Gutachten: Prof. Dr. Rolf Jürgen Behm

Darmstadt 2018

TECHNISCHE
UNIVERSITÄT
DARMSTADT

Fachbereich Chemie
Eduard-Zintl-Insitut für anorganische
und physikalische Chemie

Operando Spectroscopy and DFT Modeling of Gold/Ceria Catalysts for CO Oxidation and Water-Gas Shift Reaction
Operando-Spektroskopie und DFT-Modellierung von Gold/Ceroxid-Katalysatoren für die CO-Oxidation und Wassergas-Shift-Reaktion

vom Fachbereich Chemie der Technischen Universität Darmstadt zur Erlangung des Grades Doctor rerum naturalium (Dr. rer. nat.)
Dissertation von Christian Michael Schilling, M.Sc.

1. Gutachten: Prof. Dr. Christian Hess
2. Gutachten: Prof. Dr. Rolf Schäfer
3. Gutachten: Prof. Dr. Rolf Jürgen Behm

Tag der Einreichung: 9. Mai 2018
Tag der mündlichen Prüfung: 2. Juli 2018

Darmstadt 2018

Bitte zitieren Sie dieses Dokument als:
URN: urn:nbn:de:tuda-tuprints-75467
URL: http://tuprints.ulb.tu-darmstadt.de/7546

Erklärungen zur Dissertation

Ich erkläre hiermit, dass ich meine Dissertation selbstständig und nur mit den angegebenen Hilfsmitteln angefertigt und noch keinen Promotionsversuch unternommen habe.

Darmstadt, den 9. Mai 2018

(Christian Schilling)

Ich erkläre hiermit, dass die elektronische Version und die schriftliche Version dieser Dissertation übereinstimmen.

Darmstadt, den 9. Mai 2018

(Christian Schilling)

Publications

Parts of this thesis have been published so far in peer reviewed journals and at national and international conferences.

Journal articles:

- Schilling, C.; Ganduglia-Pirovano, M. V.; Hess, C., Active Gold Sites in Au/CeO_2 Catalysts Probed by Infrared Spectroscopy and DFT Vibrational Analysis. **in preparation**
- Schilling, C.; Hess, C., Water-gas Shift at Au/CeO_2 Catalysts: Mechanistic Insight from *Operando* Raman Spectroscopy. **in preparation**
- Schilling, C.; Ganduglia-Pirovano, M. V.; Hess, C., Oxygen Adsorption and Activation at Ceria Nanoparticles Exposing (111) and (100) Facets: The *in Situ* Raman Perspective. **in preparation**
- Schilling, C.; Hess, C., Real-Time Observation of the Defect Dynamics in Working Au/CeO_2 Catalysts by Combined *Operando* Raman/UV-Vis Spectroscopy. *J. Phys. Chem. C* **2018**, *122*, 2909-2917.
- Schilling, C.; Hofmann, A.; Hess, C.; Ganduglia-Pirovano, M. V., Raman Spectra of Polycrystalline CeO_2: A Density Functional Theory Study. *J. Phys. Chem. C* **2017**, *121*, 20834-20849.
- Schilling, C.; Hess, C., CO Oxidation on Ceria Supported Gold Catalysts Studied by Combined *Operando* Raman/UV-Vis and IR Spectroscopy. *Top. Catal.* **2017**, *60*, 131-140.
- Heber, M.; Schilling, C.; Gross, T.; Hess, C., *In Situ* Raman and UV-Vis Spectroscopic Analysis of Lithium-Ion Batteries. *Mater. Res. Soc. Symp. Proc.* **2015**, *1773*, 33-40.

Oral Presentations:

- Schilling, C.; Hess, C., Real-Time Observation of the Oxygen Dynamics in Working Au/CeO_2 Catalysts Probed by Combined *Operando* Spectroscopy.
  51. Katalytikertagung, Weimar, Germany, **2018**.
- Schilling, C.; Lohrenscheit, M.; Hess, C., Ceria Supported Gold Catalysts: Mechanistic Studies of CO Oxidation Using a Combined *Operando* Spectroscopic Approach.
  XII. European Congress on Catalysis, Kazan, Russia, **2015**.
- Schilling, C.; Lohrenscheit, M.; Hess, C., The Mechanism of CO Oxidation over Gold Loaded Ceria: A Combined *Operando* Spectroscopic Approach.
  114. Bunsentagung, Bochum, Germany, **2015**.

Posters Presentations:

- Schilling, C.; Ganduglia-Pirovano, M. V.; Hess, C., Bulk and Surface Defects in Au/CeO_2 Catalysts: Combined Operando Spectroscopy and DFT Based Interpretation of Support Effects.
  50. Katalytikertagung, Weimar, Germany, **2017**.

- Schilling, C.; Hess, C., Operando Raman/UV-Vis and Drifts Spectroscopy of Au/CeO_2: Oxygen Vacancy Creation in Ceria During CO Oxidation and Water-Gas Shift.
  Gordon Conference on Catalysis, New London, USA, **2016**.

- Schilling, C.; Hess, C., Understanding the Defect Dynamics in Au/CeO_2 Catalysts: Combined *Operando* Raman/UV-Vis and IR Spectroscopy.
  Manfred-Eigen Nachwuchswissenschaftler Gespräche, Mülheim a. d. Ruhr, Germany, **2016**.

- Schilling, C.; Hess, C., Role of Defects on Au/CeO_2 Catalysts During CO Oxidation Using Combined *Operando* Raman/UV-Vis and IR Spectroscopy.
  49. Katalytikertagung, Weimar, Germany, **2016**. **Awarded Poster**

- Schilling, C.; Hess, C., Probing the Influence of Defects in Au/CeO_2 During CO Oxidation by a Combined *in Situ* Spectroscopic Approach.
  Workshop an CeO_2-based materials in catalysis and electrochemistry, Schloss Rauischholzhausen, Germany, **2015**.

Acknowledgements

I would like to thank Prof. Dr. Christian Hess for supervision of my thesis work, fruitful discussion and continuous support during the thesis and during my work in his research group. I thank Dr. M. Verónica Ganduglia Pirovano for the supervision of the DFT modeling studies, an instructive and pleasant research stay in Madrid, continuous support and close cooperation.

I would like to thank Prof. Dr. Klaus Griesar for beneficial discussions and mentorship during and beyond the funding period of the Merck scholarship.

I would like to acknowledge Dr. Alexander Hofmann from Umicore AG & Co. KG, Hanau for the introduction on Raman intensity calculations, continuous support and fruitful discussions, Dr. Pablo G. Lustemberg from the Institute of Physics, Rosario, Argentina for the introduction on VASP and continuous support and Dr. Jochen Rohrer from the group of Prof. Dr. Karsten Albe for support with the VASP code.
Dr. Stefan Lauterbach from group of Prof. Dr. Hans-Joachim Kleebe is acknowledged for transmission electron microscopy measurements and support during the evaluation, Stefan Knoche from the group of Prof. Dr. Herbert Vogel for water-gas shift activity measurements, Martin Brodrecht from the group of Prof. Dr. Gerd Buntkowsky for nitrogen adsorption measurements and Dr. Katrin Hofmann from the group of Prof. Dr. Barbara Albert for XRD measurements.
Dr. Annette Trunschke, Dr. Olaf Timpe, Dr. Frank Girgsdies, Alexander Klyushin and Maike Hashagen from the group of Prof. Dr. Robert Schlögl at the Fritz-Haber-Institut in Berlin are thanked for measurements and discussions during the evaluation.
I would like to thank Anastasia Filtschew, Marcel Heber, Karl Kopp, Dr. Marno Lohrenscheit, Simone Rogg, Philip Ruff, Dr. Nicolas Sobel, as well as former and current members of the group of Prof. Dr. Christian Hess for lively discussions and support. Also I acknowledge Moritz Buchhorn, Hauke Christians, Thomas Fuchs and Marc Ziemba, who contributed measurements and discussions during their bachelor thesis and research internships.

This project would have been impossible without the support of the Merck'sche Gesellschaft für Kunst und Wisschenschaft e.V. by providing a scholarship as well as financial support for materials, research stays, numerous conference attendances and literature.

The calculations for this research were conducted on the Lichtenberg high performance computer of the TU Darmstadt, Germany, and on the Barcelona Supercomputing Center in Barcelona, Spain.

I would like to thank my friends, my family and my wife, Sandra.

Zusammenfassung

Mehr als 80% der Produkte der chemischen Industrie kommen mit einem Katalysator in Berührung.[1] Deshalb ist die Katalyse eine Schlüsseltechnologie der chemischen Industrie. Das anorganische Oxid Ceroxid (CeO_2) ist aus der Autoabgasnachbehandlung in Drei-Wege-Katalysatoren bekannt. Hierbei katalysieren Edelmetalle z.B. Pt, Pd und Rh im Kontakt mit einem Oxid (Edelmetall/Oxid) die Umsetzung von Gasphasenmolekülen wie CO, NO_x und unverbrannten Kohlenwasserstoffen zu CO_2, H_2O und N_2. Dieser Prozess ist ein Beispiel für die heterogene Katalyse von Gasphasenmolekülen an Festkörpern. Ceroxid kann dabei Sauerstoff aus dem Kristallgitter für die Reaktion zur Verfügung stellen. Dadurch können Sauerstofffehlstellen durch Reduktion gebildet und durch Oxidation die Fehlstellen wieder gefüllt werden. Dies charakterisiert Ceroxid als Sauerstoffspeichermaterial. Trotz der weiten Verbreitung dieser Katalysatorgruppe ist die Wirkungsweise von Oxid geträgerten Edelmetallkatalysatoren auf molekularer Ebene noch nicht vollständig aufgeklärt.

In dieser Arbeit wird der Katalysator Gold/Ceroxid (Au/CeO_2) behandelt. Es soll der Effekt des Ceroxid-Trägers auf die Aktivität der Katalysators nachgewiesen werden und die Rolle von Sauertsofffehlstellen im Ceroxid-Gitter auf die Aktivität geklärt werden. Das Ziel ist es, den Mechanismus von Oxidationsreaktionen über Gold/Ceroxid-Katalysatoren auf molekularer Ebene besser zu verstehen. Mit dem Wissen über die Funktionsweise und die aktiven Zentren des Katalysatores könnten diese aktiven Zentren gezielt auf dem Katalysator synthetisiert werden. Oxid geträgerte Edelmetallkatalysatoren könnten dann systematisch im Hinblick auf ihre Aktivität, Selektivität und Lebensdauer verbessert werden (wissensbasiertes Design von Katalysatoren).

Zur Klärung dieser Fragestellung wird in dieser Arbeit ein kombinierter spektroskopischer Ansatz aus Raman-, UV-Vis- und Infrarot-Spektroskopie unter Reaktionsbedingungen etabliert (*operando* Ansatz). Die schwingungspektroskopischen Beobachtungen werden mithilfe berechneter Schwingungsfrequenzen von Modellsystemen bzw. berechneter Raman- und Infrarot-Spektren auf Basis der Dichtefunktionaltheorie (DFT) interpretiert. Dies erlaubt eine Deutung der experimentellen spektroskopischen Ergebnisse auf molekularer Ebene.

Der experimentelle Ansatz ist in Abbildung 1 zusammengefasst. Während der Katalysator Reaktionsbedingungen ausgesetzt ist, wird simultan die Aktivität nachgewiesen und optische Spektroskopie am Katalysator durchgeführt. Dabei wird die *operando* Raman- und UV-Vis-Spektroskopie in einem Aufbau und die Infrarot-Spektroskopie in diffuser Reflexion (DRIFTS) in einem zweiten Aufbau eingesetzt. In beiden Aufbauten ist das Aktivitätsverhalten des Katalysators identisch (siehe Kapitel 2). Um gezielt Sauerstofffehlstellen und die strukturellen Eigenschaften von Ceroxid unter Reaktionsbedingungen zu

---

[1] In dieser Zusammenfassung werden keine Literaturstellen angegeben. Die entsprechenden Literaturnachweise können der englischsprachigen Einleitung bzw. der Arbeit entnommen werden.

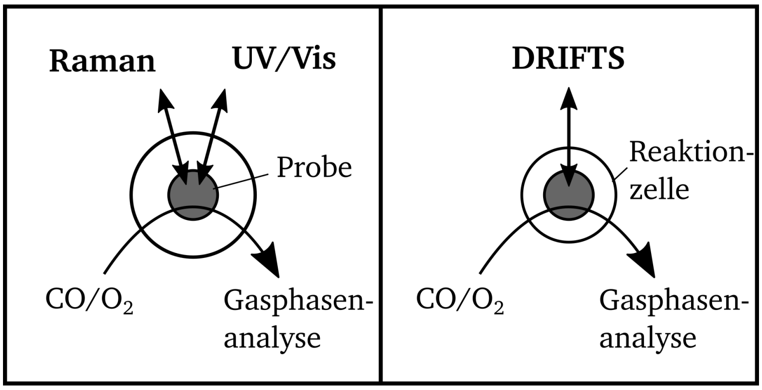

Abbildung 1: Schematische Darstellung des kombinierten Raman-, UV-Vis- und Infrarot-Spektroskopie Ansatzes. Während der Katalysator Reaktionsbedingungen ausgesetzt ist, wird gleichzeitig im ersten Setup (links) Raman- und UV-Vis-Spektroskopie am aktiven Katalysator durchgeführt (*operando* Ansatz). Im zweiten Setup (rechts) zeigt der Katalysator identische Aktivtität und kann mittels Infrarot-Spektroskopie in diffuser Reflexion (DRIFTS) charakterisiert werden.

charakterisieren, wird vor allem die Raman-Spektroskopie herangezogen. Neben Festkörperphononen (Schwingungen des Ceroxid-Festkörpers) können mit dieser Technik auch die Schwingungseigenschaften von Oberflächenadsorbaten zum Beispiel Peroxide ($O_2{}^{2-}$) und Superoxide ($O_2{}^{-}$) nachgewiesen werden. Die Infrarot-Spektroskopie ist als komplementäre Methode für adsorbierte Oberflächenmoleküle wie zum Beispiel Carbonyl- (CO), Carbonat- (COO, COOH) und Formatspezies (CHO) sensitiv.

Als Modellreaktion wird zunächst die CO-Oxidation ($CO + O_2 \rightarrow CO_2$) diskutiert. Die verwandte Wassergas-Shift-Reaktion ($CO + H_2O \rightarrow CO_2 + H_2$) ist anwendungstechnisch für die Produktion von Wasserstoff von Relevanz. Technisch wird der Wassergas-Shift zweistufig über Eisen(III)- und Chrom(III)oxid bei 450°C und Kupfer(II)- und Zinkoxid bei 250°C durchgeführt. Bei hohen Temperaturen liegt zwar eine schnelle Kinetik der Reaktion, aber eine ungünstige Lage des thermodynamischen Gleichgewichtes vor. Gold/Ceroxid-Katalysatoren bieten bereits bei niedrigen Temperaturen (200°C) eine vergleichbare Kinetik wie Kupfer(II)- und Zinkoxid-Katalysatoren und sind deshalb eine Alternative zu den technisch eingesetzten Katalysatoren.

Sowohl für die CO-Oxidation als auch die Wassergas-Shift-Reaktion werden in dieser Arbeit Verbindungen zwischen der Aktivität des Katalysators und der molekularen Struktur abgeleitet (Struktur-Aktivitätsbeziehungen), mit dem Ziel ein mechanistisches Bild der Oxidationsreaktionen über Gold/Ceroxid zu gewinnen. Insbesondere wird der Unterschied in der Aktivierung der oxidierenden Reaktanden, dies sind Sauerstoff für die CO-Oxidation und Wasser für die Wassergas-Shift-Reaktion, auf dem Ceroxid-Träger untersucht. Es kann dabei gezeigt werden, dass die erhöhte Aktivität eines reduzierten Katalysators auf die Sauerstofffehlstellenkonzentration im Ceroxid-Träger zurückzuführen ist. Außerdem wird die Aktivierung von CO am Goldpartikel experimentell mithilfe der Streckschwingung adsorbierter CO-Moleküle nachgewiesen. Durch berechnete Schwingungsfrequenzen an Modellstrukturen auf Basis der Dichtefunktionaltheorie kann daraus die aktive Spezies (*active site*) für die CO-Oxidation in dieser Arbeit erstmalig abgeleitet werden.

Im Folgenden werden die wichtigsten Ergebnisse mit Verweis auf die entsprechenden Kapitel der Arbeit kurz zusammengefasst und im nächsten Abschnitt detailliert beschrieben. Die Vorgänge auf einem Gold/Ceroxid-Katalysator während der CO Oxidation sind in Abbildung 2 schematisch zusammengefasst. Bei der Adsorption aktiver Goldpartikel auf dem Ceroxid-Träger kommt es zu einer Übertragung von Elektronen vom Goldpartikel auf den Ceroxid-Partikel, dies lässt Goldatome in oxidierter Form (Au^+) zurück. An diesen oxidierten Goldspezies kommt es zu einer präferierten Adsorption von Kohlenmonoxid (Schritt 1 in Abbildung 2). Die gebildete $O_{lattice}$-Au^+-CO Struktureinheit wird mittels Infrarot-Spektroskopie als aktive Spezies (*active site*) charakterisiert, da die Konzentration dieser Spezies direkt mit der Aktivtität des Katalysators in Zusammenhang gebracht werden kann. Dichtefunktionaltheoretische Rechnungen zeigen eindeutig, dass es sich bei der gemessenen Frequenz der CO Streckschwingung von 2125 – 2130 cm^{-1} um ein CO-Molekül handelt, das an oxidierten Goldatomen (Au^+) in direktem Kontakt mit dem Ceroxid-Träger ($O_{lattice}$) adsorbiert. Außerdem zeigen die DFT-Rechnungen, dass diese isolierte Goldspezies auch dynamisch nach CO-Adsorption aus einem dreidimensionalen Goldpartikel gebildet werden kann. Der entsprechende Ausschnitt aus dem Infrarot-Spektrum ist in Abbildung 3 dargestellt (rotes Spektrum). Das Gesamtsignal wird in drei Komponenten aufgeteilt, die jeweils bestimmten Adsorptionsplätzen für CO auf der Katalysatoroberfläche zugeordnet werden. Die Strukturen mit blauem Rahmen entsprechen der aktiven $O_{lattice}$-Au^+-CO Spezies und können der Komponente bei 2125 – 2130 cm^{-1} zugeordnet werden. Ein bildgebender Beweis für isolierte Goldatome mittels Transmissionselektronenmikroskopie (TEM) ist schwer möglich. Allerdings ist dies der erste spektroskopische Beweis für die Bildung von atomar verteilten Goldatomen auf polykristallinem Ceroxid. Die Studie ist ausführlich in Kapitel 8 beschrieben.

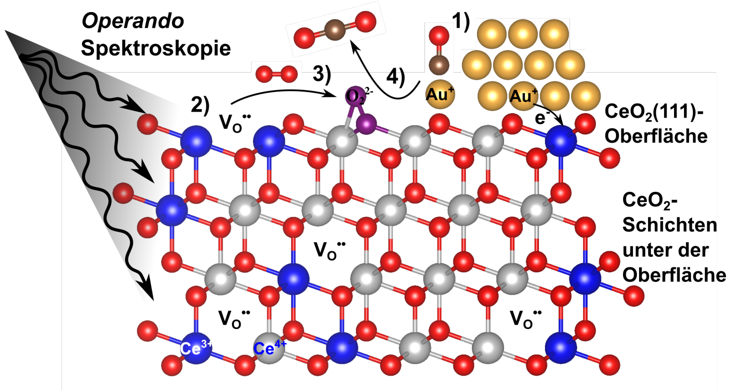

Abbildung 2: Schematische Darstellung wichtiger Reaktionsschritte auf Gold/Ceroxid-Katalysatoren auf molekularer Ebene. 1) CO-Adsorption auf Au^+ Spezies in direktem Kontakt mit dem Ceroxid-Träger 2) Bildung von Sauerstofffehlstellen $V_O^{\bullet\bullet}$ und Ce^{3+} (blaue Ionen) auf der $CeO_2(111)$-Oberfläche und in den darunter liegenden Ceroxid-Schichten durch Reaktion von CO mit Oberflächensauerstoff. 3) Adsorption von molekularem O_2 an Sauerstofffehlstellen der Oberfläche als Peroxid (O_2^{2-}) und 4) Bildung und Desorption von CO_2 aus CO und Peroxiden.

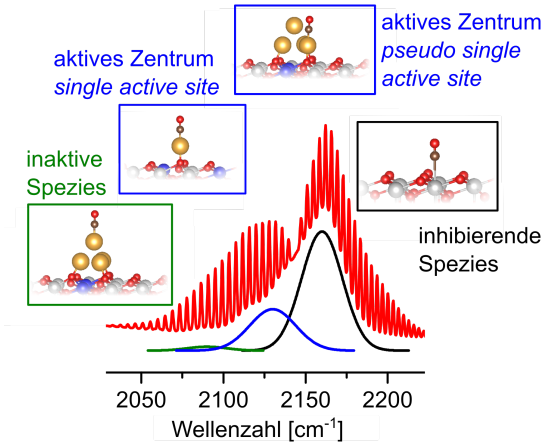

Abbildung 3: Ausschnitt aus dem Infrarot-Spektrum eines Gold/Ceroxid-Katalysators unter Reaktionsbedingungen (rot) und Entfaltung des Signals in drei Komponenten, die auf Basis von DFT-Rechnungen der aktiven Spezies $O_{lattice}$-Au^+-CO (blau), der Adsorption von CO am dreidimensionalem Goldpartikel (grün) und der Adsorption von CO am Support (schwarz) zugeordnet werden können.

Für die Aktivierung der oxidierenden Moleküle O_2 und H_2O spielen Sauerstofffehlstellen ($V_O^{\bullet\bullet}$ und Schritt 2 in Abbildung 2) auf dem Ceroxid-Träger eine entscheidende Rolle. Diese Sauerstofffehlstellen können durch Reaktion des adsorbierten CO der $O_{lattice}$-Au^+-CO Einheit mit Oberflächensauerstoff unter Bildung von CO_2 entstehen. An den Sauerstofffehlstellen kann molekularer Sauerstoff in Form reduzierter Sauerstoffspezies als Peroxid (O_2^{2-}, lila Molekül und Schritt 3 in Abbildung 2) oder Superoxid (O_2^{-}) aktiviert werden bzw. Wasser dissoziativ adsorbieren (nicht gezeigt). Die Raman-Spektroskopie erlaubt die Charakterisierung von Peroxid- und Superoxidspezies anhand ihrer Streckschwingungsfrequenz. Für eine vollständige Charakterisierung dieser reduzierten Sauerstoffspezies auf Ceroxid werden Ceroxid-Nanopartikel synthetisiert, die selektiv die $CeO_2(111)$ (dargestellt in Abbildung 2) oder die $CeO_2(100)$-Oberfläche ausbilden. Anschließend wird das Adsorptionsverhalten von Sauerstoff mittels *in situ*-Raman-Spektroskopie analysiert und mit theoretischen Modellen verknüpft. Im Rahmen dieser Studie (siehe Kapitel 5) können zum ersten Mal Superoxide auf Ceroxid-Nanopartikeln nachgewiesen werden, die selektiv die $CeO_2(100)$-Oberfläche ausbilden. Darüber hinaus kann eine erleichterte Bildung von Peroxiden und Superoxiden an der $CeO_2(100)$-Oberfläche im Vergleich zur $CeO_2(111)$-Oberfläche nachgewiesen werden. Aus den Ergebnissen wird geschlossen, dass die instabilere $CeO_2(100)$-Oberfläche für die Aktivierung von Sauerstoff in Form von Peroxiden und Superoxiden besser geeignet ist als die thermodynamisch stabile $CeO_2(111)$ Oberfläche.

Die Konzentration von Sauerstofffehlstellen ($V_O^{\bullet\bullet}$ in Abbildung 2) im Ceroxid-Träger kann mittels *operando* Raman-Spektroskopie unter Reaktionsbedingungen quantifiziert werden. Die DFT+U-Studie in Kapitel 4 zeigt, dass die Position (Frequenz) der intensiven Raman-Bande, die der F_{2g}-Mode im Ceroxid-Kristall zugeordnet werden kann, mit erhöhter Konzentration der Sauerstofffehlstellen zu niedrigeren Wellenzahlen verschoben ist (F_{2g}-Rotverschiebung). Daraus kann eine direkte Korrelation der Aktivität des Au/CeO_2-Katalysators mit dem Reduktionsgrad des Ceroxid-Trägers unter Reaktionsbedingungen abgeleitet werden (siehe Kapitel 7). Außerdem bietet die Raman-Spektroskopie Zugang zu den Sauerstoffionen an der Oberfläche von polykristallinem Ceroxid, sprich jenen Sauerstoffatomen, die direkt am Oxidationsprozess beteiligt sind (rote Ionen an der Oberfläche in Abbildung 2). Die Bande bei 246 cm^{-1} im Raman-Spektrum von CeO_2 und Au/CeO_2 kann im Rahmen dieser Arbeit erstmals einer longitudinalen Streckschwingung der Sauerstoff- und Cerionen an der $CeO_2(111)$-Oberfläche von polykristallinem Ceroxid zugeordnet werden. Damit kann der Oberflächenreduktionsgrad bzw. die Konzentration der Sauerstofffehlstellen an der Oberfläche unter Reaktionsbedingungen bestimmt werden. Die Dichtefunktionaltheorie sagt nämlich nicht nur die Frequenz der longitudinalen Oberflächenmode in sehr guter Übereinstimmung mit dem Experiment voraus, sondern auch eine Abnahme der Intensität der Bande bei Bildung von Sauerstofffehlstellen an der Oberfläche ($V_O^{\bullet\bullet}$ an der Oberfläche in Abbildung 2).

Die in Kapitel 7 gezeigten Ergebnisse zur CO-Oxidation stellen die Dynamik von Sauerstoffionen und Fehlstellen im Ceroxid-Träger von Gold/Ceroxid-Katalysatoren heraus. Diese Dynamik ist auch für andere Edelmetalle/Ceroxid-Systeme und möglicherweise auch für weitere oxidische Trägermaterialien direkt relevant (zum Beispiel TiO_2).

Für die Wassergas-Shift-Reaktion über Au/CeO_2-Katalysatoren (siehe Studie in Kapitel 9) kann eine vergleichbare Dynamik von Sauerstoff im Ceroxid-Träger gezeigt werden. Die Ergebnisse der *operando* Raman-Spektroskopie lassen vermuten, dass die Oberfläche unter Reaktionsbedingungen hydroxyliert vorliegt. Des Weiteren zeigen Experimente mit dem $H_2^{18}O$ Isotop, dass bei Anwesenheit von Gold auf dem Ceroxid-Träger, die ^{16}O-Sauerstoffionen der Ceroxid-Oberfläche vollständig durch ^{18}O-Ionen ausgetauscht werde können. Dies geschieht ohne die Bildung von Formaten oder Carboxylaten als Intermediate. Unter Reaktionsbedingungen (CO/$H_2{}^{18}O$) zeigt sich ein vollständiger Austausch von Sauerstoff ^{16}O zu ^{18}O im Ceroxid-Kristall. Vermutlich reicht dieser Austausch nur in die ersten Ceroxid-Schichten unter der Oberfläche. Die detaillierte Analyse zeigt, dass ein Redox-Mechanismus über Au/CeO_2-Katalysatoren für die Wassergas-Shift-Reaktion möglich ist und nicht wie in der Literatur postuliert, gegenüber assoziierten Mechanismen (Format- und Carboxylat-Intermediaten) stark benachteiligt ist.

Zusammenfassend kann das Potential der Raman-Spektroskopie als komplementäre schwingungsspektroskopische Methode zur Infrarot-Spektroskopie herausgestellt werden. Durch das Zusammenspiel von experimentellen Spektren unter Reaktionsbedingungen (*operando* Ansatz) und Berechnungen von Schwingungseigenschaften von Modellsystemen kann ein molekulares Bild geschaffen werden, das wichtige Rückschlüsse auf den Mechanismus zulässt. Insbesondere kann der Zusammenhang zwischen der Sauerstofffehlstellenkonzentration des Ceroxid-Trägers auf die Aktivität von Gold/Ceroxid-Katalysatoren nachgewiesen werden. Dieses Verhalten ist möglicherweise direkt auf weitere Edelmetall/Ceroxid-Systeme übertragbar und verdeutlicht den fundamentalen Charakter der Studie. Des Weiteren kann mittels Infrarot-Spektroskopie für Gold/Ceroxid-Katalysatoren eine isolierte Goldspezies unter Bildung der aktive $O_{lattice}$-Au^{+}-CO Spezies nachgewiesen werden. Die hohe Dynamik der Sauerstoffionen, die starke Änderung des Oxidationszustandes beim Wechsel der Gasumgebung und die Bildung der aktiven Spezies ($O_{lattice}$-Au^{+}-CO) erst unter Reaktionsbedingungen unterstreichen den Bedarf für eine direkte Charakterisierung von oxidischen Katalysatormaterialien unter Reaktionsbedingungen (*operando* Ansatz).

Detaillierte Beschreibung der Ergebnisse

In diesem Abschnitt werden die Daten detailliert beschrieben, die zu den vorher zusammengefassten Ergebnissen führen. Es wird zunächst die DFT-Studie zur Interpretation von Raman-Spektren von nanostrukturierten Ceroxid-Partikeln diskutiert. Diese Studie ist direkt relevant für die Charakterisierung von Gold/Ceroxid-Katalysatoren unter Reaktionsbedingungen der CO-Oxidation und der Wassergas-Shift-Reaktion.

Mithilfe der Dichtefunktionaltheorie (DFT) können Strukturauschnitte des Katalysators modelliert und geometrisch optimiert werden. Dabei wird in dieser Arbeit das Austausch-Korrelations-Funktional (PBE) mit zusätzlichem Korrekturterm $U_{\mathrm{eff}} = 4.5$ eV für das Ce4f-Orbital (PBE+U/4.5 eV) bzw. ein Hybrid-Funktional (HSE06) genutzt, bei dem die Austauschenergie exakt berechnet wird. Anschließend werden die Normalmoden des Strukturmodells und die nicht-resonanten Intensitäten der Raman-Streuung der Moden mithilfe eines störungstheoretischen Ansatzes (*Density Functional Perturbation Theory*) berechnet. Die Vorgehensweise und technischen Details sind in Kapitel 3 beschrieben. Die Position der Raman-aktiven Mode erster Ordnung (F_{2g}) von stöchiometrischem Ceroxid (CeO_2) kann mit beiden Funktionalen bestimmt werden. Das Hybrid-Funktional beschreibt mit 450.8 cm^{-1} die experimentell beobachtete Position von 465 cm^{-1} besser als das PBE+U/4.5 eV-Funktional mit 437.3 cm^{-1}. Die vollständige Diskussion der Schwingungsanalyse ist in Kapitel 4 beschrieben. Aufgrund des circa 100-fach erhöhten Rechenaufwandes für Rechnungen mit dem Hybrid-Funktional wird im Folgenden das PBE+U/4.5 eV-Funktional mit einem Skalierungsfaktor ($\tilde{\nu}_{\mathrm{Exp.}} = 1.06\ \tilde{\nu}_{\mathrm{PBE+U}}$) genutzt. Die Positionen der Raman aktiven Moden zweiter Ordnung werden bei 256, 409, 584, 948 und 1159 cm^{-1} (skaliert) aus der Dichte der Schwingungszustände bestimmt und stimmen sehr gut mit dem experimentell beobachteten Banden zweiter Ordnung überein.

Die Schwingungseigenschaften von reduziertem Ceroxid (CeO_{2-x}) werden anhand von $Ce_{32}O_{63}$- und $Ce_{32}O_{62}$-Strukturen ermittelt. Für diese Strukturen wird eine Bande bei 480 cm^{-1} (experimentell bei ∼540 cm^{-1}) für Konfigurationen vorhergesagt, in denen die Sauerstofffehlstelle und Ce^{3+} nicht in unmittelbarer Nähe auftreten (kubische $Ce^{3+}O_8$-Koordination). Eine zweite Bande wird bei 500 cm^{-1} (experimentell bei ∼560 cm^{-1}) für die Konfiguration mit einer Fehlstelle und Ce^{3+} in unmittelbarer Nähe vorhergesagt (kubische $Ce^{3+}O_7V_O^{\bullet\bullet}$-Koordination). Aufgrund der Bildung von Ce^{3+} in Zuge der Sauerstofffehlstellenbildung kommt es außerdem zu einer Ausdehnung des Ionengitters von Ceroxid und zu einer Verschiebung der F_{2g}-Bande zu kleineren Frequenzen (F_{2g}-Rotverschiebung). Sowohl die Ausdehnung des Gitters als auch die experimentell beobachtete Rotverschiebung der F_{2g}-Bande können mit DFT+U-Rechnungen für kleine Abweichungen der Stöchiometrie vom oxidierten Kristall bis $CeO_{2-0.07}$ quantifiziert werden. Die Stöchiometrie von $CeO_{2-\delta}$ kann auf Basis von DFT+U-Rechnungen mit der Rotverschiebung ($\Delta\omega$) der F_{2g}-Bande in folgenden direkten, quantitativen Zusammenhang gebracht werden: $\delta = (0.024 \pm 0.05)\ \Delta\omega/\mathrm{cm}^{-1}$.

Um die Oberflächenterminierung von Ceroxid-Nanopartikeln zu berücksichtigen, wird zusätzlich die Ceroxid (111)- und (100)-Oberfläche modelliert. Die Schwingungsanalyse für die CeO_2(111)-Oberfläche ergibt ein longitudinales (parallel zur Oberfläche) und ein transversales (orthogonal zur Oberfläche) Phonon der Cer- und Sauerstoffionen an der Oberfläche mit einer Frequenz von 225 cm^{-1} bzw. 364 cm^{-1} (PBE+U/4.5 eV). Für die CeO_2(100)-Oberfläche werden zwei Moden bei 331 und 563 cm^{-1}

vorhergesagt, die nicht unmittelbar an der Oberfläche lokalisiert sind. Für den Vergleich mit experimentellen Spektren müssen die berechneten Frequenzen mit dem oben beschriebenen Faktor 1.06 multipliziert (skaliert) werden. Tatsächlich werden an Ceroxid-Proben, die selektiv die CeO_2(111)-Oberfläche exponieren (Polyeder, charakterisiert mithilfe von TEM), Banden bei 246 cm^{-1} und 402 cm^{-1} im Raman-Spektrum beobachtet. Da die Banden auch an polykristallinen Ceroxid-Nanopartikeln beobachtet werden, wird daraus geschlossen, dass polykristallines Ceroxid vorzugsweise in CeO_2(111) Richtung terminiert. An Ceroxid-Proben mit (100)-Oberfläche (kubische Partikel in TEM-Bildern) können diese Banden nicht beobachtet werden, aber es werden schwache Banden bei 350 und 600 cm^{-1} identifiziert, die mit den berechneten Banden bei 331 und 563 cm^{-1} gut übereinstimmen. Die Oberflächenterminierung der synthetisierten Nanokristalle bzw. des polykristallinen Ceroxids kann zusätzlich durch Bestimmung der Netzebenenabstände (0.27 nm für die (100)-Richtung und 0.31 nm für die (111)-Richtung) aus Transmissions-Elektronenmikroskopie-Messungen verifiziert werden. Mithilfe dieser Studie kann die Bande bei 246 cm^{-1} im Raman-Spektrum von polykristallinem Ceroxid zweifelsfrei der Oberflächenmode der CeO_2(111) Oberfläche zugeordnet werden. Bisher wurde diese Bande einem Oberton in Ceroxid zugeordnet. Zusätzlich kann anhand dieser Bande (Position und Intensität) eine Aussage über den Reduktionsgrad der Oberfläche getroffen werden, da die DFT-Rechnungen eine Abnahme der Intensität der Bande nach Bildung von Sauerstofffehlstellen an der Oberfläche vorhersagen.

An den Nanopartikeln mit CeO_2(111)- und CeO_2(100)-Oberfläche wird mittels *in situ*- Raman-Spektroskopie das Adsorptionsverhalten von Sauerstoff als reduziertes Peroxid- ($O_2{}^{2-}$) und Superoxidanion ($O_2{}^{-}$) untersucht. Die Sauerstoffanionen können anhand der O-O-Streckschwingungsfrequenz unterschieden und charakterisiert werden. Die gemessenen Frequenzen werden mit berechneten Frequenzen (PBE+U/4.5 eV) von Modellstrukturen verglichen, die neben einem molekularen Bild von der Adsorptionsgeometrie auch eine Aussage über die Stabilität der Sauerstoffspezies auf der Ceroxid-Oberfläche liefern. Mithilfe der Modelle kann zunächst gezeigt werden, dass es auf der CeO_2(111)-Oberfläche bei einer Bedeckung von $\leq$0.25 Monolagen (ML, 25 % der Sauerstoffatome an der Oberfläche sind durch Peroxidanionen ersetzt) zwei Peroxid-Konfigurationen vergleichbarer Stabilität gibt ($\Delta E_{\text{tot}} < 20$ meV), deren Schwingungsfrequenz mit einem Abstand von 38 cm^{-1} vorgesagt werden. Verglichen damit wird experimentell ein Abstand von 30 cm^{-1} beobachtet (830 und 860 cm^{-1}). Zusätzlich kann die experimentell vermutete Blauverschiebung der Peroxidbande bei höherer Bedeckung der Oberfläche ($\geq$0.5 ML) durch Peroxide mittels DFT-Rechnungen bestätigt werden, wobei eine Verschiebung der Schwingungsfrequenz um 40 cm^{-1} für vollständige Bedeckung (1 ML) verglichen mit einer Bedeckung von 0.06 ML vorhergesagt wird. In guter Übereinstimmung wird experimentell eine maximale Verschiebung der Bande um 17 cm^{-1} von 860 cm^{-1} auf 877 cm^{-1} beobachtet. Darüberhinaus wird für die Bildung von Ce^{3+}-Ionen in der Nähe von Peroxiden eine chemischen Verschiebung der Frequenz von bis zu 30 cm^{-1} vorhergesagt. Eine entsprechende Schwingungsfrequenz (847 cm^{-1}) wurde zuvor für Au/CeO_2-Katalysatoren postuliert und kann durch Ce^{3+}-Bildung im Zuge der Goldabscheidung erklärt werden.

Für die Frequenz der Streckschwingung von Superoxiden ($O_2{}^{-}$) auf der CeO_2(111)-Oberfläche wird nur ein schmaler Bereich <2 cm^{-1} unabhängig von der Superoxidkonfiguration und der Lokalisation des Ce^{3+}-Ions vorhergesagt. Die erhaltenen theoretischen Ergebnisse spiegeln die Beobachtungen einer scharfen Bande bei ~1128 cm^{-1} in der Literatur wieder.

Auf Ceroxid-Nanopartikeln, die die CeO_2(100)-Oberfläche exponieren, können unter den gleichen Bedingungen wie zuvor für die CeO_2(111)-Oberfläche Banden bei 1505 cm^{-1} der Streckschwingung von adsorbiertem molekularem Sauerstoff ($O_2{}^{\delta-}$), bei 1137 und 1103 cm^{-1} der Streckschwingung von Superoxiden ($O_2{}^{-}$) und bei 832 und 862 cm^{-1} der Streckschwingung von Peroxiden ($O_2{}^{2-}$) zugeordnet werden. Dieses Verhalten kann mit einer höheren Stabilität der Sauerstoffspezies auf der CeO_2(100) Oberfläche erklärt werden. Die beiden Banden bei 1137 und 1103 cm^{-1} können anhand von Modellsystemen durch Superoxidanionen erklärt werden, die parallel (*side on*) auf der Oberfläche adsorbieren und in unmittelbarer Nähe eines Ce^{3+}-Ions (1137 cm^{-1}) und in zweiter Koordinationsphäre eines Ce^{3+}-Ions (1103 cm^{-1}) lokalisiert sind. Die erste Konfiguration wird dynamisch bei 35° in CO/O_2 und die zweite durch einen Elektronentransfer bei Temperaturen von ∼120°C gebildet. Es handelt sich um den ersten Bericht von Superoxidspezies auf CeO_2-Nanopartikeln, die selektiv die CeO_2(100)-Oberfläche exponieren.

Für Peroxide auf der CeO_2(100)-Oberfläche wird wie bei der CeO_2(111)-Oberfläche eine Verschiebung der Frequenzen beobachtet, die vom Bedeckungsgrad abhängt. Es ergibt sich eine berechnete Blauverschiebung von 39 cm^{-1} für Bedeckungen von 1 ML verglichen mit einer Bedeckung von 0.125 ML in guter Übereinstimmung mit der experimentell gemessenen Verschiebung von 30 cm^{-1} und den Ergebnissen für die CeO_2(111)-Oberfläche (siehe oben).

Für Gold/Ceroxid-Katalysatoren kann durch *dynamische operando* Raman-Spektroskopie eine Abhängigkeit der Aktivität vom Reduktionsgrad des Ceroxid-Trägers nachgewiesen werden. Dies gelingt durch eine oxidative und reduktive Vorbehandlung des Katalysators und anschließende Bestimmung der Aktivität unter Reaktionsbedingungen. Die dynamischen Raman-Spektren zeigen quantitativ, dass der Katalysator während der CO-Oxidation (2% CO, 10% O_2) reduziert wird. Die Stöchiometrie verändert sich von $CeO_{1.988-x}$ zu $CeO_{1.952-x}$. Eine reduktive Vorbehandlung (2% CO) kann die Oberfläche reduzieren und die diese Reduktion kann sich in den Ceroxid-Kristall ausdehnen. Dies wird durch Abnahme der longitudinalen Oberflächenmode bei 246 cm^{-1} qualitativ geschlossen und anhand der Rotverschiebung der F_{2g}-Bande wird die Stöchiomerie unter reduktiven Bedingungen zu $CeO_{1.916-x}$ bestimmt. Unter anschließenden Reaktionsbedingungen wird die Oberfläche schnell oxidiert, während die Reoxidation des Ceroxid-Kristalls zeitgleich mit der Relaxation (circa eine Stunde) der Aktivität in den Gleichgewichtszustand erfolgt. Deshalb wird die erhöhte Aktivität (100% Erhöhung) des reduzierten Katalysators auf die Reduktion des Ceroxid-Kristalls zurückgeführt. Die Ergebnisse zeigen die außergewöhnliche Sauerstoffdynamik in Edelmetall/Ceroxid-Systemen und die Kopplung des Oxidationszustands des Katalysators an die entsprechenden Gasphase über dem Katalysator.

Ein theoretisch vorhergesagter Elektronentransfer von adsorbiertem Gold auf den Ceroxid-Träger unter Bildung von Au^+, kann mittels Röntgenphotoelektronen-Spektroskopie (XPS) durch die Beobachtung von zwei Komponenten des Au4f-Signals bei 84.0 eV (Au^0) und 84.9 eV (Au^+) bestätigt werden. Des Weiteren wird in der Literatur die Adsorption von CO auf oxidierten Goldionen (Au^+) im Kontakt mit der Ceroxid-Oberfläche vorhergesagt. In dieser Arbeit wird zum ersten Mal ein spektroskopischer Beweis für eine $O_{lattice}$-Au^+-CO Spezies erbracht. Infrarot-Spektroskopie am Katalysator unter Reaktionsbedingungen zeigt, dass die Intensität der Bande bei 2125 − 2130 cm^{-1} direkt mit der Aktivtität des Katalysators korreliert. Eine Schwingungsanalyse mittels DFT mit einem PBE+U/4.5 eV- oder HSE06-Funktional von CO-CeO_2(111)-, CO-$Au_1{}^+$/CeO_2(111)-, CO-$Au_4{}^{2+}$/CeO_2(111)-, CO-Au_1- und CO-Au(111)-Modellstrukturen lässt den Schluss zu, dass es sich bei der Frequenz von 2125 — 2130 cm^{-1} um die Streckschwingung von Kohlenmonoxid adsorbiert an einem Au^+-Kation in direktem Kontakt mit der CeO_2(111)-Oberfläche handeln muss ($O_{lattice}$-Au^+-CO Spezies). Aufgrund des geringen Kontrasts zwischen ^{79}Au und ^{58}Ce konnten in der Literatur bisher nur sehr schwer isolierte Gold-Atome oder Gold-Ionen auf Ceroxid-Nanopartikeln durch elektronenmikroskopische Methoden nachgewiesen werden. Deshalb wird hier der indirekte spektroskopische Beweis dieser isolierten Goldatome (ohne Bildgebung) mithilfe der Streckschwingung von adsorbierten CO herangezogen. Durch Infrarot-Spektroskopie-Messungen kann außerdem eine Inhibierung der CO-Oxidation durch adsorbiertes CO (Bande bei 2160 — 2170 cm^{-1}) und Hydrogencarbonat (Bande bei 1218 cm^{-1}) auf der CeO_2(111)-Oberfläche von polykristallinem Ceroxid gezeigt werden.

Gold/Ceroxid-Katalysatoren, deren Ceroxid-Träger selektiv die CeO_2(111)- oder CeO_2(100)-Oberfläche exponieren (nachgewiesen mittels Raman-Spektroskopie und TEM-Messungen), zeigen für die (100)-Oberfläche eine dreifache erhöhte CO_2-Bildungsrate pro Au^+-Atom. Allerdings zeigt ein Au/CeO_2(111)-Katalysator, dessen Träger eine polykristalline gestufte CeO_2(111)-Oberfläche aufweist (aus TEM-Bildern bekannt), eine fünffach erhöhte Bildungsrate verglichen mit dem Au/CeO_2(100)-Katalysator. Dies verdeutlicht, dass es einen Effekt der Oberflächenterminierung gibt, allerdings ist die Bildung von Stufen auf der Oberfläche ebenfalls entscheidend für die Aktivtität des Katalysators. Dieses Verhalten kann durch eine Verringerung der benötigten Energie zur Erzeugung einer Sauerstofffehlstelle an Stufen erklärt werden. Außerdem ist die Energie zur Erzeugung einer Sauerstofffehlstelle auf der flachen CeO_2(100)-Oberfläche gegenüber der flachen CeO_2(111)-Oberfläche um 0.45 eV herabgesetzt (vergleiche auch die erleichterte Bildung von Peroxiden und Superoxiden auf der CeO_2(100)-Oberfläche in dieser Arbeit). Mit diesen kombinierten Experimenten zur Bestimmung der Aktivität und der Oberflächenterminierung mittels Raman-Spektroskopie- und TEM-Messungen, kann demnach gezeigt werden, dass durch molekulare Strukturierung der Edelmetall/Ceroxid-Katalysatoroberfläche die Aktivität für Oxidationsreaktionen gezielt gesteuert werden kann.

Für die Wassergas-Shift-Reaktion kann zunächst gezeigt werden, dass der hier untersuche Au/CeO_2-Katalysator das gleiche Verhalten (Umsatz und Aktivierungsenergie, E_A) aufweist, das in der Literatur für diese Katalysatorgruppe beschrieben wird. *Operando* Raman-Messungen lassen vermuten, dass die Oberfläche unter Reaktionsbedingungen hydroxyliert (OH-Gruppen) vorliegt. Des Weiteren kann die Bildung von Formatspezies unter Reaktionsbedingungen beobachtet werden (1590 cm^{-1}). Experimente mit dem $H_2{}^{18}O$-Isotop zeigen, dass terminale Hydroxylgruppen auch auf reinem Ceroxid vollständig von ^{16}OH zu ^{18}OH umgewandelt werden. In Gegenwart von Gold (0.5 wt% Au/CeO_2-Katalysator) können die Sauerstoffionen (^{16}O) an der CeO_2(111)-Oberfläche vollständig durch ^{18}O ausgetauscht werden. Dies geht eindeutig aus der Verschiebung der Banden der longitudinalen und transversalen Oberflächenmode von 242 cm^{-1} zu 231 cm^{-1} bzw. 402 cm^{-1} zu 385 cm^{-1} hervor. Interessant ist hierbei, dass dies nicht die Anwesenheit von CO und die Bildung von Formaten oder Carboxylaten bedingt, wie in der Literatur vorgeschlagen. Unter Reaktionsbedingungen (2% CO, 8% $H_2{}^{18}O$) werden auch die Sauerstoffionen der Ceroxid-Kristalls in ^{18}O umgewandelt, da zwei benachbarte F_{2g}-Banden bei 456 cm^{-1} ($Ce^{16}O_2$) und 436 cm^{-1} ($Ce^{18}O_2$) beobachtet werden. Die Ergebnisse zeigen, dass ein Redox-Mechanismus (vergleiche Mars-van Krevelen Mechanismus) für die Wassergas-Shift-Reaktion möglich ist, während in der Literatur vorrangig assoziierte Mechanismen mit einem Format- oder Carboxylat als Zwischenstufe postuliert werden.

Zusammenfassend zeigen die Ergebnisse die besonderen Eigenschaften von Ceroxid als Träger für Edelmetalle und den Einfluss des Ceroxid-Trägers auf die Reaktivität von Edelmetall/Oxid-Katalysatoren. Insbesondere das unterschiedliche Adsorptionsverhalten von Sauerstoff auf der $CeO_2(111)$- und $CeO_2(100)$-Oberfläche und die Defektdynamik des Trägers während der CO-Oxidation (Reduktion und Oxidation) sollen hervorgehoben werden. Die Adsorption von CO an oxidierten Goldionen und die gebildete $O_{lattice}$-Au^+-CO Spezies kann als aktive Spezies (*active site*) für CO-Oxidationsreaktionen über Gold/Ceroxid-Katalysatoren nachgewiesen werden. Somit sind sowohl für die Aktivierung und Reaktion von CO, als auch für die Aktivierung von Sauerstoff bzw. Wasser als oxidierende Spezies entscheidende Informationen gewonnen worden, die auch auf weitere oxidische Trägermaterialien mit ähnlichen Eigenschaften übertragen werden können. Mit diesen Informationen sollte es möglich sein Edelmetall/Oxid-Katalysatoren, die auch technisch breite Anwendung finden, systematisch im Hinblick auf ihre Aktivität, Selektivität und Lebensdauer verbessert werden.

Abstract

The aim of this work is to elucidate the reaction mechanism of the CO oxidation and the water-gas shift reaction over gold/ceria as a prototype heterogeneous oxide supported metal catalyst. In this contribution a combined setup was developed to apply Raman/UV-Vis and infrared spectroscopy under reaction conditions to the active catalyst (*operando* approach). Along with density functional theory calculations (DFT) of ceria and gold/ceria model systems the experimental results are interpreted at the molecular level. With the PBE+U/4.5 eV functional Raman and infrared active vibrations of model systems are calculated and experimental bands are assigned to the vibrational modes properly.

With this approach a comprehensive interpretation of the Raman spectra of nanoparticle ceria is possible by predicting the first-order allowed Raman band (F_{2g} mode) and second-order allowed Raman bands (overtones). Additionally, the effect of oxygen vacancies on the precise position of the F_{2g} band can be quantified and an interpretation for the defect band region ($520 - 600$ cm^{-1}) can be given. Besides, the surface faceting of ceria can be probed by reassigning the band at 246 cm^{-1} of polycrystalline ceria to a mode confined at the CeO_2(111) surface. The behavior is confirmed at hydrothermally synthesized ceria nanocrystals exposing selectively the CeO_2(111) and CeO_2(100) surface facet. These nanoparticles possess a polyhedral and cubic shape, respectively, as evident from transmission electron microscopy images.

At the well defined ceria nanocrystals the facet dependent oxygen adsorption behavior is studied. Oxygen adsorbes as peroxide (O_2^{2-}) or superoxide (O_2^{-}) species preferably at surface oxygen vacancies of ceria. These species are probed by the respective O-O stretching mode employing Raman spectroscopy. The results reveal an overall facilitated oxygen adsorption and peroxide formation at the CeO_2(100) surface facet. This is supported by the DFT calculations predicting a higher adsorption energy for the CeO_2(100) facet. Superoxide formation at ceria nanoparticles exposing the CeO_2(100) facet is observed in this work for the first time. On the basis of DFT calculations the two bands in the superoxide region at 1103 cm^{-1} and 1137 cm^{-1} are assigned to two distinct superoxide configurations with Ce^{3+} in next nearest neighbor and nearest neighbor position, respectively.

These facet dependent properties of ceria are furthermore stressed by gold catalysts with a faceted ceria support. The flat CeO_2(100) support surface is three times more active than the flat CeO_2(111) surface for CO oxidation. However, the stepped CeO_2(111) surface of a polycrystalline ceria support is even more active than the CeO_2(100) surface. This clearly shows that the activity can be drastically enhanced by surface faceting and structuring of the ceria support.

To gain deeper insight into the support oxygen defect dynamics, time resolved *operando* Raman spectroscopy is applied to the Au/CeO_2 catalyst. Raman spectroscopy is able to probe the surface (246 cm^{-1} surface mode) and subsurface oxygen defect dynamics (F_{2g} position and defect bands) and hydroxyl groups. The results reveal that the subsurface oxidation state alters the activity of a gold/ceria catalyst for CO oxidation. An initially doubled activity is observed at a reduced catalyst compared to an oxidized catalyst. *Operando* Raman experiments at the Au/CeO_2 catalyst during water-gas shift revealed

similar oxygen dynamics. On the basis of the experiments a redox type mechanism (Mars-van Krevelen mechanism) is concluded for oxidations reactions over gold/ceria catalysts.

By a combined infrared and DFT study the active site for CO oxidation at Au/CeO_2 catalysts is found as CO adsorbed to a single Au^+ site in direct contact with the ceria support surface (CO-Au^+-$O_{lattice}$ species). The intensity of the band assigned to this species ($2125\ cm^{-1} - 2130\ cm^{-1}$) directly correlates with the activity of the catalyst. The assignment of the band to this distinct species is based on a thorough DFT study covering all possible adsorption sites of CO at a model Au/CeO_2 catalyst. The results, which are obtained with the PBE+U/4.5 eV functional, are confirmed with a hybrid (HSE06) functional to provide a robust basis for the assignment of the experimentally observed band.

Concluding, the results underline the potential of vibrational spectroscopy for *operando* characterization of catalyst materials. Together with DFT calculations, which allow a proper assignment of the bands in Raman or infrared spectra, this provides an interpretation on the molecular scale and direct conclusions for the reaction mechanism. The results may be directly transferable to other oxide supported metal catalysts highlighting the general relevance of the results presented in this study.

Table of Contents

1 Introduction

In 2010 catalysts with a market value of almost 20 billion dollars have been traded not including the value of the chemical products generated by these catalysts. [1] Additionally, more than 80 % of the products of the chemical industry have been in contact with a catalyst during production [1, 2] making catalysis a key technology of the chemical industry. The worlds largest chemical processes such as fluid catalytic cracking (FCC) over zeolithes or ammonia synthesis over iron are heterogeneously catalyzed highlighting particularly the relevance of heterogeneous catalysis. [2]

Another essential example for heterogeneous catalysis is the automotive exhaust treatment in three-way catalytic converters. With almost one billion cars worldwide and 45 million German cars more than every second person in Germany relies on this technology on a daily basis. [3]

In three-way catalytic converters crucial components are ceria and ceria containing materials which act as oxygen storage component. [4–6] Other components are active precious metal particles (Pt, Pd, Rh) which are deposited onto these oxide supports. [7, 8]

Ceria is not only applied as oxygen storage material but also in fuel cell applications [9] and as a photo catalyst [10–12] highlighting its wide spread applicability and the enormous potential that is linked to its redox properties.

In this work ceria is studied as a prototype active (non innocent) support material for deposited gold nanoparticles. The feature of an active support is an accelerated activity of the deposited precious metal nanoparticles compared to deposited particles at an inactive support, e.g., SiO_2, MgO, Al_2O_3. [13–15] Before the work of Haruta on heterogeneous catalysis [16, 17] and the work of Hashmi on homogeneous catalysis [18] gold was proposed to be a catalytically inert material.

Reactions which are catalyzed by ceria supported gold catalysts are the CO oxidation (equation 1.1), the water-gas shift reaction (equation 1.2) [19, 20], ethanol reforming [21] and the preferential CO oxidation in a H_2 rich stream, which can be employed for the purification of hydrogen streams from natural gas. [12, 22]

Although the CO oxidation and the water-gas shift reaction are oxidation reactions of small molecules with practically no side reaction, the mode of operation (mechanism) over metal/oxide catalysts is not yet fully understood. In contrast the CO oxidation over the single crystal Pd(111) surface [23] or the ammonia synthesis over the Fe(111) surface are understood on a molecular level. [24]

Therefore, in this work the oxidation of carbon monoxide was employed as a model reaction to study and characterize heterogeneous nanoparticle gold/ceria catalysts under reaction conditions. [25]

$$CO + \frac{1}{2}O_2 \rightarrow CO_2 \quad \Delta H^0 = -283\ \mathrm{kJ\ mol^{-1}} \tag{1.1}$$

As a related reaction the water-gas shift reaction was additionally studied over gold/ceria catalysts. Gold/ceria catalysts provide an alternative [19] to technically employed water-gas shift catalysts such as iron-chromia or copper zinc oxide [26] because gold/ceria catalysts show fast kinetics at low temperatures (473 K). Low temperatures are desirable for the process because the thermodynamic equilibrium favors the product formation (see equation 1.2).

$$CO + H_2O \rightleftharpoons CO_2 + H_2 \quad \Delta H^0 = -41.2 \text{ kJ mol}^{-1} \tag{1.2}$$

The reverse water-gas shift reaction (RWGS), i.e., the backward reaction of reaction 1.2, [27] might be of future interest as it allows the fixation of CO_2 with hydrogen. If hydrogen can be derived from a solar source, there is a possibility to create hydrocarbons sustainably from CO_2. Recent research activities on the mode of operation of gold/ceria catalysts for the CO oxidation and the water-gas shift reaction are summarized in the following section 1.1.

For a better understanding of the mode of operation of metal/oxide supported catalysts optical spectroscopy was applied under reaction conditions in this work. The approach is called *operando* spectroscopy. The requirements and recent developments on *operando* and *in situ* spectroscopy are discussed in section 1.2. The direct correlation of spectroscopic information and catalytic activity (*operando* approach) allows to derive structure activity relations. Additionally, the combination of optical spectroscopy and density functional theory (DFT) calculations of model structures provides an interpretation of the experimental results on a molecular scale.

The redox properties of ceria originate from the ease with which oxygen can be released from the ceria crystal. This leads to a distortion of the ceria lattice and a variation of the vibrational properties (solid state phonons). Replenishment of oxygen into the crystal starts at the surface by the formation of reduced oxygen species such as peroxides ($O_2{}^{2-}$) and superoxides ($O_2{}^{-}$). A versatile technique to probe solid state vibrational and adsorbate properties of nanoparticle ceria is vibrational Raman spectroscopy. It can be applied under a wide range of pressures and temperatures [28, 29] and is able to probe solid state phonons [30, 31] as well as adsorbed molecules such as peroxides and superoxides. [32, 33]

Infrared spectroscopy as complementary method (see section 1.3 for a detailed discussion of the complementary character of Raman and infrared spectroscopy) is a wide spread method for the characterization of adsorbates such as adsorbed CO as carbonyl (CO), carbonate (COO) and formate (CHO) species as well as surface hydroxyl groups at ceria [34–36] and gold/ceria catalysts. [37–39]

In this context the present work reports on the realization and application of a combined *operando* Raman/UV-Vis and infrared spectroscopic approach (see chapter 2) to study oxide supported metal catalysts. In the literature no detailed study about the assignment of Raman bands to the vibrational modes of polycrystalline ceria nanoparticles has been published yet. In particular, the vibrational properties of the low index surface facets such as the $CeO_2(111)$ and the $CeO_2(100)$ surface were not reported at all. Therefore, a comprehensive DFT study on the vibrational properties of polycrystalline ceria nanoparticles is shown in chapter 4. An introduction to DFT and the methodology to derive normal modes and Raman active modes of model systems is given in chapter 3. The DFT study includes the derivation of a quantitative relation between the position of the band assigned to the first-order allowed F_{2g} mode and the oxygen defect concentration of ceria. Besides, the Raman active vibrational modes of the $CeO_2(111)$ and $CeO_2(100)$ surface facets are derived and compared to experimental Raman spectra of nanosized ceria particles in chapter 5. The combination of Raman spectroscopy and DFT calculations allows to reassign the Raman band observed at 246 cm^{-1} at polycrystalline ceria to a longitudinal surface mode of the $CeO_2(111)$ surface. Therefore, Raman spectroscopy provides access to the surface oxygen ions of ceria under reaction conditions. As will be shown these oxygen ions are of direct relevance for oxidation reactions over ceria and metal/ceria catalysts. Molecular adsorption of oxygen as peroxide and superoxide at the ceria nanoparticles exposing the $CeO_2(111)$ and $CeO_2(100)$ facet was studied by *in situ* Raman spectroscopy and is reported in chapter 5. DFT models of peroxide and superoxide structures allow for determination of the adsorption geometry and the stability of the oxygen species. This leads to the first spectroscopic observation of a superoxide species at nanoparticle ceria exposing selectively the $CeO_2(100)$ surface in this work.

The results from the combined DFT and experimental spectroscopy study on the bare ceria support are of direct relevance for gold/ceria catalysts. Therefore, chapter 6 summarizes the influence of the ceria surface termination on the activity of gold particles highlighting that catalysts can be strongly improved by systematic surface nanostructuring. [40] It is found that the same amount of gold deposited at the thermodynamically less stable $CeO_2(100)$ surface facet is more active than on the flat $CeO_2(111)$ facet. However, at a polycrystalline support with a stepped $CeO_2(111)$ surface the catalyst revealed a fivefold activity compared to the flat $CeO_2(100)$ surface. These findings are rationalized by the oxygen vacancy formation energy that is lowered at the flat $CeO_2(100)$ surface compared to the flat $CeO_2(111)$ and is the lowest for stepped sites at the $CeO_2(111)$ surface facet.

In this context chapter 7 highlights the surface and subsurface oxygen and oxygen defect dynamics of gold/ceria catalysts. A direct quantitative relation between the oxygen vacancy concentration in the ceria support and the activity of gold/ceria catalysts is evidenced by *operando* Raman spectroscopy in conjunction with DFT calculations summarized in chapter 4.

Operando infrared spectroscopy was used to show that the concentration of adsorbed CO exhibiting a stretch frequency of $2125 - 2130$ cm^{-1} is proportional to the activity of the catalyst. By a thorough density functional theory study this frequency can be assigned to CO adsorbed to an oxidized gold atom (Au^+) in direct contact with a surface oxygen ion ($O_{lattice}$) of the ceria support. This allows to pin down the active site of a gold/ceria catalyst to a single gold site ($O_{lattice}$-Au^+-CO). DFT results show that this isolated species is also formed dynamically from three dimensional gold particles under reaction conditions. For details on this study see chapter 8.

Chapter 9 focuses on the ceria support dynamics in Au/CeO_2 catalysts during water-gas shift reaction. A redox type mechanism (Mars-van Krevelen mechanism) is proposed on the basis of *operando* Raman spectroscopy and isotopic labeling experiments using $H_2{}^{18}O$. Raman spectroscopy revealed an insertion of ^{18}O ions into the ceria support surface in the absence of CO and without the formation of formate or carbonate intermediate species. In the literature such molecules are proposed as intermediate species. [41–44]

In conclusion, the potential of a combined and complementary *operando* Raman and infrared spectroscopy approach is emphasized. The interlinkage of experimental spectra and calculated vibrational properties of model systems by density functional theory provides an interpretation on the molecular scale. This allows to clarify key aspect of the reaction mechanism. In particular the influence of oxygen vacancies in the ceria support on the catalyst activity is evidenced in this work. Potentially the properties are directly transferrable to other oxide supported precious metal catalysts. The dynamics of oxygen ions in the support and the liability of the oxidation state with respect to the gas-phase environment highlight the requirement for a direct characterization of oxide catalysts under working conditions (*operando* approach).

1.1 Research activities

For the synthesis of nanosized and faceted ceria nanostructures hydrothermal conditions can be employed according to prior reports [45] (compare also [46] for a thorough review on shape selective synthesis of ceria). The properties of ceria with different surface facets have been reviewed by D. Mullins [47] while the relevance for catalysis and oxygen storage capacity has recently been highlighted by A. Trovarelli and J. Llorca. [48]. Polycrystalline ceria with different particle sizes and an increased initial oxygen defect concentration can be yielded without impurities from decomposition of a nitrate $Ce(NO_3)_3$ precursor at temperatures above 600°C. [49]
Regarding the characterization of the bare ceria support or metal/ceria catalysts Raman spectroscopy has proven to be a versatile method. [50, 51] Raman spectroscopy probes the solid state phonons of ceria. The oxygen defect formation can be followed by a shift of the phonon bands after oxygen vacancy and Ce^{3+} formation and characteristic phonons originating from an oxygen defect in the ceria crystal. [50] Therefore, Raman spectroscopy is very sensitive for oxygen vacancies in the ceria lattice and can be applied under reaction conditions. [52] A comparable sensitivity for Ce^{3+} formation under reaction conditions has recently been achieved in a study on Pt/CeO_2 catalysts by synchrotron based resonant X-ray emission spectroscopy. [53] Besides, molecular oxygen adsorption into the surface oxygen defects and formation of peroxide and superoxide molecules at polycrystalline ceria and faceted ceria particles has been studied by Raman spectroscopy. [32, 33] However, at $CeO_2(100)$ facets superoxide formation has not been observed before. The process of oxygen adsorption and the formation of peroxide and superoxides has been studied by DFT [54,55] and even combined experimental (Raman) and DFT studies exist. [56] But an in-depth understanding of oxygen adsorption at polycrystalline ceria and faceted ceria is lacking. The aspect of oxygen adsorption at distinct surface facets of ceria has recently been studied at single crystal surfaces employing infrared reflection absorption spectroscopy (IRRAS). [57]
Apart from one study at polycrystalline ceria [49] the literature assignments of Raman bands <1200 cm^{-1} of ceria are based on single crystal studies. [30] Nevertheless, these fundamental aspects on the bare ceria support are of direct relevance for the understanding of metal/oxide supported catalysts.

For the CO oxidation over gold/ceria catalysts a support effect was proposed based on nanosizing [13] and nanofaceting [58] of the ceria support. An increased activity upon nanosizing or nanofaceting of the ceria support suggests a participation of the support in the reaction mechanism. These observation are in line with the proposal of an active fraction of oxygen ions of ceria in the proximity of gold particles as concluded from temporal analysis of products (TAP) experiments by D. Widmann and R. J. Behm. [59] Additionally, the gold particle size was shown to play a major role [38, 60] and the adsorption sites of deposited gold particles were studied by transmission electron microscopy (TEM). [61] An optimum size of gold particles was proposed for TiO_2 single crystals as a support material under low pressure conditions. [62]

Density functional theory allows to predict the CO oxidation reaction mechanism at model structures (for an introduction see section 3.1). The authors propose the CO oxidation to proceed at the perimeter between gold (Au_1, [63] Au_3, [64] Au_{13} [65,66], Au_{20} [67]) and the $CeO_2(111)$ support surface. Recently, also the dynamic formation of a single gold site Au_1 was proposed that can also be formed by abstraction of Au_1 from a three dimensional particle in the presence of CO. [67] The reaction is predicted to proceed via adsorption of CO at gold and oxidation by a lattice oxygen atom resembling a Mars-van Krevelen type mechanism. Meanwhile the ceria lattice is reduced by two electrons that localize at the cerium centers forming Ce^{3+} ions. [65,67] The reoxidation is assumed to proceed via gas-phase O_2 adsorption into the defect forming reduced molecular oxygen species such as peroxides (${O_2}^{2-}$). [65,67] For a detailed discussion on reduced oxygen species at the ceria surface the reader is referred to chapter 4 for DFT and to chapter 5 for experimental results. However, the mechanism of CO oxidation over gold/ceria has not been verified experimentally up to now.

For the water-gas shift reaction at Au/CeO_2 catalysts a support effect was shown for polycrystalline ceria [19] and ceria single crystals [68] but the reaction mechanism remains unclear. A formate intermediate was proposed on the basis of results from infrared spectroscopy originally for Rh/CeO_2 [41,42,69] and later for Au/CeO_2 catalysts. [43,44] This mechanism was questioned by experimental [70,71] and theoretical [72] studies. Likewise a redox type mechanism [19] that is comparable to a Mars-van Krevelen type mechanism was questioned on the basis of DFT calculations. [72] Theoretical approaches predicted a carboxyl intermediate [73] that was not confirmed experimentally for polycrystalline ceria catalysts but a carboxyl intermediate was observed for inverse catalysts. [74] The inverse catalysts consist of ceria (CeO_x) or titania (TiO_x) deposited on a Au(111) surface. Therefore the observations highlight also the non inert character of a gold surface. [74,75] However, no evidence for the type of mechanism and formate or carboxylate intermediate has been provided in the literature so far. Besides no *operando* Raman study of Au/CeO_2 catalysts under water-gas shift reaction conditions has been reported.

In summary, the support properties of gold/ceria catalysts in oxidation reaction and especially the defect dynamics have not yet been fully understood. Besides the effect of ceria surface faceting with respect to the low index surface planes is not known and there has been no direct spectroscopic evidence for the active site in oxidation reactions over gold/ceria catalysts.

1.2 The *in situ/operando* spectroscopy approach

The difference between the *in situ* and the *operando* spectroscopy approach is essential. While *in situ* spectroscopy refers to a spectroscopic method applied to a material under specified conditions, *operando* spectroscopy refers to the reaction conditions of a catalytically active material. Besides that, the activity of the catalyst must be verified. The term *operando* is sometimes also related to so-called realistic reaction conditions for the corresponding chemical process. This means that the same reactor type and geometry as in the corresponding chemical process needs to be applied to observe the same conversion and selectivity in the *operando* experiment. [76,77] It should be mentioned that with *in situ* approaches valuable structural information can be found. [78] In contrast, direct structure-activity relations can only be drawn from *operando* experiments, because this approach allows the characterization of the catalyst during reaction while monitoring simultaneously the activity.

In this work the *operando* approach is applied in a *dynamic* way (see section 2.4) that allows to measure the spectroscopy and the activity of the catalyst fast enough to follow activation and deactivation process of the catalyst in a *time-resolved* fashion. Ceria materials and gold/ceria catalysts are studied as active catalysts. For Au/CeO_2 catalysts during CO oxidation and water-gas shift reaction no distinct *operando* conditions are defined. Therefore spectroscopy applied under reaction conditions while monitoring the activity of a catalyst is called *operando* spectroscopy in this work.

An overview and critical review on *in situ* techniques applied at heterogeneous catalysts has been given in a special issue of Chemical Society Reviews 39, 2010 edited by B. Weckhuysen. [78] In this special issue the combination of different *in situ* techniques in one cell is highlighted by U. Bentrup [79]. The combination of spectroscopic methods was also described by Brückner [80] and by Tinnemans *et al.* [81] before. These articles conclude that materials relevant for catalytic reactions are so complex that characterization with only one technique is insufficient to fully reveal the mode of operation. The combination of techniques preferably in one cell guarantees identical conditions for *in situ* characterization. This provides insight from different spectroscopic angles. Furthermore the conclusions drawn from each method individually can be cross linked to another method to gain detailed structural information.

The first Raman setup reported as *operando* setup in the literature dates back to 2002. This was also the introduction of the term *operando spectroscopy* by M. A. Bañares. [82–84] The studies focused on oxide catalysts and the activity was measured by gas chromatography.

The use of Raman and UV-Vis spectroscopy in one setup is a common combination of *in situ* methods. It was used, e.g., for the study of Cr/Al_2O_3 catalysts during propane dehydrogenation. [85] Due to coke formation during the reaction the absorption of the sample increases drastically. This decreases the overall intensity of the Raman spectra. With the aid of UV-Vis spectroscopy the intensity of the Raman spectra could be corrected for changes in absorption without adding an internal standard to the sample. [85]

Besides X-ray techniques have also been combined with Raman and UV-Vis spectroscopy, for example in the group of B. Weckhuysen in Utrecht. Cells combining these two spectroscopic techniques with X-ray diffraction techniques, e.g., wide angle X-ray scattering (WAXS) [86] and small angle X-ray scattering (SAXS) were developed. [87] Besides, X-ray absorption spectroscopy (allowing NEXAFS, EXAFS) has also been combined with Raman and UV-Vis spectroscopy. [88]

In opposite to Raman and UV-Vis spectroscopy, combining Raman and diffuse reflectance infrared spectroscopy in one setup is rare. Le Bourdon *et al.* [89] described such a setup to study alumina supported Pd catalysts. The same setup was also used for a study on Mo/Al_2O_3 catalysts following the formation of the active phase and adsorbed species simultaneously. [90]

To my knowledge, a combination of Raman/UV-Vis and infrared spectroscopy under comparable conditions where the catalyst shows quantitatively the same activity behavior as described in chapter 2 [52] has not been reported in the literature yet.

1.3 Comparison of infrared and Raman spectroscopy

Infrared and Raman [91, 92] spectroscopy are complementary spectroscopic methods for the characterization of vibrational properties of molecules and solids. In figure 1.1 the Raman *scattering* and infrared *absorption* process are schematically shown for the same transition between the vibrational ground state ($v = 0$) and the first excited state ($v = 1$). In infrared spectroscopy a photon with a frequency $h\nu_{\text{vib}}$ is absorbed to excite the molecule ($v = 1$), whereas in Raman spectroscopy monochromatic light ($h\nu_{\text{ex}}$) from a laser is scattered at the molecule. The energy $h\nu_{\text{ex}}$ does not necessarily correspond to a difference between eigenstates of the system. However, if an eigenstate is close in energy the scattering process can be intensified leading to so-called resonance Raman spectroscopy. [92]

Elastic scattering gives rise to Rayleigh scattered photons. The scattered photons have the same energy $h\nu_{\text{ex}}$ as the incident photons. Inelastic scattering at a molecule in an excited state (for example $v = 1$) can transfer energy to the scattered photon $h(\nu_{\text{ex}} + \nu_{\text{vib}})$ (Anti-Stokes scattering). Molecules in any vibrational state can take up energy from the incident photons $h(\nu_{\text{ex}} - \nu_{\text{vib}})$ (Stokes scattering). The Rayleigh scattering provides no information about the molecule and needs to be filtered by an absorbing material (Notch Filter) [52] or a triple-stage spectrograph [93] although it represents the scattering process that is by far the most probable. [92] Due to the higher population of the vibrational ground state $v = 0$ the Stokes scattering is practically more relevant than Anti-Stokes scattering. In practice $h\nu_{\text{ex}}$ ranges from near IR (1100 nm) to the UV region (200 nm). In this work a visible excitation of $\lambda_{\text{ex}} = 532$ nm was employed. From the scheme it is clear that Stokes scattered photons are slightly redshifted from the excitation $h(\nu_{\text{ex}} - \nu_{\text{vib}})$. The polychromatic scattered light is dispersed at a diffraction grating and measured by a CCD array (multiplexing, for further details on the experimental setup see section 2.1).

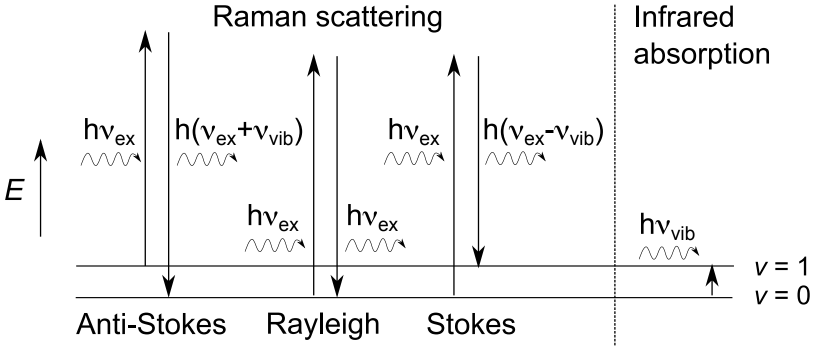

Figure 1.1.: Raman scattering and infrared absorption process for two vibrational states $v = 0$ and $v = 1$ of a molecule. Elastic scattering causes Rayleigh scattered photons and inelastic scattering Anti-Stokes and Stokes scattered photons.

In infrared spectroscopy the polychromatic light is dispersed by an interferometer and the interferogram is Fourier transformed (spectrometer and software supplied by Bruker) to measure an absorption spectrum ($4000 - 400$ cm^{-1}) with a resolution of 1 cm^{-1} in ~1 second. Both vibrational spectroscopic techniques are quantitative.

The complementary character of the two techniques originates from the different selection rules that are discussed in the following for a diatomic molecule, where x refers to the internuclear distance of the molecule. [94] The transition moment for an infrared absorption process can be written as follows.

$$\boldsymbol{R}_v = \int \psi_v^{\prime *} \boldsymbol{\mu} \psi_v^{\prime\prime} dx \tag{1.3}$$

The dipole moment is then expanded in a Taylor series

$$\boldsymbol{\mu} = \boldsymbol{\mu}_0 + \left(\frac{d\boldsymbol{\mu}}{dx}\right)_0 x + \frac{1}{2}\left(\frac{d^2\boldsymbol{\mu}}{dx^2}\right)_0 x^2 + \ldots \tag{1.4}$$

resulting in the transition moment

$$\boldsymbol{R}_v = \boldsymbol{\mu}_0 \int \psi_v^{\prime *} \psi_v^{\prime\prime} dx + \left(\frac{d\boldsymbol{\mu}}{dx}\right)_0 \int \psi_v^{\prime *} x \psi_v^{\prime\prime} dx + \ldots \tag{1.5}$$

The first term is zero due to the fact that the eigenfunctions to the Hamiltonian for the vibrations in the harmonic approximation form an orthonormal set. From the second summand the selection rule $\Delta v = \pm 1$ can be derived. [94] Moreover, the dipole moment must vary during vibration along the mode $\left(\frac{d\mu}{dx}\right)_0 \neq 0$. This property can be derived for model systems from the effective charge of the atoms and the normal mode vector of any vibration (see chapter 3).

In contrast, for Raman spectroscopy the induced dipole moment which is proportional to the electric field needs to be analyzed. The proportional factor $\boldsymbol{\alpha}$ is the polarizability. [94]

$$\boldsymbol{\mu}_{\text{ind}} = \boldsymbol{\alpha}\, \boldsymbol{E} \tag{1.6}$$

For a diatomic molecule $\boldsymbol{\alpha}$ can be expanded in a Taylor series.

$$\boldsymbol{\alpha} = \boldsymbol{\alpha}_0 + \left(\frac{d\boldsymbol{\alpha}}{dx}\right)_0 x + \frac{1}{2}\left(\frac{d^2\boldsymbol{\alpha}}{dx^2}\right)_0 x^2 + \ldots \tag{1.7}$$

The transition moment is shown in the following and can be directly compared to the equation 1.5 given above.

$$\boldsymbol{R}_v = \left(\frac{d\boldsymbol{\alpha}}{dx}\right)_0 E \int \psi_v^{\prime *} x \psi_v^{\prime\prime} dx + \ldots \tag{1.8}$$

For a polyatomic molecule $\boldsymbol{\alpha}$ is a symmetric matrix with $\alpha_{ij} = \alpha_{ji}$:

$$\begin{pmatrix} \mu_x \\ \mu_y \\ \mu_z \end{pmatrix} = \begin{pmatrix} \alpha_{xx} & \alpha_{xy} & \alpha_{xz} \\ \alpha_{yx} & \alpha_{yy} & \alpha_{yz} \\ \alpha_{zx} & \alpha_{zy} & \alpha_{zz} \end{pmatrix} \begin{pmatrix} E_x \\ E_y \\ E_z \end{pmatrix} \tag{1.9}$$

The relation between the off-resonant Raman scattering intensity and the matrix elements for an ensemble of randomly oriented molecules or particles is described in section 3.3. In contrast to infrared spectroscopy, the polarizability must vary during vibration along the normal mode vector, i.e., $\left(\frac{d\boldsymbol{\alpha}}{dx}\right)_0 \neq 0$. The major advantage of Raman spectroscopy is that the stretching mode of homoatomar diatomic molecules and ions such as O_2 and reduced ${O_2}^{x-}$ can be probed.

1.4 Normal mode analysis

Density functional theory (DFT) calculations were employed in this work to determine the normal modes and corresponding frequencies of model systems. DFT calculations provide a proper description of the electronic structure specifically of reduced ceria systems. [95] However, a normal mode analysis as described in the following is not limited to DFT calculations but can also be performed by application of a suitable force field.

In general, to calculate the normal modes of the system the kinetic energy T of the nuclei and potential energy V for bond stretching can be written within the framework of classical mechanics as follows: [96]

$$T = \frac{1}{2}\sum_{i=1}^{3N}\dot{q}_i^2 \qquad V = V_0 + \sum_{i=1}^{3N}\left(\frac{\partial V}{\partial q_i}\right)_0 q_i + \frac{1}{2}\sum_{i=1}^{3N}\left(\frac{\partial^2 V}{\partial q_i \partial q_j}\right)_0 q_i q_j + \ldots \tag{1.10}$$

Here q_i refers to mass weighted normal coordinates, e.g., $q_1 = \sqrt{M_1}\Delta x_1$. [96] Within the harmonic approximation the first term of the potential energy V is set to zero. The second term cancels due to the vanishing derivative of the potential energy with respect to the normal mode at the equilibrium bond length. The terms of higher order than the third order are neglected and the third term $\left(\frac{\partial^2 V}{\partial q_i \partial q_j}\right)_0$ is abbreviated as f_{ij} in the following. Inserting this into the Newton equation of motion $F = m\ddot{q}$ and leaving out cross-products results in a differential equation that can be solved by periodic functions for q_i with an angular frequency $\omega = \sqrt{\lambda}$ and amplitude a. [96]

$$\ddot{q}_j + \sum_{i=1}^{3N} f_{ji} q_i = 0 \tag{1.11}$$

This leads to a matrix eigenvalue problem.

$$\sum_{i=1}^{3N}(f_{ji} - \delta_{ji}\lambda)a_i = 0 \quad j = 1, 2, \ldots, 3N \tag{1.12}$$

The matrix eigenvalue problem is solved by equating the so called secular determinant to zero. [96]

$$\begin{vmatrix} f_{1,1}-\lambda & \cdots & f_{1,3N} \\ \vdots & \ddots & \vdots \\ f_{3N,1} & \cdots & f_{3N,3N}-\lambda \end{vmatrix} = 0 \tag{1.13}$$

To calculate the normal modes for a model structure, the coefficients of the matrix can either be determined by a finite differences approach, i.e, by calculating the second derivative numerically or by density functional perturbation theory (DFPT). [97, 98] In the DFPT approach and for phonon calculations of extended systems the Fourier transformed matrix of the coefficients is calculated analytically. [97] Both approaches are implemented in modern DFT codes. The matrix containing the second derivatives of the potential energy with respect to the positions is called the Hessian matrix and $6N$ calculations are necessary when N is the number of atoms of the considered model system. Usually a symmetry adaptation is implemented in the DFT code, which reduces the $N \times N$ matrix to matrices that are solved separately. [99]

It can be stated qualitatively that for a calculation of the vibrational frequencies the second derivatives of the energy with respect to the normal modes need to be calculated. For the calculation of Raman intensities the third derivatives of the energy with respect to the normal mode are calculated as will be shown in section 3.3. This already provides an idea of the high computational demand to calculate Raman intensities of normal modes.

1.5 Density functional theory (DFT) applied to ceria model systems

The approaches to model titania, zirconia, vanadia, and ceria with density functional theory (DFT) were reviewed by M. V. Ganduglia-Pirovano, A. Hofmann, and J. Sauer in 2007. [95] A further review article, which compared DFT to experimental results, was published by J. Paier *et al.* [100] and the role of ceria in catalysis from theoretical point of view was reviewed by M. V. Ganduglia-Priovano. [101]

The above mentioned studies [102–104] agree that the conventional local density approximation (LDA) and generalized gradient approximations (GGA) for the exchange correlation are not able to describe the properties of reduced ceria properly. For these systems the exchange correlation functionals predict a false metallic character corresponding to a delocalized excess electron density in opposite to the experimentally observed localization of the electron density at a cationic center (Ce^{3+}). The localization of the excess charge at a cerium center is correctly described with hybrid functionals such as the one reported by Heyd, Scuceria, and Ernzerhof (HSE06). [105, 106] A computationally less demanding alternative is a DFT+U [107] approach, where the actual value of U_{eff} applied to a Ce 4*f* orbital is still under research. A value of $U_{\mathrm{eff}} = 4.5$ eV for the Ce 4*f* orbital has been proposed by Fabris *et al.* [108] and this value has been applied in the most recent studies. [57, 109, 110] As exchange correlation functional the GGA type functional by Perdew, Burke, and Ernzerhof (PBE) is employed. This setup is referred to as PBE+U/4.5 eV in the following.

Experiments at well defined ceria thin films and single crystals under ultra-high vacuum conditions such as scanning tunneling microscopy (STM) [111, 112] and atomic force microscopy (AFM) [113] elucidated the structure of oxygen vacancies at the $CeO_2(111)$ surface. DFT calculations with the PBE+U/4.5 eV functional reproduced the experimentally observed structures. [103, 114] Furthermore combined experimental and theory studies found ceria stoichiometries of CeO_2, Ce_7O_{12}, Ce_3O_5, and Ce_2O_3, that could be modeled by the DFT+U approach properly. [115, 116] Therefore this setup is also chosen as basis for the vibrational analysis of stoichiometric and reduced ceria and ceria surface calculations.

To investigate the ceria surface by density functional theory usually a periodic approach is employed with an infinite surface slab in x and y direction and an added vacuum on top the surface slab in z direction. The bottom three ionic layers (O-Ce-O) are fixed to the bulk position and the other layers are allowed to relax. Then the formation of oxygen vacancy or adsorption of atoms or molecules is studied. For a description of the employed model systems in this work and the computational details see section 3.2. The ceria surface that is studied mostly is the non polar $CeO_2(111)$ surface. The $CeO_2(100)$ surface has a polar character and can be modeled by a checkerboard type of arrangement of oxygen ions for the surface and bottom oxygen layer (see section 4.6). However, other surface reconstructions have been considered. [95,117] The surface energy increases for the low index surfaces according to $(100) < (110) < (111)$ whereas the relaxation energy for the surfaces increases in opposite direction. [118] Therefore the $CeO_2(111)$ surface is also predicted as the moste stable and the $CeO_2(100)$ as the least stable surface structure. [119, 120]

The interaction of the low index surfaces with CO is widely studied [121–124] as well as the interaction of water with the $CeO_2(111)$ [125, 126] and $CeO_2(100)$ surface. [127] Peroxide formation at the $CeO_2(111)$ surface has been modeled in various studies, [54–56] but only rarely studied on the $CeO_2(100)$ surface. [57] However, a comprehensive analysis of the vibrational properties of peroxide and superoxides at the low index ceria surfaces in conjunction with experiment is limited to an infrared study at ceria single crystals [57] and Raman intensities as well as a coverage-dependence have not been addressed at all. The vibrational properties of doped ceria have been studied with a rigid ion model [128] but the vibrational properties of reduced ceria and the low index surface facets have not been tackled.

The interaction of gold (Au) with the reduced $CeO_{2-x}(111)$ surface is debated in the literature. [129–131] And the interaction with the oxidized $CeO_2(111)$ surface is rather clear. [131, 132] But a detailed analysis of CO adsorption sites at $Au/CeO_2(111)$ model systems and calculations of the CO stretch frequency that allow for a direct comparison with infrared experiments are lacking in the literature.

Besides a vibrational analysis, reaction mechanisms can be calculated by DFT employing the nudge elastic band (NEB) method that predicts transitions states, i.e., the lowest saddle points in the potential energy surface. [133] With this method the reaction mechanisms and energy barriers for reactions at Au/CeO_2 catalyst model systems have been calculated. [63–65, 67, 73] In this work it is frequently referred to these studies and model structures of this study compare to those in the literature, but the NEB method is not explicitly employed here.

2 Experimental[1]

In section 1.2 the *operando* spectroscopic approach is explained. This experimental chapter describes the combined *operando* Raman, UV-Vis, and infrared spectroscopic approach that was established in this work in sections 2.1 to 2.3. To my knowledge such a complementary setup has not been reported in the literature. Dynamic *operando* measurements, i.e., continuous spectroscopic measurements at the catalyst during activation and deactivation processes of the catalyst are described in section 2.4. Section 2.5 covers the synthesis of CeO_2 nanoparticles and gold deposition. The last section 2.6 describes the *ex situ* characterization methods.

2.1 *Operando* Raman/UV-Vis spectroscopy setup

Operando Raman and UV-Vis spectroscopy was combined in one cell (see Figure 2.1). The cell (volume: <100 ml) is directly attached to the vacuum chambers of an X-ray photoelectron spectrometer (XPS, see LHS/SPECS spectrometer in section 2.6). [135] The samples can be studied with the optical spectroscopic methods at ambient pressure in various gas atmospheres. Furthermore the reaction cell can be evacuated and samples can be transferred to the high vacuum chamber for XPS measurements without exposure to air. However, these *quasi in situ* XPS measurements are not reported in this work. [135]

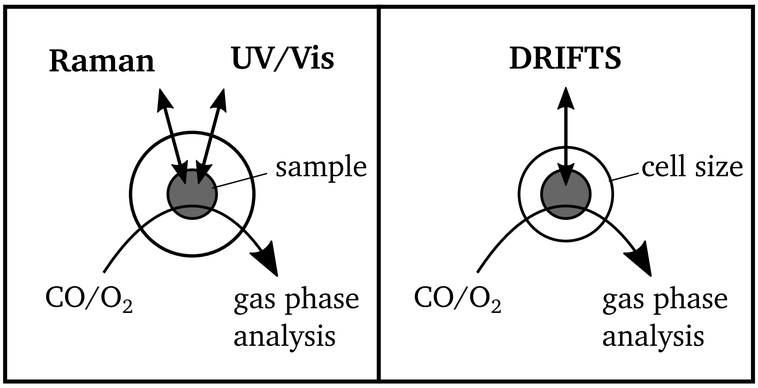

Figure 2.1.: Scheme of the *operando* approach. While the catalyst is exposed to reaction conditions spectroscopy is applied to the catalyst. For the combined *operando* approach Raman and UV-Vis spectroscopy is done in one setup (left panel) and diffuse reflection infrared (DRIFT) spectroscopy at comparable conditions in another setup (right panel).

Raman spectra at ambient pressure were recorded in backscattering mode on a HL5R transmission spectrometer (Kaiser Optical) with a laser excitation of λ_{ex} = 532 nm from a frequency doubled Nd:YAG laser (Cobolt). The spectral resolution was specified as 5 cm^{-1}, but the stability over 300 minutes and the

---

[1] The details about the experimental setup are already published. Parts of the publication including figures are reprinted/adapted with permission from Springer Nature, C. Schilling, C. Hess, *Top. Catal.*, **2017**, *60*, 131-140. Copyright 2016. Further details are given in ref. [134].

reproducibility of the band position of the F_{2g} mode of polycrystalline ceria was better than 0.3 cm^{-1}. The MR Filtered Probe Head (Kaiser) is employed to filter the Rayleigh scattered light with a Super-Notch-Filter allowing the detection of Raman shifts as low as $\sim$150 cm^{-1}. The charged-coupled device (CCD) array was calibrated by 18 emissions of an Argon lamp across the spectral region between 532 nm (corresponding to the Rayleigh light and a Raman shift of 0 cm^{-1}) and 675 nm (Raman shift of 4000 cm^{-1}). The precise spectral position of the Rayleigh frequency was obtained by shifting the frequency of the C-C stretching mode of cyclohexane (measure in liquid phase) to the Raman shift value of 801.8 cm^{-1}.

For the measurements an 1/2” immersion probe (with sapphire optics, Kaiser) is applied to the reaction chamber and with a laser power of 2.0 mW or 1.0 mW (measured with an Ophir® Nova device at the sample position) identical Raman spectra were recorded. Additionally the measured effects such as band shifts and intensity variations as for example reported in chapter 7 are reproducible for both laser powers. Therefore a laser power of 1.0 mW was used to avoid damage caused by the laser beam. The sampling time ranged between 10 s for bare ceria materials (low absorption at λ_{ex}, see black UV-Vis spectrum in figure 2.3) and 80 s for Au/CeO_2 during water-gas shift (stronger absorption at λ_{ex}, see figure 9.5). The shown Raman spectra are the average of five accumulations and a background spectrum (CCD array not illuminated) was recorded before each spectrum and subtracted from the measured spectrum. Two similar measurements were made to delete artifacts from cosmic rays (cosmic ray filter, CRF). For the dynamic *operando* Raman spectra the background was recorded prior to a series of spectra ($\sim$1 h) and cosmic rays were not filtered. The sampling time amounted to 200 s for an average of five spectra (40 s) for the continuous measurements.

Unless otherwise state the intensity of the Raman spectra are reported as measured (see for example chapter 7). In chapter 9 the spectra are corrected for the sample absorption at the laser excitation wavelength. The Raman intensity is plotted as a function of the Raman shift, i.e., the deviation of the measured frequency from the excitation frequency as reciprocal wavelength $\frac{1}{\lambda}$ (wavenumber $\tilde{\nu}$, in units of cm^{-1}).

UV-Vis spectra were conducted in diffuse reflection mode on an AvaSpec-ULS2048 (Avantes). As excitation sources a D_2 and a halogen lamp were employed. Magnesium oxide (MgO, Sigma Aldrich) powder was used as reference sample providing no absorption between 170 and 1100 nm. The sampling time is 60 s as a result of a 300 ms exposure and averaging over 200 spectra.

During dynamic measurements (see section 2.4) Raman and UV-Vis spectra were continuously conducted in an alternating fashion.

For *in situ/operando* measurements 25-35 mg of the sample was placed in a stainless steel sample holder (∅: 8 mm, depth: 0.5 mm). The sample holder was fixed on top of an electric heating in the ambient pressure cell of a modified X-ray photoelectron spectrometer already reported in reference [135].

The gas feed for the cell (see Figure A.1 in the appendix) can be mixed from CO (99.997 %, Air Liquide, 0.6 − 20 ml/min), O_2 (99.999 % Westfalen, 1.6 − 200 ml/min), and Argon (99.996 %, Westfalen, 1 − 200 ml/min) by digital mass flow controllers (Bronkhorst®). Additionally, a system was installed, where fluids can be evaporated into a gas stream in a controlled evaporator mixer (CEM, Bronkhorst®). The amount of fluid is measured by a liquid mass flow meter (0 − 5.0 g/h, LFM, Bronkhorst®). For details see Figure A.1.

For the studies on the water-gas shift reaction up to 10 % water were added resulting in a total gas stream of 100 ml/min. Therefore heated gas pipes were employed and the whole reaction cell was heated to at least 60°C. The minimum volume of fluid to be added in the fluid reservoir (stainless steel pressure vessel) is 10 ml to allow the evaporation of expensive water isotopes, e.g., $H_2{}^{18}O$ (compare chapter 9).

The effluent gas stream of the reaction cell was analyzed continuously by gas phase Fourier transform infrared spectroscopy (FTIR, Tensor 20, Bruker) with a resolution of 4 cm^{-1}. A spectrum corresponds to the average of 120 spectra recorded in one minute. A >6 point calibration curve comparing infrared absorption and concentration of CO_2 (CRYSTAL mixture of 1.020 % ± 0.020 %, 99.995 % CO_2 and 99.999 % N_2), of CO (99.997 %, Air Liquid), and of evaporated deionized water (electric conductivity <3 μS m^{-1}) in Argon allow for a quantitative analysis of the gas stream. For a calibration and quantitative evaluation of the product gas stream the infrared absorption spectra were evaluated in the spectral regions $2273 - 2400$ cm^{-1}, $2142 - 2210$ cm^{-1}, and $1218 - 1853$ cm^{-1} for CO_2, CO, and H_2O, respectively. The $H_2{}^{18}O$ concentration was not evaluated explicitly, neither the $C^{16}O^{18}O$ concentration due to slight shifts of the corresponding vibrational frequencies caused by the ^{18}O isotope.

The reaction gas mixture (100 ml/min) during CO oxidation was composed of 2 % CO and 10 % O_2 balanced with Argon. To realize oxidizing conditions for pretreatment 25 % O_2 was balanced with Argon. In this work 2 % CO concentration refers to a stream consisting of 2 ml/min CO balanced to a total stream of 100 ml/min mixed by MFCs (see above). For the exposure to reducing conditions 2 % CO was balanced with Argon. For the water-gas shift reaction the gas phase was composed of 8 % or 10 % H_2O (deionized) and 2 % CO balanced with Argon. Experiments were repeated with the $H_2{}^{18}O$ isotope (97 %+ ^{18}O, euriso-top®). Prior to water-gas shift experiments the cell was thoroughly flushed with argon to avoid CO_2 production from residual oxygen in the cell (CO oxidation).

The conversion of CO can be derived from the CO signal at 2143 cm^{-1} in FTIR spectra (compare to the evaluated regions given above). Due to the higher absorption cross section of CO_2 at 2349 cm^{-1} the catalytic activity was rather derived from the CO_2 concentration in the effluent gas stream. As no other by-products were detected and the mass balance is completely balanced, it is proposed that the catalytic activity derived from the CO_2 concentration resembles the conversion of CO for the CO oxidation and the water-gas shift reaction here.

The cell is furthermore equipped with a thermocouple and the thermovoltage of a Ni/Cr-Ni thermocouple (Type K) was monitored continuously with a multimeter (Tektronix DMM 4050). The thermocouple revealed the actual sample temperature as it was placed in direct proximity to the sample. During room temperature (21°C ± 2°C) CO oxidation a maximum temperature increase of ~2°C was observed.

2.2 *Operando* diffuse reflectance infrared spectroscopy setup

Diffuse reflectance infrared Fourier transform spectroscopy (DRIFTS) of the working catalyst material was performed at a Vertex 70 spectrometer (Bruker) equipped with a liquid N_2 cooled mercury cadmium telluride (MCT) detector operating at a resolution of 1 cm^{-1}. A commercial cell (Praying Mantis™High Temperature Reaction Chamber, Harrick Scientific Products) with CaF_2 windows was employed as reaction cell. The cell was equipped with an electric heating allowing for measurements between room temperature and ~400°C. Potassium bromide (KBr) powder was used as infrared transparent sample for the background spectrum. The powder was heated to 200°C for 1h in 25 % O_2 balanced with Argon prior to the measurement of the background spectrum at room temperature (21°C).

The sample holder exposed the same amount of sample in the same geometry (stainless steel, ∅: 8 mm, depth: 0.5 mm) as in the *operando* Raman/UV-Vis setup. The thermocouple was placed in direct proximity to the sample as described above and revealed the same temperature increase of 2°C as in the Raman/UV-Vis setup during room temperature CO oxidation (21°C ± 2°C). Due to the minor temperature increase thermal effects at the sample can be safely ruled out.

2.3 Combined *operando* Raman/UV-Vis and infrared spectroscopy setup

Operando Raman and UV-Vis spectroscopy was combined in one cell under identical conditions as described above. So, there was no influence of different cell geometries on the reaction conditions. The *operando* diffuse reflectance infrared spectroscopy (DRIFTS) setup had a slightly different cell geometry. To avoid influences of the cell geometry on the activity of the catalyst in both setups the same amount of a 0.5 wt% Au/CeO_2 catalyst was provided in an identical sample holder geometry (see above). Then the gas composition over the catalyst was monitored continuously in both setups by FTIR gas phase spectroscopy (see figure 2.2).

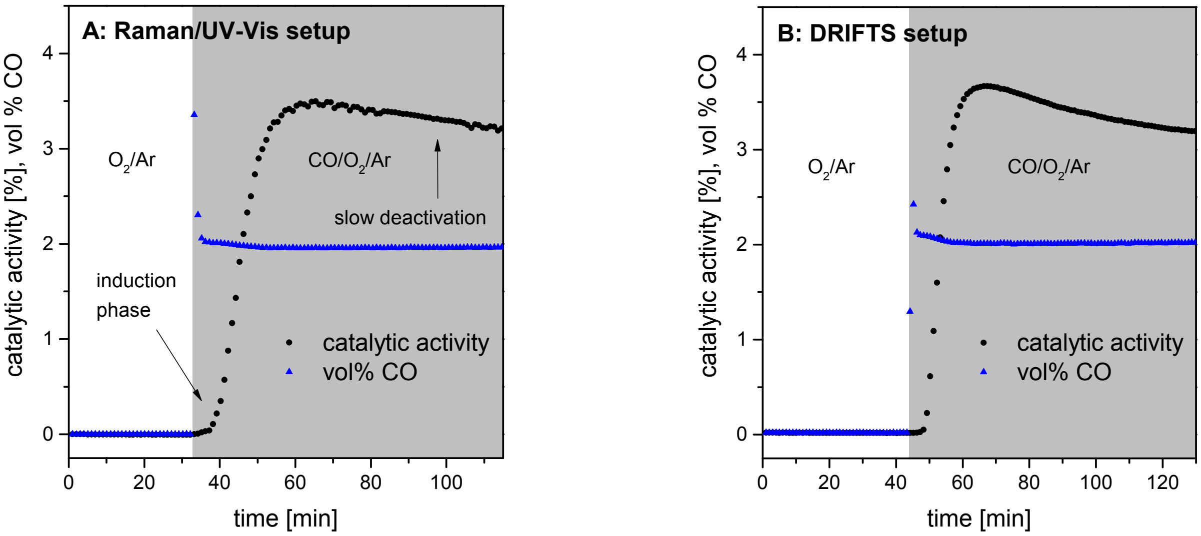

Figure 2.2.: Temporal evolution of the CO concentration (blue triangles) and the catalytic activity (black circles) during room temperature (21°C) CO oxidation over 0.5 wt% Au/CeO_2 in the A) Raman/UV-Vis spectroscopy setup and B) diffuse reflectance infrared spectroscopy (DRIFTS) setup. The gas feed is composed of 2 % CO and 10 % O_2 in Argon (total flow rate: 100 ml/min) for reaction conditions (grey background).

In both setups a strong resemblance of the CO concentration and the catalytic activity is observed. The catalyst is inactive during the first five minutes in reaction conditions (induction phase), after reaching a maximum after about 20-25 minutes a slow deactivation is observed. This slow activation behavior (20 min) has also been observed before for a dry reaction gas mixture over a Au/CeO_2 catalyst opposite to a humid gas mixture (activation <1 min). [37] Such a mediation of the reaction activity and reaction pathway by water has also been proposed for Pt_1/CeO_2 catalysts. [136]

This confirms that the catalyst is exposed to identical conditions in the two setups. Therefore, all information from the three spectroscopic techniques (Raman, UV-Vis, and infrared) derived for a certain activity of the catalyst refer to the same state of the catalyst.

2.4 *Dynamic operando* measurements

To elucidate the structural properties of the catalyst in a time-resolved fashion and to gain insight into the activation and deactivation behavior described in the previous section Raman, UV-Vis, and infrared spectra were recorded continuously during activation an deactivation of the catalyst in the two setups described in sections 2.1 and 2.2. The spectroscopic information were then directly correlated to the activity of the catalyst. Similar *in situ* infrared experiments were done before [43, 44] and are proposed as *dynamic operando* measurements here. [137] As an example, the UV-Vis spectra and the activity of a 0.5 wt% Au/CeO_2 catalyst is illustrated in Figure 2.3. The inset shows the temporal evolution of the activity and the colored dots indicate the time point, at which the corresponding UV-Vis spectrum was measured. The interpretation of UV-Vis spectra of a Au/CeO_2 catalysts is given in chapter 7 and by this approach structure-activity relationships can be drawn by proper interpretation of the spectroscopic data.

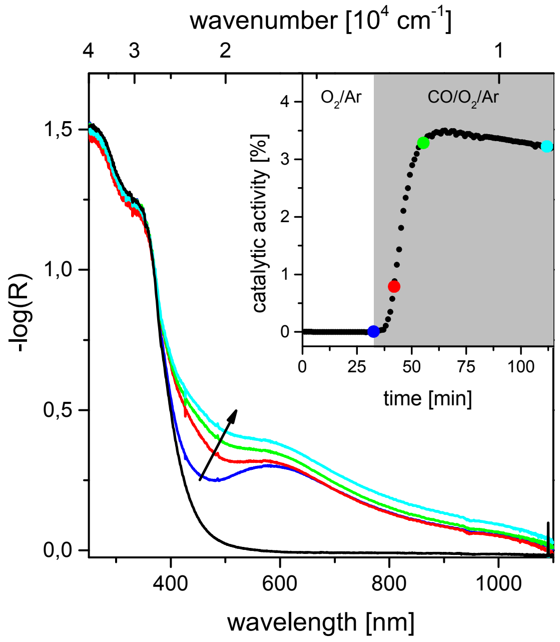

Figure 2.3.: *Operando* UV-Vis spectra recorded during activation (induction phase) of a 0.5 wt% Au/CeO_2 catalyst at room temperature (21°C) during CO oxidation. The gas feed is composed of 2 % CO and 10 % O_2 in Argon (total flow rate: 100 ml/min) for reaction conditions. The arrow indicates the temporal evolution of the spectra and the inset shows the catalytic activity over time during the induction phase. The UV-Vis spectra were measured at the indicated points of the activity profile (inset). The spectrum of the bare ceria support measured in O_2/Ar is shown as black line.

The approach is employed in chapter 7 to follow the oxygen defect dynamics in the ceria support of working Au/CeO_2 catalysts in real time by Raman spectroscopy and to evidence the influence of the ceria support on the activity of the catalyst at room temperature. Moreover the approach is employed to determine the active site of the Au/CeO$_2$ catalyst as described in chapter 8 by correlating the intensity of an infrared band assigned to a CO stretching mode to the activity of the catalyst. The assignment of the CO stretch frequency to a certain species is then successfully made with the aid of DFT calculations.

2.5 Synthesis of ceria supports and gold/ceria catalysts

Ceria nanosheets also referred to as polycrystalline ceria nanoparticles were yielded from decomposition of $Ce(NO_3)_3 \cdot 6H_2O$ (99.5 %, Alfa Aesar). The precursor was heated with a rate of 6°C/min to 600°C and calcined for 12 h at this temperature. After cooling and sieving (200 μm) the product was calcined again employing the same protocol. At 600°C calcination temperature all nitrate impurities are removed from the sample as shown before [49] and by the absence of bands in Raman spectra attributed to nitrate (see Raman spectra of ceria *sheets* in chapter 5).

Ceria nanopolyhedra and ceria nanocubes were synthesized according to the hydrothermal synthesis protocol described by Mai *et al.* [45] For ceria nanopolyhedra 1.946 g $Ce(NO_3)_3 \cdot 6H_2O$ were dissolved in 11 ml deionized water (electric conductivity <3 μS m^{-1}) and added to 79 ml of a 0.011 M NaOH solution (98 %, Grüssing GmbH). After stirring for 30 min the suspension was transferred into a selfmade Teflon autoclave (volume ca. 140 ml) and heated in an electric oven to 180°C with a ramp of 1°C/min and kept at 180°C for 18 h. To yield ceria nanocubes 22.5 g NaOH (7.120 M, 98 %, Grüssing GmbH) were dissolved in 79 ml deionized water. A solution of 1.946 g $Ce(NO_3)_3 \cdot 6H_2O$ (Alfa Aesar, 99.5 %) in 11 ml deionized water was added and the suspension was stirred for 30 min. Afterwards the suspension was filled into the Teflon autoclave and put into an electric oven. The oven was heated with 1°C/min to 180°C and kept at 180°C for 18 h.

After hydrothermal treatment the precipitate was washed with water at least three times and dried at 65°C for more than 24 hours. The yield was 95 % for ceria nanocubes and $10 - 12$ % for nanopolyhedra. For a thorough characterization including *in situ* Raman spectroscopy, transmission electron microscopy, N_2 adsorption, and X-ray diffraction refer to chapter 5.

Active gold/ceria (Au/CeO$_2$) catalysts were yielded by deposition precipitation [138, 139] of a $HAuCl_4 \cdot 3H_2O$ (>99.99 %, Sigma Aldrich) precursor onto the synthesized ceria nanostructures. 2 g of the ceria support were suspended in 300 ml deionized water. The pH value of the suspension was constantly monitored by a pH meter and a temperature sensor (InoLab, three point calibration at pH 4, 7, 10 prior to usage). After adjusting the pH value to 9 with a 0.1 M NaOH solution 50 ml of a 10^{-3} M $HAuCl_4 \cdot 3H_2O$ solution at a pH value of 9 were added dropwise to the ceria suspension. The suspension was heated to 65°C for 2 h, cooled down to room temperature and treated for 30 min in an ultrasound bath (Bandelin). The precipitate was centrifuged, washed with 0.25 % ammonia solution (for nanosheets only) and water three times each and dried at 85°C for at least 48 h. The samples were employed *as prepared* without further calcination for *operando* measurements.

The Au/CeO$_2$ catalyst materials are used throughout this work. X-ray photoelectron spectroscopy and transmission electron microscopy characterization is described in chapter 7.

2.6 *Ex situ* characterization techniques

X-ray photoelectron spectroscopy was conducted at a modified LHS/SPECS EA200 MCD with a Mg K_α source (1253.6 eV, 168 W) operated at 12 kV and 14 mA. The photoelectron spectra were recorded at pressures $<10^{-8}$ mbar. The spectrometer was calibrated by analysis of the Au4f emission of gold foil at 84.0 eV and the Cu2p emission of a copper plate at 932.7 eV. A Shirley model was employed for background subtraction. [140] Due to the semiconductor properties of ceria materials it was necessary to account for charging of the sample by shifting the Ce3d u"' signal to 916.7 eV, [141] resulting in a C1s position at 284.7 eV. Binding energies reported in the literature for ubiquitous carbon (285.0 eV [135], 284.5 eV [140]) agree with this value. A detailed analysis of the Au4f and Ce3d emission is given in chapter 7.

Certain XP spectra were measured or repeated at a SSX 100 ESCA Spectrometer (Surface Science Laboratories Inc.). A monochromatic Al Kα source (1486.5 eV) operated at 9 kV and 10 mA was employed. The sample was positioned as follows: The normal vector of the sample surface and the analyzer are oriented parallel having a 55° angle with respect to the horizontal plane (x, y direction). The incident X-ray beam has a 35° angle with respect to the horizontal. In the projection to the x, y plane the X-ray beam and the analyzer are orthogonal. In this configuration the sample is rotated by 16° with respect to the z direction towards the X-ray beam. The spectral resolution was 0.054 eV. Calibration was done with gold foil (84.0 eV) and a copper plate (932.7 eV) as described above.

Transmission electron microscopy (TEM) characterization was done at a JEOL JEM-2100F (Tokyo, Japan) equipped with a Schottky field emitter operating at a nominal acceleration voltage of 200 kV. Energy dispersive X-ray (EDX) spectra were recorded on an Oxford X-MAX 80 silicon drift detector (Oxford Instruments Nanoanalysis, High Wycombe, UK) attached to the JEM-2100F. A small amount of powder is dispersed in ethanol by ultrasound treatment (Bandelin) for 30 s. A droplet of the dispersion was applied to a holey carbon grid (Plano) and allowed to dry. To avoid charging under the electron beam, the grid was coated with carbon (Baltec MED010). The results of the TEM analysis are discussed in chapter 7. [137]

X-ray diffraction measurements were conducted at a STADI P spectrometer (Stoe & Cie. GmbH, Darmstadt) with a Ge[111] monochromator and a Cu $K_{\alpha,1}$ source with a wavelength of 1.54060 Å. The sample geometry was flat and the spectrometer was operated in transmission.

N_2 adsorption/desorption were conducted at a SURFER (ThermoFisher Scientific). The sample was outgased at 65°C in high vacuum for 24 hours. For the specific surface area determination a BET model [142] was fit to the N_2 adsorption/desorption isotherm in the region between 0.05 and 0.35 relative pressure assuming that a N_2 molecule covers an area of 0.162 nm^2 at the sample surface.

Raman spectroscopy with an excitation in the ultra-violet region (UV-Raman) was carried out at 256.7 nm and 385.1 nm excitation wavelength using a setup described in reference [93]. The modification of the setup is described in reference [143]. Spectra were measured at 8.0 mW laser power at the sample (256.7 nm) and at 5.3 mW (385.1 nm) resulting in an identical phonon flux at the sample. The laser spot was 0.6 mm^2 in size. For *in situ* measurements a reaction cell provided by Linkam (CCR100) was employed at a gas flow rate of 50 ml/min and 25 % O_2 concentration.

3 Density Functional Theory (DFT) Approach

A comprehensive introduction into the field of density functional theory (DFT) is given in the literature. [144–146] Here the Hartree-Fock approach is compared to the Kohn-Sham approach and the type of exchange correlation functionals which are mandatory to tackle reduced ceria, i.e., the formation of Ce^{3+}, are briefly discussed in section 3.1. In section 3.2 the considered model systems are described and the computational parameters are given. In the following section 3.3 the vibrational analysis of model systems and the method to derive infrared and Raman cross sections of vibrational modes is described. The last section 3.4 covers the calculated lattice parameters of CeO_2 and Ce_2O_3 and the corresponding first-order vibrational modes in comparison with experimental data. In chapter 4 further results are presented focusing on second-order Raman vibrations in ceria, calculated Raman spectra of reduced bulk ceria (CeO_{2-x}), and of the low index $CeO_2(111)$ and $CeO_2(100)$ surfaces. Additionally, adsorbate vibrations with a distinct focus on oxygen adsorption in the form of peroxides (${O_2}^{2-}$) and superoxides (${O_2}^{-}$) at the two considered low index surfaces are discussed.

3.1 Introduction to density functional theory and exchange correlation functionals

The goal of electronic structure calculations is to describe the properties of a molecular or extended system of N nuclei and M electrons (see equation 3.1). For such a system the full Hamiltonian can be written as follows: [144]

$$\hat{H} = \underbrace{-\frac{1}{2}\sum_{i=1}^{M}\nabla_i^2}_{\substack{\text{kinetic energy}\\ \text{of the electrons}}} \underbrace{-\frac{1}{2}\sum_{A=1}^{N}\frac{1}{M_A}\nabla_A^2}_{\substack{\text{kinetic energy}\\ \text{of the nuclei}}} \underbrace{-\sum_{i=1}^{M}\sum_{A=1}^{N}\frac{Z_A}{r_{iA}}}_{\substack{\text{electron-nuclei}\\ \text{interaction}}} + \underbrace{\sum_{i=1}^{M}\sum_{j>i}^{M}\frac{1}{r_{ij}}}_{\substack{\text{electron-electron}\\ \text{interaction}}} + \underbrace{\sum_{A=1}^{N}\sum_{B>A}^{N}\frac{Z_A Z_B}{r_{AB}}}_{\substack{\text{nuclei-nuclei}\\ \text{interaction}}} \tag{3.1}$$

Please note that atomic units are employed throughout this description which means that the constants $m_e = \hbar = 4\pi\epsilon_0 = |e|$ are set to 1. The wave function that is an eigenfunction of the Hamiltonian (Schrödinger equation) covers all information about the system but can only be solved in an analytical form for a system with a single electron. Moreover, it is assumed that the electron motion and the nuclear motion can be separated (Born-Oppenheimer approximation). [144] More precisely, for a given configuration of the nuclei only the electronic energy is calculated and the electronic energy depends parametrically on the considered nuclei positions. For the total energy the nuclei-nuclei interactions are added to construct the potential energy surface (PES). The PES is the total energy as a function of all internal nuclei coordinates of the system. [146]

There are useful approximated methods to solve the Schrödinger equation. To this end, the variational principle is introduced which together with suitable approximations for the electron-electron interactions form the basis for most approaches to the solution of the Schrödinger equation. The variational principle states that the expectation value of any trial wave function is higher than the ground state energy which is the expectation value of the ground state wave function. By optimizing the energy of a trial wave function the energy E_{trial} converges to the ground state energy without knowing the ground state wave function explicitly.

$$\langle \Psi_{\text{Trial}} | \hat{H} | \Psi_{\text{Trial}} \rangle \; = E_{\text{Trial}} \geq E_0 = \; \langle \Psi_0 | \hat{H} | \Psi_0 \rangle \tag{3.2}$$

Introduction of an antisymmetric Slater determinant for the M electron wave function Ψ was done by Hartree and Fock. Minimization of the energy under the constraint of an orthonormal basis $\langle \chi_i | \chi_j \rangle = \delta_{ij}$ and introduction of Lagrangian multipliers ϵ_i reveals a set of M eigenfunctions χ_i to the so called Fock-Operator $\hat{F}$ (see also [146]).

$$\hat{F} \chi_i = \epsilon_i \chi_i \quad i = 1, 2, ..., M \tag{3.3}$$

The Fock operator consists of four parts accounting for the kinetic energy of the electrons, the interaction of the electrons with the nuclei, electron-electron coulomb interaction, and exchange interaction. The latter has no physical analogue and is a non-local potential.

$$\hat{F}_i = -\frac{1}{2} \nabla_i^2 - \sum_{A=1}^{N} \frac{Z_A}{r_{iA}} + \sum_{j}^{M} J_i(\vec{x}_1) - K_j(\vec{x}_1) \tag{3.4}$$

The advantage of the Hartree Fock approach is that it cancels the self interaction of electrons but completely neglects the correlation of electrons. [144]

First approaches to treat the electrons as an electron density where proposed by Thomas, Fermi, and Dirac on the basis of the homogeneous electron gas, i.e., the electrons form an infinite electron gas where the electron density is finite. The energy can be written as a functional of the electron density $n(\vec{r})$ consisting of the sum of a term accounting for the kinetic energy, the classic Coulomb interaction, and the quantum mechanical exchange effects. The correlation energy for a homogenous electron gas can be calculated very accurately by Monte Carlo methods. [147] This provides the basis for the local density approximation (LDA) for the exchange and correlation within the DFT framework. The inhomogeneous electron density is evaluated by the functional expression for exchange and correlation $\epsilon_{\text{xc}}(n(\vec{r}))$ of the homogeneous electron gas. Please note that the homogeneous electron gas is the only system for which the exchange and correlation functional is known exactly and to a very high accuracy, respectively. [144]

$$E_{\text{xc}}^{\text{LDA}}[n(\vec{r})] = \int n(\vec{r}) \epsilon_{\text{xc}}(n(\vec{r})) d\vec{r} \tag{3.5}$$

In 1964 Hohenberg and Kohn provided the justification for the electron density to cover all properties of the electronic system within an external potential $V_{\text{ext}}(\vec{r})$ by proofing the two following theorems.

- "*The external potential $V_{ext}(\vec{r})$ is (to within a constant) a unique functional of $n(\vec{r})$; since in turn $V_{ext}(\vec{r})$ fixes $\hat{H}$ we see that the full many particle ground state is a unique functional of $n(\vec{r})$.*" [148, 149]

- "*A universal functional for the energy in terms of the density can be defined such that the exact ground state energy is the global minimum of the functional and that the density that minimizes the functional is the ground state density.*" [148, 149]

The Hohenberg-Kohn theorems are the basis for the Kohn-Sham approach. Therefore the wave functions are constructed from one electron auxiliary functions (KSO) that lead to an improved description of the kinetic energy T_S, while neglecting the correlation of the electrons. The correlation and exchange energy functional are summarized in the exchange correlation functional E_{xc}, while the functional expression is not known.

$$E[n(\vec{r})] = T_s[n(\vec{r})] + J[n(\vec{r})] + E_{\text{xc}}[n(\vec{r})] + E_{\text{ncl}}[n(\vec{r})] \tag{3.6}$$

Minimizing the energy under the constraint of an orthonormal basis $\langle\phi_i|\phi_j\rangle = \delta_{ij}$ of auxiliary wave functions $\phi_i(\vec{r})$ that constructs the electron density $n(\vec{r})$ from occupied orbitals

$$n(\vec{r}) = \sum_i^N \phi_i^*(\vec{r})\phi_i(\vec{r}) \tag{3.7}$$

and the introduction of the Lagrangian multipliers ϵ_i lead to the Kohn-Sham equations (KSE) which are a coupled set of eigenfunctions (see [150]).

$$\left[-\frac{1}{2}\nabla^2 + \int \frac{n(\vec{r}_2)}{r_{12}} d\vec{r}_2 + V_{\text{xc}}(\vec{r}_1) - \sum_{A=1}^{N} \frac{Z_A}{r_{1A}}\right]\phi_i = \epsilon_i \phi_i \tag{3.8}$$

Up to here the derivation of the approach is exact and approximations come with the exchange correlation potential V_{xc} which is defined as a functional derivative of the energy E_{xc} with respect to the electron density n:

$$V_{\text{xc}} \equiv \frac{\partial E_{\text{xc}}}{\partial n} \tag{3.9}$$

As $V_{\text{eff}} = V_{\text{H}} + V_{\text{ncl}} + V_{\text{xc}}$ is a functional of ϕ_i the Kohn-Sham equations need to be solved iteratively and a convergence criterion needs to be defined.

To treat the Kohn-Sham equations technically a basis set expansion is employed which reduces the problem from a set of coupled differential equations to a matrix eigenvalue problem that can be solved by algebraic methods. [144] In the case of solids it is advantageous to employ plane waves as basis functions. If an infinite number of plane waves could be considered this would correspond to a complete basis, practically this set is truncated at a certain point defined by a cutoff energy (E_{cutoff}).

$$\phi_i(\vec{r}) = \sum_{\mu=1}^{L} c_{\mu i}\eta_\mu(\vec{r}) \qquad \eta^{\text{PW}}(\vec{r}) = \exp(i\vec{k}\vec{r}) \tag{3.10}$$

To reduce the numerical load for the DFT calculations the core electrons together with the nuclei are treated as pseudopotentials and only the valence electrons are considered explicitly. Here the projector augmented wave (PAW) potentials are employed, [151] which allow to reconstruct the all-electron density, due to the fact that the core electrons are frozen. The PAW pseudopotential are considered as the most accurate pseudopotentials to date. [152]
Finally it is noted, that the KSE need to be solved at each k-point in the Brillouin zone, due to the periodicity of the system. The total density is obtained by summing over the calculated density at the k-points $n_k(\vec{r})$. As k-point sampling method the Monkhorst-Pack scheme is employed that generates uniformly distributed k-points in the irreducible Brillouin zone. [153]

As mentioned before there is no systematic way for the improvement of the exchange correlation functional beyond the local density approximation (see equation 3.5). One improvement is to take also the gradient ($\bigtriangledown n$) of the electron density into account. These functionals are so-called generalized gradient approximation (GGA) functionals where the exact functional dependence is parameterized in an empirical way, rather than having a physical background. A functional of this type that is only based on physical constants (parameter-free) was proposed by Perdew, Burke, and Ernzerhof in 1996 which is known and abbreviated as PBE functional. [109]
A common problem within density functional theory with LDA or GGA functionals is that electron self interactions are not fully cancelled. The consequence of this is that its application to materials with strongly localized electrons, e.g., 3d transition metal oxides and the oxides of lanthanides has been only partly successful, since spurious self interactions prevent the localization of 3d and 4f electrons. Simultaneously the electrons remain itinerant and many oxides are predicted to be metals instead of the experimentally observed insulators. Moreover, band gaps and energy barriers are underestimated. These problems can be overcome by adding a fraction of the exact exchange energy as known from Hartree-Fock theory to the exchange correlation functional, as this is the major contribution to E_{xc}. From Hartree-Fock theory it is also known that the self interaction is cancelled by considering the exchange interaction. Heyd, Scuseria, and Ernzerhof proposed a parametrization of the exchange correlation functional and simultaneously separated the coulomb operator ($\frac{1}{r}$) into a part for long (LR) and short range (SR) interaction. [154, 155]

$$\frac{1}{r} = \frac{1-\text{erf}(\mu r)}{r} + \frac{\text{erf}(\mu r)}{r} \tag{3.11}$$

Here μ is a screening parameter defining the region for long (LR) and short range (SR) interactions to reduce the computational demand. Setting the screening parameter to $\mu = 0.2$ leads to the so-called HSE06 functional. [105]

$$E_{\mathrm{xc}}^{\mathrm{HSE}} = \frac{1}{4}E_{\mathrm{x}}^{\mathrm{SR}}(\mu) + \frac{3}{4}E_{\mathrm{x}}^{\mathrm{PBE,SR}}(\mu) + E_{\mathrm{x}}^{\mathrm{PBE,LR}}(\mu) + E_{\mathrm{c}}^{\mathrm{PBE}} \tag{3.12}$$

An alternative and computationally less demanding possibility to overcome the self interaction problem is to add a repulsive term for certain strongly correlated (very localized) orbitals of specified atoms, usually these are d and f orbitals. The $U_{\mathrm{eff}} = U - J$ can be understood as a penalty energy for an electron to localize close to each other. [107] For ceria the value $U_{\mathrm{eff}} = 4.5$ eV is applied to the Ce4f orbital together with a PBE functional. This is referred to as PBE+U/4.5 eV.

Both approaches the HSE06 and PBE+U/4.5 eV functional can be used to overcome the self interaction problem and to describe reduced ceria, i.e., the localization of excess charge at one Ce^{3+} ion rather than a delocalized electron corresponding to an erroneous metallic character of reduced ceria. [95, 106]

3.2 Computational details

Density functional theory calculations were performed with the Vienna ab initio simulations package (VASP, version 5.3.5., http://www.vasp.at/). [152, 156–159] Spin-polarized calculations considering both spin up and spin down electron densities were conducted. The generalized gradient approximation (GGA) parameterized by Perdew, Burke, and Ernzerhof (PBE) [109] was employed. To account for proper localization of excess electrons at cerium ions, that is on-site coulombic interaction, the DFT+U approach by Dudarev *et al.* [107] was applied with a empirical Hubbard U_{eff} parameter of $U_{\mathrm{eff}} = 4.5$ eV for the Ce4f state (PBE+U/4.5 eV). This value has initially been proposed by Fabris *et al.* [108], and its validity was critically discussed in the literature. [95, 100] Such a value has been extensively applied to study reduced ceria-based systems. [57, 102, 127] For comparison the hybrid functional by Heyd, Scuseria, and Ernzerhof (HSE06) [105, 154, 155] with a screening parameter of 0.207 Å^{-1} [105] was also employed as implemented in the VASP code.

Only valence electrons were treated with a plane wave cutoff of 400 eV (Ce: 5s, 5p, 6s, 4f, 5d; O: 2s,2p; C: 2s, 2p, H: 1s, Au: 5d, 6s). The pseudopotentials of VASP version 5.4. were employed throughout the work. The Kohn-Sham equations were solved by the projected augmented wave (PAW) method. [151, 152]

The lattice constants of CeO_2 ($Fm\bar{3}m$) and sesquioxide A-type Ce_2O_3 ($P\bar{3}m1$,[1] see figure 3.1 A and C) as given in table 3.1 were determined by relaxing the structure after calculations of the stress tensor with an energy cutoff of 800 eV. The energy was converged to 10^{-8} eV for calculations with the PBE+U/4.5 eV and 10^{-6} eV for calculations with the HSE06 functional. Maximum residual forces were smaller than 10^{-6} and 10^{-4} eV Å^{-1} for the two functionals, respectively. The Brillouin zone was sampled using the following Monkhorst-Pack grids [153] for the calculations: A (6 × 6 × 6) grid for the primitive cell of

---

[1] Sesquioxide A-type Ce_2O_3 is often referred to as hexagonal Ce_2O_3 due to the same axis systems of primitive trigonal and hexagonal crystal structures.

bulk CeO_2 and a (6 × 6 × 3) grid for A-type Ce_2O_3. Ceria supercells with a (2 × 2 × 2) expansion of the conventional cubic cell ($Ce_{32}O_{64}$, see figure 3.1 B for Ce_4O_8) were modeled with a (2 × 2 × 2) grid.

The calculated bulk lattice constant was used to study $Ce_{32}O_{63}$ and $Ce_{32}O_{62}$ structures (CeO_{2-x}) as well as the $CeO_2(111)$ and $CeO_2(100)$ surface. The convergence criteria for the maximum force per atom was 0.01 eV $Å^{-1}$ and for the energy 10^{-6} eV for all CeO_{2-x} bulk as well as $CeO_2(111)$ and $CeO_2(100)$ surface structures (see below).

The bulk lattice expansion upon oxygen vacancy creation ($Ce_{32}O_{62}$) was obtained in two steps in order to avoid changes in the crystal shape due to the localization of the excess charge. First, calculations at different volumes using the same energy cutoff of 800 eV for each calculation were performed and the final energies were fitted to a Murnaghan's equation of state. [160] In these calculations the initial symmetry of the structure was kept fixed, i.e., a symmetry compatible excess charge density distribution was obtained. Next, the excess charge distribution is optimized according to its preferred location (compare chapter 4). [161] In this second step the equilibrium lattice volume obtained in the first step was kept fixed, whereas ionic relaxations were performed without any symmetry constrains.

The $CeO_2(111)$ and $CeO_2(100)$ surfaces (see figure 3.1 D to G) were modeled with a supercell approach at a lattice constant according to the value shown in table 3.1. A minimum of 15 Å of vacuum is added between two surface slabs in z direction revealing an infinite surface in x and y direction. For the $CeO_2(111)$ surface three O-Ce-O trilayers were modeled and the atoms of the bottom trilayer were fixed to their bulk lattice position. [103] Various periodicities were employed and refer to the conventional $p(n \times n)$ representation of the cell. For clarity, these are referred to as $(n \times n)$ periodicity. For PBE+U/4.5 eV calculations the Brillouin zone was sampled with a (6 × 6 × 1), (3 × 3 × 1), (2 × 2 × 1), and (1 × 1 × 1) Monkhorst-Pack grid [153] for surface cells with (1 × 1), (2 × 2), (3 × 3), and (4 × 4) periodicities,

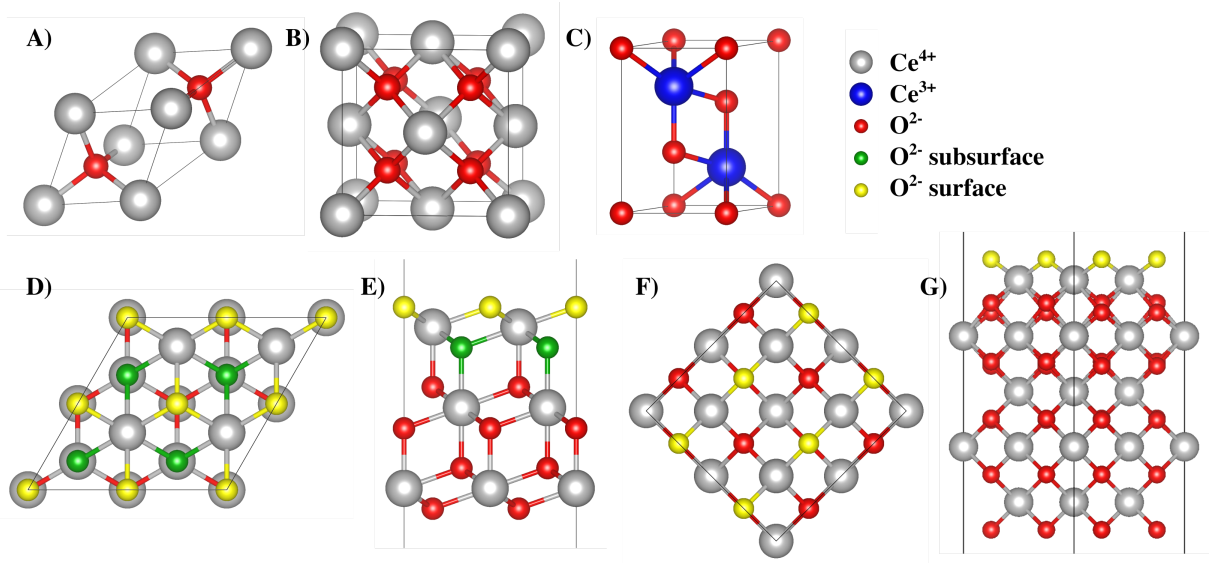

Figure 3.1.: A) Primitive and B) conventional cubic representation of CeO_2 ($Fm\bar{3}m$). C) Sesquioxide A-type Ce_2O_3 ($P\bar{3}m1$). D) Top and E) side view of the oxidized $CeO_2(111)$ surface with (2 × 2) periodicity. F) Top and G) side view of the oxidized $CeO_2(100)$ surface with $p(2 \times 2)$ periodicity. Gray and blue balls represent Ce^{4+} and Ce^{3+} cations, red balls bulk oxygen, and yellow and green balls represent surface and subsurface oxygen atoms. This color code is used throughout the text.

respectively. For HSE06 calculations structure optimization was done at the Γ-point first and restarted with (2 × 2 × 1) and (1 × 1 × 1) grids for (2 × 2) and (3 × 3) periodicities, respectively.

For the $CeO_2(100)$ surface 11 atomic layers were shown to be sufficient to stabilize the surface energy (see figure 4.11 in this work and in the recent literature [127]). The atoms of the bottom three ionic layers were fixed to their bulk lattice positions. Due to the fact that each bilayer (Ce_2-O_4) maintains the bulk composition, the surface is classified as a Tasker type III surface with a permanent dipole moment. [162] The dipole moment cancels by termination of the slab with a half oxygen layer on the top side and the bottom side. Both sides form a mirrored checkerboard of populated and unpopulated surface oxygen positions. [57, 119, 127] Figure 4.10 depicts the $c(1 \times 1)$, $p(2 \times 2)$, and $c(2 \times 2)$ periodicity of the surface slabs. These are modeled with (4 × 4 × 1), (3 × 3 × 1), and (2 × 2 × 1) Monkhorst-Pack grids, respectively. [153]

For all calculations of surface slabs the cell was kept fix at the bulk lattice constant and only the ions were allowed to relax.

Certain calculations were repeated to account for dispersion (van der Waals, vdW) contributions. The approach of Grimme [163, 164] was employed with semi-empirical parameters, which have been optimized before for Ce and Au on the basis of second-order Møller Plesset perturbation theory. [165] As global scaling factor $s_6 = 0.75$ was used. For C_6 values of 20.0, 0.70, 21.23, 1.75 J nm^6 mol^{-1} and for R_0 values of 1.860, 1.342, 1.772, 1.452 Å were employed for Ce, O, Au and C, respectively. [118] The cutoff distance for interactions was set to a radius of 30 Å.

3.3 Vibrational analysis and calculation of infrared and Raman intensities

For a normal mode analysis (compare section 1.4) of a considered crystal structure or surface model within the harmonic frequency approximation the mass-weighted Hessian matrix is calculated. Two methods were used to calculate the coefficients f_{ji} of the secular determinant. A finite differences approach with ±0.015 Å displacements of the atoms or a density functional perturbation approach (or linear response) technique (DFPT) as implemented in the VASP code. [97, 98] The DFPT approach is not implemented for the hybrid functional or for parallel consideration of vdW contributions. Therefore Raman intensities were calculated with the PBE+U/4.5 eV functional and without considering vdW contributions. In chapter 4 the finite differences and the DFPT approach are compared for the first-order vibration of ceria (F_{2g} mode). For the determination of the normal modes with the finite differences approach a tight self consistent field criterium of 10^{-8} eV was considered for accurate results. Unless otherwise stated, only non-scaled values for the calculated frequencies are reported.

To calculate the corresponding infrared absorption intensity of normal mode vibrations the Born effective charge (from DFPT calculation) [166] and the displacement vector are employed according to equation 3.13: [97, 167]

$$I^{\mathrm{IR}}(\nu) = \sum_{\alpha} \left| \sum_{s\beta} Z_s^{\star\alpha\beta} U_s^{\beta}(\nu) \right|^2 \qquad (3.13)$$

For calculations of Raman intensities of normal modes the off-resonant differential cross section is expressed according to Porezag and Pederson [168] as follows (see also [91, 92]):

$$\frac{d\sigma_i}{d\Omega} = \frac{(2\pi\nu_S)^4}{c^4}\,\frac{h(n_i^b+1)}{8\pi^2\nu_i}\,\frac{I^{\mathrm{Raman}}}{45} \tag{3.14}$$

Throughout the work the Raman scattering activity I^{Raman} is calculated according to equation 3.15 and given in units of $\text{Å}^2\ \mathrm{u}^{\frac{1}{2}}$, where u refers to the atomic mass unit.

$$I^{\mathrm{Raman}} = 45\left(\frac{d\alpha}{dQ}\right)^2 + 7\left(\frac{d\beta}{dQ}\right)^2 = 45\alpha'^2 + 7\beta'^2 \tag{3.15}$$

where

$$\alpha' = \frac{1}{3}(\bar{\alpha}'_{xx} + \bar{\alpha}'_{yy} + \bar{\alpha}'_{zz}) \tag{3.16}$$

and

$$\beta'^2 = \frac{1}{2}\left[(\bar{\alpha}'_{xx} - \bar{\alpha}'_{yy})^2 + (\bar{\alpha}'_{yy} - \bar{\alpha}'_{zz})^2 + (\bar{\alpha}'_{zz} - \bar{\alpha}'_{xx})^2 + 6\left(\bar{\alpha}'^{\,2}_{xx} + \bar{\alpha}'^{\,2}_{yy} + \bar{\alpha}'^{\,2}_{zz}\right)\right] \tag{3.17}$$

The derivatives of the polarizability with respect to the atomic coordinates are expressed based on the definition for the polarizability [169] as a direct response to an external electric field.

$$\frac{\partial \bar{\alpha}_{ij}}{\partial R_k} = -\frac{\partial^3 E^{\mathrm{el}}}{\partial E_i \partial E_j \partial R_k} \qquad i, j = x, y, z \tag{3.18}$$

According to Lazzeri *et al.* [169] the components of the dielectric tensor can be expressed as follows.

$$\epsilon^{\infty}_{ij} = \delta_{ij} - \frac{4\pi}{\Omega_{\mathrm{cell}}}\frac{\partial^2 E^{\mathrm{el}}}{\partial E_i \partial E_j} \quad \Leftrightarrow \quad \frac{\partial^2 E^{\mathrm{el}}}{\partial E_i \partial E_j} = -\frac{\Omega_{\mathrm{cell}}}{4\pi}\epsilon^{\infty}_{ij} + \frac{\Omega_{\mathrm{cell}}}{4\pi}\delta_{ij} \tag{3.19}$$

The third derivative of the energy with respect to the atomic coordinate is expressed as a finite difference.

$$\frac{\partial \bar{\alpha}_{ij}}{\partial R_k} = -\left[\left(\frac{\partial^2 E^{\mathrm{el}}}{\partial E_i \partial E_j}\right)_+ - \left(\frac{\partial^2 E^{\mathrm{el}}}{\partial E_i \partial E_j}\right)_-\right]\frac{1}{\Delta R_k} = \frac{\Omega_{\mathrm{cell}}}{4\pi}\left[(\epsilon^{\infty}_{ij})_+ - (\epsilon^{\infty}_{ij})_-\right]\frac{1}{\Delta R_k} \tag{3.20}$$

Here $(\epsilon^{\infty}_{ij})_+$ and $(\epsilon^{\infty}_{ij})_-$ refer to the ij-component of the dielectric matrix determined at a structure where the atoms are displaced by +0.005 Å and −0.005 Å along the normal mode vector and therefore $\Delta R_k = 0.01$ Å. Ω_{cell} is the unit cell volume of the model structure.

VASP calculates the full dielectric matrix (6 linear response calculations) in one DFPT run. Two of such runs are required to determine the Raman intensity I^{Raman} of one mode. Hence, a total of $3N_{\mathrm{at}} \times 2 \times 6 = 36\ N_{\mathrm{at}}$ linear response calculations are necessary to obtain a Raman spectrum, where N_{at} is the number of atoms per unit cell. A more efficient method has been developed, [169] however, it is not yet implemented in the VASP code. To set up proper input for the VASP code and evaluate the output according to the above considerations a python script written by Fonari and Stauffer is employed. [170] To create a spectrum and account for line broadening, the calculated intensities are multiplied by a Gaussian function with a 10 cm^{-1} full width at half maximum (fwhm).

The phonon dispersion and the density of vibrational states, DOS(ω), of CeO_2 were calculated with the PHONOPY package [171] and a (4 × 4 × 4) expansion of the primitive ceria cell. A finite differences method is applied here with the a convergence criterion of 10^{-8} eV. To account for TO-LO splitting, i.e., the non-analytic term correction the dielectric constant and Born effective charges were used from a DFPT calculation ($\epsilon = 6.667$, $Z^*(\mathrm{Ce}) = 5.524$, $Z^*(\mathrm{O}) = -2.765$). [166, 172] The experimental value for the dielectric constant ($\epsilon = 5.31$) [173] is overestimated by DFPT calculations.

3.4 Calculated properties of CeO_2 and Ce_2O_3 crystal structures

Ceria (CeO_2) crystallizes in the cubic fluorite type structure (see Figure 3.1 A and B for the primitive and conventional cubic representation of the structure). The space group is $Fm\bar{3}m$ and in this structure the Ce is 8-fold and the O 4-fold coordinated. The lattice constant as determined by PBE+U/4.5 eV calculations is $a_0 = 5.484$ Å which overestimates the experimental value of 5.412 Å by 1.3 % as measured for polycrystalline ceria (see table 3.1). [49] With the hybrid functional (HSE06, $a_0 = 5.395$ Å) the lattice constant is slightly underestimated. The results are in line with those published in the literature. [106, 174, 175]

The lattice parameters of A-type Ce_2O_3 ($P\bar{3}m1$) are summarized in table 3.1. Again the PBE+U/4.5 eV results ($a_0 = 3.913$ Å, $c_0 = 6.177$ Å) overestimate the experimental lattice constants ($a_0 = 3.89$ Å, $c_0 = 6.06$ Å) [176], while the HSE06 results ($a_0 = 3.862$ Å, $c_0 = 6.095$ Å) [106, 174, 177] slightly underestimate the experimental values. Generally, the HSE06 results match the experimental results better in accordance with the literature. [106] The first-order vibrational properties of CeO_2 and A-type Ce_2O_3 as depicted in table 3.1 are discussed in the following chapter 4.

Table 3.1.: Calculated lattice parameters and vibrational frequencies of first-order modes for CeO_2 (space group $Fm\bar{3}m$, calculations for the primitive unit cell) and A-type Ce_2O_3 ($P\bar{3}m1$) in comparison with experimental data. The lattice parameter refers to the representation of the unit cell as shown in Figure 3.1 B and C for CeO_2 and A-type Ce_2O_3, respectively. The calculated vibrational frequencies are reported as received (not scaled).

method	PBE+U/ DFPT	PBE+U/ finite differences	HSE06/ finite differences	experimental value	experimental method
structure			CeO_2		
a_0 [Å]	5.484	5.484	5.395	5.412	XRD [49]
F_{2g} [cm^{-1}]	437.3	437.2	450.8	464	Raman [49]
				465	Raman at single crystals [30, 178, 179]
F_{1u} [cm^{-1}]	269.2	269.2	267.9	272	infrared [173]
				218	derived from reflectivity [180]
				276	inelastic neutron scattering [181]
structure			Ce_2O_3		
a_0 [Å]	3.913		3.862	3.89	XRD [176]
c_0 [Å]	6.177		6.095	6.06	XRD [176]
c_0/a_0	1.579		1.578	1.558	
E_g [cm^{-1}]	409.2 (100)		410.6	409 (67)	Raman, [182]
				408	this work
A_{1g} [cm^{-1}]	389.4 (79)		408.2	409 (not resolved)	Raman [182]
A_{1g} [cm^{-1}] (bending mode)	196.5 (4)		197.8	189 (13)	Raman [182]
E_g [cm^{-1}] (bending mode)	90.7		100.0	103 (100)	Raman [182]

4 DFT Study on Raman Spectra of Ceria Nanoparticles[1]

Based on the computational details described in the previous chapter the vibrational properties of model systems that mimic ceria nanoparticles are discussed in this chapter. First the focus is put on first-order allowed Raman modes and overtones (second-order Raman modes) of bulk ceria (CeO_2) and reduced bulk ceria (CeO_{2-x}). Second the properties of the $CeO_2(111)$ and $CeO_2(100)$ surface facets are discussed. Finally adsorption of oxygen as peroxide ($O_2{}^{2-}$) and superoxide ($O_2{}^{-}$) and adsorption of water at the $CeO_2(111)$ and $CeO_2(100)$ surfaces is addressed. The Raman spectra of large and nanosized ceria particles as depicted in figure 4.1 can be completely understood by critical analysis of prior assignments of Raman bands to vibrational modes from the literature and new assignments based on the DFT calculations presented here. [183]

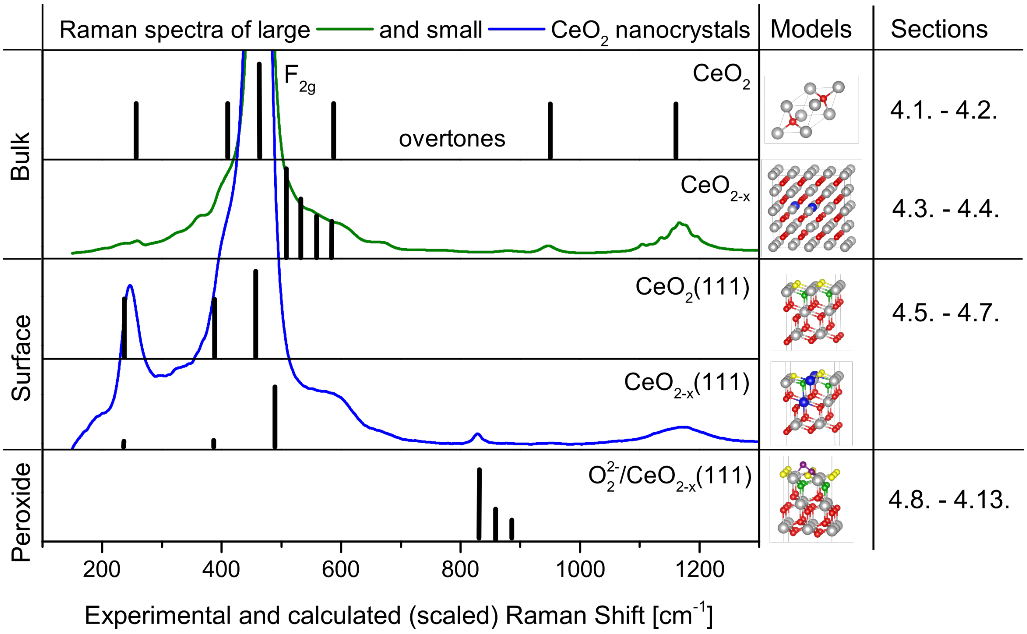

Figure 4.1.: Comparison of the experimental Raman spectra ($\lambda_{ex} = 514$ nm from reference [49]) of ceria with a particle size <25 nm (blue) and >1000 nm (green) with the calculated modes of the indicated ceria model systems. The calculated Raman shifts were scaled by a factor of 1.06 except for peroxide vibrations, $O_2{}^{2-}/CeO_{2-x}(111)$. The calculated frequencies of the peroxide molecule are correlated to the experimental bands by assigning the calculated frequencies of 893 and 932 cm^{-1} to the observed bands at 830 and 860 cm^{-1}, respectively. For convenience only the calculated peroxide frequencies corresponding to the lowest (0.06 ML, *a* and *b* structures) and to the highest (1 ML) $O_2{}^{2-}$ coverage are displayed here. The outlined approach allows for a consistent description of the experimental Raman spectra.

---

[1] Parts of the this chapter are already published. The publication including figures is reprinted/adapted with permission from C. Schilling, A. Hofmann, C. Hess, M. V. Ganduglia-Pirovano, *J. Phys. Chem. C*, **2017**, *121*, 20834-20849. Copyright 2017 American Chemical Society. (see reference [183]).

4.1 First-order Raman modes of CeO_2 and Ce_2O_3

Experimental Raman spectra of polycrystalline ceria (see figure 4.1) exhibit an intense band at 464 cm^{-1}. This is assigned to the triply degenerated F_{2g} mode. At ceria single crystals the frequency of the mode is determined as 465 cm^{-1}.[2] [30, 178, 179]

Here the frequency of the F_{2g} mode of ceria was calculated as 437.3 cm^{-1} and as 437.2 cm^{-1} employing the PBE+U/4.5 eV exchange correlation functional and the density functional perturbation theory (DFPT) or the finite differences approach, respectively. The results on ceria crystals are summarized in table 3.1 and chapter 3 describes the computational details. With a hybrid exchange correlation functional (HSE06) the frequency of the F_{2g} mode is predicted as 450.8 cm^{-1}. The calculated frequency with the HSE06 functional reproduces the experimental value better that the PBE+U/4.5 eV functional. In section 3.4 it is shown that the HSE06 functional also reproduces the lattice constant better than the PBE+U/4.5 eV functional. The second triply degenerated vibrational mode, which possesses F_{1u} symmetry, is predicted with a frequency of 269.2 cm^{-1} with the PBE+U/4.5 eV functional regardless of the method and with a frequency of 267.9 cm^{-1} with the HSE06 functional. Both functionals reproduce the experimental frequency of 272 cm^{-1} fairly well.

The A-type Ce_2O_3 was considered as an example for strongly reduced ceria, although it possesses a different crystal structure than the fluorite type. Please note that a cubic C-type Ce_2O_3 (bixbyite type) structure also exists. The Raman spectrum of A-type Ce_2O_3 (not shown), which was synthesized according to reference [184], exhibited a band at 408 cm^{-1}.[3] An Anti-Stokes Raman spectrum of A-type Ce_2O_3 has also been reported by Avisar and Livneh [182]. The band at 409 cm^{-1} was proposed to result from the stretching modes with E_g and A_{1g} symmetry. Indeed, with the HSE06 functional the frequency of the E_g mode is predicted as 410.6 and that of the A_{1g} mode as 408.2 cm^{-1}, whereas with the PBE+U/4.5 eV functional a separation of $\sim$20 cm^{-1} is predicted (E_g: 409.2 cm^{-1} and A_{1g}: 389.4 cm^{-1}). The bending modes are nicely reproduced with both functionals whereas the Raman intensities for all modes as derived from PBE+U/DFPT (see section 3.3) calculations do not match the experimental values (compare table 3.1) for strongly reduced Ce_2O_3.

4.2 Second-order Raman modes of CeO_2

Besides the band assigned to the first-order allowed Raman mode (F_{2g}), more bands have been observed at ceria single crystals. [30] These have been assigned to second-order Raman modes which are also called overtones. According to Weber *et al.*, [30] the most active phonons are those containing the total symmetric representation. Overtones originating from two sides of the Brillouin zone with $+k$ and $-k$ possess this symmetry and will therefore dominate the second-order Raman spectrum. [30] To derive the position of second-order Raman bands, the phonon dispersion curve of CeO_2 was calculated employing a (4 × 4 × 4) expansion of the primitive cell and the PHONOPY package. [171] The calculated phonon dispersion is shown in the left panel of figure 4.2 which is in accordance with a calculated phonon dispersion from the literature (PBEsol+U/5 eV) [172] and experimental data. [181] From the phonon

---

[2] For convenience the frequencies of the experimental and calculated vibrational modes are given as reciprocal wavelengths $\frac{1}{\lambda}$ (wavenumber) of the electromagnetic radiation.

[3] Synthesis of the A-type Ce_2O_3 sample by Lea Totzauer from the group of Prof. B. Albert, TU Darmstadt, is acknowledged.

dispersion the density of vibrational states was derived and is plotted against 2ω in the right panel of figure 4.2. This results in the 2ω-DOS (density of vibrational states). [30] The frequency axis is scaled by a factor of 1.06 to account for the deviation of the calculated frequency of the F_{2g} band employing the PBE+U/4.5 eV functional (437 cm^{-1}) compared to the experimental Raman shift (464 cm^{-1}). The Raman active vibrations are named according to the dominant contribution of the phonon dispersion to the phonon density (2ω-DOS). The derived peaks are located at 256 cm^{-1} (2TA), 409 cm^{-1} (2TA), 584 cm^{-1} (2TO), 948 cm^{-1} (2TO), and 1159 cm^{-1} (2LO). This agrees well with the observed bands at 250, 402, 595, 950, and 1170 cm^{-1} in the Raman spectrum of polycrystalline ceria with large particles (>1000 nm, see figure 4.1 and reference [49]) or ceria single crystals. [30] However, the overtones can not solely be responsible for the drastic increase in intensity of the bands at 246 and 402 cm^{-1} for ceria nanoparticles with particle size diameters of <25 nm (see figure 4.1). The origin of these bands is attributed to the surface of polycrystalline ceria as discussed in-depth in chapter 4.5.

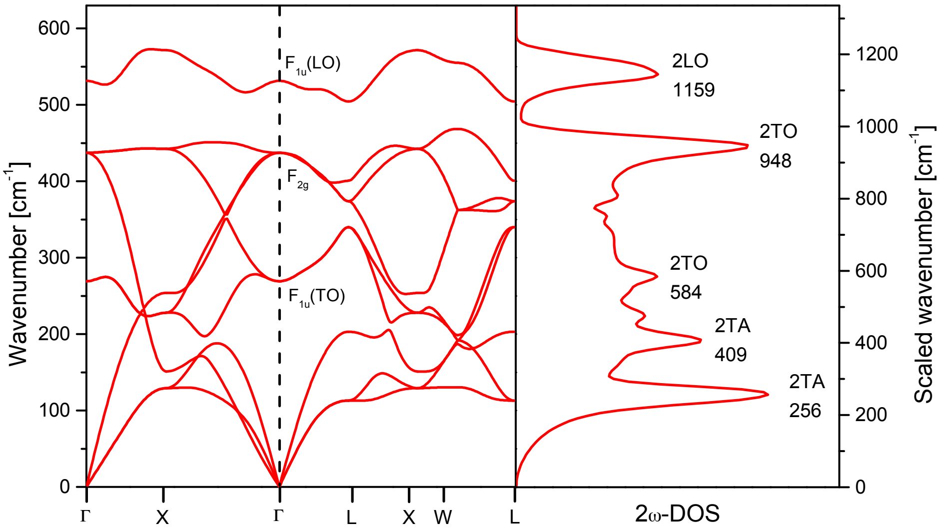

Figure 4.2.: Left panel: Phonon dispersion (not scaled) of CeO_2 derived from a (4 × 4 × 4) expansion of the primitive unit cell with a PBE+U/4.5 eV functional (a_0 = 5.484 Å), along high symmetry directions. The symmetry of the vibrations at the Γ-point is indicated by F_{1u}(LO), F_{2g}, and F_{1u}(TO). Right panel: Derived density of vibrational states for a (4 × 4 × 4) primitive CeO_2 cell plotted against 2ω, resulting in the 2ω-DOS. The wavenumber axis is scaled by a factor of $F_{2g,exp}$ / $F_{2g,PBE+U/4.5\ eV}$ = 464 cm^{-1} / 437 cm^{-1} = 1.06. Based on the 2ω-DOS experimentally observed overtones of CeO_2 can be assigned.

4.3 Raman active vibrations of reduced ceria CeO_{2-x}

Up to this point the crucial property of ceria of being reducible, by which oxygen vacancies can easily form, has not been taken into account. The removal of one (neutral) oxygen atom is followed by the localization of two electrons in 4f states of Ce, driving the Ce^{4+} ($4f^0$) to Ce^{3+} ($4f^1$) reduction of a pair of cations according to the following chemical equation 4.1. In section 1.5 it is discussed that the PBE+U/4.5 eV functional properly describes the process of localization of excess charge at cationic sites. Due to the excess charge located at the Ce^{3+} ion, the ionic radius increases with respect to that of Ce^{4+} (compare 1.143 Å and 0.970 Å for Ce^{3+} and Ce^{4+}, respectively). [50]

$$2\ \mathrm{Ce}^{4+} + \mathrm{O}_\mathrm{O}^{x} \rightarrow 2\ \mathrm{Ce}^{3+} + \mathrm{V}_\mathrm{O}^{\bullet\bullet} + \frac{1}{2}\ \mathrm{O}_2 \tag{4.1}$$

The effect of oxygen vacancies on the vibrational properties is studied for a (2 × 2 × 2) expansion of the conventional cubic ceria cell resulting in a $Ce_{32}O_{64}$ supercell. Abstraction of one or two oxygen ions from this supercell corresponds to a stoichiometry of $CeO_{1.969}$ or $CeO_{1.938}$, respectively. As already pointed out by Murgida *et al.* [161] there are different possible configurations for the excess charge localization. The $Ce_{32}O_{63}$ configurations are named as (nN-mN, lN), where nN-mN indicates a pair of Ce^{3+} ions in the nth and mth neighboring shells to the defect, and the closest distance between Ce^{3+} ions (Ce^{3+} - Ce^{4+}) is given as lth neighbor (lN) in the Ce sublattice. The three considered structures are (1N-1N, 1N), (2N-2N, 4N), and (1N-2N, 3N) as shown in figure 4.3 A-C. The corresponding vacancy formation energies were calculated as 2.91, 2.85, and 2.86 eV (see table B.1) in accordance with the literature [161]. This indicates that the Ce^{3+} and the oxygen vacancy tend to avoid each other since the (2N-2N, 4N) configuration is energetically slightly favored over the (1N-1N, 1N) and (1N-2N, 3N) configurations.

The Raman active vibrations of the oxidized ($Ce_{32}O_{64}$) and defective ceria supercells ($Ce_{32}O_{63}$) were calculated with the DFPT approach. The resulting calculated Raman spectrum is shown in figure 4.4. The oxidized $Ce_{32}O_{64}$ supercell possesses only the F_{2g} mode as Raman active vibration. Besides that, the Raman active modes of the defective CeO_{2-x} structures are predicted with frequencies between 480 and 600 cm^{-1}. This spectral region is also known from experiment as defect-related region. Four distinct regions are observed, as indicated by the white and grey background in figure 4.4. The regions are located around ∼437 cm^{-1} (F_{2g} mode), ∼480 cm^{-1}, ∼500 cm^{-1}, ∼525 cm^{-1}, and ∼550 cm^{-1}. The detailed analysis of the model structures suggests, that the regions can be assigned to four different $Ce^{4+/3+}$ coordination cubes. The structural building blocks of the oxygen defective CeO_{2-x} structures in figure 4.3 are shown in table 4.1 namely, $Ce^{4+}O_8$, $Ce^{3+}O_8$, $Ce^{3+}O_7V_O^{\bullet\bullet}$, and $Ce^{4+}O_7V_O^{\bullet\bullet}$. The $Ce^{4+}O_8$ is the regular 8-fold coordination of the oxidized CeO_2 crystal and it is present in all four structures. It gives rise to the F_{2g} mode as already discussed before for the primitive CeO_2 cell. The predicted slight blueshift of this mode compared to the $Ce_{32}O_{64}$ structure is a spurious effect which is discussed below and in the following section. The $Ce^{3+}O_8$ coordination is only present in the (2N-2N, 4N) and the (1N-2N, 3N) configurations, i.e., only those configurations where Ce^{3+} is located outside the first coordination sphere of the oxygen defect. Only these two configurations (green and blue spectrum) possess a Raman active mode in the region around 480 cm^{-1}. Therefore, it is proposed that the $Ce^{3+}O_8$ coordination gives

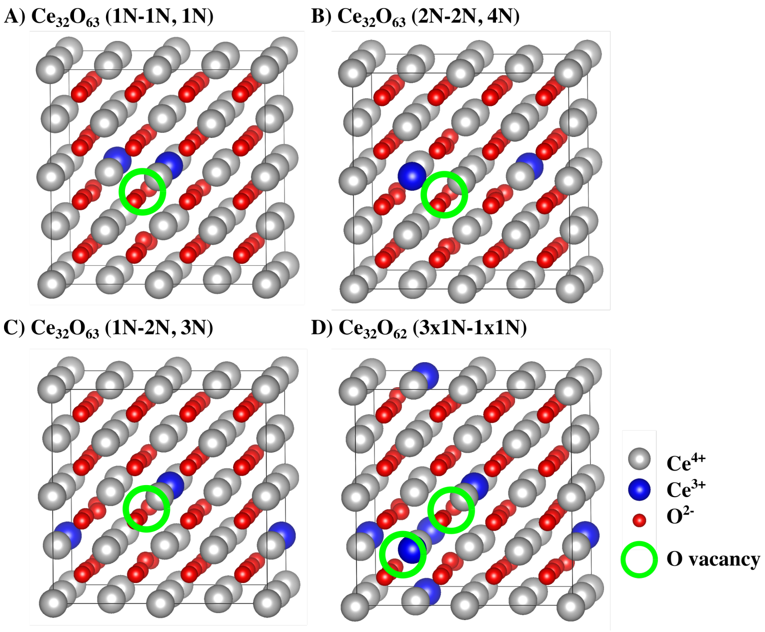

Figure 4.3.: Non stoichiometric (reduced) CeO_{2-x} structures corresponding to the $Ce_{32}O_{64}$ supercell with one (A-C, $Ce_{32}O_{63}$) or two oxygen defects (D, $Ce_{32}O_{62}$) according to ref [161]. The green circles mark the defect positions. The Ce^{3+} configuration is labeled as (nN-mN, lN), where nN-mN indicates a pair of Ce^{3+} ions in the nth and mth neighboring shells to the defect, and the closest distance between Ce^{3+} ions (Ce^{3+} - Ce^{4+}) is given as lth neighbor (lN) in the Ce sublattice. In structure D both oxygen vacancies are located in [111] direction and Ce^{3+} localizes in the first coordination sphere. The oxygen vacancy formation energies are given in Table B.1. The gray balls indicate Ce^{4+} and the blue balls Ce^{3+}.

rise to a mode in that region. For the (1N-1N, 1N) configuration no band is predicted in this region. Following the same arguments, the $Ce^{3+}O_7V_O^{\bullet\bullet}$ coordination sphere gives rise to vibrational modes with frequencies of 500 and 550 cm^{-1}. This coordination is only present if the excess charge is localized in the first coordination sphere of the oxygen defect, for example in the (1N-1N, 1N) and (1N-2N, 3N) configurations but not in the (2N-2N, 4N) configuration. The $Ce^{4+}O_7V_O^{\bullet\bullet}$ local coordination is present in all structures. Accordingly, for all structures a mode with a frequency of 525 cm^{-1} is predicted. A quantitative analysis of these bands and the additional bands > 550 cm^{-1} can not be made on the basis of such a rather simple coordination model. However, one can distinguish between configurations with Ce^{3+} in the vicinity of the defect showing a band at 500 cm^{-1} and Ce^{3+} in the second coordination sphere of the oxygen defect with a band at 480 cm^{-1}. Together with the information that Ce^{3+} ions and oxygen defects tend to avoid each other, [161] it is proposed that Raman bands calculated at 480 cm^{-1} ($\sim$540 cm^{-1} in experiment) correspond to a lower concentration of oxygen vacancies, because Ce^{3+} and the oxygen defect can avoid each other and the calculated band at 500 cm^{-1} ($\sim$560 cm^{-1} in experiment) corresponds to a higher concentration of oxygen vacancies, where Ce^{3+} and oxygen can no longer avoid each other.

Besides the information on the defect concentration by Raman bands in the defect band region (spectral region $500 - 600$ cm^{-1} in experiment) discussed above, a direct quantitative relation between spectroscopic information and CeO_{2-x} stoichiometry can be derived from the precise position of the band assigned to the F_{2g} mode.

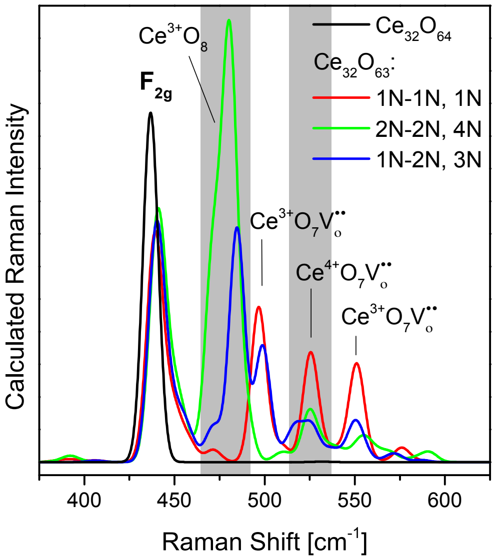

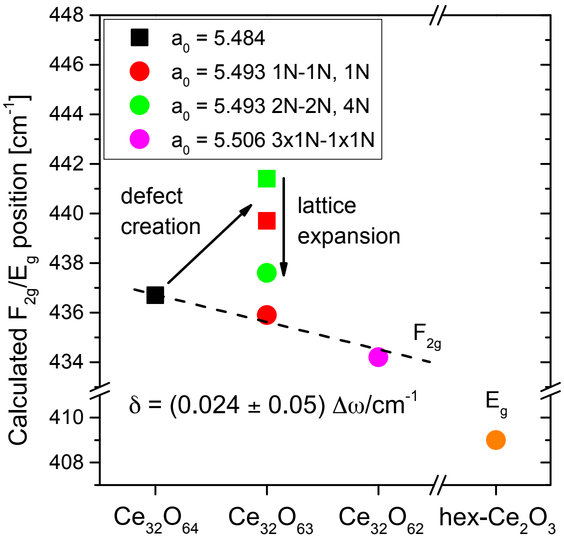

Figure 4.4.: Calculated Raman spectrum for CeO_2 ($Ce_{32}O_{64}$) and CeO_{2-x} ($Ce_{32}O_{63}$) structures with different Ce^{3+} configurations (see figure 4.3). For better comparison with the experiment, a Gaussian type broadening of 10 cm^{-1} full width at half maximum (fwhm) was applied to the calculated frequencies.

Figure 4.5.: Calculated position of the F_{2g} band of CeO_2 and CeO_{2-x} after oxygen vacancy creation followed by ionic relaxation at a fixed fixed lattice constant (squares) and with a relaxed lattice constant (circles). The dashed line indicates the interpolated linear relation between the F_{2g} Raman shift and CeO_{2-x} stoichiometry (Ce^{3+} in nearest neighbor position). The frequency of the E_g mode in the A-type Ce_2O_3 (orange) is considered as a limit for the redshift in CeO_{2-x} despite the different crystal structures.

After oxygen vacancy creation and Ce^{3+} formation strain is introduced in the lattice due to the larger ionic radius of Ce^{3+}. As a consequence the Ce^{3+}-O bonds become longer, but in a supercell with a fixed lattice constant the Ce^{4+}-O bonds become shorter as compared to the non-defective structure. This results in a spurious blueshift of the calculated F_{2g} band position (see figure 4.4). However, if the volume is allowed to expand due to the presence of the larger Ce^{3+}, the blueshift of the F_{2g} band is not observed. As described in chapter 3 the volume expansion and localization of the excess charge in CeO_{2-x} supercells were obtained in a two-step procedure. Expansions of 0.5 % and 1.2 % for the $Ce_{32}O_{63}$ (a_0=5.493 Å) and $Ce_{32}O_{63}$ (a_0=5.506 Å) structures were obtained, respectively, as compared to the non-defective $Ce_{32}O_{64}$ (a_0=5.484) structure. A lattice expansion has also been observed for Ce_2O_3 in the cubic structure (C-type, not shown) before. Employing a GGA+U/4.5 eV functional Da Silva [177] reported a 4 – 9 % larger cell volume as compared to the oxidized CeO_2 cell.

In Figure 4.5 the calculated position of the F_{2g} band is plotted for the three considered CeO_{2-x} structures together with the E_g stretching mode of A-type Ce_2O_3 at 409 cm^{-1}. For $Ce_{32}O_{63}$ stoichiometry the (1N-1N, 1N) and (2N-2N, 4N) configurations were considered, in accordance with the calculated Raman spectra in figure 4.4. Squares indicate the position of the F_{2g} mode for the unrelaxed lattice constants and circles the position for the relaxed lattice constants. A redshift of 4.0 cm^{-1} is observed between

Table 4.1.: Scheme of the cubic Ce-O coordination spheres around cerium ions in CeO_2 and CeO_{2-x}, the number of appearances of the local coordination spheres and calculated Raman active modes for the considered $Ce_{32}O_{63}$ structures. Distortion is not considered in the depicted schemes in this table.

Cubic coordination	$Ce^{4+}O_8$	$Ce^{3+}O_8$	$Ce^{3+}O_7V_O^{\bullet\bullet}$	$Ce^{4+}O_7V_O^{\bullet\bullet}$
	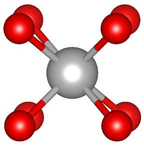	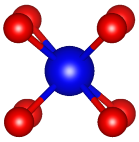	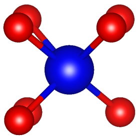	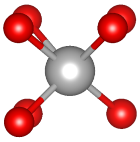
Frequency	F_{2g} 437 cm^{-1}	480 cm^{-1}	500 cm^{-1}, (550 cm^{-1})	525 cm^{-1}
Structures	Appearances in the structures			
$Ce_{32}O_{64}$	32	-	-	-
$Ce_{32}O_{63}$ 1N-1N, 1N	28	-	2	2
$Ce_{32}O_{63}$ 2N-2N, 4N	26	2	-	4
$Ce_{32}O_{63}$ 1N-2N, 3N	28	1	1	3

the predicted band for a supercell with a relaxed lattice constant as compared to a supercell with an unrelaxed one. Compared to the oxidized crystal ($Ce_{32}O_{64}$) a redshift of 2.5 cm^{-1} is observed for the $Ce_{32}O_{62}$ structure. By fitting a linear curve using the calculated F_{2g} band positions for the three considered stoichiometries $Ce_{32}O_{64}$ (black square), $Ce_{32}O_{63}$ (1N-1N, 1N, red circle), and $Ce_{32}O_{62}$ (purple circle), a direct quantitative relation between the F_{2g} redshift ($\Delta\omega$) and the stoichiometry of $CeO_{2-\delta}$ is derived as

$$\delta = (0.024 \pm 0.05)\ \Delta\omega/\mathrm{cm}^{-1}. \tag{4.2}$$

Although the E_g stretching mode of A-type Ce_2O_3 at 408 cm^{-1} (see orange circle in figure 4.5) possesses a different symmetry than the F_{2g} mode of CeO_2, it might be interpreted as a limit for the redshift of the F_{2g} mode in CeO_{2-x} as both, the F_{2g} and E_g mode, correspond to a Ce^{4+}/Ce^{3+}-O stretching modes.

4.4 Discussion on Raman modes of CeO_2 and CeO_{2-x}

As described in section 4.1 the frequency of the first-order allowed Raman mode (F_{2g}) was determined at the primitive ceria cell (three atoms). With the HSE06 functional the frequency is predicted as 450.8 cm^{-1} which reproduces the experimental frequency as determined for ceria single crystals, [30,178,179] thin films, [185] and polycrystalline ceria powder [49] better, than the PBE+U/4.5 eV functional (437.3 cm^{-1}). The difference between a vibrational analysis with a DFPT or a finite differences approach is negligible (0.1 cm^{-1}). To properly compare the calculated frequencies in the PBE+U/4.5 eV framework to the observed experimental bands a scaling factor of 464 cm^{-1} / 437 cm^{-1} = 1.06 is proposed. The calculated overtone frequencies were scaled by this factor and match the experimentally observed bands in the Raman spectrum of polycrystalline ceria with particles >1000 nm well (see Figure 4.1). However, for small nanoparticles the considered models can not explain the increase in intensity at ∼250 and ∼400 cm^{-1}. This gives rise to the proposal that a single component assigned to a TA overtone at ∼250 cm^{-1} [30] is insufficient. This point is addressed in the following section, where the surface termination of polycrystalline ceria nanoparticles is taken into account.

Previously a redshift of the F_{2g} band (5 cm^{-1}) and an expansion of the lattice (1.4 %, derived from XRD) has been observed upon decreasing the size of ceria nanoparticles from 25 to 6.1 nm. This leads to the suggestion of an increased oxygen vacancy concentration in smaller ceria nanoparticles. [31] This is supported by recent theoretical results, which report a smaller oxygen vacancy formation energy for ceria nanoparticles compared to extended ceria surfaces. [186] The observation of the F_{2g} redshift and the lattice expansion can be rationalized based on the results for the reduced CeO_{2-x} structures. For the $Ce_{32}O_{62}$ structure a 2.5 cm^{-1} redshift and a 1.2 % expansion of the lattice is predicted here. In the literature a lattice expansion of $4 - 9$ % has been predicted for C-type Ce_2O_3 (cubic) with a GGA+U/4.5 eV functional. [177] Although only A-type Ce_2O_3 is considered in this work, the E_g vibration may provide a limit for the F_{2g} redshift (~ 27 cm^{-1}) for reduced CeO_{2-x}. A redshift of the F_{2g} band from 464 to 449 cm^{-1} has also been observed upon temperature increase of the ceria samples from -200 to 600°C (thermal effect). [31] For Au/CeO_2 catalysts upon reduction in CO [50] and under reaction conditions of CO oxidation a redshift of the F_{2g} band was also linked to an increased oxygen vacancy concentration. [52] Thus, if temperature effects and particle sintering are avoided the F_{2g} band position serves as a quantitative measure for the bulk reduction state of ceria nanoparticles. The relation between the F_{2g} band position and the stoichiometry of CeO_{2-x} can be quantified based on the DFT+U calculation (see equation 4.2), similar to the approach of Lee *et al.* who compared the ionic radii of Ce^{4+} and Ce^{3+}. [50] The Grüneisen parameter which relates the frequency change to the volume expansion is calculated as $\gamma = 0.51$ based on the DFT+U results presented here. Thus it is significantly smaller than the value $\gamma = 1.24$ determined by Sato *et al.* [187] and the value $\gamma = 1.44$ determined by Kourouklis *et al.* measuring the pressure dependence of the F_{2g} mode and employing the bulk modulus of ThO_2. [178] However, the discussed approach rationalizes not only the redshift due to oxygen vacancy creation but might also quantify the redshift upon doping of ceria with trivalent ions which are larger than Ce^{4+}. [128]

Raman modes between 480 and 600 cm^{-1} have been attributed to oxygen vacancies accompanied by Ce^{3+} formation. This is known as the defect band region from experiment. [33, 128, 188] The calculated Raman spectra offer an explanation for the origin of the Raman bands in this spectral region. The analysis revealed that the coordination cube around $Ce^{4+/3+}$ in CeO_{2-x} strongly influences the vibrational properties. A clear distinction between bands arising from Ce^{3+} in direct proximity to the oxygen defect and from Ce^{3+} located in the second coordination sphere of the oxygen vacancy can be made. For the former a Raman active mode at 500 cm^{-1} is predicted whereas for the latter it is at 480 cm^{-1}. After application of the scaling factor the defect band between 480 and 540 cm^{-1} can be assigned to a lower concentration of oxygen defects, i.e., Ce^{3+} and oxygen defect avoiding each other, whereas the defect band region between 540 and 560 cm^{-1} is assigned to a higher concentration of oxygen defects.

An analysis allowing for quantitative evaluation of the oxygen defect concentration by the precise F_{2g} band position and an evaluation of the defect band region with a simple coordination model on the basis of DFT+U calculations is unique and new in the literature about ceria. [183]

4.5 Vibrational properties of the $CeO_2(111)$ surface

To take the surface termination of ceria nanoparticles into account the $CeO_2(111)$ and $CeO_2(100)$ surfaces were modeled. The results on the $CeO_2(111)$ surface are described in this section and the results on the $CeO_2(100)$ surface are described in section 4.6. In section 4.7 the results are discussed together with experimental Raman spectra. The normal modes and Raman intensities were calculated with the DFPT approach employing a PBE+U/4.5 eV functional.

First, surface slabs with three O-Ce-O trilayer (TL) and (1×1) and (2×2) periodicities were considered (see figure 3.1 D and E for top and side views of a slab with (2×2) periodicity). For all structures the bottom trilayer was kept fix at its bulk-truncated position during geometry optimization. In figure 4.6 the calculated Raman spectrum for these surface slabs is shown as black dotted and solid lines. The frequencies of the predicted normal modes and the corresponding Raman intensities are listed in table B.3 in the appendix. Neither the position nor the intensity changes between the two considered periodicities. Please note that the Raman intensities of the slabs with (1×1) periodicity are multiplied by a factor of four. This indicates that the vibrations are invariant with respect to the surface periodicity (x, y direction).

Second, a surface slab with (1×1) periodicity and five O-Ce-O trilayers was considered. The position of the bands upon increasing of the the slab thickness in z direction is discussed in the following (see red line in figure 4.6). The F_{2g} analog vibration in the surface slab shifts from 423 to 432 cm^{-1} as compared to the three trilayer slab. A deviation of the frequency with respect to the position determined for bulk CeO_2 (437 cm^{-1}), and a lift of the triple degeneracy to a doubled degeneracy is observed. This can be rationalized by the confinement of the vibration between the surface and the fixed bottom trilayer in z direction and the degeneracy of the surface in x and y direction. However, three modes keep their frequency of 225, 363 (364 cm^{-1} for five O-Ce-O trilayers) and 475 cm^{-1} upon enlargement of the slab from three to five trilayers. The analysis of the vibration vectors revealed that the band at 475 cm^{-1} is the vibration of deepest not fixed oxygen layer against the fixed Ce layer. Therefore, it is concluded that this band is a model artifact due to keeping the atoms of the bottom trilayer fixed at the bulk lattice positions. In contrast, the vibrations with a frequency of 225 cm^{-1} and 363 cm^{-1} are clearly localized at the $CeO_2(111)$ surface. More precisely, these are a longitudinal stretching modes (movement in x and y direction) of the surface oxygen layer against the surface Ce layer (225 cm^{-1}) and a transversal stretching mode (movement in z direction) of the two layers (363 cm^{-1}). The corresponding frequencies were calculated as 216 cm^{-1} and 407 cm^{-1} with a HSE06 functional and a finite differences approach. The longitudinal vibration is twice degenerated whereas the transversal vibration is not degenerated. This is fully consistent with the symmetry of the slab, i.e., an infinite repetition in x, y direction and a truncation of the slab in z direction.[4]

To account for the incorporation (exchange) of an ^{18}O isotope in the $Ce^{16}O_2(111)$ surface, the $Ce^{18}O_2(111)$ surface with three TL was modeled with the ^{18}O isotope instead of the ^{16}O isotope. The calculated Raman spectrum is shown in figure 4.7 (red) where it is compared to that of the $Ce^{16}O_2(111)$ surface (black). The calculations revealed a redshift of 11 cm^{-1}, 17 cm^{-1} and 24 cm^{-1} for the longitu-

---

[4] Videos of the vibrational modes are available online as supporting material to *J. Phys. Chem. C*, **2017**, 121, 20834-20849. (http://pubs.acs.org/doi/suppl/10.1021/acs.jpcc.7b06643)

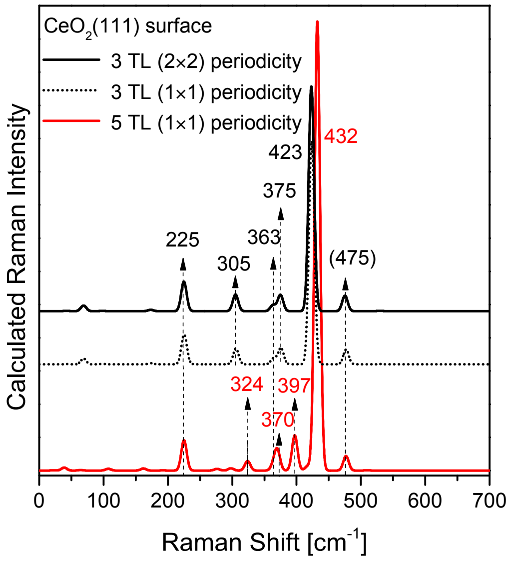

Figure 4.6.: Calculated Raman spectra (PBE+U/4.5 eV functional) of the oxidized $CeO_2(111)$ surface. Black line: three O-Ce-O trilayer (TL) and (2×2) periodicity. Dotted black line: three TL and (1×1) periodicity. Red line: five TL and (1×1) periodicity. The intensities of the spectra for structures with (1×1) periodicity are multiplied by four.

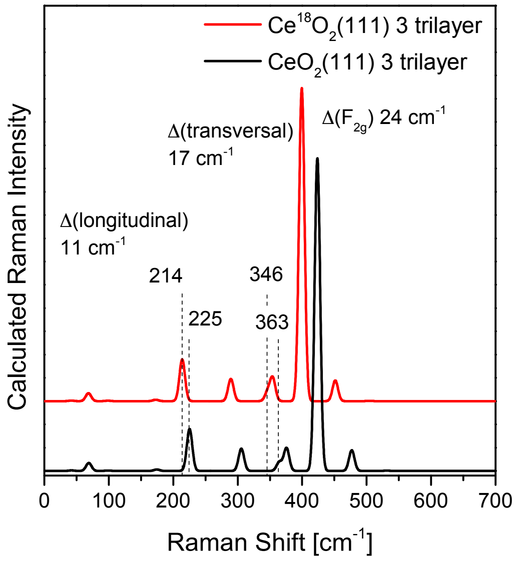

Figure 4.7.: Comparison of the calculated Raman spectra of the $Ce^{16}O_2(111)$ (black line) and $Ce^{18}O_2(111)$ surface (red line). Three O-Ce-O trilayers (TL) were considered at (1×1) periodicity.

dinal and transversal surface modes and the F_{2g} bulk mode, respectively. Although the modes are solid state phonons, the shift can be approximated by an isolated ^{140}Ce-$^{16/18}O$ vibration within the harmonic oscillator approach, assuming the same bond strength between Ce-^{16}O and Ce-^{18}O. To this end the shift of the vibrations can be calculated as $\tilde{\nu}_{Ce^{18}O_2(111)} = 0.949 \cdot \tilde{\nu}_{Ce^{16}O_2(111)}$. The frequencies determined by this isolated oscillator model of 213.5, 344.5 and 410.0 cm^{-1} are in agreement with the calculated frequencies from DFT+U calculations.

The vibrational properties of a reduced $CeO_{2-x}(111)$ surface are studied for two different structures with either a surface or a subsurface oxygen defect (0.25 ML). The Ce^{3+} configurations as depicted in figure 4.8 A for a surface oxygen defect and B for a subsurface oxygen defect are in accordance with those found by Murgida *et al.* [103] as are the corresponding oxygen vacancy formation energies $E_{vac,O}$ of 2.27 eV and 1.89 eV, respectively (see also the calculated total energies in table B.2). In the depicted structures both Ce^{3+} are located in the second coordination sphere of the oxygen defect whereas one Ce^{3+} is located in the surface cerium layer and the second Ce^{3+} is located in the subsurface cerium layer.

Regarding the calculated Raman spectra of the $CeO_{2-x}(111)$ surface structures in figure 4.9, the variety of Raman active modes is caused by the lift of the symmetry in the surface slab upon oxygen defect creation. The frequency of the F_{2g} mode is shifted by 38 cm^{-1} and 45 cm^{-1} compared to the oxidized $CeO_2(111)$ surface for a surface and subsurface oxygen defect structure, respectively. As before for the bulk CeO_{2-x} structures this blueshift is due to the calculation at the fixed surface lattice constant which introduces strain after Ce^{3+} formation. In the spectral region between 480 and 525 cm^{-1} bands are also

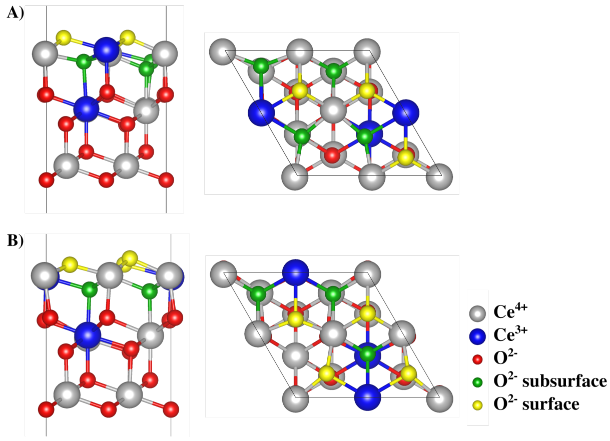

Figure 4.8.: Side (left) and top (right) views of the $CeO_{2-x}(111)$ surface with A) a surface vacancy and B) a subsurface oxygen vacancy.

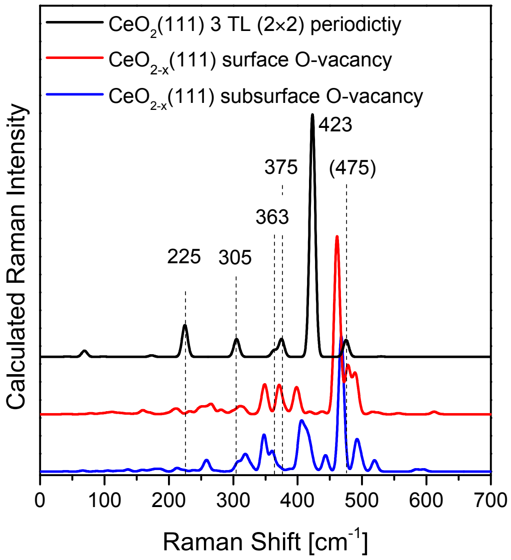

Figure 4.9.: Calculated Raman spectra of the $CeO_2(111)$ surface with (2×2) periodicity (black line) and a $CeO_{2-x}(111)$ surface containing a surface (red line) and subsurface (blue line) oxygen vacancy.

observed and related to the oxygen defects. As defects in the bulk also near surface defects account for bands in the defect band region between 480 and 600 cm^{-1}.

The longitudinal surface mode at 225 cm^{-1} is completely damped upon introduction of a surface oxygen defect (red line in figure 4.9). For a subsurface oxygen defect a blueshifted band at ∼250 cm^{-1} with a much lower intensity as compared to the oxidized surface is observed. Therefore it is proposed that the band at 225 cm^{-1} (246 cm^{-1} in experiment) serves as a semi-quantitative measure for the surface oxidation state of ceria nanoparticles with a $CeO_2(111)$ surface termination. This is directly relevant for the characterization of Au/CeO_2 catalysts and will be employed for the characterization of Au/CeO_2 catalysts under reaction conditions in chapter 7.

4.6 Vibrational properties of the $CeO_2(100)$ surface

Besides nanoparticles with a $CeO_2(111)$ surface termination, nanoparticles with a $CeO_2(100)$ surface termination can be synthesized hydrothermally [45] (see chapter 2 for the synthesis procedure and chapter 5 for *in situ* characterization results). The $CeO_2(100)$ surface is a Tasker type III surface [162] consisting of ionic layers of Ce^{4+} and O^{2-}, where each Ce_2-O_4 bilayer maintains the bulk composition but possessing a permanent dipole moment. To avoid a permanent dipole moment in the $CeO_2(100)$ surface slab, [162] half of the topmost oxygen layer is moved to the bottom, i.e., the slab maintains the bulk composition. Thus, only half of the oxygen lattice positions at the surface are occupied in a checkerboard type of arrangement (see figure 4.10). The checkerboard arrangement is the most stable configuration for the $CeO_2(100)$ surface termination, whereas other arrangements have been considered. [95,117,119] A discussion on the experimental characterization of the $CeO_2(100)$ surface termination is given in chapter 5. The bottom three ionic layers were fixed to the bulk lattice positions in agreement with the $CeO_2(111)$ surface slabs. The relaxation of the ions after surface creation is larger for the $CeO_2(100)$ surface (see figure 4.10) than for the $CeO_2(111)$ surface, where only a minor shortening of the Ce-O bonds in z direction is observed.

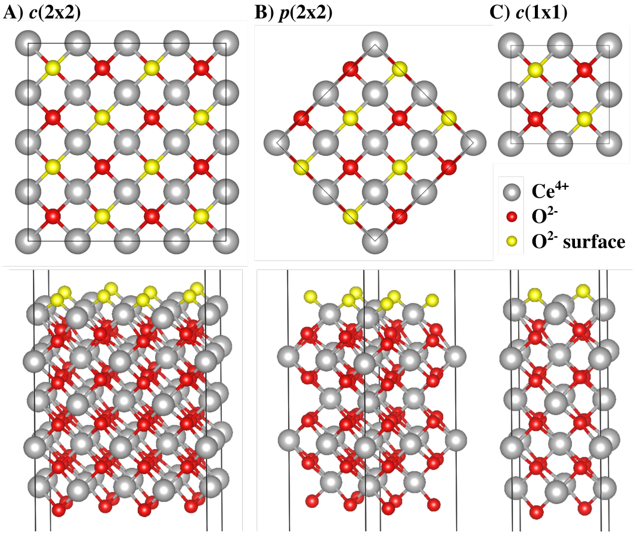

Figure 4.10.: Top and side views of the models systems for the $CeO_2(100)$ surface consisting of 11 atomic layers and A) $c(2\times2)$, B) $p(2\times2)$ and C) $c(1\times1)$ periodicity.

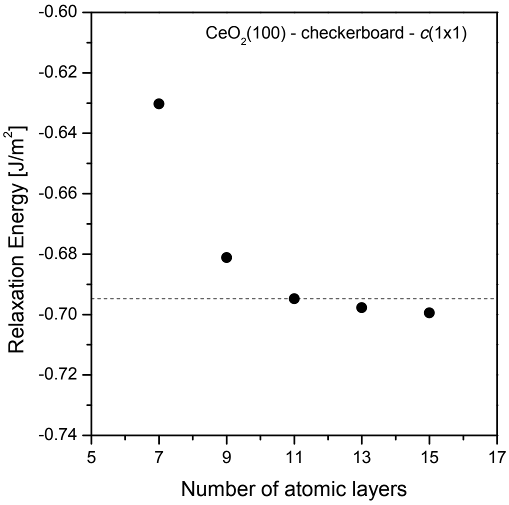

Figure 4.11.: Convergence for the slab thickness is confirmed by plotting the relaxation energy (see text) as a function of the number of ionic layers of the $CeO_2(100)$ surface. The dashed line indicates that 11 ionic layers are sufficient to model the $CeO_2(100)$ surface. [127]

Kropp *et al.* [127] already verified the convergence of the $CeO_2(100)$ slab model with respect to its thickness by calculating the surface energy. For this purpose the surface energy associated to a bulk truncated slab ($E_{\mathrm{surf,cut}}$) is calculated, first.

$$E_{\mathrm{surf,cut}} = \frac{E_{\mathrm{cut}} - (n-1)\cdot E_{\mathrm{CeO_2}}}{2A} \tag{4.3}$$

In equation 4.3 E_{cut} is the total energy of the bulk truncated slab with $c(1\times1)$ periodicity, $E_{\mathrm{CeO_2}}$ is the total energy of the primitive CeO_2 unit cell, n is the number of atomic layers and A is the area of the surface unit cell. Second, the relaxation energy $E_{\mathrm{surf,relax}}$ is derived from the total energy of the relaxed slab. It should be noted that before relaxation the bottom three trilayers are fixed and therefore the energy is divided only by A.

$$E_{\mathrm{surf,relax}} = \frac{E_{\mathrm{CeO_2(100)}} - E_{\mathrm{surf,cut}}}{A} \tag{4.4}$$

Finally, the total surface energy is the sum of $E_{\mathrm{surf,cut}}$ and $E_{\mathrm{surf,relax}}$.

$$E_{\mathrm{surf}} = E_{\mathrm{surf,cut}} + E_{\mathrm{surf,relax}} = 1.45\ \mathrm{J\ m^{-2}} \tag{4.5}$$

Convergence with respect to the number of ionic layers is verified by stabilization of the relaxation energy ($E_{\mathrm{surf,relax}}$) for increasing number of layers (see figure 4.11) and is achieved for 11 ionic layers. The calculated surface energy for this slab is 1.454 J m^{-2} in accordance with the literature (1.44 J m^{-2}) [127]. Correction of the spurious dipole moment in the cell shows a deviation of less than 1 % in the calculated surface energy. Therefore dipole contributions are neglected in the whole study.

For the surface slabs with 7 to 15 ionic layers and $c(1\times1)$ periodicity the Raman spectrum was calculated and is shown in figure 4.12. Like for the $CeO_2(111)$ surface the modes which are confined at the surface of the slab do not shift in frequency upon increasing the number of ionic layers. These are the modes which are predicted with a frequency of 370, 467, and 481 cm^{-1} and correspond to two types of longitudinal like vibrations of the second oxygen layer (370 and 481 cm^{-1}) and a transversal mode of the outmost oxygen ions at 467 cm^{-1} (compare also figure 4.14 for a visualization of the vibrational vectors).

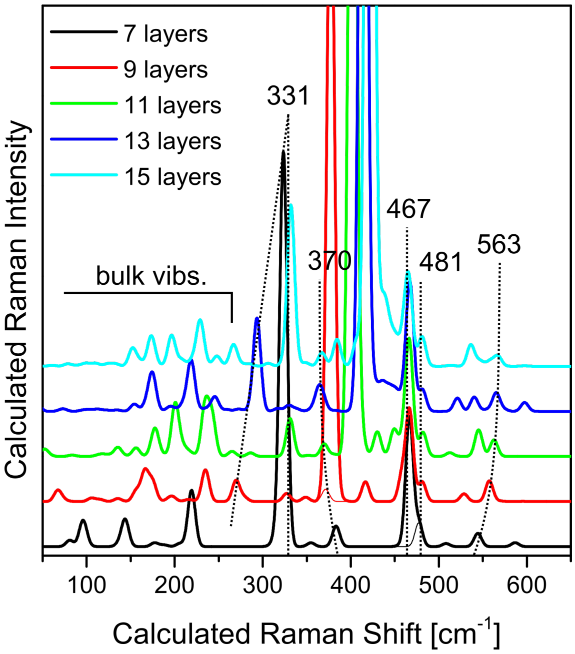

Figure 4.12.: Calculated Raman spectra of the $CeO_2(100)$ surface with $c(1 \times 1)$ periodicity. From the bottom to the top the number of ionic layers increases from 7 to 15. The dashed lines indicate vibrational modes with comparable vibrational vectors for the surface slabs with 7 to 15 ionic layers.

Two further modes are proposed to occur due to the surface termination in (100) direction with a frequency of 331 cm^{-1} and 563 cm^{-1}. The modes are indicated by dashed lines in figure 4.12 and belong to comparable vibrational patterns in the surface slabs with 7 to 15 ionic layers. This is verified by the analysis of the normal mode vectors (see figure 4.14). The mode with a frequency of 331 cm^{-1} (11 layers) is only slightly blueshifted for 15 layers (332 cm^{-1}) and slightly redshifted for 7 layers (323 cm^{-1}) but strongly redshifted for 9 (269 cm^{-1}) and for 13 layers (293 cm^{-1}). This is attributed to the different symmetry of the slabs with 9 and 13 ionic layers compared to the slabs with 7, 11, and 15 ionic layers. But there is a clear tendency that for an increasing number of layers the position approaches a value of ~331 cm^{-1}. Therefore five bands at 331, 370, 467, 481, and 563 cm^{-1} are expected in the experimental Raman spectrum of $CeO_2(100)$ terminated nanoparticles.

To summarize the vibrational analysis of the ceria surface facets the results for the CeO_2(111) and the CeO_2(100) surface are compared to experimental Raman spectra in figure 4.13. The corresponding normal mode vectors are schematically shown in figure 4.14. Clearly polycrystalline CeO_2 sheets (blue line in figure 4.13) exposing the CeO_2(111) surface (compare TEM images in chapter 5) exhibit bands at 246 cm^{-1} and 402 cm^{-1} corresponding to the longitudinal and transversal stretching modes of the CeO_2(111) surface, respectively. These two bands are not observed for ceria nanocubes exposing the CeO_2(100) surface (compare TEM images in chapter 5). The modes which can be ascribed to the CeO_2(100) checkerboard termination at 370, 467, and 481 cm^{-1} can not be observed for the ceria nanocubes as the region of the spectrum is superimposed by the dominant band assigned to the F_{2g} mode. This is in contrast to the bands related to vibrations within the CeO_2(100) subsurface region which are clearly observed at 350 cm^{-1} (shoulder) and 600 cm^{-1}. Please note that the calculated vibrational frequencies in figure 4.14 were scaled by a factor of 1.06 (see table 3.1) to be comparable to the experimental spectra in figure 4.13. The scaling factor is derived in section 4.4.

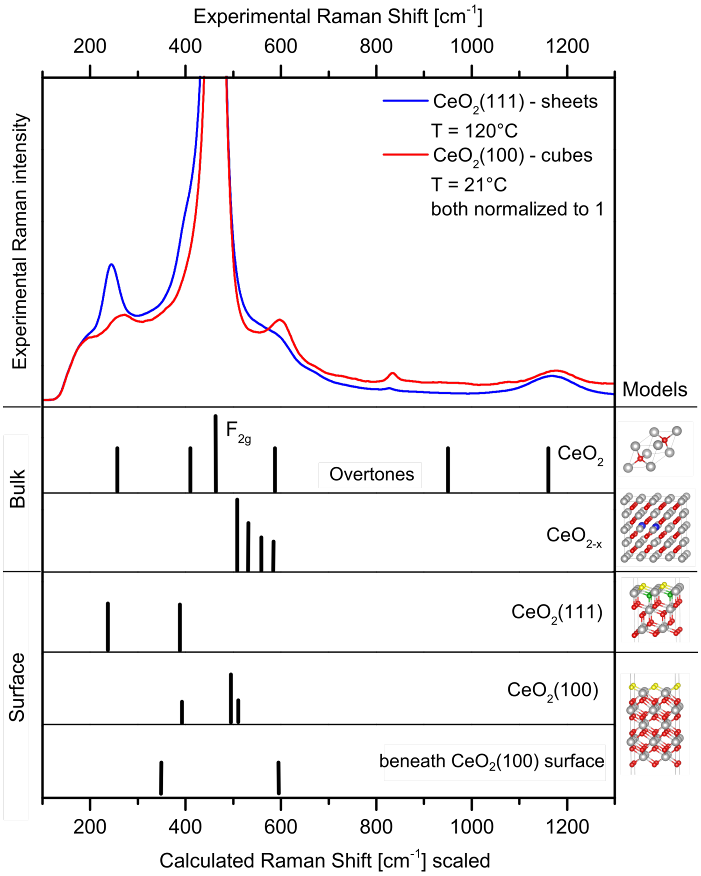

Figure 4.13.: Comparison of the experimental Raman spectra of ceria nanoparticles exposing the CeO_2(111) (blue) and CeO_2(100) surface (red) together with the calculated frequencies determined for the indicated ceria model systems. The calculated Raman shifts were scaled by a factor of 1.06.

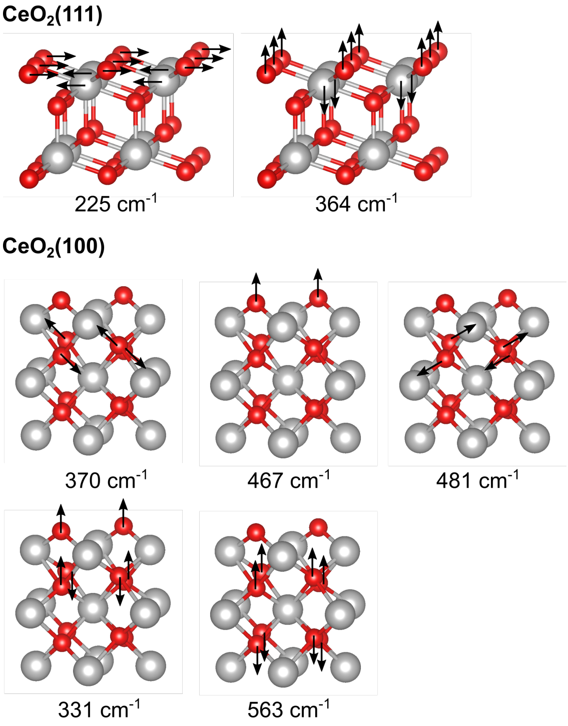

Figure 4.14.: Calculated vibrational modes of the CeO_2(111) surface (top) and CeO_2(100) surface (bottom). The frequencies were not scaled.

Previously the Raman band at ~250 cm^{-1} of polycrystalline ceria powder samples has been assigned to the 2TA overtone in accordance with single crystal data. [30, 32, 33] Raman spectra of polycrystalline ceria with different nanoparticle size (see figure 4.1) suggested a second component in this spectral region due to the nanoparticle surface. Based on infrared experiments that band has been assigned to a Ce-OH stretching vibration. [49] The DFT+U results on the $CeO_2(111)$ surface presented here clearly evidence that the band at ~246 cm^{-1} can be assigned to the longitudinal stretch of the topmost Ce and O layer of the $CeO_2(111)$ surface. There is also a component attributed to a 2TA overtone (264 cm^{-1}). However, at ceria nanoparticles exposing the $CeO_2(111)$ facet the 2TA overtone is superimposed by the longitudinal surface mode.

The results from the vibrational analysis of the $CeO_2(111)$ and the $CeO_2(100)$ surfaces provide the basis for the interpretation of experimental Raman spectra for ceria nanoparticles and thus it is suggested here that *in situ* Raman spectroscopy as applied in chapter 5 is sensitive for the surface faceting of ceria nanoparticles. This aspect has not been considered before although visible and UV-Raman spectroscopy were conducted at faceted ceria nanoparticles (nanocubes and nanooctahedra). [33, 189]

4.8 Peroxide formation at the $CeO_2(111)$ surface

Besides allowing the examination of the vibrational properties of oxidized (CeO_2) and reduced (CeO_{2-x}) bulk ceria as well as their surface facets Raman spectroscopy permit probing adsorbed molecular oxygen species such as peroxides ($O_2{}^{2-}$), superoxides ($O_2{}^{-}$), as well as weakly adsorbed oxygen ($O_{2,ads}$) and gas phase oxygen (O_2) by the corresponding O-O stretch frequencies. The formation of peroxide and superoxide species at the $CeO_2(111)$ surface is discussed in this and the two following sections. The formation of the above mentioned oxygen species at the $CeO_2(100)$ surface facet is then described in the subsequent sections 4.11-4.13.

Due to the fact that molecular oxygen is reduced in the course of peroxide and superoxide formation, this process is expected to occur at surface oxygen vacancy sites and in the vicinity of Ce^{3+} ions that can transfer electrons to the oxygen molecule. Therefore, peroxides have been used as indicator for the presence of surface oxygen vacancies at ceria powders before. [32, 33] Additionally, the absence of peroxide or superoxide species indicated a subsurface oxygen vacancy formation at ceria single crystals under vacuum conditions. [57] Recently, Raman spectroscopy has evidenced that peroxides act as an intermediate during the CO oxidation over ceria supported gold catalysts, highlighting the relevance of these species on ceria based materials in catalysis. [190]

To study the adsorption geometry, the stability and the vibrational properties of adsorbed peroxide molecules, $O_2{}^{2-}/CeO_{2-x}(111)$, as a function of their surface concentration, various peroxide coverages were modeled with the PBE+U/4.5 eV functional. Five different $CeO_2(111)$ surface periodicities, (4×4), (3×3), (2×2), (1×2), and (1×1), with one peroxide molecule resulted in $O_2{}^{2-}$ coverages of 0.06, 0.11, 0.25, 0.5, and 1 monolayer (ML), respectively. In all structures a surface oxygen ion of the oxidized $CeO_2(111)$ surface is replaced by a peroxide molecule corresponding to a $O_2{}^{2-}/O_{vac}$ ratio of 1. The structures may also result from adsorption of molecular oxygen at the oxygen vacancy site at the reduced ceria surface $CeO_{2-x}(111)$. The oxygen lattice position is filled and the excess charge initially located at 2 Ce^{3+} is transferred to the oxygen molecule to form a peroxide molecule ($O_2{}^{2-}$).

The stable peroxide $O_2^{2-}/CeO_{2-x}(111)$ structures are shown in figure B.2 and the corresponding reduced $CeO_{2-x}(111)$ surface structures in figure B.3. Huang *et al.* [54] already pointed out that two peroxide configurations $O_2^{2-}/CeO_{2-x}(111)$ are stable which differ by an angle of 60° with respect to the peroxide orientation. In one configuration the outer oxygen of the peroxide molecule leans towards a nearest neighboring surface Ce^{4+}. This configuration is named *a* and is shown in figure B.2 A and C. In the other configuration the outer oxygen leans towards a subsurface Ce^{4+}, i.e., between two neighboring surface Ce^{4+}. This configuration is shown in figure B.2 B, D, F-H and named configuration *b*. The DFT+U total energies for all structures and configurations are given in table B.4. From these values it is derived that the relative stability between configuration *a* and *b* varies with coverage. For coverages of 0.06 ML and 0.11 ML configuration *a* is by 25 and 15 meV more stable than *b*, respectively, whereas at 0.25 ML coverage configuration *b* is by 20 meV more stable than *a*. The latter value is in full accordance with results from the literature. [54] At higher coverages (≥0.5 ML) configuration *a* is not stable. For 0.5 ML coverage two configurations of type *b* are considered (figure B.2 F and G). The configuration in which two O_2^{2-} molecules form a rectangle (1×2)-*b*-1 is by 50 meV more stable than the configuration in which two O_2^{2-} molecules form a parallelogram (1×2)-*b*-2.

The O-O bond length of the peroxide molecules is slightly shortened from 1.444 (0.06 ML) to 1.433 Å (1 ML) with increasing coverage (see table B.4) and the calculated bond length of the peroxide molecules is in agreement with the bond length of hydrogen peroxide of 1.453 Å as determined by neutron diffraction experiments. [191]

To analyze the stability of the peroxide structures, the molecular oxygen adsorption energy $E_{\mathrm{ads,O_2^{2-}}} = E_{\mathrm{O_2^{2-}/CeO_{2-x}(111)}} - E_{\mathrm{O_2}} - E_{\mathrm{CeO_{2-x}(111)}}$ together with the negative oxygen vacancy formation energy $-E_{\mathrm{vac,O}} = -[E_{\mathrm{CeO_{2-x}(111)}} + \frac{1}{2}E_{\mathrm{O_2}} - E_{\mathrm{CeO_2(111)}}]$ is shown in figure 4.15. The former $E_{\mathrm{ads,O_2^{2-}}}$ refers to the adsorption of molecular oxygen at an oxygen defect at the reduced $CeO_{2-x}(111)$ surface and the latter, $-E_{\mathrm{vac,O}}$, to the adsorption of an oxygen atom at the oxygen defect (oxygen vacancy healing). In addition, the adsorption of a single oxygen atom to the oxidized $CeO_2(111)$ surface forming a peroxide molecule $E_{\mathrm{ads,O}}$ is defined as $E_{\mathrm{ads,O}} = E_{\mathrm{O_2^{2-}/CeO_{2-x}(111)}} - \frac{1}{2}E_{\mathrm{O_2}} - E_{\mathrm{CeO_2(111)}}$. Figure 4.15 clearly shows that the adsorption energy $E_{\mathrm{ads,O_2^{2-}}}$ strongly resembles the oxygen vacancy healing energy $-E_{\mathrm{vac,O}}$, apart from the small fraction $E_{\mathrm{ads,O}}$ that accounts for the repulsive interaction of the adsorbed peroxide molecules $E_{\mathrm{ads,O_2^{2-}}} = -E_{\mathrm{vac,O}} + E_{\mathrm{ads,O}}$.

Please note $+E_{\mathrm{vac,O}}$, i.e., the defect formation energy becomes larger as the defect concentration increases within a range that varies from $+E_{\mathrm{vac,O}} = 1.89$ eV for 0.06 ML coverage over 2.01 eV for 0.11 ML and 2.27 eV for 0.25 ML to 2.70 eV for 0.5 ML. For an oxygen vacancy coverage of 0.06, 0.11 and 0.25 ML the Ce^{3+} ions localize in next nearest neighbor positions to the defect. Specifically, for 0.06 and 0.11 ML coverage Ce^{3+} localizes at the surface cerium layer whereas for 0.25 ML one Ce^{3+} is located at the surface and one in the subsurface cerium layer (see figure 4.8). At 0.5 ML oxygen vacancy coverage nearest neighbor localization of the excess charge is no longer unavoidable resulting in Ce^{3+} localization in nearest neighbor positions at the surface. For 1 ML surface oxygen vacancy coverage the structure undergoes a strong reorganization by relaxation of the subsurface oxygen layer outwards [192] and a subsequent reconstruction with a change in the stacking resulting in the formation of a quintuple layer of A-type Ce_2O_3 on one regular O-Ce-O trilayer of the $CeO_2(111)$ surface. [110]

The gradual increase observed for $E_{\mathrm{ads,O}}$ from 0.28 eV for 0.11 ML to 0.5 eV for 1 ML coverage reflects the repulsive interaction between the adsorbed peroxide molecules.

Besides peroxide formation, the formation of superoxide molecules is also possible at the $CeO_{2-x}(111)$ surface and was exemplarily modeled with (2×2) periodicity (0.25 ML coverage, see figure B.2 E and the detailed discussion on the vibrational properties in section 4.10). The considered superoxide structure is by >0.6 eV less stable than the corresponding peroxide structure. A Bader charge analysis [193] revealed a charge transfer of one and two electrons to molecular oxygen (Bader charge: 11.98 *e*; O-O bond length: 1.234 Å) in the superoxide (12.73 *e*; 1.345 Å) and peroxide structure (configuration *a*, 13.19 *e*; 1.446 Å), respectively. These values can be compared to the Bader charge determined for two lattice oxygen ions (O^{2-}) of 14.42 *e*.

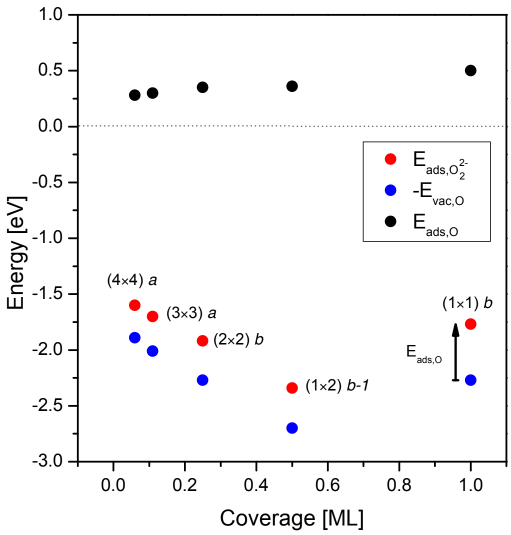

Figure 4.15.: Adsorption energies of molecular O_2 forming a peroxide species at the reduced $CeO_{2-x}(111)$ surface, $E_{\mathrm{ads,O_2^{2-}}}$ (red), for the most stable peroxide structures (as indicated) and the vacancy healing energy, $-E_{\mathrm{vac,O}}$ (blue), plus adsorption energy of a single O atom to the $CeO_2(111)$ surface forming a peroxide species, $E_{\mathrm{ads,O}}$ (black), as a function of peroxide coverage from 0.06 to 1 ML. The relation $E_{\mathrm{ads,O_2^{2-}}} = -E_{\mathrm{vac,O}} + E_{\mathrm{ads,O}}$ is illustrated by a black arrow for a coverage of 1 ML indicating that $E_{\mathrm{ads,O}} > 0$.

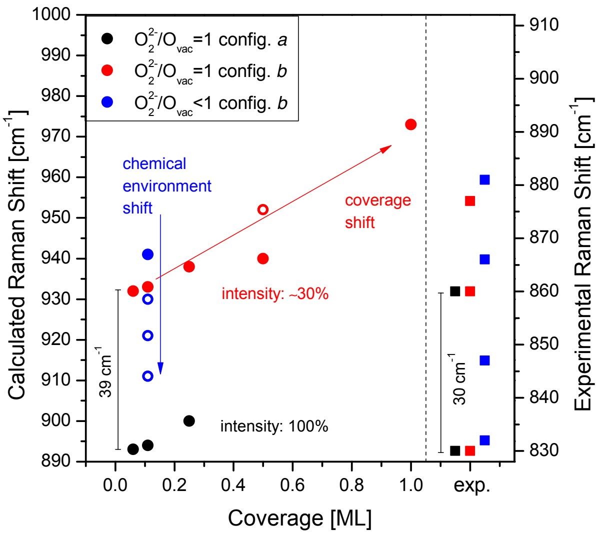

Figure 4.16.: Calculated vibrational frequencies of the peroxide molecule in $O_2^{2-}/CeO_{2-x}(111)$ structures with O_2^{2-}/O_{vac} = 1 (circles) in configuration *a* (black) and configuration *b* (red) as a function of O_2^{2-} coverage as well as for $O_2^{2-}/CeO_{2-x}(111)$ structures with O_2^{2-}/O_{vac} = 0.5 (blue). Filled circles refer to the most stable configuration, while open circles refer to metastable configurations. The position of experimental Raman bands (squares) from reference [49] (black), reference [32] (red), and reference [190] (blue, Au/CeO_2) are compared to the calculated frequencies by assigning the calculated frequencies of 893 and 932 cm^{-1} to the observed bands at 830 and 860 cm^{-1}. For details see text.

For the vibrational analysis of the peroxide molecules adsorbed at the $CeO_{2-x}(111)$ surface all atoms of the surface slab except for the peroxide molecule are fixed to their position after relaxation. This drastically reduces the computational demand. In fact, the difference between this method and the consideration of all atoms for the vibrational analysis was <0.1 % with respect to the predicted vibrational frequency of the peroxide molecule and <1 % for the predicted Raman intensity, as exemplarily tested at the structure in figure B.2 C.

In figure 4.16 the calculated vibrational frequency of the O-O stretching mode is plotted as a function of peroxide coverage. The black circles refer to configuration *a* and the red circles to configuration *b*. Precisely, for 0.06 ML coverage the frequency of configuration *a* is predicted as 893 cm^{-1} and for configuration *b* as 932 cm^{-1}. The Raman intensity of the former is predicted as ~4 times higher than that of the latter. For coverages up to 0.25 ML the frequency of the O-O stretching mode of the two configurations is predicted to show a difference of 38 − 39 cm^{-1}. A slight blueshift of the mode (7 cm^{-1}) is observed for both configurations at 0.25 ML coverage. Whereas for 0.5 ML coverage, the stretch frequency of configuration *b*-1 is predicted as 940 cm^{-1} and that of configuration *b*-2 as 952 cm^{-1}, i.e., 8 and 20 cm^{-1} blueshifted as compared to the frequency at 0.06 ML coverage. As mentioned above configuration *a* is unstable at coverages >0.25 ML. A shift of the frequency to 973 cm^{-1} is observed for a full monolayer coverage. Thus, a blueshift with respect to a coverage increase is evident from the DFT+U calculations.

To compare the calculated frequencies to experimentally observed Raman shifts, the calculated frequencies of 893 cm^{-1} and 932 cm^{-1} were assigned to the observed bands at 830 and 860 cm^{-1} for ceria nanoparticles (see [32, 33] and discussion below). A linear relation between the calculated vibrational frequency $\tilde{\nu}_{\mathrm{PBE+U}}$ and experimental Raman shift $\tilde{\nu}_{\mathrm{exp}}$ with a slope of 1.30 and a y-intercept of −186 cm^{-1} is proposed ($\tilde{\nu}_{\mathrm{PBE+U/4.5\ eV}} = 1.30 \cdot \tilde{\nu}_{\mathrm{exp.}} - 186\ \mathrm{cm}^{-1}$). The assignment of the calculated frequencies of 893 cm^{-1} and 932 cm^{-1} to the experimental bands seems valid as the calculated intensity ratio between the two bands of ~4 resembles the experimental observation of an intense band at 830 cm^{-1} and a shoulder at 860 cm^{-1} (see discussion below).

To study the influence of the presence of Ce^{3+} ions in the vicinity of a peroxides molecule, a $\mathrm{CeO}_{2-x}(111)$ surface with (3 × 3) periodicity and two third neighbor oxygen defects at the surface was considered (see figure B.3 C). One oxygen defect is occupied by a peroxide molecule resulting in a $\mathrm{O_2}^{2-}/\mathrm{CeO}_{2-x}(111)$ structure with a $\mathrm{O_2}^{2-}/\mathrm{O_{vac}}$ ratio of 0.5. At this ratio four different configurations were considered where the configurations differ in the location of the Ce^{3+} ions (see figure B.4). Configuration 1 refers to the most stable localization of the excess charge (see table B.4) and configurations 2, 3, and 4 are by 69, 89, and 175 meV less stable, respectively. The decreasing stability is connected to the Ce^{3+} localization in the proximity of the peroxide molecule.

A Bader charge analysis [193] revealed no significant difference between the charge localized at the peroxide in configuration 1 at $\mathrm{O_2}^{2-}/\mathrm{O_{vac}} = 0.5$ and in structure *b* at $\mathrm{O_2}^{2-}/\mathrm{O_{vac}} = 1$ (13.23 e). A blueshift of the O-O stretch frequency from 933 to 941 cm^{-1} is accompanied by a minor shortening of the bond length from 1.445 to 1.443 Å. These minor differences can be attributed to steric effects originating from the Ce^{3+} and the oxygen vacancy. However, a gradual increase of charge density at the peroxide molecule in configurations 1, 2, 3, and 4 is observed (13.23 e, 13.26 e, 13.30 e, 13.33 e) together with an elongation of the bond length (1.443 Å, 1.448 Å, 1.458 Å, 1.461 Å). This is in line with an overall redshift of 30 cm^{-1} of the predicted peroxide stretch frequency. This shift originates from the vicinity of Ce^{3+} near the peroxide molecule and is proposed as a chemical environment shift (compare the frequencies determined from an oxidized terrace *a*: 894 cm^{-1} and *b*: 933 cm^{-1}, $O_2^{2-}/O_{vac} = 1$, with a reduced terrace between 911 and 941 cm^{-1}, $O_2^{2-}/O_{vac} = 0.5$). This is further elaborated in conjunction with the discussion on experimental data below.

4.9 Discussion on peroxide formation at the CeO_2(111) surface

In prior studies peroxide species (O_2^{2-}) were employed for the characterization of oxygen defects at the ceria surface [32, 33, 194] and as a activated intermediate of gas phase oxygen for oxidation reactions over ceria catalysts. [51, 190] Additionally, peroxide formation has been modeled by density functional theory before. [54–56, 195]

In this and the previous section the focus is put on peroxide (O_2^{2-}) formation at the CeO_{2-x}(111) surfaces and on the effect of various surface coverages (0.06 ML to 1 ML at $O_2^{2-}/O_{vac} = 1$) plus the effect of Ce^{3+} in the vicinity of the peroxide molecule (0.11 ML at $O_2^{2-}/O_{vac} = 0.5$). In the stable configurations (see figure B.2) the peroxide molecule occupies a lattice oxygen position. For coverages up to 0.25 ML two stable configurations were found. In configuration *a* the outer oxygen leans towards a neighboring surface Ce^{4+} whereas in configuration *b* the outer oxygen resides between two surface Ce^{4+}. For 0.25 ML coverage the results completely resemble the data on the adsorption geometry and the relative energy published by Huang *et al.* before, who also reported a barrier of 20 meV for an interchange of the two configurations. Thus the interchange is predicted as "*quasi barrier free*". [54]

The vibrational properties of the the peroxide molecule have also been studied employing DFT by Choi *et al.* [56] at a coverage of 0.5 ML but with a PW91 functional. Although the PW91 functional is not able to describe the localization of excess charge at ceria properly, [106] the bond elongation (0.011 Å) and the relative energy stabilization of configuration (1 × 2)-*b*-1 compared to configuration (1 × 2)-*b*-2 (50 meV, see figure B.2 F and table B.4) is in line with the bond elongation of 0.010 Å and the stabilization of 57 meV of configuration (1 × 2)-*b*-1 obtained here. Regarding the peroxide vibration the frequency of 960 and 978 cm^{-1} are in line with the calculated frequencies of 940 cm^{-1} for structure (1 × 2)-*b*-1 and 952 cm^{-1} for (1 × 2)-*b*-2 (see figure B.2 G). Besides, peroxides in configuration *a* were modeled by Zhao *et al.* [55] with a PW91+U/5 eV functional and at comparable periodicities of $(2\sqrt{3} \times 3)$ and $(2 \times \sqrt{3})$, resulting in 0.083 ML and 0.25 ML coverage, respectively. This closely resembles the coverage of 0.11 ML and 0.25 ML considered in this work. The peroxide bond length determined by Zhao *et al.* is smaller only by 0.015 Å and the frequency higher by 21 cm^{-1} providing fair agreement with results reported in section 4.8. A structure with a $O_2^{2-}/O_{vac} = 0.5$ ratio was studied by Kullgren *et al.* [195], but the considered structure had a subsurface oxygen vacancy opposite to the structure considered in this work. Although a change in the electronic structure is reported, the study does not focus on the vibrational properties of the formed peroxide molecules.

For an experimental identification of peroxides at ceria, polycrystalline powder samples are usually studied by Raman spectroscopy at temperatures well below room temperature (93 K) after reduction at elevated temperatures (>473 K). It should be noted that in section 4.7 a preferred CeO_2(111) surface termination was concluded for polycrystalline ceria. This allows a direct comparison of the experimental Raman spectra and the calculated frequencies of peroxide molecules at the CeO_2(111) surface. Previously reduced ceria (673 K in H_2) shows an asymmetric Raman peak at 831 cm^{-1} with a shoulder at 860 cm^{-1}. [33] A similar behavior is observed after reduction at 473 K with CO. Upon reduction in CO at

573 and 673 K an additional band at 877 cm^{-1} is observed during subsequent exposure to O_2. [32] The band at 830 cm^{-1} with a shoulder is also observed at 173 K after reduction in H_2 at 773 K [194] and at room temperature without prior reduction. [49]

Oxygen adsorption at defined ceria nanostructures has been studied by Wu *et al.* [33]. At nanorods two peaks at 830 and 862 cm^{-1} were observed at room temperature after prior reduction (673 K) whereas for nanocubes the bands shift slightly to 833 cm^{-1} and an additional shoulder at >860 cm^{-1} is observed. No reliable statement can be made for nanooctahedra, because the surface area is considerably lower. [33]

For Au/CeO_2 catalysts *ex situ* Raman measurements reveal a peroxide band at 831 cm^{-1} [51] and *operando* Raman measurements reveal four components at 832, 847, 866, and 881 cm^{-1}, highlighting also the relevance of peroxides for oxidation reactions over ceria supported materials.

The summary on the calculated peroxide frequencies and the experimental data in the literature together with the obtained results in the previous section lead to the following proposal. The two experimentally observed Raman bands at ~830 cm^{-1} and at ~860 cm^{-1} originate from the two peroxide configurations *a* and *b* at the CeO_{2-x}(111) surface, which are very close in energy with a negligible barrier for interchange. [54] Precisely, for 0.25 ML coverage the bands are separated by 38 cm^{-1} compared to an experimental separation of 30 cm^{-1}. An overall blueshift of the calculated absolute frequencies of ~63-70 cm^{-1} is observed with respect to the experimentally measured frequencies. However, this issue is known from previous reports. [55,56] The predicted Raman scattering intensity for the peroxide related bands is also in line with the experimental data. For an increased coverage from 0.06 ML to 0.25 ML, the predicted intensity ratio decreases from ~4 to ~2.5. Prior reduced ceria samples clearly show a band at 860 cm^{-1} [32,33] whereas non-reduced samples [49] do not exhibit such an intense shoulder. This indicates that the Raman intensity ratio of the bands at 830 and 860 cm^{-1} is also related to the surface peroxide coverage.

Further blueshifted bands at 877 cm^{-1} [32] and 874 cm^{-1} [194] are observed at bare ceria after harsh reducing conditions (>573 K in CO) and may therefore represent strongly agglomerated peroxide species. Additionally, at Au/CeO_2 catalysts a band at 881 cm^{-1} is observed during room temperature CO oxidation. [190] In the DFT+U calculations three species with a coverage of ≥0.5 ML were considered with a predicted Raman shift of 940 cm^{-1} for structure (1×2)-*b*-1 (0.5 ML, figure B.2 F), 952 cm^{-1} for structure (1 × 2)-*b*-2 (0.5 ML, figure B.2 G), and 973 cm^{-1} for a full monolayer coverage (1 ML, figure B.2 H), corresponding to blueshifts of 47, 59, and 80 cm^{-1} with respect to the most intense band predicted at 893 cm^{-1}, respectively.

The presence of Ce^{3+} in the vicinity of the peroxide molecule could give rise to an additional band between those at 830 cm^{-1} and 860 cm^{-1} in experiment. So the band at 847 cm^{-1} observed at Au/CeO_2 catalysts under reaction conditions was originate from peroxide species located close to a Ce^{3+} rather than gold as proposed in this study. [190] However, it has to be mentioned that gold tends to transfer an electron to the ceria support (see chapter 7 and 8), which can result in a configuration where peroxide, gold and Ce^{3+} are located in direct proximity to each other.

From the comprehensive study on peroxide adsorption on the CeO_2(111) surface and the critical review of experimental data from the literature, it is concluded that the DFT+U approach is able to reliably predict also the vibrational properties of adsorbed peroxide species. Together with the prediction of the vibrational properties of ceria (CeO_2), reduced ceria (CeO_{2-x}), and the $CeO_2(111)$ surface this provides the first thorough study to interpret Raman spectra of polycrystalline ceria materials on the basis of DFT+U calculations. [183]

4.10 Superoxide formation at the $CeO_2(111)$ surface

Besides peroxide formation (${O_2}^{2-}$) that is discussed in the two previous sections superoxide formation (${O_2}^{-}$) has been observed at the polycrystalline ceria surfaces. Superoxides have been probed by infrared [57, 196, 197] and Raman vibrational spectroscopy, [32, 33, 51, 190] as well as electron paramagnetic resonance (EPR) spectroscopy due to the radical character of the superoxide molecule. [198]

Therefore, the oxygen adsorption at the $CeO_{2-x}(111)$ surface forming superoxides using a surface slab with (2×2) periodicity was studied and is described in this section. After creation of an oxygen vacancy at the $CeO_2(111)$ surface two excess electrons are transferred to Ce^{4+} ions resulting in two Ce^{3+} ions (see figure 4.8 A for the stable charge localization after surface oxygen vacancy creation). For superoxide formation only one of these excess electrons is transferred to the oxygen molecule and the other one resides at a cerium ion (see figure B.5 A-C). After superoxide creation the excess charge (Ce^{3+}) can be located in a nearest (NN) or next nearest neighbor (NNN) position with respect to the superoxide. Besides, the outer oxygen atom of the superoxide molecule can lean towards a surface Ce^{4+}, representing configuration a, in accordance to the nomenclature of the peroxide structures in section 4.8, or between two cations Ce^{3+}/Ce^{4+} and Ce^{4+} (configuration b), or to a surface Ce^{3+} (configuration c). None of the type b configurations is stable, regardless of the position of the Ce^{3+} ion. The configuration c is only feasible when Ce^{3+} is located in NN position with respect to the superoxide. This results in three stable superoxide configurations, namely a-NN and c-NN (Ce^{3+} in NN position) and a-NNN (Ce^{3+} in NNN position).

The adsorption energy $E_{\mathrm{ads},O_2^-} = E_{O_2^-/CeO_{2-x}(111)} - E_{O_2} - E_{CeO_{2-x}(111)}$ is calculated as -1.42 eV for configuration a-NNN representing the most stable configuration compared to $E_{\mathrm{ads},O_2^-} = -1.29$ eV for configuration a-NN. Configuration c-NN ($E_{\mathrm{ads},O_2^-} = -1.28$ eV) is only little less stable than the corresponding configuration a-NN (see also table B.4). In comparison to the peroxide, the superoxide structures are predicted to be ~0.50 eV less stable. This is also mirrored in the increase of $E_{\mathrm{ads},O} = 0.85$ eV revealing that oxygen vacancy creation and superoxide adsorption is a net endothermic process. In contrast to the recent literature [57] no upright superoxide species with the superoxide molecular axis possessing a 90° angle with respect to the surface was found.

With respect to the stretch frequency of the superoxide radical, a value of 1134 cm^{-1} was calculated for configuration a-NN. The same frequency was found for configuration a-NNN. The frequency of configuration c-NN is predicted to be only 2 cm^{-1} redshifted to 1132 cm^{-1}. Similarly the bond length varies only slightly (see table B.4). The intensity for Raman scattering at superoxides species is predicted to be considerably larger as compared to that of peroxide species (2900-11800 $Å^2\ u^{\frac{1}{2}}$).

Raman [32, 51, 56, 199] and infrared [196, 200] spectra reveal a sharp band at a frequency of 1123 cm^{-1} (Raman, [51]), 1126 cm^{-1} (IR, [196] and Raman, [199]), 1128 cm^{-1} (IR, [200]), 1131 cm^{-1} (Raman, [56]), or at 1127 cm^{-1} with a shoulder at 1135 cm^{-1} (Raman, [32]) assigned to superoxides at polycrystalline ceria. Additionally, at ceria microflowers a superoxide band at 1128 cm^{-1} was measured by Raman spectroscopy. [201] Assuming that polycrystalline ceria exposes predominantly the $CeO_2(111)$ surface these results can be compared to the above calculations. The rather narrow region for experimentally observed frequencies (1123 cm^{-1} – 1131 cm^{-1}) coincides well with the calculated frequencies (DFT+U) between 1132 cm^{-1} and 1134 cm^{-1} of superoxide structures at the $CeO_{2-x}(111)$ surface. Due to the observation of a superoxide band in infrared spectra [196, 200] the superoxide species can not reside in a flat configuration, i.e., parallel to the surface. [57] Again this coincides well with the DFT+U results, as all stable structures possess an angle with respect to the surface (see figure B.5).

4.11 Peroxide formation at the $CeO_2(100)$ surface

In accordance to the peroxide ($O_2{}^{2-}$) formation at the $CeO_{2-x}(111)$ surface the adsorption of oxygen at the $CeO_{2-x}(100)$ surface resulting in peroxide $O_2{}^{2-}/CeO_{2-x}(100)$ structures was studied and is discussed in this section.

In a recent study Yang *et al.* [57] considered $O_2{}^{2-}/CeO_{2-x}(100)$ structures to explain experimental infrared data (IRRAS) at faceted ceria single crystals. The authors proposed a checkerboard type of arrangement for oxygen ions at the $CeO_2(100)$ surface (compare above) and a flat peroxide molecule adsorbed at the $CeO_{2-x}(100)$ surface with $p(2 \times 2)$ periodicity (see figure B.6 B). To provide a benchmark, the same structure was employed here at 600 eV energy cutoff for the plane wave basis, with a tight energy convergence criterion of 10^{-8} eV and including van der Waals (vdW) contributions. This resembles the setup employed in the prior study. [57] The calculations revealed an adsorption energy of $E_{\mathrm{ads},O_2^{2-}} = -2.29$ eV compared to -2.26 eV and an $O_2{}^{2-}$ stretch frequency of 857.2 cm^{-1} compared to 852.9 cm^{-1} in the prior study. [57]

For a direct comparison with the study on the peroxide and superoxide formation at the $CeO_2(111)$ in section 4.8 [183] and 4.10, the results obtained with the same setup as before are reported in the following (energy cutoff of 400 eV for the plane wave basis, an energy convergence criterion of 10^{-6} eV and neglecting vdW contributions). With these parameters the adsorption energy is calculated as -2.14 eV and the peroxide stretch frequency shifts to 868 cm^{-1}. Taking vdW contributions exemplarily into account revealed an adsorption energy of -2.34 eV but the stretch frequency is still predicted as 868 cm^{-1}. Therefore, it is concluded that vdW contributions have no influence on the calculated peroxide stretch frequency, while the smaller plane wave basis set causes a blueshift of 11 cm^{-1}. As the employed parameter set provided agreement between theory and experiments for peroxide $O_2{}^{2-}/CeO_{2-x}(111)$ structures in the prior sections these are also used in the following (400 eV energy cutoff for the plane wave basis, neglecting vdW contributions and energy convergence criterion of 10^{-6} eV).

The coverage-dependent peroxide formation was studied for $CeO_2(100)$ surface slabs with three periodicities. The surface slabs with $c(2 \times 2)$, $p(2 \times 2)$ and $c(1 \times 1)$ periodicity are depicted in figure 4.10. For these surface slabs the surface oxygen vacancy formation energy $E_{\mathrm{vac,O}}$ is calculated first. The considered Ce^{3+} configurations are shown in figure B.10. At the surface slab with $c(2 \times 2)$ periodicity the Ce^{3+} locate preferably in direct proximity to the oxygen defect ($c(2 \times 2)$-1, most stable configuration with $E_{\mathrm{vac,O}} = 1.392$ eV). In a slightly less stable configuration one Ce^{3+} locates in direct proximity and the other one in next nearest neighbor position while the Ce^{3+} ions themselves are next nearest neighbors ($c(2 \times 2)$-2, $E_{\mathrm{vac,O}} = 1.446$ eV) or nearest neighbors ($c(2 \times 2)$-3, $E_{\mathrm{vac,O}} = 1.473$ eV). These structures have been discussed before by Kropp *et al.* [127] and reveal the same trend with respect to the stability although the authors included vdW contributions. For the $p(2\times2)$-1 ($E_{vac,O}$ = 1.970 eV) and $p(2\times2)$-2 configurations ($E_{vac,O}$ = 1.875 eV) the same Ce^{3+} pattern as for the $c(2\times2)$-1 and $c(2\times2)$-2 configurations are employed. However, in the most stable configuration one Ce^{3+} is in direct proximity to the oxygen vacancy at the surface cerium layer and one Ce^{3+} is located in the subsurface cerium layer in a nearest neighbor position to the surface Ce^{3+} ($E_{vac,O}$ = 1.824 eV). Including vdW contributions the vacancy formation energy of 1.928 eV from the literature is fully reproduced. [57] The $CeO_{2-x}(100)$ structure with $c(1\times1)$ periodicity and two Ce^{3+} at the surface cerium layer is more stable ($c(1\times1)$-1, $E_{vac,O}$ = 2.044) than the configuration in which one Ce^{3+} is located at the surface and the second in the subsurface ($c(1\times1)$-2, $E_{vac,O}$ = 2.055). As for the $CeO_2(111)$ surface the vacancy formation energy at the $CeO_2(100)$ surface rises for increasing coverage of oxygen vacancies up to 0.5 ML as indicated by the values of $-E_{vac,O}$ (blue dots) in figure 4.17.

Molecular oxygen adsorption at the reduced $CeO_{2-x}(100)$ surface resulted in peroxide ${O_2}^{2-}/CeO_2(100)$ formation as the most stable structure. In these structures the peroxide molecule is adsorbed in a flat configuration (parallel to the surface) for a coverage of 0.125 ML $c(2\times2)$, 0.25 ML $p(2\times2)$ and 0.5 ML $c(1\times1)$. The oxygen adsorption energy follows the trend $E_{ads,O_2^{2-}} = -1.732$ eV for 0.125 ML coverage, -2.141 eV for 0.25 ML coverage, and -2.367 eV for $c(1\times1)$ 0.5 ML coverage. This resembles the vacancy healing energy $-E_{vac,O}$ due to the fact that the peroxide molecule resides at the position of the initially surface oxygen vacant site. By replacing all surface oxygen ions by peroxide molecules (1 ML coverage), the peroxide molecule is slightly tilted possessing an angle of 14° with respect to the surface plane. As no stable $CeO_{2-x}(100)$ reference state for two surface oxygen vacancies at $c(1\times1)$ was found, no adsorption energy $E_{ads,O_2^{2-}}$ can be calculated for this coverage.

Peroxide formation also resembles the hypothetical adsorption of a single O atom to the oxidized $CeO_2(100)$ surface. The adsorption energy of the O atom $E_{ads,O} = E_{O_2^{2-}/CeO_{2-x}(100)} - \frac{1}{2}E_{O_2} - E_{CeO_2(100)}$ increases slightly with higher coverage, indicating the repulsive interaction of peroxide molecules at the $CeO_2(100)$ surface. Please note that $E_{ads,O}$ is the difference between $E_{ads,O_2^{2-}}$ and the $-E_{vac,O}$ and is calculated as -0.317 eV for the structure with $p(2\times2)$ periodicity. Therefore the formation of peroxides at $CeO_2(100)$ surface is calculated as a net exothermic process opposite to the $CeO_2(111)$ surface (compare $E_{ads,O} = 0.32$ for ${O_2}^{2-}/CeO_2(111)$, (2×2) periodicity). Including vdW contributions (grey dots in figure 4.17) reduces $\mathrm{E}_{ads,O}$ only slightly, due to the fact that $E_{vac,O}$ (blue and dark blue dots) is slightly increased and $E_{ads,O_2^{2-}}$ (red and orange dots) is decreased stronger.

The predicted vibrational frequency of the peroxide molecule adsorbed at the $CeO_{2-x}(100)$ surface is derived as described in section 4.8 and plotted as a function of coverage in figure 4.18. Up to 0.25 ML coverage the peroxide stretch frequency is constant at 868 cm^{-1}, for 0.5 ML coverage the frequency is 5 cm^{-1} blueshifted to 873 cm^{-1}. and for a full monolayer coverage the frequency is 29 cm^{-1} blueshifted to 907 cm^{-1}. As already pointed out, the inclusion of vdW contributions (orange dots) has only a minor influence on the calculated peroxide stretch frequency.

The experimental frequencies as observed by Raman spectroscopy at ceria nanocubes exposing the $CeO_2(100)$ facet at 832 cm^{-1} and the shoulder at 862 cm^{-1} (see figure 5.6) are assigned to the calculated frequencies for 0.125 ML peroxide coverage (868 cm^{-1}, red dashed line) and the frequency for

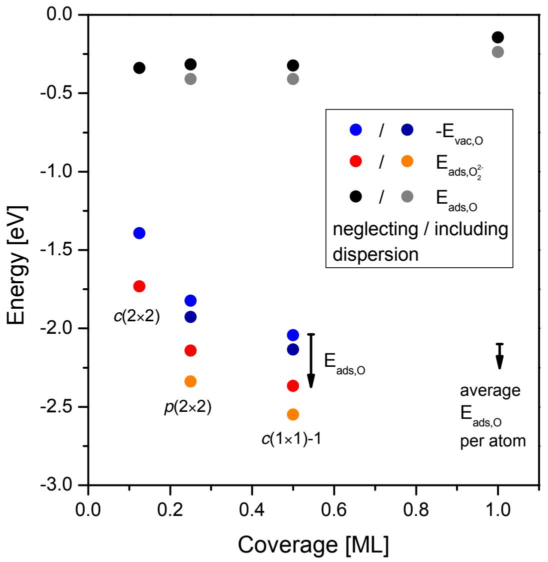

Figure 4.17.: Adsorption energies of molecular O_2 forming a peroxide species at the reduced $CeO_{2-x}(100)$ surface, $E_{ads,O_2^{2-}}$ (red), and the vacancy healing energy, $-E_{vac,O}$ (blue), plus adsorption energy of a single O atom to the $CeO_2(100)$ surface forming a peroxide species, $E_{ads,O}$ (black) as a function of coverage. Grey, orange and dark blue dots represent the corresponding energy including vdW contributions. The black arrow indicates that $E_{ads,O} < 0$.

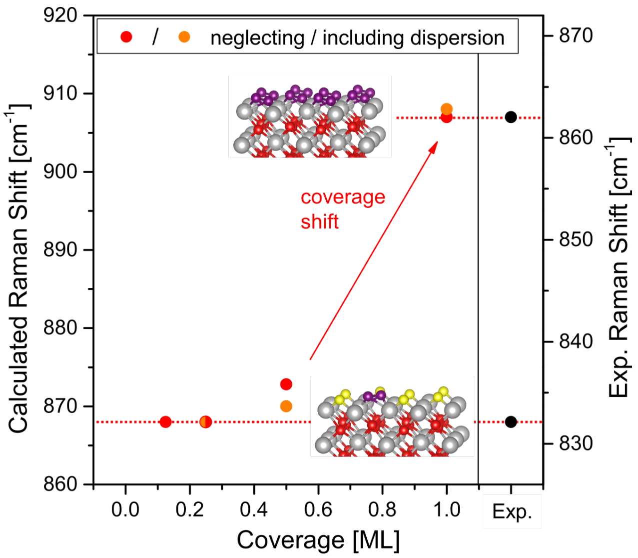

Figure 4.18.: Calculated vibrational frequency for peroxide structures $O_2^{2-}/CeO_{2-x}(100)$ neglecting (red) and including vdW contributions (orange) as a function of coverage. Black dots represent the assigned experimental stretch frequencies from Raman spectra (see chapter 5).

1 ML coverage at 907 cm^{-1}. As for the peroxides at the $CeO_2(111)$ surface a linear relation between the experimental and predicted frequencies is proposed ($\tilde{\nu}_{PBE+U} = 1.30 \cdot \tilde{\nu}_{exp.} - 214\ cm^{-1}$). It needs to be highlighted that the slope (1.30) is identical to that resulting from the analysis of the $O_2^{2-}/CeO_{2-x}(111)$ structures with a decreased y-intercept. This indicates that the phenomena which govern the blueshift of the peroxide stretch frequency, i.e., the configuration change at the $CeO_2(111)$ and the increased coverage, are identical for the $CeO_2(111)$ and $CeO_2(100)$ surface facets and are properly modeled by DFT+U methods.

Experimentally, peroxide formation at ceria nanocubes exposing selectively the $CeO_2(100)$ surface has been studied by Wu *et al.* [33] before. At 80 K Raman bands at 840 cm^{-1} and 863 cm^{-1} were observed. These bands were located at 833 cm^{-1} and 860 cm^{-1} at room temperature in good agreement with data described in chapter 5 and the results from the DFT+U calculations discussed above.

4.12 Superoxide formation at the $CeO_2(100)$ surface

The formation of a superoxide radical (O_2^-) at the $CeO_{2-x}(100)$ results from molecular oxygen adsorption on the reduced $CeO_{2-x}(100)$ surface where only one electron is transferred from the $CeO_{2-x}(100)$ surface to the oxygen molecule while the other remains at the $CeO_{2-x}(100)$ surface.

The reduced $CeO_{2-x}(100)$ structures with $c(2 \times 2)$, $p(2 \times 2)$ and $c(1 \times 1)$ periodicity which possess a surface oxygen defect are discussed in the previous section.

The calculated stable superoxide $O_2{}^-/CeO_{2-x}(100)$ structures are shown in figure B.8 for varying coverage. The corresponding adsorption energies E_{ads,O_2^-} are listed in table B.5. For a surface slab with $c(2 \times 2)$ periodicity three different Ce^{3+} configurations were considered. The stable superoxide configuration is the one in which the superoxide molecule is positioned flat (side on, parallel to the surface) at the position of the former oxygen vacancy. The excess charge can be located at the $CeO_2(100)$ surface in direct proximity to the superoxide (NN, $E_{\mathrm{ads},O_2^-} = -1.344$ eV), in the second coordination sphere at the surface (NNN, $E_{\mathrm{ads},O_2^-} = -1.176$ eV), or in the subsurface cerium layer (sub, $E_{\mathrm{ads},O_2^-} = -1.061$ eV). For a structure with $p(2 \times 2)$ periodicity the adsorption energy is -1.625 eV for the NN configuration and -1.379 eV for the sub configuration. For the $c(1 \times 1)$ periodicity an adsorption energies of -1.833 eV for the NN and -1.517 eV for the sub configuration were calculated. Regardless of the periodicity the Ce^{3+} is located preferably in NN position. The trend for the adsorption energy mirrors the one which is discussed above for the peroxide species. Due to the increased energy gain from oxygen vacancy healing $-E_{\mathrm{vac},O}$, the O_2 adsorption energy E_{ads,O_2^-} increases with coverage. This trend is visualized in figure 4.19, where circles indicate NN, triangles indicate NNN and the squares indicate sub configuration, respectively. The calculated $E_{\mathrm{ads},O}$, i.e., the hypothetical creation of superoxide by adsorption a single O atom at the oxidized $CeO_2(100)$ surface, is predicted to be slightly endothermic, 0.048 eV for NN and 0.216 for NNN configuration at $c(2 \times 2)$ periodicity. As for the peroxide species, $E_{\mathrm{ads},O}$ increases with higher coverage indicating repulsive interaction of the superoxide molecules. The calculated $E_{\mathrm{ads},O}$ for superoxide formation at the $CeO_2(100)$ surface is by ~0.5 eV smaller compared to superoxide formation at the $CeO_2(111)$ surface, indicating that superoxide formation is strongly facilitated at the $CeO_2(100)$ surface compared to the $CeO_2(111)$ surface (see chapter 5 for further discussion on experimental results).

Concerning the superoxide stretch frequency two regimes are proposed, indicated by the two red dashed lines in figure 4.20. For Ce^{3+} in direct proximity (NN configuration) with $c(2\times2)$ and $p(2\times2)$ periodicities the superoxide stretch frequency is predicted around $\sim$1050 cm^{-1}. Upon locating the excess charge in the NNN or sub position (in the second coordination sphere of the superoxide) a stretch frequency of $\sim$1024 cm^{-1} is predicted. This corresponds to a frequency difference of 26 cm^{-1} for $c(2 \times 2)$ periodicity (red bar in figure 4.20) and a difference of 17 cm^{-1} including vdW contributions at $p(2 \times 2)$ periodicity (orange bar). The frequencies are blueshifted by $\sim$20 cm^{-1} for 0.5 ML coverage ($c(1 \times 1)$ periodicity).

Recently, a superoxide structure $O_2{}^-/CeO_2(100)$ has been proposed, where the superoxide is tilted by only 6° with respect to the surface normal vector. [57] Here, a structure with an angle of 6.9° was found with a vibrational frequency of 1125 cm^{-1} for the superoxide stretching mode (see figure B.9 E). It should be noted, that with the same parameter setup as in the literature [57] two imaginary frequencies (negative eigenvalues of the Hessian matrix) were observed at 56 cm^{-1} and 58 cm^{-1}. The vibrational modes are sketched in figure 4.21 on the right, corresponding to an angle tilting in direction of the indicated ϑ angle (56 cm^{-1}) and a twist following the φ angle (58 cm^{-1}). To study the origin of the rather small frequencies values, superoxide configurations with a constant Ce^{4+}-O bond length of 2.42 Å, a Ce^{3+}-O bond length of 2.51 Å and a superoxide O-O bond length of 1.342 Å, but varying ϑ and φ were constructed and the total energy was determined with the same parameters as in the previous study. [57] The total

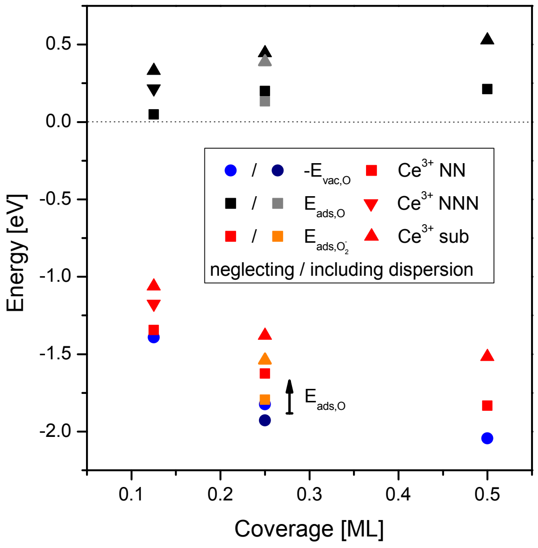

Figure 4.19.: Adsorption energies of molecular O_2 forming a superoxide species at the reduced $CeO_{2-x}(100)$ surface, $E_{\text{ads,}O_2^-}$ (red symbols), and the vacancy healing energy, $-E_{\text{vac,O}}$ (blue circles), plus adsorption energy of a single O atom to the $CeO_2(100)$ surface forming a superoxide species, $E_{\text{ads,O}}$ (black symbols) as a function of coverage. Squares indicate Ce^{3+} in nearest neighbor position, triangles down Ce^{3+} in next nearest neighbor position to the superoxide and triangles up indicate Ce^{3+} in the subsurface. Grey, orange and dark blue symbols represent the corresponding energy including vdW contributions. The arrow indicates that $E_{\text{ads,O}} > 0$.

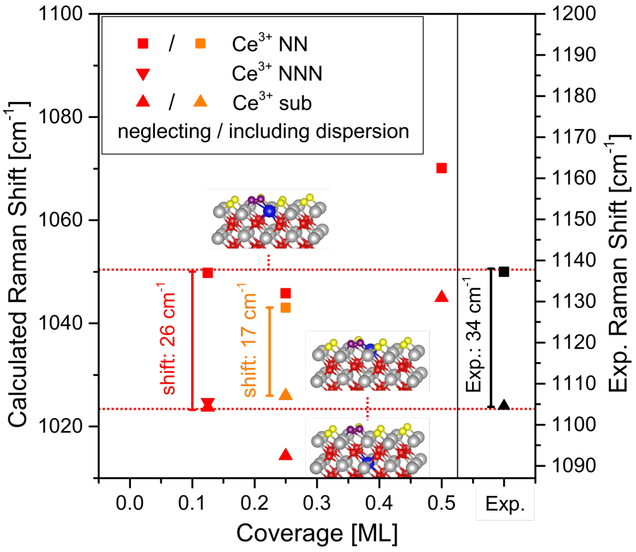

Figure 4.20.: Calculated superoxide stretch frequencies for $O_2^-/CeO_{2-x}(100)$ structures as a function of coverage. Squares indicate Ce^{3+} in nearest neighbor position, triangles down Ce^{3+} in next nearest neighbor position to the superoxide and triangles up indicate Ce^{3+} in the subsurface. Dashed lines indicate the two regimes of Ce^{3+} in direct proximity to superoxide (1050 cm^{-1}) and in the second coordination sphere (1024 cm^{-1}). Experimental frequencies from Raman spectra are shown as black symbols.

energy is plotted as a function of ϑ and φ in the left diagram of figure 4.21. Due to symmetry considerations $+\varphi$ and $-\varphi$ reveal identical total energies. Therefore only the total energy of structures with $+\varphi$ are shown but structures with $-\varphi$ were calculated as well. Based on the graph the imaginary frequencies of the $\vartheta = 6.9°$ and $\varphi = 0$ configuration can be rationalized by a maximum of the total energy at $\vartheta = 6.9°$ and $\varphi = 0$. The potential energy surface with respect to the two angles is rather flat around these angles and therefore the imaginary frequencies are small (<100 cm^{-1}). However, a superoxide structure with $\vartheta = 6.9°$ and $\varphi = 0$ can be excluded as a stable superoxide structure at the $CeO_{2-x}(100)$ surface and such a structure should not be observed in the experiment. For $\varphi = 0$ minima at $\vartheta = +45°$ and $\vartheta = -45°$ are suggested. Relaxation of these configurations reveal the structures -up-1 ($\vartheta = 53.2°$) and -up-2 ($\vartheta = -47.5°$) at $p(2 \times 2)$ periodicity (see figure B.9 C and D). Both structures are predicted to be transition states (one imaginary frequency). The minimum of the total energy with respect to the two angles lies at $\varphi = 90°$ and $0° < \vartheta < 10°$. This strongly suggests that flat lying superoxides (side on, parallel to the surface) as found above are the most stable superoxide configurations at the $CeO_2(100)$ surface.

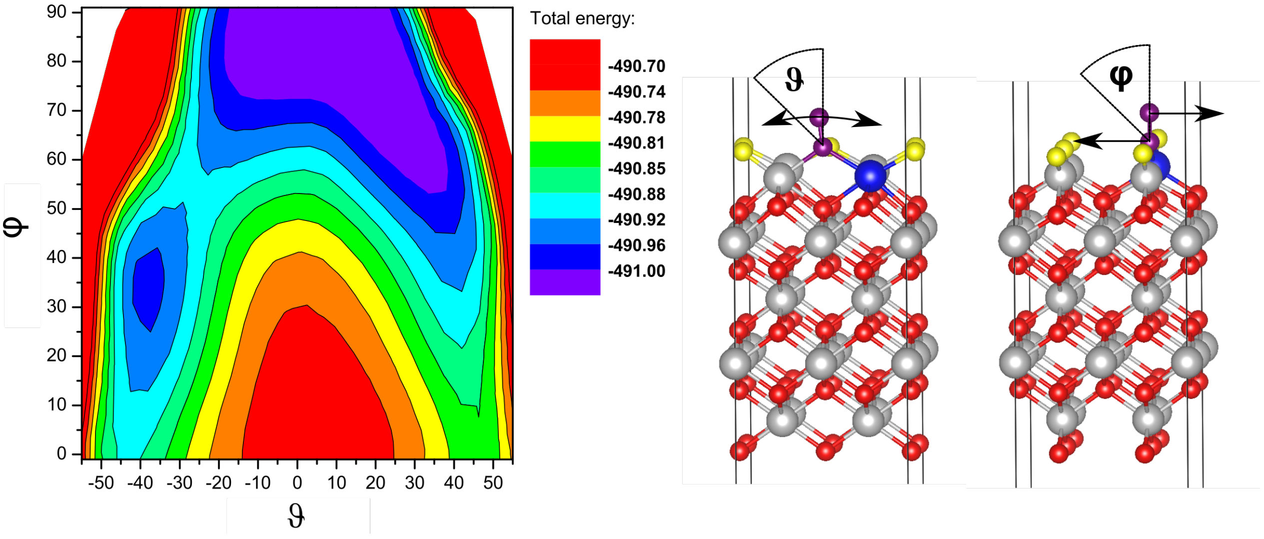

Figure 4.21.: Left: Potential energy surface of a superoxide structure $O_2^-/CeO_2(100)$ at $p(2 \times 2)$ periodicity with respect to the angles ϑ and φ according to the schemes on the right. The O-O bond length is set to 1.342 Å and the Ce^{4+}-O and Ce^{3+}-O bond length is set 2.42 and 2.51 Å, respectively. Due to the symmetry of the cell, the total energy of $+\varphi$ and $-\varphi$ structures are identical. The arrows indicate the two vibrational modes with predicted imaginary frequencies calculated for the structure with φ = 0° and ϑ = 6.9° at 600 eV energy cutoff, including vdW contributions and an energy convergence criterion of 10^{-8} eV.

Experimentally the observation of superoxides at nanoparticles with distinct $CeO_2(100)$ facets by Raman spectroscopy has not been reported in the literature. [33] However, Raman spectra of ceria nanocubes in various gas atmospheres and at temperatures between 21°C and 120°C (see section 5.5) clearly reveal two bands at 1103 cm^{-1} and 1137 cm^{-1} (34 cm^{-1} difference) in this work. The bands are assigned to the superoxide configurations with Ce^{3+} in NNN position and Ce^{3+} in NN position, respectively (see figure 4.20).

4.13 Adsorption of oxygen at the $CeO_2(100)$ surface

The adsorption of oxygen at the oxidized $CeO_2(100)$ surface is studied employing a $CeO_2(100)$ surface slab with $c(2 \times 2)$, $p(2 \times 2)$ and $c(1 \times 1)$ periodicity. Molecular oxygen adsorbs upright at an unoccupied surface oxygen position (from checkerboard arrangement of surface oxygen ions) with a slight tilting towards a nearest neighbor Ce^{4+}. The adsorption energy of $E_{ads,O_2^{\delta-}} = -0.066$ eV is invariant of the coverage as is the vibrational frequency of the oxygen molecule (1545 cm^{-1}, for $p(2 \times 2)$ periodicity). With respect to gas phase oxygen (1561 cm^{-1}) the frequency is 16 cm^{-1} redshifted. The results for all periodicities are summarized in table B.7 and the structures are shown in figure B.10.

4.14 Adsorption of H_2O at the $CeO_2(111)$ and $CeO_2(100)$ surface

The adsorption of water (H_2O) was studied at the oxidized $CeO_2(111)$ and $CeO_2(100)$ surfaces (see figure B.11 A and B.12 A). For the $CeO_2(111)$ a surface slab with (2×2) periodicity, and for the $CeO_2(100)$ surface slabs with $p(2 \times 2)$ and $c(2 \times 2)$ periodicity were employed for the adsorption of a single H_2O molecule.

The water molecule can adsorb in a molecular form (MS1) or as a hydroxyl pair (HP1) at the oxidized $CeO_2(111)$ surface, keeping the water molecule intact (figure B.11 B) or transfer a proton to the surface forming a hydroxyl pair type adsorption (figure B.11 C). [126] The molecular adsorption energy was calculated as $E_{\mathrm{ads,H_2O}} = -0.535$ eV and hydroxyl pair adsorption as $E_{\mathrm{ads,H_2O}} = -0.512$ eV. Here, only the most stable structures are reported which resemble the results obtained in previous studies (see reference [202] and [126] and references therein).

The adsorption of water into a surface oxygen vacancy at a reduced $CeO_{2-x}(111)$ surface results in dissociative adsorption, where a hydroxyl group (OH) locates at the position of the oxygen vacancy and a proton is transferred to the $CeO_{2-x}(111)$ surface (see figure B.11 D for the most stable configuration). In accordance with the literature, [202,203] this process is calculated as strongly exothermic process with an adsorption energy of $E_{\mathrm{ads,H_2O}} = -2.024$ eV, indicating that a reduced $CeO_{2-x}(111)$ surface facilitates dissociative water adsorption. For comparison the oxygen vacancy healing energy was calculated as $-E_{\mathrm{vac,O}} = -2.27$ eV.

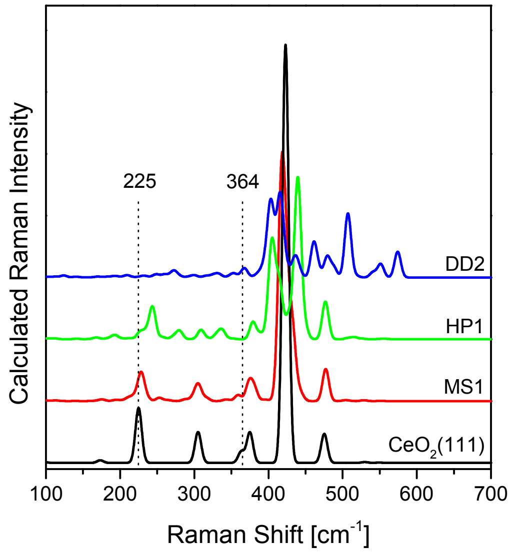

Figure 4.22.: Calculated Raman spectra of molecular (MS1) and hydroxyl pair adsorption (HP1) of H_2O at the oxidized $CeO_2(111)$ surface and dissociative adsorption (DD2) at the reduced $CeO_{2-x}(111)$ surface.

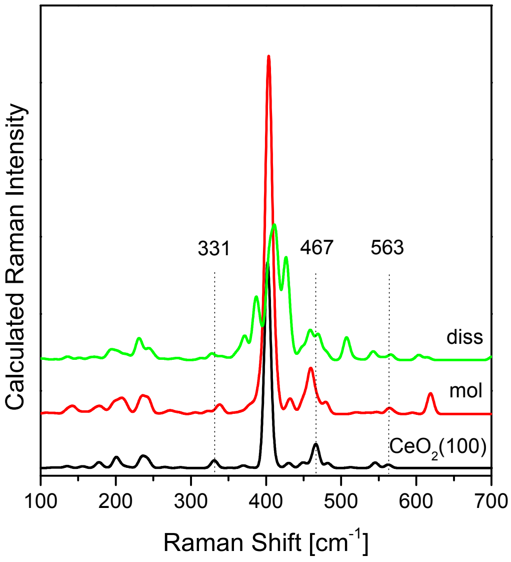

Figure 4.23.: Calculated Raman spectra of molecular (mol) and dissociative adsorption (diss) of H_2O at the oxidized $CeO_2(100)$ surface.

Regarding the adsorption of water at the oxidized $CeO_2(100)$ surface dissociative adsorption is favored over molecular adsorption. For molecular adsorption the adsorption energy was calculated as $E_{\mathrm{ads,H_2O}} =$

-0.975 eV and -0.986 eV for a surface slab with $p(2 \times 2)$ and $c(2 \times 2)$ periodicity, respectively. For the dissociative adsorption the adsorption energy was calculated as $E_{\text{ads,H}_2\text{O}} = -1.549$ eV and -1.670 eV for the two considered periodicities. The calculated structures and adsorption energies resemble the results obtained in previous studies. [202, 204] Most probably due to the oxygen depleted $CeO_2(100)$ surface the dissociative adsorption, i.e., filling an empty oxygen lattice position at the checkerboard surface, is favored by ∼0.6 eV. For water adsorption at a defective $CeO_{2-x}(100)$ surface with $p(2 \times 2)$ periodicity the adsorption energy for dissociative adsorption was found to be strongly exothermic $E_{\text{ads,H}_2\text{O}} = -2.736$ eV. This is significantly larger than the surface oxygen vacancy healing energy $-E_{\text{vac,O}} = -2.134$ eV. Generally, for water adsorption a facilitated adsorption was found at the $CeO_2(100)$ compared to the $CeO_2(111)$ surface, as is also predicted for peroxide or superoxide formation in previous sections.

To study the effect of adsorbed water on the Raman spectra of the $CeO_2(111)$ and the $CeO_2(100)$ surface, the Raman spectra of the $H_2O/CeO_2(111)$ and $H_2O/CeO_2(100)$ structures were calculated and are compared to the spectrum of the oxidized $CeO_2(111)$ and $CeO_2(100)$ surfaces in figures 4.22 and 4.23. For the oxidized $CeO_2(111)$ surface a longitudinal and transversal stretching mode of the topmost Ce-O layer was predicted at 225 cm^{-1} and 364 cm^{-1} (see section 4.5 for details). Upon molecular and hydroxyl pair type water adsorption at the oxidized $CeO_2(111)$ surface (red and green line in figure 4.22) the band at 225 cm^{-1} blueshifts, lowers in intensity, and broadens. The blueshift is more pronounced for hydroxyl pair type adsorption. For the transversal mode, such an analysis cannot be made, as it is over layered by other Raman active vibrations. In the case of dissociative adsorption at the reduced $CeO_{2-x}(111)$ surface, hardly any Raman active vibration is predicted in the region between 200 cm^{-1} and 250 cm^{-1}. The results indicate that upon water adsorption at the oxidized surface the band at 225 cm^{-1} (246 cm^{-1} in experiment) blueshifts and shrinks, whereas the band is predicted to disappear upon vacancy creation (see figure 4.9) and dissociative water adsorption at the oxygen vacant site (see figure 4.22).

In summary, for the longitudinal surface mode of the $CeO_2(111)$ surface a sensitivity for adsorbed water is predicted here. This is of importance as water is omnipresent at oxide nanoparticles and water acts as a reactant that is activated at the metal/ceria catalysts during the water-gas shift reaction (see chapter 9). [75, 203]

For the $CeO_2(100)$ surface vibrations of the oxidized surface were found at 467 cm^{-1} and 481 cm^{-1} (see also section 4.6). These modes redshift upon molecular and remain at the position for dissociative water adsorption. The modes in the subsurface below the $CeO_2(100)$ surface at 331 cm^{-1} and 563 cm^{-1} shift only slightly, due to the location further away from the surface. So the modes which are experimentally observed in Raman spectra are hardly affected by the adsorption of water at the $CeO_2(100)$ surface.

4.15 Carbonate and formate formation at the $CeO_2(111)$ surface

The formation of carbonate, hydrogen carbonate, and formate species at the polycrystalline ceria surface is known from experiment by the identification of characteristic vibrations which are probed by infrared spectroscopy [34–36, 205, 206]. Wu *et al.* [207] also studied the carbonate formation at faceted ceria particles such as nanorods, nanooctahedra, and nanocubes.

The adsorption of CO_2 at the $CeO_2(111)$ surface from first principle calculations (DFT+U) has been studied by Hahn *et al.* [208] and an extensive analysis of stable configurations of carbonate, hydrogen carbonate, and formate at a ceria cluster ($Ce_{21}O_{42}$) plus vibrational analysis has been reported by

Vayssilov *et al.* [205] Moreover, Lustemberg *et al.* [206] provided a detailed analysis of the nature of formate species on ceria surfaces using a combination of temperature-programmed surface reaction infrared (TPSR-IR) spectroscopy on a powder catalyst support and DFT together with statistical thermodynamics for model $CeO_2(111)$ surfaces, where the existence of monodentate species was discussed in terms of a stabilization effect of hydrogen bonds. [206]

Here it is briefly reported on the structures of carbonate, hydrogen carbonate, and formate at the $CeO_2(111)$ surface studied employing a surface slab with (2 × 2) periodicity. The slab consists of three O-Ce-O trilayers and the bottom trilayer was kept fix during structure optimization and vibrational analysis.

Carbonate formation by CO_2 adsorption at the oxidized $CeO_2(111)$ surface resulted in a monodentate carbonate structure shown in figure B.13 A. The calculated adsorption energy of $E_{\mathrm{ads,CO_2}} = -0.515$ eV (see table B.9) resembles the calculated values of previous studies. [205, 208] The vibrational analysis revealed that the asymmetric (asym) and symmetric (sym) stretching modes $\nu(CO_2)$ are located at 1592 cm^{-1} and 1239 cm^{-1}, respectively, in accordance with the reported frequencies in the literature of 1570 cm^{-1} and 1238 cm^{-1}. [205] For the asymmetric stretching vibration a fourfold infrared absorption intensity is predicted and the modes can be assigned to the observed bands at 1575 cm^{-1} and 1298 cm^{-1} in infrared spectra (see figure 8.3 in chapter 8).

The most stable hydrogen carbonate structure is shown in figure B.13 B. Considering a reduced $CeO_{2-x}(111)$ surface as starting point, one oxygen atom of the carbonate molecule (CO_3H) fills the position of a lattice oxygen ion and due to the proton bound at the carbonate molecule, an excess electron is located at the $CeO_2(111)$ surface. This could either reside at a cation in next nearest neighbor (NNN) position, as in the most stable structure, in nearest neighbor (NN) position next to the plane spanned by the carbonate molecule, or in NN position in the plane spanned by the carbonate molecule. The two latter configurations are by ∼160 meV less stable than the first. Moreover, the proton can either point away from the surface or to the surface. The structure where the proton points to the surface is by ∼40 meV less stable. For the most stable structure the vibrations are listed in table 4.2, in good agreement with the reported frequencies by Vayssilov *et al.* [205] It needs to be mentioned that all the structures lie in a rather narrow energy region of ∼200 meV and might be present in experiment. Therefore, a range for every vibrational mode is reported in table 4.2 to allow for a better comparison with the bands observed in experiment (see figure 8.3). For the ν(O-H) a narrow region between 3659 cm^{-1} and 3668 cm^{-1} is predicted which coincides well with the narrow band observed at 3619 cm^{-1} in diffuse reflectance infrared experiments (not shown). The ν(OCO, asym), i.e., the asymmetric stretch of OCO, is predicted in a broader region between 1608 cm^{-1} and 1655 cm^{-1} again in agreement with infrared and Raman experiments (see figures 7.5 and 8.3 as well as table 4.2). The region for the ν(OCO, sym) mode is predicted between 1336 cm^{-1} and 1388 cm^{-1} and the δ(OCOH), i.e., the bending mode of OCOH, [36] between 1170 cm^{-1} and 1176 cm^{-1} both in agreement with a broad and a narrow band in infrared experiments, respectively (see figure 8.3).

For the stable formate structure and its vibrational analysis agreement with the literature is also observed. [205, 206] The formate species was created by adsorption of formate (HCO_2) to the oxygen defective $CeO_{2-x}(111)$ surface, with one oxygen of the formate filling the initially vacant lattice oxygen position that is indicated as O_{lattice} while the outer oxygen is indicated as O_{outer}. The same discussion concerning the Ce^{3+} location as for the hydrogen carbonate configurations holds true for the formate configurations. The configuration in which the Ce^{3+} is in NNN position is the most stable one (see figure B.13 C). The two structures with NN position are by only ~160 meV less stable. The structure resembles a bridged structure at the reduced $CeO_{2-x}(111)$ surface considered by Lustemberg *et al.* [206] The authors considered a bridged structure where the formate species is coadsorbed with a nearby $HO_{lattice}$ hydroxyl group for vibrational analysis and found an asymmetric stretching mode ν(OCO, asym) with a frequency of 1542 cm^{-1} and a symmetric stretching mode ν(OCO, sym) with a frequency of 1355 cm^{-1}. Here, the former is predicted as blueshifted to 1580 cm^{-1} and the latter as redshifted to 1340 cm^{-1} (see table 4.2). However, spectral regions are reported for formate vibrations in table 4.2 as before for hydrogen carbonates. Rather narrow regions are calculated for ν(CH), ν(OCO, sym) and δ(HCOO) as 2930 cm^{-1} – 2937 cm^{-1}, 1338 cm^{-1} – 1340 cm^{-1}, 1017 cm^{-1} – 1020 cm^{-1}, respectively. The latter two modes refer to an symmetric stretching mode of OCO and a bending mode of the adsorbed formate molecule, respectively. Broader regions are calculated for the ν(OCO, asym, O_{outer}) and ν(OCO, asym, $O_{lattice}$) as 1580 cm^{-1} – 1602 cm^{-1} and 1253 cm^{-1} – 1283 cm^{-1}, these modes refer to asymmetric stretching modes of OCO with a larger vibrational amplitude for the outer (O_{outer}) and lattice ($O_{lattice}$) oxygen, respectively.

For comparison with the water-gas shift experiments ($CO/H_2{}^{18}O$) the most stable formate configuration with $^{12}CH^{16}O_{outer}/Ce^{18}O_2(111)$ and $^{12}CH^{18}O_{outer}/Ce^{18}O_2(111)$ isotopes were calculated. Both structures possess a $^{18}O_{lattice}$ oxygen.

The first structure corresponds to an insertion of $C^{16}O$ into a $H/Ce^{18}O_2(111)$ surface. With respect to the $^{12}CH^{16}O_{outer}/Ce^{16}O_2(111)$ structure, shifts of <2 cm^{-1} are observed for the ν(CH) at 2931 cm^{-1}, the $\nu(^{16}OC^{18}O$, asym, $O_{outer})$ at 1579 cm^{-1}, the $\nu(^{16}OC^{18}O$, sym) at 1339 cm^{-1}, and the $\delta(HC^{16}O^{18}O)$ at 1018 cm^{-1}. The $\nu(^{16}OC^{18}O$, asym, $O_{lattice})$ is shifted by 30 cm^{-1} from 1283 cm^{-1} to 1253 cm^{-1} for this structure.

The $^{12}CH^{18}O_{outer}/Ce^{18}O_2(111)$ structure corresponds to an insertion of $C^{18}O$ into a $H/Ce^{18}O_2(111)$ surface. With respect to the $^{12}CH^{16}O_{outer}/Ce^{16}O_2(111)$ structure, the $\nu(^{18}OC^{18}O$, asym, $O_{outer})$ redshifts by 28 cm^{-1} to 1552 cm^{-1} and the $\nu(^{18}OC^{18}O$, asym, $O_{lattice})$ redshifts by 34 cm^{-1} to 1249 cm^{-1}, whereas no shift for the ν(CH) and only minor shifts (<10cm^{-1}) are observed for the $\nu(^{18}OC^{18}O$, sym) and the $\delta(HC^{18}O^{18}O)$.

The obtained results provide the basis for a profound interpretation of the carbonate region (800 – 1800 cm^{-1}) of *operando* Raman and infrared spectra. With the proposal that polycrystalline ceria exposes predominantly the $CeO_2(111)$ surface, the results allow for an assignment of experimentally observed bands of adsorbed carbon species at polycrystalline ceria materials.

Table 4.2.: Calculated vibrational properties of gas phase CO_2 and adsorbed carbonate, hydrogen carbonate, and formate species at the $CeO_2(111)$ surface and experimentally observed band positions in infrared and Raman spectra. The spectral region printed bold refers to the maximum and minimum frequency of the vibrations as determined at all considered configurations. For the formate structure vibrational properties of adsorbed $CH^{16}O$ and $CH^{18}O$ to the $Ce^{18}O_2(111)$ are reported for the most stable formate configuration. (asym) and (sym) refer to asymmetric and symmetric stretching modes, respectively. For the formate species (O_{outer}) and ($O_{lattice}$) refer to a larger vibrational amplitude of the outer or lattice oxygen atom, respectively.

Structure	DFT+U			Experimental		Assignment
	Frequency / **region**	IR	Raman	IR	Raman	
	[cm^{-1}]	[%]	$\mathrm{Å}^2\ u^{\frac{1}{2}}$	[cm^{-1}]	[cm^{-1}]	
CO_2 gas	2358	100	-	2349		$\nu(CO_2$, asym)
	1316	0	-			$\nu(CO_2$, sym)
	633	4	-			$\delta(CO_2)$
carbonate	1592	100	119	1575		$\nu(CO_2$, asym)
	1239	27	127	1298		$\nu(CO_2$, sym)
	949	27	262	988		$\nu(CO_{lattice})$
hydrogen carbonate	3667 / **3659-3672**	9	339	3619		ν(O-H)
	1608 / **1608-1655**	100	73	1620	1650	ν(OCO, asym)
	1395 / **1336-1388**	41	37	1393		ν(OCO, sym)
	1178 / **1170-1181**	30	10	1218		δ(OCOH)
	1007 / **999-1008**	4	25	1023		$\nu(CO_3$, sym)
formate $^{12}CH^{16}O_{outer}$/ $Ce^{16}O_2(111)$ ($^{16}O_{lattice}$)	2931 / **2930-2937**	7	262	2937		ν(CH)
	1580 / **1580-1602**	87	94	1549	1590	ν(OCO, asym, O_{outer})
	1340 / **1338-1340**	2	27	1358	1375	ν(OCO, sym)
	1283 / **1253-1283**	29	45	1254	1250	ν(OCO, asym, $O_{lattice}$)
	1020 / **1017-1020**	0	52	1050	-	δ(HCOO)
formate/ $^{12}CH^{16}O_{outer}$/ $Ce^{18}O_2(111)$ ($^{18}O_{lattice}$)	2931	7	262			ν(CH)
	1579	87	94		1590	$\nu(^{16}O^{18}CO$, asym, O_{outer}))
	1339	2	27		1375	$\nu(^{16}OC^{18}O$, sym)
	1253	29	45		1220	$\nu(^{16}OC^{18}O$, asym, $O_{lattice}$)
	1018	0	52		-	$\delta(HC^{16}O^{18}O)$
formate/ $^{12}CH^{18}O_{outer}$/ $Ce^{18}O_2(111)$ ($^{18}O_{lattice}$)	2931	7	262			ν(CH)
	1552	87	94		-	$\nu(^{18}OC^{18}O$, asym, O_{outer}))
	1330	2	27		-	$\nu(^{18}OC^{18}O$, sym)
	1249	29	45		-	$\nu(^{18}OC^{18}O$, asym, $O_{lattice}$)
	1017	0	52		-	$\delta(HC^{18}O^{18}O)$

5 Ceria Nanocrystals with (111) and (100) Surface Facets: *In situ* Raman Spectroscopy

A ceria (CeO_2) single crystal or a nanocrystal with a fluorite type crystal structure can grow predominantly in the three low index directions <100>, <110>, and <111>. This leads to a termination of the crystal with one of the surface planes $CeO_2(100)$, $CeO_2(110)$, and $CeO_2(111)$, respectively. The derivation of the $CeO_2(100)$ and $CeO_2(111)$ surface from the conventional cubic representation of the bulk ceria crystal (Ce_4O_8) is illustrated in figure 5.1 and can be derived for the $CeO_2(110)$ surface termination in an analogue fashion.

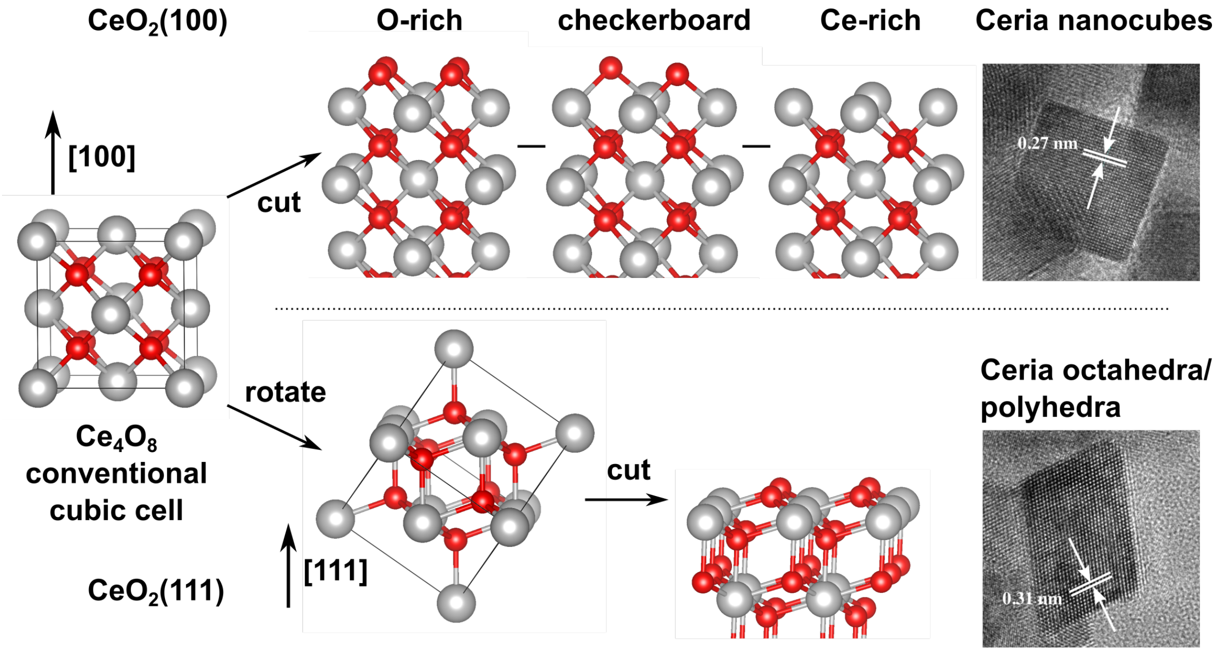

Figure 5.1.: Derivation of the (111) and (100) surface termination (surface facet) from the conventional cubic Ce_4O_8 cell. For the (100) surface facet (top row) the oxygen (O-) and cerium (Ce-) rich termination plus the checkerboard type of arrangement of surface oxygen ions and for the (111) facet the O-Ce-O trilayer configuration is shown. The TEM images show ceria nanoparticles exposing these surface facets.

In detail the x, y, and z axis of the conventional cubic cell point in the [100], [010], and [001] direction of the crystal. Cutting the crystal orthogonal to one of these directions result in the $CeO_2(100)$ surface. In this case each ionic layer consists of either Ce^{4+} or O^{2-} ions (see top panel of figure 5.1). In one possible configuration the surface slab terminates with an oxygen layer at the surface (see O-rich termination). For the correct stoichiometry the bottom layer would then consist of a cerium layer (see Ce-rich). This causes an undesirable permanent dipole moment in the cell pointing to the surface. [162] Alternatively, one half of the topmost oxygen layer can be transferred to the bottom of the cell releasing occupied and unoccupied oxygen lattice positions, that can be arranged as idealized checkerboard of occupied and unoccupied lattice oxygen ions at the surface. [57,119,127] The validity of this surface configuration for ceria single crystals, thin films, or nanoparticles is discussed in section 5.1.

To construct the $CeO_2(111)$ surface, the conventional cubic cell is rotated to have the [111] direction (the space diagonal of the cubic cell) pointing to the top and is cut along the orthogonal plane. In this case each layer consists of an O-Ce-O trilayer without a permanent dipole.

Ceria single crystals can be macroscopically cut to terminate with one of the low index surfaces, also referred to as surface *facet*. [57] Additionally, thin films of ceria terminating with the $CeO_2(111)$, $CeO_2(110)$, or $CeO_2(100)$ surface can be grown on a target with the correct match of lattice constants (see reference [47] and references therein). Although highly ordered systems are received, the resulting substrates are planar and do not allow direct catalytic studies.

However, ceria nanostructures can be synthesized (compare section 2.5) which can be employed for catalysis and expose distinct ceria surface facets at the same time. [45] Nanocrystals exposing the $CeO_2(100)$ facet possess a cubic shape and those exposing the $CeO_2(111)$ facet are polyhedra (compare transmission electron microscopy images in 5.1). Please note that ideal crystal growth would result in an octahedral shape of the nanocrystals. The topic of so-called ”*nanoshaping*” has been reviewed by A. Trovarelli and J. Llorca [48] and by Zhang *et al.* [209] before. The surface chemistry of the low index surfaces from a surface science point of view (single crystal and thin films) has been reviewed by D. Mullins. [47] In the context of nanoparticles the term ”*well-defined*” refers to the book edited by Z. Wu and S. Overbury [210] on nanoparticles selectively exposing one of the low index surfaces. Therefore, the hydrothermal synthesis of faceted ceria nanoparticles is a platform to transfer the results from single crystals and thin films to particles which are active for catalysis.

Various studies on ceria nanoparticles have highlighted the effect of different surface shapes [48] on CO oxidation activity [207,211,212], the defect chemistry of the ceria surface, [189] or the oxygen storage capacity (OSC). [45,207,213] For example regarding the oxygen storage capacity Mai *et al.* [45] found a doubled capacity per surface area for cubes compared to polyhedra. Similar observations for cubes and octahedra were made by Wu *et al.*, [207] who also observed an increased CO oxidation activity for ceria cubes. [207] Besides, a superior oxygen storage capacity has been reported for cubes compared to polycrystalline CeO_2. [213]

While ceria nanocubes exhibit selectively the $CeO_2(100)$ surface and octahedra/polyhedra the $CeO_2(111)$ surface, ceria nanorods and nanowires usually consist of crystallites exposing either the $CeO_2(110)$ together with the $CeO_2(100)$ [45,212,214] or exclusively the $CeO_2(111)$ [61,189,215,216] surface. However, the $CeO_2(110)$ and $CeO_2(100)$ surface facets of ceria nanorods can undergo reconstruction to $CeO_2(111)$ facets. [217] Therefore, the focus is put on ceria nanocubes and polyhedra predominantly exposing the $CeO_2(100)$ and $CeO_2(111)$ surface, respectively. Furthermore, polycrystalline ceria nanoparticles are studied which possess $CeO_2(111)$ surface facets.

DFT+U calculations on the low index surfaces reported the $CeO_2(111)$ as the most stable surface termination followed by the $CeO_2(110)$ and the $CeO_2(100)$ surface. [95, 119, 120] The surface oxygen vacancy formation energy was calculated by DFT+U calculations as 2.27 eV for the $CeO_2(111)$ and 1.82 eV for the $CeO_2(100)$ surface with comparable oxygen vacancy concentration (0.25 ML) in this work (see chapter 4), which is in line with previous results. [103,218]

In this contribution, ceria nanostructures (polycrystalline ceria, nanopolyhedra, and nanocubes, compare section 2.5) were synthesized and characterized by of TEM, XRD, and N_2 adsorption (see 5.2). Additionally, the detailed analysis of visible Raman spectra (λ_{ex} = 532 nm) of the nanostructures is discussed in section 5.3 with a focus on Raman active surface phonons. Although *in situ* Raman spectra of nanostructures have been obtained before, [189, 207] the Raman phonons of ceria confined at the surface have not been addressed till date. [183]

Furthermore, oxygen adsorption in the form of peroxides (O_2^{2-}) and superoxides (O_2^{-}) at the defined ceria surface facets is reported in section 5.5. Although peroxide and superoxide species were observed in Raman [32,33,51,56,201] and infrared [196,197,200,219] spectra plus have been modeled by DFT, [54–57, 220] the first observation of superoxide species at ceria nanoparticles exposing the CeO_2(100) surface facet by Raman spectroscopy is reported here. The results are also directly compared to the DFT+U calculations of peroxide and superoxide model systems for the (111) and (100) surface facets presented in chapter 4.

5.1 Discussion on the CeO_2(111) and CeO_2(100) surface configuration

The structural configuration of the CeO_2(111) surface termination with a full O-Ce-O trilayer is rather clear (see section 3 of reference [47] and references therein). This configuration is also confirmed by the results using *in situ* Raman spectroscopy discussed in section 5.3. However, the surface configuration of the CeO_2(100) surface ”*has not been definitive*” [47]. As outlined above and in section 4.6 from a modeling point of view (DFT) the checkerboard type of arrangement of oxygen ions is the most stable configuration, as it is the intermediate between an oxygen or a cerium rich termination. Although other configurations have been considered and are close in energy, [95, 117, 119] the checkerboard configuration provides a fair starting point. [119, 120]

Direct recoil spectroscopy at a CeO_2(100) thin film revealed an oxygen rich termination (compare figure 5.1). [221] In contrast, mass spectroscopy of recoil ions (MSRI) at a CeO_2(100) thin film indicated a half oxygen layer at the surface and the checkerboard type of arrangement of oxygen atoms. [222] This has been confirmed by scanning tunneling microscopy (STM) experiments at single crystals combined with calculations. [223]

At ceria nanocubes high resolution TEM images revealed regions where the crystallite terminates with a full cerium, a full oxygen, or a half oxygen layer. [224] This indicates that the different terminations vary and oxygen ions ”*may be in a constant flux*”. [47] Recently, in TEM images of ceria nanocubes regions with a ”*normal*” and ”*reversed*” cerium arrangement have been observed. ”*Normal*” refers to the structure depicted in figure 5.1 and ”*reversed*” refers to a reconstruction where the outermost cerium layer of a cerium rich surface is exchanged with the oxygen layer below, resulting in two cerium layers with 1.49 Å spacing compared to 2.69 Å spacing in the normal arrangement. [225]

In conclusion, the checkerboard arrangement of oxygen ions at the CeO_2(100) surface provide an idealized average of the reported configurations from O-rich to Ce-rich and is computationally best affordable. Therefore, it was employed for the calculations presented in chapter 4 as in the recent literature. [57, 127, 218, 226] It should be noted that for ceria nanoparticles exposing the CeO_2(100) surface facet no definite statement on the surface configuration can be made from experiment.

5.2 Characterization of faceted ceria nanoparticles

The characterization of the synthesized ceria nanocrystals is summarized in table 5.1. Ceria *sheets* or polycrystalline ceria refers to nanoparticles yielded from decomposition of cerium(III)nitrate precursor at 600°C. Ceria *polyhedra* and *cubes* are synthesized hydrothermally at 180°C with a 0.01 M and 6 M NaOH concentration, respectively.

Table 5.1.: Properties of the synthesized ceria nanoparticles reporting the BET specific surface area, the crystal size as determined from TEM images and as calculated from the BET specific surface area assuming spherical particles for polyhedra and sheets, and cubic particles for nanocubes plus reporting the lattice plane spacing and the derived surface termination.

Nanostructure	BET surface [m^2/g]	Crystal size BET surface [nm]	Crystal size TEM [nm]	Lattice plane spacing [nm]	Surface
Sheets	61	13.5	12	0.31	$CeO_2(111)$
Polyhedra	124	6.6	6-10	0.31	$CeO_2(111)$
Cubes	51	16.2	11-60	0.27	$CeO_2(100)$

By X-ray diffraction (XRD) a cubic fluorite type structured ceria was concluded for all samples. The specific surface area was determined by fitting a Brunauer-Emmett-Teller (BET) model [142] to the N_2 adsorption isotherm. The specific surface area of the nanosheets (61 m^2/g) is comparable to that of the nanocubes (51 m^2/g) and about half the size of the nanopolyhedra (124 m^2/g). Assuming ideal spherical and cubic nanoparticles a crystal size of 13.5 nm, 6.6 nm and 16.1 nm was derived for sheets, polyhedra, and cubes from the specific surface area, respectively. These values resemble the crystal sizes of 12 nm, 6-10 nm, and 11-60 nm as determined from the particles observed in TEM measurements (no particle size statistics was calculated). From the TEM images a rather broad size range is observed for the cubes which is smaller for polyhedra, whereas the sheets are rather uniform in size.

From the TEM images depicted in figure 5.2 the lattice plane spacings of the nanoparticles can be determined. At the CeO_2 sheets and polyhedra a 0.31 nm lattice plane spacing in direction of the surface was observed, corresponding to the lattice spacing in [111] direction of a cubic fluorite type $Fm\bar{3}m$ structure with $a_0 = 5.411$ Å. [49] Using this lattice constant a theoretical lattice plane spacing d_{hkl} for the $h = 1$, $k = 1$, and $l = 1$ direction of $d_{111} = 0.312$ nm was calculated. [227] For the ceria nanocubes a spacing of 0.27 nm was determined, corresponding to the lattice spacing in [200] direction as $d_{200} = 0.271$ nm for $h = 2$, $k = 0$, and $l = 0$ with $a_0 = 5.411$ Å. These results strongly suggest a $CeO_2(111)$ surface termination of the ceria sheets and polyhedra and a $CeO_2(100)$ surface termination for the cubes. However, it should be noted that TEM is a method that provides only a local picture of the sample and can therefore not be considered as an integral method.

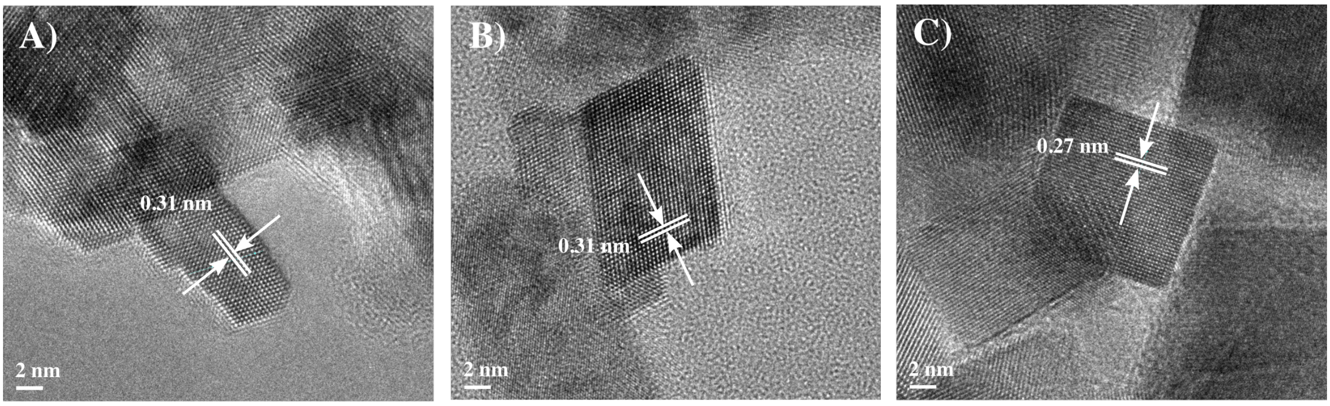

Figure 5.2.: Transmission electron microscopy (TEM) images of the synthesized ceria nanostructures: A) ceria sheets, B) ceria polyhedra, and C) ceria cubes. The arrows indicate the lattice plane spacing in direction of the particle surface.

5.3 *In situ* Raman spectroscopy at faceted ceria nanoparticles: Surface phonon modes

To characterize the vibrational properties of the $CeO_2(111)$ and $CeO_2(100)$ surface facets, *in situ* Raman spectra of the nanoshaped ceria samples were recorded (see Figure 5.3). The spectra are normalized to the most intense F_{2g} band, observed at all ceria samples. The shoulder at 560 cm^{-1} can be assigned to defect bands [183] and small impurities due to nitrates are observed at 735 cm^{-1}. [49]

At nanosheets and nanopolyhedra bands at 246 cm^{-1} and 402 cm^{-1} (shoulder) are observed. Besides that at cubes bands at 264 cm^{-1}, 350 cm^{-1} (shoulder) and 600 cm^{-1} are observed. On the basis of DFT+U calculations (see section 4.7) the bands at 246 cm^{-1} and 402 cm^{-1} are assigned to the longitudinal and transversal stretching mode of the $CeO_2(111)$ surface, respectively. [183] An almost doubled intensity of the band at 246 cm^{-1} is observed for the polyhedra compared to the sheets. This is caused by the doubled specific surface area of the polyhedra compared to the sheets and shows that the intensity correlates with the exposed surface area per mass (or volume) of the sample. These two bands are not observed at the ceria nanocubes, clearly indicating that the bands are distinctive for the $CeO_2(111)$ surface facet. The two bands observed at the nanocubes at 350 cm^{-1} and 600 cm^{-1} are assigned to stretching modes of the subsurface below the $CeO_2(100)$ surface on the basis of DFT+U calculations (see figure 5.4 and section 4.7 for explanations).

A band at 264 cm^{-1} has been assigned to a 2TA mode in Raman spectra of CeO_2 single crystals before. [30] Therefore, the band at 264 cm^{-1} at cubes is assigned to the 2TA overtone which is also present at the sheets and polyhedra. However, it is superimposed by the intense surface mode at 246 cm^{-1}. The assignment is further supported by the above mentioned correlation of the intensity of the band at 246 cm^{-1} and the relative surface area of the ceria particles. [49] With the aid of DFT+U calculations and TEM images, indicating the surface faceting, evidence is provided here, that this band corresponds to the $CeO_2(111)$ surface termination of (111) faceted ceria nanoparticles and polycrystalline ceria samples. The band at 402 cm^{-1} has been observed before by visible Raman spectra of polycrystalline [49] and UV-Raman spectra of nanooctahedra. [189] It is assigned to the transversal surface mode of the $CeO_2(111)$ surface accordingly as discussed in section 4.7.

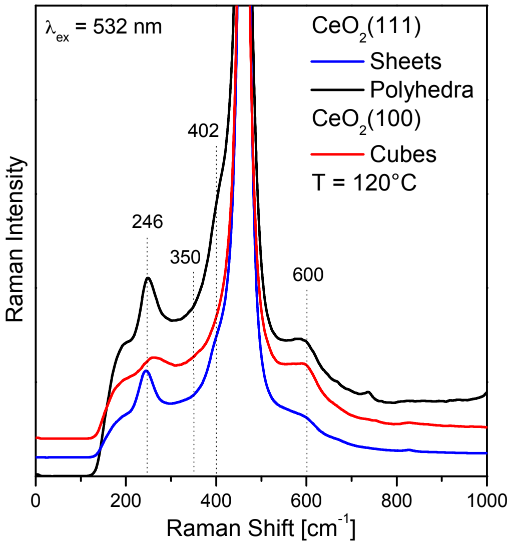

Figure 5.3.: *In situ* Raman spectra of ceria nanostructures at 120°C. Spectra were taken in a constant gas flow of 100 ml/min 25 % O_2/Ar. The spectra were normalized to the F_{2g} band intensity and offset for clarity.

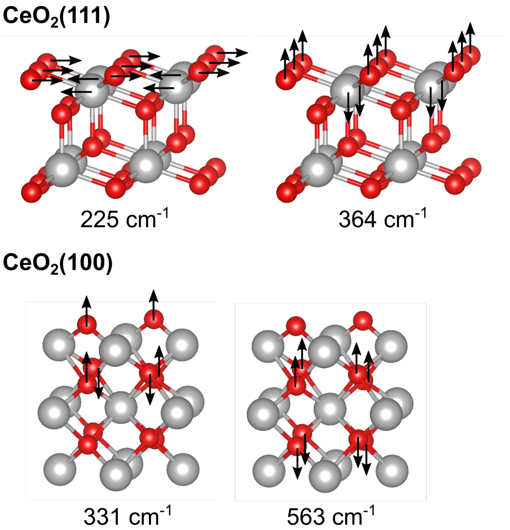

Figure 5.4.: Vibrational modes of CeO_2(111) (top) and CeO_2(100) surface (bottom) as derived by DFT+U calculations. The frequencies values are not scaled. The scaling factor determined in chapter 4 is 1.06.

A band observed at 594 cm^{-1} in Raman spectra of ceria nanocubes has been reported for UV-Raman spectra opposite to nanooctahedra. However, the authors did not assign the band to a surface phonon mode. [189] The band at 350 cm^{-1} observed in Raman spectra of ceria cubes has not been discussed before in the literature.

In conclusion, this is the first proposal that Raman spectroscopy can be used to probe ceria surface faceting. It is clearly shown that visible Raman spectroscopy is sensitive to surface faceting of ceria nanocrystals, besides the known characterization of bulk ceria by solid state phonons. Please note that this is only possible by a combination of experimental Raman spectra and modeling of the surface facets by DFT+U calculations (compare section 4.7). This concept might be enlarged to other oxide materials and exemplifies the variability of Raman spectroscopy for metal oxide and reducible metal oxide surface characterization.

5.4 *In situ* Raman spectroscopy at faceted ceria nanoparticles: Temperature dependence

To study the temperature dependence of the surface phonon modes figure 5.5 depicts *in situ* Raman spectra of the ceria nanostructures at room temperature and elevated temperatures (120°C) in a 25 % O_2 gas stream. Besides the F_{2g} band at 464 cm^{-1} and the defect bands around 560 cm^{-1}, ceria sheets and polyhedra exhibit bands at 246 cm^{-1} and 402 cm^{-1} as already discussed above. The band at 246 cm^{-1} is blueshifted and rather broad at room temperature. At 60°C and 120°C the intensity of the band redshifts to its original position while the band at 402 cm^{-1} (shoulder) increases in intensity as well.

The insets in figure 5.5 show the region of the H_2O bending mode of molecularly absorbed water at the ceria surface. Above room temperature this band decreases indicating water desorption. In section 4.14

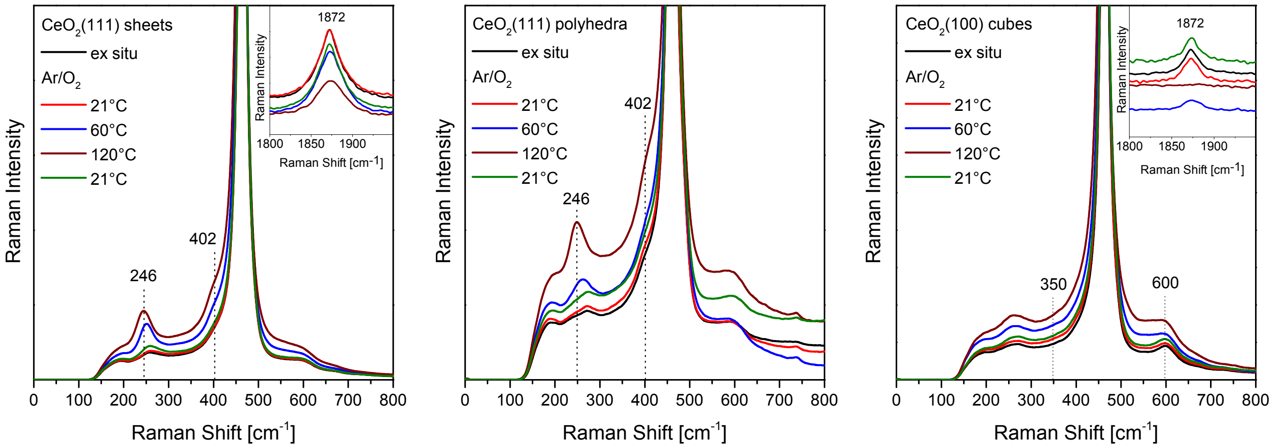

Figure 5.5.: Phonon region of *in situ* Raman spectra of CeO_2 sheets (left), CeO_2 polyhedra (middle), and CeO_2 cubes (right) at room temperature and at elevated temperatures. The insets show the spectral region of the bending mode of adsorbed H_2O. The spectra were normalized to the F_{2g} band intensity.

a blueshift of the surface mode after adsorption of molecular water at the $CeO_2(111)$ surface is suggested from DFT+U calculations. Therefore, water desorption from the surface at elevated temperatures rationalizes the redshift and the increase in intensity of the band at 246 cm^{-1}.

Regarding ceria nanocubes bands at 264 cm^{-1} (broad), 350 cm^{-1} (weak), and 600 cm^{-1} are observed, besides the F_{2g} band and the defect band around 560 cm^{-1}. The defect band increases slightly at elevated temperatures as it does for sheets and polyhedra. The other bands remain stable, while the intensity of the H_2O bending mode (inset) is zero at 120°C. Therefore it is concluded, that the band at 264 cm^{-1} can be safely assigned to the 2TA overtone of the ceria crystal. The bands at 350 and 600 cm^{-1} are assigned to phonon vibrations of the subsurface beneath the $CeO_2(100)$ surface (see above) and remain stable in intensity. This also means that the modes are hardly influenced by absorbed water at the surface.

From the *in situ* measurements it can be concluded that ceria sheets and polyhedra expose the $CeO_2(111)$ surface facet and the cubes the $CeO_2(100)$ surface facet. Due to the reversibility of the band intensity these nanostructure moieties are proposed to remain stable up to the tested temperature of 120°C.

Although it is shown that the cubes terminate in $CeO_2(100)$ direction, no clear indication for a checkerboard configuration of surface oxygen ions can be seen (predicted Raman bands at 370, 467, and 481 cm^{-1}, see section 4.6) as this region of the spectrum is overlayed by the F_{2g} band and the defect band region. However, it is suggested that occupied and unoccupied oxygen position are present at the surface due to the observed bands at 350 cm^{-1} and 600 cm^{-1}. These are assigned to transversal vibrations of subsurface oxygen atoms, which are slightly displaced from their bulk lattice positions due to occupied and unoccupied surface oxygen positions (see figures 4.10 and 4.14 in section 4.7). To this end, a partly occupied oxygen layer is suggested, but no conclusion on the exact surface configuration for ceria nanocubes can be made from *in situ* Raman spectroscopy. In contrast, for the sheets and polyhedra a $CeO_2(111)$ surface termination with an O-Ce-O trilayer can be concluded from the observation of the bands assigned to the surface vibrational modes.

5.5 Peroxide and superoxide formation at faceted ceria nanoparticles

At the ceria nanostructures the formation of reduced molecular oxygen species was studied. In general one can distinguish four different states of molecular oxygen ($O_2{}^{x-}$) plus oxygen ions which are part of the ceria lattice ($2\ O^{2-}$, $x = 4$ plus dissociation). These represent different states of electron transfer to the oxygen molecule and finally dissociation of the oxygen molecule to oxygen ions. Due to the fact that excess electrons populate the antibonding orbitals, the O_2 molecular bond is weakened. This corresponds to an activated oxygen molecule and the O-O stretch frequency is redshifted with respect to the frequency of molecular oxygen ($O_2{}^{x-}$, $x = 0$) at 1556 cm^{-1}. [228] Weakly bound oxygen ($O_2{}^{x-}$, $0 < x << 1$) exhibits a stretch frequency at around ~1500 cm^{-1}, the frequency of superoxide ($x = 1$) species is located within the region $1100 - 1140$, cm^{-1} [32, 196] and that of peroxide species ($O_2{}^{x-}$, $x = 2$) at around ~830 cm^{-1}. [32, 33] The course of electron transfer from molecular oxygen to lattice oxygen is shown in the following scheme 5.1:

$$O_{2,\text{gas}} \rightarrow O_{2,\text{ads}^{\delta-}} \xrightarrow{+e^-} O_2^- \xrightarrow{+e^-} O_2^{2-} \xrightarrow{+2e^-} 2\ O^{2-} \tag{5.1}$$

The most popular method to study adsorbates at oxide surfaces is infrared spectroscopy. [34, 36, 207] Although superoxide [196, 197, 200] and peroxides [57, 219] species have been observed with infrared spectroscopy before, here the potential of Raman spectroscopy for the characterization of oxygen adsorbed species at ceria nanoparticles is explored. [32, 33]

Regarding nanoparticles selectively exposing distinct surface facets, Wu *et al.* focused on the oxygen adsorption properties of ceria octahedra, rods, and cubes in the temperature range between 80 K and room temperature before. However, superoxide species at ceria nanocubes were not reported. [33] Yang *et al.* studied the adsorption of oxygen at ceria single crystals with the low index surface facets by infrared spectroscopy in reflection mode (IRRAS) and found superoxides at the $CeO_2(100)$ surface. [57] Therefore, superoxide species have not been observed by Raman spectroscopy at ceria nanocubes before.

In previous reports the adsorption of oxygen at ceria materials has been studied under *in situ* conditions, i.e., under a constant gas flow over the ceria material and at a certain temperature. The ceria nanoparticles were reduced under harsh (CO, H_2, $T > 473$ K) conditions before exposure to oxygen at temperatures as low as 80 K. [32, 33, 196] Here, the ceria nanocrystals (sheets, polyhedra, and cubes) were not reduced prior to the *in situ* measurement. The materials were studied in the temperature range between 21°C and 120°C at a constant oxygen gas flow rate (see figure 5.6, top row). Furthermore, the nanostructures were exposed to mild reducing (2 % CO) and reaction conditions (2 % CO and 10 % O_2) and subsequently to oxidizing conditions (25 % O_2) at 35°C (see figure 5.6, bottom row).

Figure 5.6 shows the spectral region between 700 and 1700 cm^{-1} of the Raman spectra. In this region molecular oxygen (O_2) and molecular oxygen adsorbates ($O_2{}^{x-}$) are detected as mentioned above. The left column depicts the Raman spectra of sheets (see figure 5.2), the middle and the right column depicts the spectra of polyhedra and cubes (see figure 5.2), respectively. Please note that it is shown by TEM and *in situ* Raman measurements that the sheets and polyhedra expose the $CeO_2(111)$ and the cubes the $CeO_2(100)$ surface facet. In all spectra gas-phase oxygen is detected by a weak band at 1556 cm^{-1}.

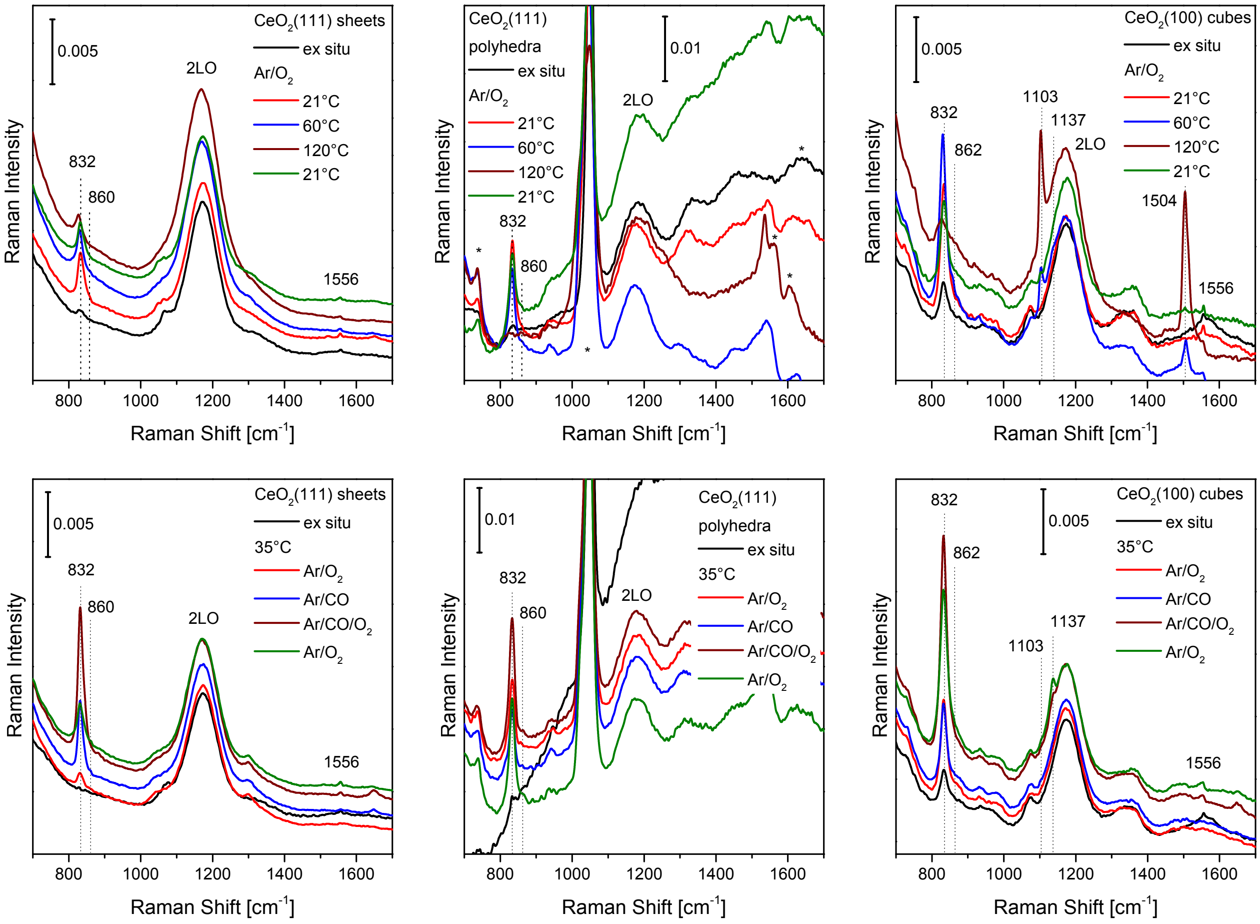

Figure 5.6.: Spectral region for adsorbates of *in situ* Raman spectra from CeO$_2$ sheets (left), CeO$_2$ polyhedra (middle) and CeO$_2$ cubes (right) at elevated temperatures (top row) and during oxidizing, reducing and reaction conditions at 35°C (bottom row). The spectra were normalized to the F_{2g} band intensity and offset for clarity. *Ex situ* refers to a measurement in the *in situ* cell without the application of a gas stream. Asterisk refers to bands attributed to nitrate impurities.

The adsorbed oxygen species at the ceria nanostructrues are discussed in the following, starting with the peroxide species (O_2^{2-}).

For the ceria sheets peroxide species are observed at 832 and 860 cm^{-1}. While the intensity is very weak under *ex situ* conditions applying oxidizing conditions the band at 832 cm^{-1} is clearly observed and the shoulder at 860 cm^{-1} is present as well. A decrease of the intensity is observed at elevated temperatures (top panel) and the bands possess the highest intensity upon exposing the sample to CO/O$_2$ at 35°C (bottom panel, brown curve). A similar behavior is observed for the polyhedra and the overall intensity is roughly doubled (see scale in the figure 5.6 or compare to the intensity of the 2LO band at 1170 cm^{-1}, which possesses comparable intensity for all samples). This can be explained by the doubled specific surface area of the ceria polyhedra compared to the sheets. However, as both samples expose the same surface facet the overall behavior is identical.

Besides, the polyhedra expose bands (indicated by an asterisk) at 735 cm^{-1} and 1040 cm^{-1}, which are assigned to bending and stretching vibrations of free nitrates. The band at 1560 cm^{-1} is assigned to bidentate nitrates and the bands at 1605 cm^{-1} and 1632 cm^{-1} are assigned to bridging nitrates. This is in accordance with the literature [229,230] and a prior NO_2 adsorption study at polycrystalline ceria. [199] The nitrate impurities originate from the synthesis and are not further discussed here.

A fundamentally different behavior is observed for the ceria nanocubes. These show the highest intensity of the 832 cm^{-1} band at 60°C while a second component (peak shoulder) is observed at 862 cm^{-1}. The band at 862 cm^{-1} is more intense at 120°C while the 832 cm^{-1} band is damped. By far the highest intensity of the peroxide bands is observed upon exposure of the nanocubes to CO/O_2 and the intensity is almost maintained under subsequent oxidizing conditions.

Under the applied conditions superoxide species ($O_2{}^-$) are only observed at the ceria nanocubes and neither at the nanosheets nor at the nanopolyhedra. Two distinct bands can be indentified indicating two different superoxide species. At 60°C and 120°C a band at 1103 cm^{-1} increases with the temperature, while a small band at 1137 cm^{-1} is observed upon exposure to CO/O_2 and subsequent oxidizing conditions. Additionally, an intense band at 1504 cm^{-1} at elevated temperatures is indicative of a weakly bound oxygen species.

The *in situ* Raman data reveal a comparable behavior of the sheet and polyhedra samples and a fundamentally different behavior for the ceria cubes. The behavior originates from the different surface facets. The sheets and polyhedra possess a (111) facet and the cubes a (100) facet. The fundamentally different character of the surface facets is demonstrated by the vibrational properties of the surface facets and the different oxygen adsorption behavior. The oxygen adsorption behavior of the two facets is discussed in the next section together with the results of the DFT+U calculations on peroxide and superoxide formation at the $CeO_2(100)$ and $CeO_2(111)$ facet (see sections 4.8 to 4.12).

5.6 Discussion on peroxide and superoxide formation at faceted ceria nanoparticles

In this section the experimental results on the oxygen adsorption at faceted ceria nanoparticles are discussed in the context of the DFT+U results presented in chapter 4 and reported here and in the literature. [32, 51, 56, 196, 197, 200, 201] As evident from the previous sections the ceria sheets and polyhedra expose the $CeO_2(111)$ surface and the cubes the $CeO_2(100)$ surface facet most probably with a half oxygen layer on the surface. In its most stable configuration this corresponds to a checkerboard type of oxygen arrangement. Coverage-dependent peroxide and superoxide formation at the $CeO_2(111)$ surface and the checkerboard $CeO_2(100)$ surface is analyzed by DFT+U calculation in sections 4.8 to 4.12.

For peroxide adsorption at polycrystalline ceria the presence of a band at ∼830 cm^{-1} and blueshifted bands at ∼860 cm^{-1} and ∼877 cm^{-1} were reported. [32,51,56] These bands have been assigned to isolated and increasingly aggregated peroxides. The same behavior was observed for ceria octahedra. [33] As also shown above polycrystalline ceria terminates with the $CeO_2(111)$ surface as the most stable surface. [119, 120] Therefore, these observations can be directly compared to the coverage-dependent DFT+U calculations on peroxide formation at the $CeO_2(111)$ surface. On the basis of the DFT calculations the bands at 830 cm^{-1} and 860 cm^{-1} are assigned to two types of isolated peroxide configurations of type *a* and *b*, whereas type *a* is more stable at low coverages. Upon increase of the peroxide coverage up to 1 ML the type *b* configuration shifts to higher frequencies and therefore only the band at 877 cm^{-1} is assigned to agglomerated peroxide species. Due to the observation of a weak band at 860 cm^{-1}

in the experimental spectra obtained here, isolated peroxide molecules are proposed at the sheets and polyhedra. This can be rationalized as the samples were not reduced prior to oxygen adsorption.

For ceria cubes the intense peroxide bands at 832 cm^{-1} and 862 cm^{-1} can be explained by a facilitated formation of oxygen vacancies at the $CeO_2(100)$ facet ($E_{vac,O}$ = 1.824 eV) compared to the $CeO_2(111)$ facet ($E_{vac,O}$ = 2.27 eV). Additionally, peroxide formation by molecular oxygen adsorption is facilitated at the reduced $CeO_{2-x}(100)$ ($E_{ads,O_2^{2-}}$ = −2.141 eV), compared to the $CeO_{2-x}(111)$ facet ($E_{ads,O_2^{2-}}$ = −1.90 eV). The difference between the adsorption energy and the vacancy formation energy is proposed as $E_{ads,O} = E_{ads,O_2^{2-}} - E_{vac,O}$ and amounts to $E_{ads,O}$ = −0.317 eV for the $CeO_2(100)$ facet and $E_{ads,O}$ = 0.37 eV for the $CeO_2(111)$ facet. The quantity $E_{ads,O}$ describes the net enthalpy of oxygen vacancy creation and peroxide formation at the defect site. The results reveal that this process is exothermic ($E_{ads,O} < 0$) for the $CeO_2(100)$ facet and endothermic ($E_{ads,O} > 0$) for the $CeO_2(111)$ facet. Additionally, for the $CeO_2(100)$ facet only one stable peroxide configuration is predicted for isolated peroxide molecules, while the second component observed at 862 cm^{-1} in the Raman spectra is attributed to agglomerated peroxide species.

For the correlation of experimental peroxide vibrational frequencies ($\tilde{\nu}_{exp.}$) and calculated frequencies ($\tilde{\nu}_{PBE+U/4.5\ eV}$) for the $CeO_2(111)$ facet the relation $\tilde{\nu}_{PBE+U/4.5\ eV} = 1.30 \cdot \tilde{\nu}_{exp.} - 186\ cm^{-1}$ is derived. Similarly, for the $CeO_2(100)$ facet the relation $\tilde{\nu}_{PBE+U/4.5\ eV} = 1.30 \cdot \tilde{\nu}_{exp.} - 214\ cm^{-1}$ is derived. This shows that configuration and coverage effects of peroxide can be modeled by the PBE+U/4.5 eV approach properly for both considered surface facets.

Regarding superoxide formation (O_2^{-}) at polycrystalline ceria, i.e., the $CeO_2(111)$ surface (see above), the vast majority of Raman [32, 51, 201] and infrared [196, 197, 200] experiments detect superoxides in a rather narrow region around 1123 - 1128 cm^{-1}. This is corroborated by the calculations on superoxide formation at the $CeO_2(111)$ surface, where all considered structures reveal an O-O stretching mode between 1132 cm^{-1} and 1134 cm^{-1}. In addition to the experimental results presented here, a prior study at ceria synthesized via the same route as the nanosheets revealed superoxide formation indicated by a narrow band at 1127 cm^{-1} in Raman spectra. In this study the sample was outgassed at 400°C prior to the Raman measurement which was conducted at room temperature in synthetic air. [199]

For ceria cubes exposing the $CeO_2(100)$ facet superoxide formation has not been observed before. [33] In this study a band is observed at 1137 cm^{-1}, considerably blueshifted with respect to the peroxide band observed at the $CeO_2(111)$ surface facet. In addition, a band at 1103 cm^{-1} is observed at temperatures at and above 60°C. This band is considerably redshifted with respect to the superoxide bands observed at the $CeO_2(111)$ facet. Based on DFT calculations the two bands are assigned to flat superoxide species at the $CeO_2(100)$ surface (see section 4.12). The two distinct bands which are separated by 34 cm^{-1} can be explained on the basis of DFT+U calculations by Ce^{3+} in direct proximity (predicted band at 1050 cm^{-1} and observed band at 1137 cm^{-1}) and Ce^{3+} in the second coordination sphere of the superoxide (predicted band at 1024 cm^{-1} and observed band at 1103 cm^{-1}). This assignment is visualized in figure 4.20 in section 4.12 and the two regimes are indicated by the two dashed lines. The observation of a superoxide species with Ce^{3+} in the second coordination sphere at elevated temperatures can be rationalized by the barrier of 0.5 eV for electron hopping in bulk ceria. [231] Although this superoxide configuration (Ce^{3+} in the second coordination sphere) is only a metastable configuration ($E_{ads,O_2^{-}}$ =

−1.379 eV), its transformation into a more stable superoxide (E_{ads,O_2^-} = −1.625 eV) or a peroxide species ($E_{\mathrm{ads},O_2^{2-}}$ = −2.141 eV) might be kinetically hindered although thermodynamically favored.
Besides the two superoxide species found at the ceria cubes, a band at 1504 cm^{-1} is observed which is absent in Raman spectra of the sheets or polyhedra. It is assigned to molecular oxygen weakly interacting with the surface ($O_2{}^{\delta-}$). DFT+U calculations (see structures in figure B.10 and table B.7) predict an adsorption energy of E_{ads,O_2} = −0.066 eV for O_2 at the oxidized CeO_2(100) surface indicating a weak attractive interaction. The vibrational frequency of adsorbed oxygen is predicted to be redshifted by 16 cm^{-1} as compared to gas-phase O_2. This underestimates the experimentally observed redshift of 52 cm^{-1}. The adsorption of weakly bound oxygen might be facilitated at the CeO_2(100) compared to the CeO_2(111) surface due to unsaturation of the surface with oxygen ions.

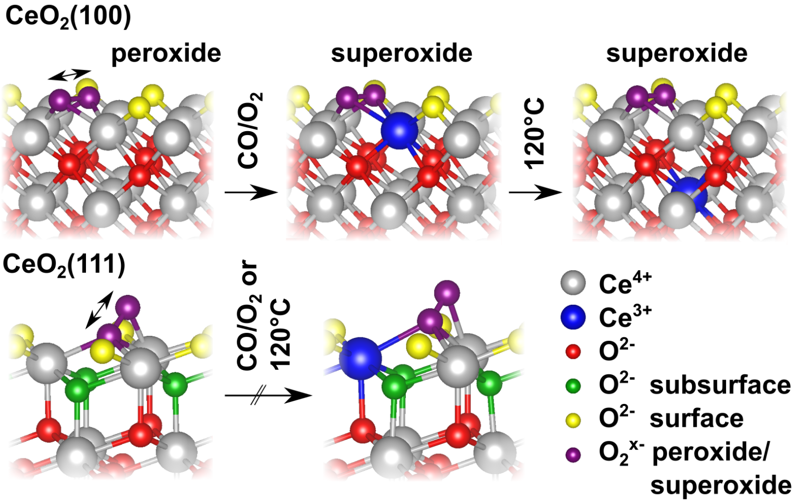

Figure 5.7.: Summary of peroxide and superoxide formation at the CeO_2(100) facet (top row) and the CeO_2(111) facet (bottom row). At the CeO_2(100) facet two distinct superoxide configurations are dynamically formed in CO/O_2 atmosphere at 35°C and at 120°C in O_2. No superoxides are observed under the same conditions at the CeO_2(111) facet.

The results on the oxygen adsorption at the two ceria surface facets are summarized in figure 5.7 revealing an overall facilitated oxygen adsorption at the CeO_2(100) facet (top panel) leading to the formation of two superoxide species (Ce^{3+} in NN and Ce^{3+} in NNN position). In contrast, superoxide formation at the CeO_2(111) facet (bottom panel) was not observed under the same conditions.

5.7 UV-Raman spectroscopy at faceted ceria nanoparticles

To compare the Raman spectra obtained with visible excitation (λ_{ex} = 532 nm) to those obtained with UV excitation that is known to decrease the intensity of the F_{2g} band, [33,189] Figure 5.8 and 5.9 depict UV-Raman spectra with an excitation wavelength of λ_{ex} = 385.1 nm (*in situ*) and λ_{ex} = 256.7 nm (*ex situ*), respectively. For λ_{ex} = 385.1 nm a better signal to noise ratio was observed although the phonon flux is identical for both excitation. This can be rationalized by the UV-Vis spectrum of ceria (see dashed line in figure 7.6 in chapter 7 for ceria sheets), where at 385.1 nm an increasing absorption (band gap region) is observed whereas at 256.7 nm the absorption reaches a maximum. In comparison to UV excitation at the visible excitation wavelength of λ_{ex} = 532 nm the absorption is considerably weaker.

With both UV excitation wavelengths the F_{2g} band and the 2LO overtone at 1170 cm^{-1} are clearly observed. Besides this, with an excitation of 385.1 nm and under *in situ* conditions of a constant 25 % O_2 flow (50 ml/min), the surface modes of the $CeO_2(111)$ at 246 cm^{-1} and 402 cm^{-1} are observed clearly at the CeO_2 sheets at 120°C and at room temperature. Due to the lowered F_{2g} band intensity the distinct band at 402 cm^{-1} can be clearly observed as an isolated band. Please note that with visible excitation only a shoulder is observed (see figure 5.3). As for the visible Raman spectra these two bands are assigned to surface modes and are absent at the ceria cubes. At the ceria cubes the band around 600 cm^{-1} is considerably blueshifted with respect to the band at the ceria sheets suggesting a second component (see section 5.3) next to the broad band at ∼580 cm^{-1} observed at all samples. The band at ∼580 cm^{-1} is assigned to the 2TO overtone, predicted at 584 cm^{-1} by DFT+U calculations (see chapter 4). Neither the bands at 246 and 402 cm^{-1} at the sheets nor the 600 cm^{-1} band at the cubes can be identified with an excitation of 256.7 nm. Due to the strong absorption of ceria in this spectral region, the signal to noise ratio is considerably lowered.

This leads to the conclusion that with visible (532 nm) and and near UV (385.1 nm) excitation, i.e., below the band gap energy, the surface modes can be probed by Raman scattering, whereas this was not possible with deep UV (256.7 nm) excitation here. However, the sampling time of about 1 h for UV-Raman spectra does not allow time-resolved measurements of a gold/ceria catalyst as done with visible excitation (sampling time <3 minutes) described in chapter 7.

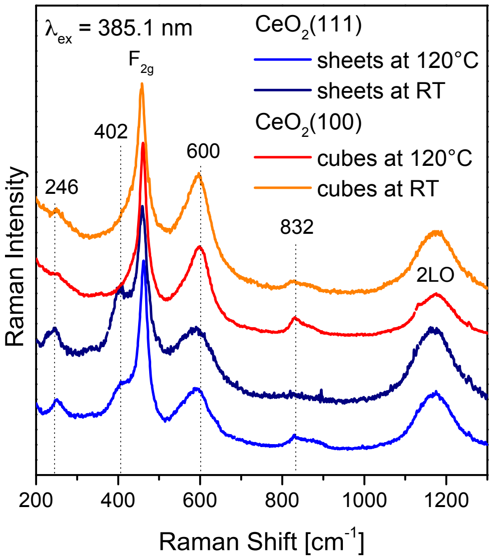

Figure 5.8.: *In situ* UV-Raman spectra (λ_{ex} = 385.1 nm) of ceria nanostructures in 25 % O_2 at 120° and after cooling at ∼25°. The sampling time was ∼1 h. Spectra are normalized to the F_{2g} band intensity and offset for clarity.

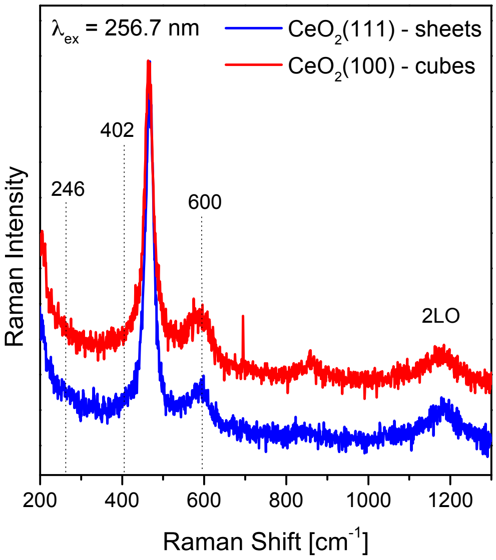

Figure 5.9.: *Ex situ* UV-Raman spectra (λ_{ex} = 256.7 nm) of ceria nanostructures at ∼25°. The sampling time was ∼1 h.

5.8 Conclusions

In this study the precise surface configuration of faceted ceria polyhedra and polycrystalline ceria is determined as a $CeO_2(111)$ surface facet with an O-Ce-O trilayer by *in situ* Raman spectroscopy. Moreover it is shown that the cubes expose the $CeO_2(100)$ surface most probably with occupied and unoccupied surface oxygen positions. This surface facet is modeled by an ideal checkerboard type arrangement of surface oxygen ions.

At the defined nanostructure moieties oxygen adsorption is studied and the observed Raman bands can be rationalized by DFT+U calculations. The coverage-dependent vibrational analysis of the O-O stretching mode by DFT+U (see chapter 4) reveals a facilitated adsorption of peroxide, superoxide, and oxygen species at the $CeO_2(100)$ surface. In fact, at the $CeO_2(111)$ facet no agglomerate peroxide (band at $\sim$877 cm^{-1}) was observed opposite to the $CeO_2(100)$ facet where the band at 862 cm^{-1} can be assigned to strongly agglomerated peroxide species. In comparison, superoxide formation was not observed at the $CeO_2(111)$ facet. In contrast, at the $CeO_2(100)$ surface two superoxide species are found and assigned to superoxide configurations in which Ce^{3+} is located in the vicinity and second coordination sphere of of the superoxide (see figure 5.7). The facilitated oxygen adsorption behavior can explain the superior oxygen storage capacity of ceria cubes with a $CeO_2(100)$ facet compared to $CeO_2(111)$ faceted ceria [45] or polycrystalline ceria. [213] Furthermore the increased performance of the $CeO_2(100)$ faceted cubes in CO oxidation can be rationalized. [207]

In summary, these results provide a transfer from ceria single crystal and thin film studies to ceria nanoparticles, which are shown to be also active catalysts for CO oxidation in the next chapter after gold deposition, while the support exposes well-defined surface facets.

6 Activity of Au/CeO_2 in CO oxidation: Ceria Support Stepped Sites and Ceria Support Surface Facets

In the last 10 years the terms *ceria nanoshape*, [48] *shape selective synthesis*, [45] and *well-defined surface planes* [207, 210] emerged in the literature about ceria materials. It needs to be differentiated between the shape of a ceria particles, e.g., rods, wires, cubes, or microflowers also referred to as *morphology* [232] and the *surface facet* [58] of the ceria nanocrystal which corresponds to the surface termination for example in [111], [110], or [100] direction revealing the low index surface facets $CeO_2(111)$, $CeO_2(110)$, or $CeO_2(100)$.

The vibrational and oxygen adsorption properties of two distinct ceria surface facets are highlighted in chapter 5, evidencing a fundamentally different oxygen adsorption behavior for the $CeO_2(111)$ and the $CeO_2(100)$ facet. The results rationalize the superior oxygen storage capacity of ceria nanocubes over faceted ceria particles [45] and polycrystalline ceria. [213] It is also shown in chapter 5 that a polycrystalline ceria material (in this work called sheets, synthesized by decomposition of a nitrate precursor at 600°C) terminates with the $CeO_2(111)$ facet and the cubic shaped particles terminate with the $CeO_2(100)$ facet, both samples having a comparable specific surface area.

The properties of different nanoshapes and their relevance for catalysis have recently been reviewed by A. Trovarelli and J. Llorca. [48] For oxidation reactions such as CO oxidation the activity followed the order (nanoparticles > nanorods > nanowires) [232] whereas also the series (nanorods > nanocubes > nanooctahedra) was measured for CO oxidation. [207] Recently, a shape-dependent activity in the reverse water-gas shift reaction was observed, where cubes exposed doubled activity compared to particles and rods. [233]

With respect to metal-loaded ceria, the activity followed the order (nanorods > nanocubes > nanooctahedra) for Pd/CeO_2 catalysts during CO oxidation but the opposite order for propane oxidation. [234]

For Au/CeO_2 catalysts DFT+U results on the $CeO_2(111)$ support surface propose the oxygen vacancy formation energy $E_{\text{vac,O}}$ as a descriptor for the CO oxidation activity. [235] At stepped sites of the $CeO_2(111)$ surface a strongly decreased oxygen vacancy formation energy has been proposed ($E_{\text{vac,O}} = 1.66$ eV, PBE+U/5 eV). [66] The DFT+U results are corroborated by the experimental observation of an increased activity of a (111) nanofaceted support (possessing steps) compared to an (100) faceted support in a Au/CeO_2 catalyst. [58] Please note that a decreased oxygen vacancy formation energy for the flat $CeO_2(100)$ surface facet ($E_{\text{vac,O}} = 1.824$ eV) compared to the flat $CeO_2(111)$ facet ($E_{\text{vac,O}} = 2.27$ eV) is also calculated in this work.

The brief overview shows that the effect of the ceria support surface facet on the activity of metal particles such as gold is not fully understood. Moreover, the strong increase in activity of nanorods has not been clarified yet. For nanorods a termination with the $CeO_2(111)$ facet [61, 189, 215, 216] or the $CeO_2(110)$

and $CeO_2(100)$ facet has been proposed. [45, 212, 214] Recently it was shown, that nanorods might undergo reconstruction of the $CeO_2(110)$ facet to the $CeO_2(111)$ facet. [217]
In this contribution, the ceria nanoparticle samples (for the discussion of the characterization see chapter 5) were employed for gold deposition. Then the activity during CO oxidation was monitored at 35°C in the same reaction chamber employed for *operando* Raman/UV-Vis measurements as in chapter 7. In chapter 7 the support dynamics of the ceria sheets in Au/CeO_2 catalyst are highlighted. An initially doubled activity for the reduced catalyst is found at room temperature. This activity increase upon reduction of the support is also observed at 35°C here.

6.1 Results and discussion

The ceria sheets (polycrystalline), polyhedra (synthesized hydrothermally to expose the $CeO_2(111)$ facet), and cubes (synthesized hydrothermally to expose the $CeO_2(100)$ facet) are investigated as support material for gold deposition. The results of the characterization and activity measurements during CO oxidation are summarized in table 6.1 and are discussed in the following. Transmission electron microscopy (TEM) images of the bare ceria support reveal that the sheets and polyhedra expose the $CeO_2(111)$ surface facet and the cubes the $CeO_2(100)$ facet (compare chapter 5). Interestingly, the sheets expose a large fraction of stepped sites at the surface, whereas for the polyhedra and cubes no steps are identified on the basis of TEM measurements. The specific surface of the ceria is determined by N_2 adsorption-desorption experiments and fitting of a BET model to the desorption isotherm (compare chapter 5). The sheets possess a specific surface of 61 m^2/g, the polyhedra 124 m^2/g, and the cubes 51 m^2/g.
XPS analysis[1] of the Au/CeO_2 samples revealed a surface gold content of 0.59 wt% for the Au/CeO_2 sheets, 0.35 wt% for the polyhedra, and 0.52 wt% for the cubes, respectively (for relative sensitivity factors of the Au4f and Ce3d emission see [236]). Deconvolution of the Au4f emission reveals a second component located at ~1.5 eV higher binding energy. This indicates Au^+ formation at the Au/CeO_2 catalyst. The fraction of Au^+ was determined as 35 % for the Au/CeO_2 sheets. By deconvolution of the Ce3d emission a 20 % fraction of Ce^{3+} was found. These values resemble the data obtained in chapter 7 where a more detailed description of the Au4f and Ce3d emission is given.[2] For the polyhedra 43 % Au^+ and 33 % Ce^{3+}, and for the cubes 12 % Au^+ and 10 % Ce^{3+} were determined. Together with an increased Au^+ content a larger Ce^{3+} fraction is observed. This can be rationalized by an electron transfer of gold to cerium ions, as suggested from DFT+U calculations which are further discussed in chapter 8. However, DFT calculations predict only the Au atoms in direct contact to the support transfers electrons to the support. Thus, the larger fraction of Au^+ at the polyhedra might result from the larger specific surface area of the ceria support. Therefore, gold might possess a higher dispersion at this support. The lowered fraction of Au^+ at the ceria cubes (one third of the sheets) might be due to the weaker interaction of gold with the $CeO_2(100)$ surface as compared to a $CeO_2(111)$ surface, this leads to larger particles and a larger fraction of metallic gold. A weaker interaction of gold with the $CeO_2(100)$ surface might be due to a lowered oxygen population at this surface facet compared to the $CeO_2(111)$ surface

---

[1] XPS measurements were conducted at a SSX 100 ESCA Spectrometer (Surface Science Laboratories Inc.) with an Al Kα source.

[2] The measurements reported in chapter 7 were conducted at a LHS/SPECS EA200 MCD with a Mg K_α source.

(see termination of surface facets in figure 5.1). Either way, this can not be confirmed in this study. Furthermore, XPS measurements reveal no impurities at the surface and from Raman spectroscopy only residual nitrate impurities are observed at the Au/CeO_2 polyhedra (the nitrate impurities are drastically lowered at the Au/CeO_2 polyhedra catalyst compared to the bare support discussed in chapter 5). Larger gold particles at the ceria nanocubes can not be confirmed by STEM measurements based on the small number of particles observed at each sample and the fact that TEM probes the sample only locally. A thorough analysis would require averaging over a larger number of particles.

The activity of the samples during CO oxidation (2 % CO and 10 % O_2 in Ar) at 35°C in the *operando* Raman/UV-Vis setup was measured as 4.81 %, 0.58 %, and 0.27 % for ceria nanosheets, nanopolyhedra, and nanocubes, respectively. Before the exposure to reaction conditions the catalysts were kept in oxidizing conditions (25 % O_2) for 1 h. The CO_2 evolution rate [min^{-1}] per Au^+ atom and per surface area of the ceria support [m^{-2}] is determined from the catalytic activity (see section 2.1 for definition). This seems legit as Au^+ sites in contact with the $CeO_2(111)$ surface (sheets) are evidenced as the site for CO adsorption and activation in chapter 8. For convenience the CO_2 evolution rate is normalized to that of the Au/CeO_2 sheets setting this rate to 100 %. The polyhedra exhibit only 8 % and the cubes 22 % of the maximum evolution rate of the sheets.

Obviously the difference in the ceria surface facet cannot be employed solely as a descriptor for the reactivity of the Au/CeO_2 samples. Due to the fact that only minor nitrate impurities were observed by the analytical methods, the only difference of the two $CeO_2(111)$ faceted samples is that the sheets possess stepped sites at the surface as observed by the TEM images depicted in the table 6.1. The stepped sites are observed at all particles in TEM and therefore the image is considered as representative for the whole sample. In contrast, the CeO_2 polyhedra and CeO_2 cubes expose only flat terraces.

As discussed before and extensively in chapter 8 the reaction of a CO molecule adsorbed at Au^+ in direct contact with the ceria support (O_{lattice}-Au^+-CO) with an adjacent lattice oxygen followed by CO_2 desorption is found as the rate determining step for the CO oxidation over gold/ceria catalysts. This releases an oxygen vacancy. [63, 67] Thus, a lowered oxygen vacancy formation energy as found for $CeO_2(111)$ steps [66] is proposed as the origin of the increased activity of the Au/CeO_2 catalyst sheets here. The activity increase amounts to a factor of ten compared to that of a flat $CeO_2(111)$ terrace at the polyhedra.

With respect to flat surfaces a lowered oxygen vacancy formation energy for the $CeO_2(100)$ surface ($E_{\text{vac,O}}$ = 1.824 eV, $p(2 \times 2)$ periodicity) compared to the $CeO_2(111)$ surface ($E_{\text{vac,O}}$ = 2.27, eV (2×2) periodicity) is found by DFT+U calculations in this work (see table B.4 and B.5). Indeed, the activity of the cubes is by a factor ∼3 higher compared to the polyhedra. But on the other hand the activity of the flat $CeO_2(100)$ terrace is only one fifth compared to the sheets which possess a stepped $CeO_2(111)$ facet. For the prior reduced catalysts (1 h in 2 % CO) an initial CO oxidation activity of ∼8.5 %, ∼1.1 %, and ∼0.4 % is measured for the sheets, polyhedra, and cubes based catalysts, respectively. This corresponds to an activity increase to 180 %, 190 %, and 150 % compared to the activity of an oxidized samples. The activity gain is larger at the catalysts with $CeO_2(111)$ facets compared to those with $CeO_2(100)$ facets.

Table 6.1.: Transmission electron microscopy images of ceria sheets, polyhedra, and cubes. Exposed surface facet, surface morphology, and specific surface area from N_2 adsorption experiments. From X-ray photoelectron spectroscopy (XPS) derived surface gold content, Au^+ fraction, Ce^{3+} fraction, and impurities. Nitrate impurity level as derived from Raman spectra and observation of Au particles in STEM. The steady-state activity of the oxidized and the initial activity of the reduced catalyst is given in % CO_2. [a] CO_2 evolution rate [min^{-1}] per Au^+ atom and per ceria surface area [m^{-2}]. [b] Relative activity when sheets are set to 100 %.

Au/CeO_2 catalysts - CO oxidation			
ceria surface facet	CeO_2(111) 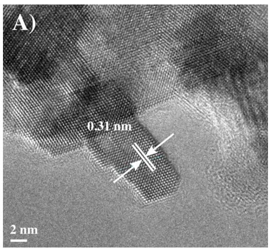 	CeO_2(111) 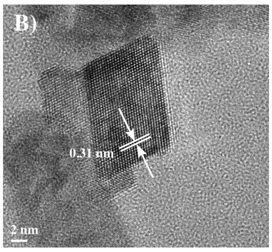 	CeO_2(100) 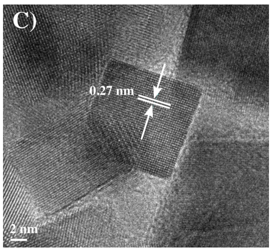
ceria sample	sheets	polyhedra	cubes
surface roughness	stepped	flat	flat
specific surface area [m^2/g]	61	124	51
gold content (XPS) [wt%]	0.59	0.35	0.52
Au^+ fraction (XPS) [%]	35	43	12
Ce^{3+} fraction (XPS) [%]	20	33	10
impurities (XPS)	none	none	none
nitrate impurities (Raman)	none	residual	none
gold particles (STEM)	yes	yes	yes
Oxidized Au/CeO_2 catalyst			
activity steady-state [%]	4.81	0.58	0.27
CO_2/Au^+ m^{-2} min^{-1} [a]	0.0746	0.0061	0.017
relative activity [b]	**100**	**8**	**22**
Reduced Au/CeO_2 catalyst			
initial activity [%]	~8.5	~1.1	~0.4
CO_2/Au^+ m^{-2} min^{-1} [a]	0.13	0.012	0.025
initial activity compared to the oxidized catalyst [%]	**180**	**190**	**150**

6.2 Conclusions

From this report it is strongly suggested that the ceria surface stepped sites alter the activity of Au/CeO_2 catalysts by a factor of ten, [58] while the flat CeO_2(100) facet provides an activity increase by a factor of three compared to a flat CeO_2(111) terrace. Thus, two effects affect the activity of gold/ceria catalysts. First, the surface facet of the ceria support and second, the stepped sites at the surface facet. The second effect was only tested at the CeO_2(111) faceted sample. However, the best catalyst might be a support with a stepped CeO_2(100) facet. Such a support was not synthesized here.

The results highlight the enormous relevance of the ceria support for the reactivity of supported gold nanoparticles and give a straight forward guidance for improving the catalyst activity by surface engineering of the ceria support towards a stepped surface. This was already suggested by DFT+U calculations before. [66]

To further elucidate the effect of oxygen vacancies on the activity of gold/ceria catalysts the defect dynamics of the polycrystalline ceria support in a gold/ceria catalyst are analyzed in chapter 7. The results show the influence of the oxygen defects present in the ceria support on the activity of gold/ceria catalysts.

7 Real-Time Observation of Support Dynamics in Ceria Supported Gold Catalysts[1]

Transition metal oxide supported gold catalysts were identified as low temperature CO oxidation catalysts by Haruta *et al.* in the late 1980s. [16] Besides Co_3O_4, NiO, and Fe_2O_3, ceria (CeO_2) acts as an active support material for gold particles. [10, 11, 237] The activity of these catalysts is known since 30 years and Pt, [19, 53, 205] Rh, [21] and Au [19, 22, 75, 190] particles deposited at CeO_2 have shown activity in CO oxidation, [53] preferential CO oxidation, [22] water-gas shift, [19, 75] and ethanol reforming. [21] Support effects, i.e., the involvement of the support in the reaction mechanism were proposed for Au/CeO_2 [13] and were spectroscopically verified for Pt containing ceria catalysts by *in situ* X-ray techniques, [53, 205] but a detailed mechanistic understanding of oxidation reactions over metal/oxide catalysts is still lacking in the literature. However, it is proposed that the reaction proceeds at the perimeter interface, that is the zone where gold and ceria are in contact and exposed to the gas-phase. [237] This was also suggested for Au/TiO_2 catalysts on the basis of TAP experiments. [238]

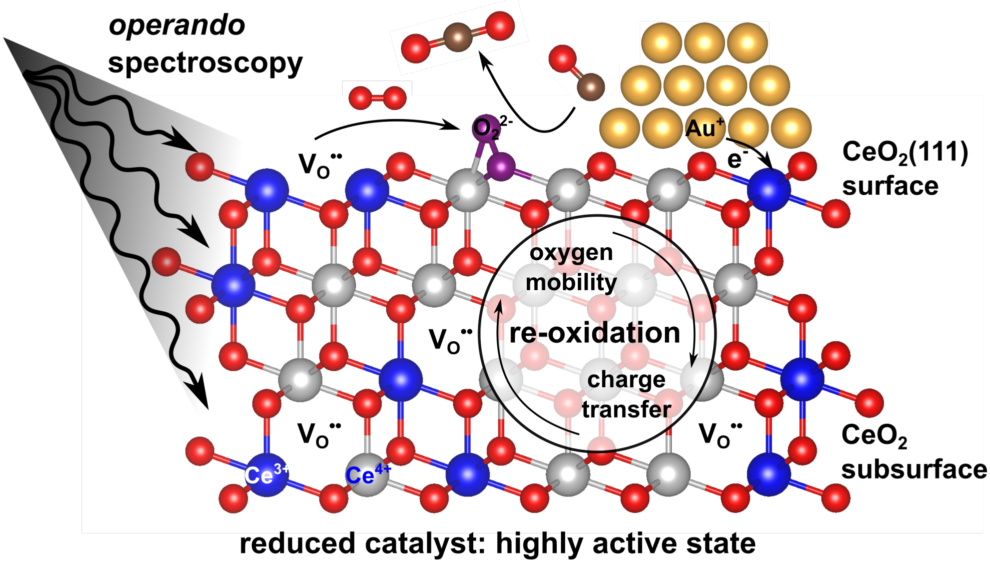

Figure 7.1.: Schematic summary of the important steps of reoxidation of a reduced Au/CeO_2 catalyst during CO oxidation highlighting the important steps of CO adsorption at the perimeter interface between gold and ceria, oxygen adsorption at surface oxygen vacancies, reaction of adsorbed CO with a peroxide molecule, and thereby reoxidizing the support. This rationalizes the greatly enhanced catalytic activity of the reduced catalyst in comparison to an oxidized catalyst.

---

[1] The results of this chapter are already published. The publication including figures is reprinted/adapted with permission from C. Schilling, C. Hess, *J. Phys. Chem. C*, **2018**, *122*, 2909-2917. Copyright 2018 American Chemical Society. (see reference [137]

Here, this topic is addressed by combining Raman and UV-Vis spectroscopy at a Au/CeO_2 catalyst under working conditions (*operando* approach), following the ceria defect dynamics in a time-resolved fashion and correlating it to the activity of the catalyst. [190]

First a thorough characterization of the 0.5 wt% Au/CeO_2 catalyst is given by XPS and TEM. Then the *operando* Raman and UV-Vis spectra are discussed followed by the analysis of time-resolved spectra to characterize the $CeO_2(111)$ surface and CeO_2 subsurface of the support. The key findings of this chapter are summarized in figure 7.1. An electron transfer from the gold particles to the ceria, releasing gold in an oxidized Au^+ state, has previously been proposed by DFT+U calculations and is experimentally verified by XPS analysis. [65,67] The ceria surface and subsurface are reduced (oxygen vacancy creation) during exposure to 2 % CO. Under reaction conditions this is followed by the adsorption of molecular oxygen at the oxygen vacancy, the formation of a peroxide molecule, [65, 190] and its reaction with CO at the perimeters interface between gold and the ceria support. [19,67] This corresponds to a reoxidation of the ceria subsurface due to the oxygen mobility in the ceria support. Simultaneously this rationalizes the greatly enhanced catalytic activity of a prior reduced catalyst. Adsorption of CO at the gold atoms of the perimeter is verified in chapter 8.

7.1 Characterization of the CeO_2 support and the Au/CeO_2 catalyst

The details about the synthesis of ceria and gold adsorption via deposition precipitation are described in section 2.5. X-ray diffraction revealed a cubic fluorite type structure of the ceria support. High resolution transmission electron microscopic images of the ceria sheets revealed ∼12 nm ceria nanoparticles exposing the $CeO_2(111)$ surface facet (0.31 nm lattice plane spacing in direction of the surface) and stepped sites at the $CeO_2(111)$ surface. The specific surface area of the ceria support is determined as 61 ± 5 m^2/g. [199]

The Ce3d photoemission of the CeO_2 support and the Au/CeO_2 catalyst (see figure C.1 in the appendix) shows a multiplet structure. The signal is deconvolved with four components (v, v', v" and v"') while v, v", and v"' account for the three final states $Ce3d^9 4f^2 O2p^4$, $Ce3d^9 4f^1 O2p^5$, and $Ce3d^9 4f^0 O2p^6$ of Ce^{4+}, respectively, and v' accounts for the $Ce3d^9 4f^1 O2p^6$ final state of Ce^{3+}. [135, 141] Due to spin orbit coupling the components denoted as v ($d_{3/2}$) have a counterpart u ($d_{5/2}$) with 1.5 times higher intensity. [140] The difference in binding energy between the u and v components is 18.1 eV. [140] For details on the constraints during deconvolution see figure C.1 of the appendix. From the deconvolution the surface reduction state of ceria is calculated as the fraction of the v' component of the sum of all v components. For the bare support a fraction of 13 % Ce^{3+} and for the 0.5 wt% Au/CeO_2 catalyst a fraction of 15 % Ce^{3+} is calculated, suggesting a charge transfer from gold to the support upon gold deposition.

The Au4f photoemission in figure 7.2 consists of two components located at 84.0 eV and at 84.9 eV. The component at 84.9 eV accounts for 30 % of the total Au signal and is assigned to Au^+ based on its binding energy. This corroborates the suggestion of a charge transfer from gold to the ceria support. Weighting the intensity of the Au4f and Ce3d photoemission with relative sensitivity factors [236] the surface gold mass fraction is estimated as 0.7 wt%. It should be noted that this value refers to the surface mass fraction, while the nominal 0.5 wt% mass fraction is based on the integral catalyst.

Gold particles were furthermore characterized by transmission electron microscopy in scanning TEM (STEM) mode. Due to the Z contrast between ^{58}Ce and ^{78}Au the gold particles can be distinguished from the ceria support (see Figure 7.3 A). The corresponding TEM image of the gold particles is shown in Figure 7.3 B. The point EDX (Figure 7.3 C) mainly exhibits peaks due to gold rather than ceria from the support and copper from the TEM grid. However, only gold particles with 10 nm in size are observed as determined exemplarily on the basis of the high resolution TEM image in figure 7.3 D. Smaller particles (3 nm) were found in a previous study at a sample synthesized identically. [190] The gold particles revealed no distinct surface faceting but the characteristic Au(111) spacing, determined after fast Fourier transform (FFT) and masking of the Fourier transformed (figure 7.3 E). It should be noted that small gold clusters in intimate contact with the support are proposed to be responsible for the high reactivity of the gold/ceria catalysts rather than larger particles observed by TEM (see also chapter 8). [19]

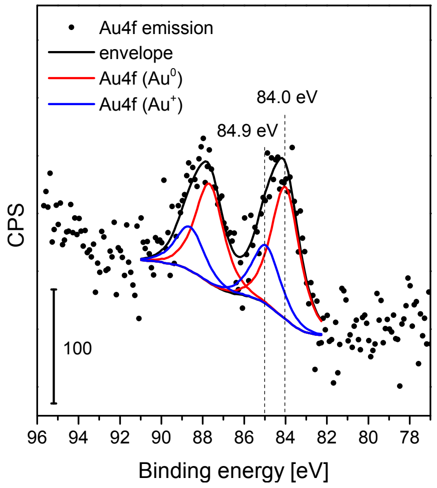

Figure 7.2.: Au4f photoelectron emission of the X-ray photoelectron spectrum of a 0.5 wt% Au/CeO$_2$ catalyst.

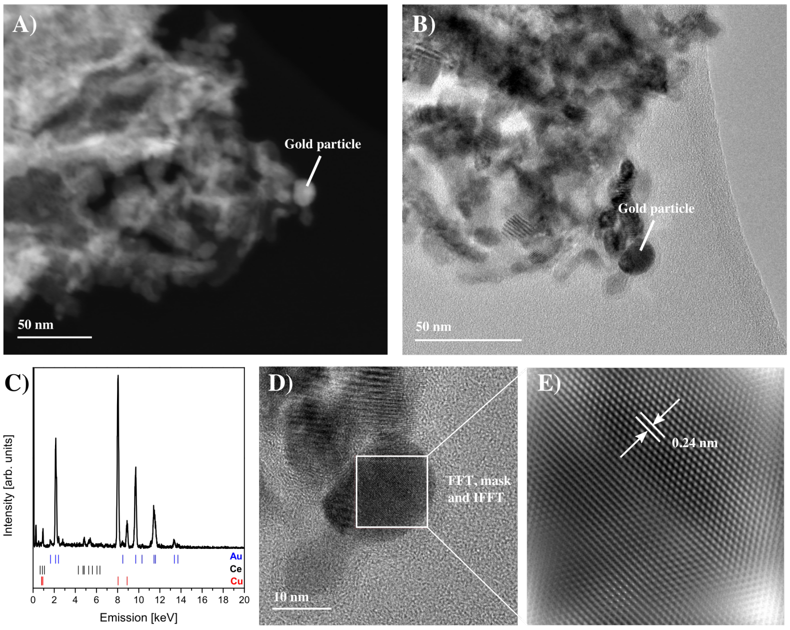

Figure 7.3.: Transmission electron microscopic characterization of the 0.5 wt% Au/CeO$_2$ catalyst: A) STEM image, B) TEM image, C) point EDX of the gold particle, D) high-resolution TEM image of the gold particle, and E) corresponding inverse Fourier transform of the FFT plus applied mask to the Fourier transformed.

7.2 Discussion of the CeO$_2$ support and Au/CeO$_2$ catalyst characterization

The *ex situ* characterization of the CeO$_2$ support (see chapter 5) and of the 0.5 wt% Au/CeO$_2$ catalyst revealed that the ceria support synthesized by decomposition at 600°C terminates with the CeO$_2$(111) surface. This is consistent with the findings that this surface is the most stable surface termination of the low index surfaces. [119, 120] Additionally, the TEM images of the bare support revealed stepped sites at the CeO$_2$(111) surface (see figure 5.2 A).

XPS analysis of the Au/CeO_2 catalyst indicates that about one third of the gold is in the oxidized Au^+ state [140] while the residual gold is in metallic Au^0 state after synthesis. [39, 140] The corresponding Ce3d photoemission revealed that the excess charge is localized at the cerium ions. [135, 141] These results are corroborated by theoretical studies in which a charge transfer from gold (Au_1, [239] Au_{13}, [65] Au_{20} [67]) to the $CeO_2(111)$ surface is proposed. Therefore the studied sample constitutes an active nanoparticle catalyst, that is directly comparable to existing DFT studies considering a $CeO_2(111)$ surface termination [183] and positively charged gold particles. [67] However, it should be mentioned that gold particles observed by TEM are larger than those capable by DFT analysis. Also it should be noted that at a catalyst synthesized by the same synthesis route previously smaller particles (3 nm) have been observed. [190] In addition, the study in chapter 8 shows that under reaction conditions isolated Au^+-CO species can be spectroscopically identified.

7.3 Catalytic activity during *operando* experiments

Details about the *operando* Raman/UV-Vis setup are given in chapter 2. It should be noted here that for this study the catalyst was pretreated in two ways prior to CO oxidation at room temperature (21°C). In the first experiment the catalyst was equilibrated in 25 % O_2 prior to exposure to reaction conditions (2 % CO and 10 % O_2), regenerated in 25 % O_2, and exposed to reaction conditions a second time. This is referred to as oxidizing pretreatment. For the second experiment the catalyst was exposed to 2 % CO after equilibration of the sample and flushing of the cell with pure Ar. Afterwards the catalyst was exposed to reaction conditions as before. This is referred to as reducing pretreatment. In figure 7.4 the concentration of CO in vol% as determined from gas-phase infrared spectra is monitored for oxidizing pretreatment in panel A and reducing pretreatment in panel B. From the CO concentration the conversion can be determined as shown in figure 7.4 A (blue dots). Simultaneously the concentration of CO_2 can be derived from the FTIR spectra as well (black dots). As the amount of consumed CO is identical to the produced CO_2 it is proposed that no other by-products are formed besides CO_2. The slightly increased CO consumption at 300 min in figure 7.4 A might be attributed to adsorption of CO to the catalyst (see chapter 8). Due to the better signal to noise ratio, which is a result of the larger infrared cross section of CO_2, in the following the CO_2 production is plotted and referred to as the catalytic activity. Please note that for the whole study the catalytic activity resembles the CO conversion.

By fitting an exponential decay curve to the CO concentration at 360 minutes in figure 7.4 A, a t_1 time of only 1 minute is determined. Due to the fast decay time the reaction chamber resembles roughly the behavior of an ideal plug-flow reactor although the geometry of the reaction chamber is much different.

The catalytic activity after oxidizing and reducing pretreatment differs strongly and is discussed in this section. The behavior can then be rationalized by *operando* Raman and UV-Vis spectroscopy applied at the catalyst under working conditions as discussed in the following sections.

During the first exposure to reaction conditions after oxidizing pretreatment an activation profile is observed that is already discussed in chapter 2. The maximum activity of 3.5 % is observed after ∼20 min, while the steady-state activity is reached after ∼70 minutes ranging at 3 %. [37] The second exposure to reaction conditions reveals a steady activity of 3 % for about 1 h.

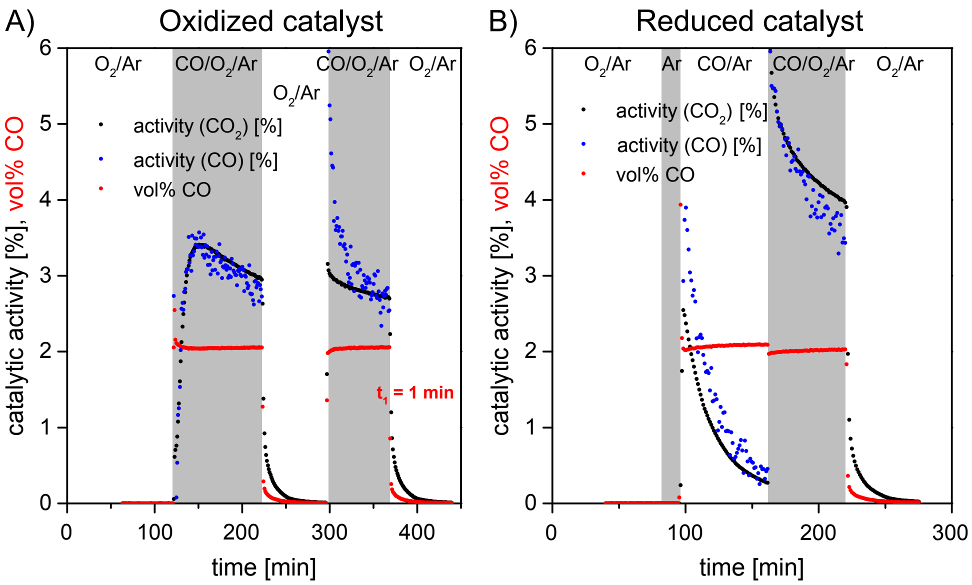

Figure 7.4.: Temporal evolution of the gas-phase composition over a 0.5 wt% Au/CeO_2 at room temperature (21°C). The catalytic activity as derived from the CO_2 concentration is indicated by black dots, the CO conversion by blue dots, and the CO concentration of the product gas stream in vol% by red dots during A) two exposures to reaction conditions (2 % CO, 10 % O_2, 100 ml/min, grey background), each after equilibration and oxidation in 25 % O_2 (white background) and B) exposure to reaction conditions (2 % CO, 10 % O_2, gray background at 160 min) after equilibration in 25 % O_2, flushing of the cell with pure Ar (grey background at 80 min), and reducing pretreatment in 2 % CO in Ar.

During reducing conditions CO_2 evolution is observed corresponding to an activity of 2.5 % decreasing to 0.5 % after 1 h. Due to absence of gas-phase oxygen, this illustrates the oxygen storage capacity of the ceria support as the support supplied oxygen for the reaction. Upon exposure of the reduced catalyst to reaction conditions a maximum activity of 6 % is initially observed decaying to 4 % after 1 h (see figure 7.4 B). Obviously the prior reduced catalyst revealed a significantly higher catalytic activity even after 1 h in reaction conditions (4 % compared to 3 % conversion). In the following it is shown by *operando* Raman and UV-Vis spectroscopy that this activity increase is indeed governed by the subsurface reduction of the ceria support of the Au/CeO_2 catalyst. The corresponding bare ceria support is inactive regardless of the pretreatment.

7.4 *Operando* Raman spectroscopy

Operando Raman spectra recorded during the experiments outlined above are depicted in figure 7.5. The left panel A shows the spectra during the sequence of steps of the oxidizing pretreatment and the right panel B shows the corresponding spectra for reducing pretreatment. First the observed bands are assigned and then their behavior during the *operando* experiments is described.

The most intense band is located between 464.0 cm^{-1} and 460.5 cm^{-1} and is assigned to the F_{2g} mode. For the bare ceria support the band is located at 464.0 cm^{-1}. A shift to smaller frequencies (redshift) of the F_{2g} band is known from experiment and attributed to oxygen vacancy creation in the ceria support. [50, 52] From the DFT+U calculations (see section 4.4) a relation between the F_{2g} shift ($\Delta\omega$) and the stoichiometry ($CeO_{2-\delta-x}$) of $\delta = 0.024 \pm 0.005\ \Delta\omega/cm^{-1}$ is calculated. However, no absolute

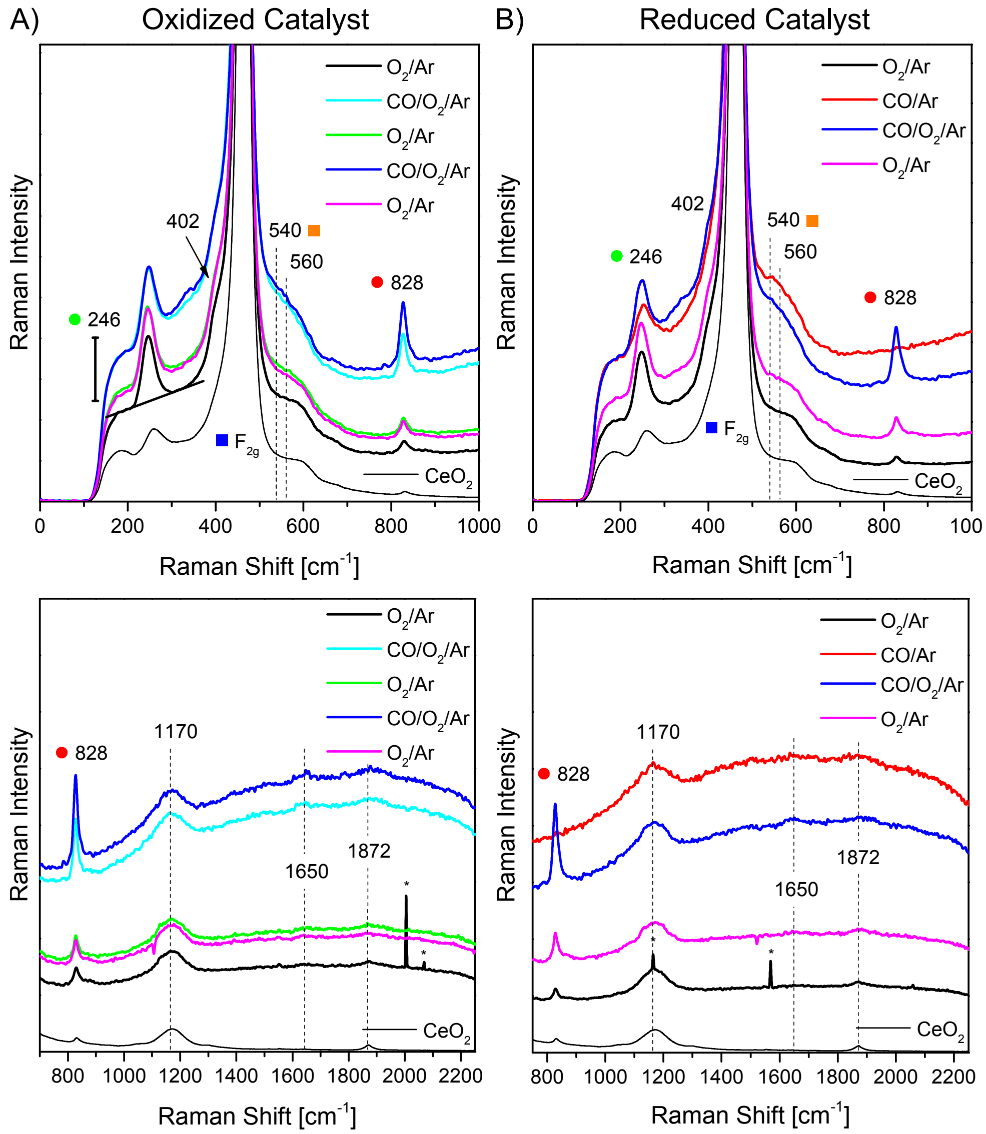

Figure 7.5.: *Operando* Raman spectra ($\lambda_{ex} = 532$ nm) of a 0.5 wt% Au/CeO_2 at 21°C normalized to F_{2g} band intensity showing the phonon region (top panel) and adsorbate region (bottom panel) during A) equilibration (black, 25 % O_2), activation under reaction conditions (light blue, 2 % CO and 10 % O_2), treatment in oxidizing conditions (green, 25 % O_2) and a second exposure to reaction conditions (blue) and oxidizing treatment (magenta). And during B) equilibration (black, 25 % O_2), pretreatment and activation in reducing conditions (red, 2 % CO) and reaction conditions (blue 2 % CO and 10 % O_2) and oxidizing treatment (magenta). The Raman spectrum of bare CeO_2 (thin black line) was measured in 25 % O_2.

relation between the band position and the stoichiometry can be drawn. Rather the position of the F_{2g} band measured at bare ceria (464.0 cm^{-1}) is used as the reference state CeO_{2-x}. Here, x refers to the value accounting for intrinsic defects also present in bare ceria. Besides, a reduction of the ceria subsurface (increase in oxygen vacancy concentration) is indicated by the defect bands at 540 and 560 cm^{-1}. These bands arise due to oxygen vacancies in the ceria support as discussed and verified by DFT+U calculations in section 4.4. Briefly, the DFT+U calculations reveal a band calculated at 480 cm^{-1} (not scaled) for Ce^{3+} in the second coordination sphere around an oxygen defect. As this is the energetically preferred arrangement, the defect and the excess charge (Ce^{3+}) tend to avoid each other. It is proposed that this is only possible if the defect concentration is rather low. A band calculated at 500 cm^{-1} is observed for Ce^{3+} in direct proximity of the oxygen defect. Therefore, this band is observed for higher oxygen defect concentrations. Experimentally these bands occur around ∼540 and ∼560 cm^{-1} while the first is assigned to a lowered and the latter to an increased oxygen vacancy concentration.

Furthermore the DFT+U results allowed an assignment of the band at 246 cm^{-1} to a longitudinal Ce-O mode of the $CeO_2(111)$ surface (see section 4.5). This is corroborated by the observation of a (111) surface facet of the ceria support in TEM images discussed in chapter 5. The corresponding Ce-O transversal vibration is located at 402 cm^{-1} and clearly observed as a shoulder next to the F_{2g} band. Upon introduction of oxygen vacancies at the surface and transfer of excess charge to cerium ions (Ce^{3+}), DFT+U calculations predict a decreased intensity of the band at 246 cm^{-1} (see section 4.5). In principle, both bands at 246 and 402 cm^{-1} can be evaluated quantitatively after background subtraction. Due to its proximity of the transversal surface mode at 402 cm^{-1} to the F_{2g} band at 464 cm^{-1} the evaluation of the 246 cm^{-1} is more convenient, thus providing a quantitative measure of the oxidation state of the ceria surface under reaction conditions.

The adsorbate region of the Raman spectra (700 to 2200 cm^{-1}) is shown in the bottom panel of figure 7.5. Peroxides at 828 cm^{-1}, carbonates at 1650 cm^{-1}, and molecular water at 1872 cm^{-1} are identified. The peroxide and carbonate vibrational modes are discussed in-depth in chapter 4 from DFT+U point of view. The integral intensity of the band located at 828 cm^{-1} is analyzed and proposed as a measure for the surface peroxide concentration. The band at 1650 cm^{-1} can be assigned to an asymmetric stretching mode ν(OCO) of carbonate or hydrogen carbonate species (see section 4.15). Increase of the band under reaction conditions indicates agglomeration of carbonate species (see also chapter 8). The band at 1872 cm^{-1} remains stable suggesting a constant amount of residual water present at the ceria surface.

The Raman spectra after equilibration and before any oxidizing or reducing pretreatment are completely identical. However, during pretreatment the spectra exhibit differences. The green spectrum in figure 7.5 A refers to a catalyst that is subject to an oxidizing pretreatment and the red spectrum in figure 7.5 B to a catalyst that is subject to a reducing pretreatment. Clearly, these two spectra differ in the intensity of the bands at 246 and 402 cm^{-1}. A decreased intensity of both bands is observed for reducing pretreatment indicating a higher concentration of oxygen vacancies at the ceria surface. In addition, the F_{2g} band is redshifted by 2.5 cm^{-1} for the reduced sample (not shown). The redshift corresponds to a stoichiometry difference of $\delta = 0.060$ or a stoichiometry of $CeO_{1.976-x}$ for oxidizing and $CeO_{1.916-x}$ for reducing conditions. This is corroborated by the defect band behavior (540 cm^{-1} and 560 cm^{-1}). A broad increase at both positions indicates a higher concentration of oxygen vacancies. Besides, after reducing pretreatment the peroxide band is absent at the catalyst which is attributed to the absence of gas-phase oxygen. Thus, supplying no oxygen for chemisorption.

Under subsequent reaction conditions (CO/O_2) the spectra are comparable again. The F_{2g} band indicates a stoichiometry of $CeO_{1.952-x}$ and also the defect band component at 560 cm^{-1} is lowered in intensity indicating an alleviated concentration of oxygen vacancies in the ceria support. The intensity of the band at 246 cm^{-1} resembles that observed after equilibration (black spectrum) indicating that the surface is reoxidized as well. The reoxidation can be rationalized by oxygen adsorption in the form of peroxides, indicated by an increased intensity of this band (see also introducing figure 7.1).

7.5 *Operando* UV-Vis spectroscopy

In general, UV-Vis spectroscopy assesses the electronic properties of the sample and therefore reveals additional information compared to Raman spectroscopy which is described in the previous section. As before, first an assignment of the observed bands is given and subsequently the behavior of the observed bands in the course of the experiment is described.

The optical band gap of ceria can be determined as 3.3 eV by UV-Vis spectroscopy. [49] This is in agreement with photoluminescence experiments, [240] optical reflectivity measurements, [180] as well as calculations within the LDA/PBE/PW91+U framework. [174]

An *in situ* UV-Vis spectrum of the bare ceria support is shown as dashed line in both panels of figure 7.6 and exhibits two bands in the near UV region at 330 nm (3.8 eV) and 255 nm (4.9 eV). These bands originate from O2p(filled) → Ce4f(empty) electronic transitions. This assignment is based on the valence band structure of CeO_2 characterized by two peaks in the electronic density of states (DOS) located 4 and 6 eV below the Ce4f states, as determined by ultraviolet photoelectron spectroscopy (UPS). [241] Therefore the O2p(filled) → Ce4f(empty) excitation explain the two bands in the UV region.

Upon reduction of CeO_2 (oxygen vacancy creation, $Ce^{4+} \rightarrow Ce^{3+}$) Ce4f states are populated which are located within the band gap, i.e., between the O2p and the empty Ce4f states. [242] From X-ray and ultraviolet photoelectron experiments the energy difference between the O2p and Ce4f(filled) states has been measured as 1.5-2.5 eV [243] and 2 eV. [242, 244] So the Ce4f(filled) → Ce4f(empty) transition energy ($Ce^{3+} \rightarrow Ce^{4+}$ charge transfer) is 1.5-2.5 eV and absorption is expected between 820 and 496 nm in the UV-Vis spectrum.

Scanning tunneling microscopy (STM) experiments at $CeO_2(111)$ single crystals [111, 113] and thin films [112] evidence that for low concentrations of oxygen vacancies at the $CeO_2(111)$ surface Ce^{3+} ions avoid each other and locate preferably in the surface cerium layer. For higher concentrations ($\geq$0.25 ML) a subsurface localization is no longer unavoidable (see also figure B.3 for model structures with 0.06 – 1 ML defect concentration). [103] However, localization of excess charge exclusively at the surface may cause a narrow absorption in the visible region of the UV-Vis spectrum, while localization at the surface and in the subsurface would cause broad absorption ($\geq$496 nm), due to the valence band structure of these two structures. [103]

The *operando* UV-Vis spectra of the 0.5 wt% Au/CeO_2 are depicted in figure 7.6. The UV-Vis spectra are measured immediately after the Raman spectra in the corresponding gas atmospheres. Besides the bands in the UV region, at the Au/CeO_2 catalysts a broad band at 570 nm is observed (compare dashed and solid black line in figure 7.6). The band has been assigned to a surface plasmon excitation of adsorbed gold nanoparticles. [22] While a contribution from surface plasmons can not be excluded, here it is rather proposed that this band originates from $Ce^{3+} \rightarrow Ce^{4+}$ transitions, as discussed in the following. The Ce^{3+} creation in Au/CeO_2 is supported by XP (Au^+ and Ce^{3+}) and Raman (F_{2g} redshift of 0.5 cm^{-1} comparing CeO_2 and Au/CeO_2) spectroscopy. The assignment to a $Ce^{4+} \rightarrow Ce^{3+}$ charge transfer is further supported by spectra observed in reducing conditions (see red spectrum in figure 7.6 B), where a broad increase extending to 1000 nm is observed indicating reduction of the surface and subsurface cerium ions. A reduction of the sample upon exposure to reducing conditions is also concluded from *operando* Raman spectroscopy (see previous section).

Upon exposure of the Au/CeO_2 catalyst to reaction conditions (2 % CO and 10 % O_2) an additional band around 450 nm is observed. This band has also been reported for Au/CeO_2 catalysts under reaction conditions of preferential oxidation of CO ($CO/O_2/H_2$). [22] Here, this band tends to correlate with the activity of the catalyst (see figure 2.3 of chapter 2) and is not observed in reducing conditions. Therefore, two assignments are possible on the basis of this study. On one hand, the band can be assigned to a $O_{lattice}$-Au^+-CO species which correlates with the activity as shown in chapter 8. On the other hand, this band can be attributed to peroxide species adsorbed to the ceria surface. Please note that peroxide species are not identified by Raman spectroscopy under reducing conditions but increase strongly in intensity under reaction conditions (see figure 7.5 B).

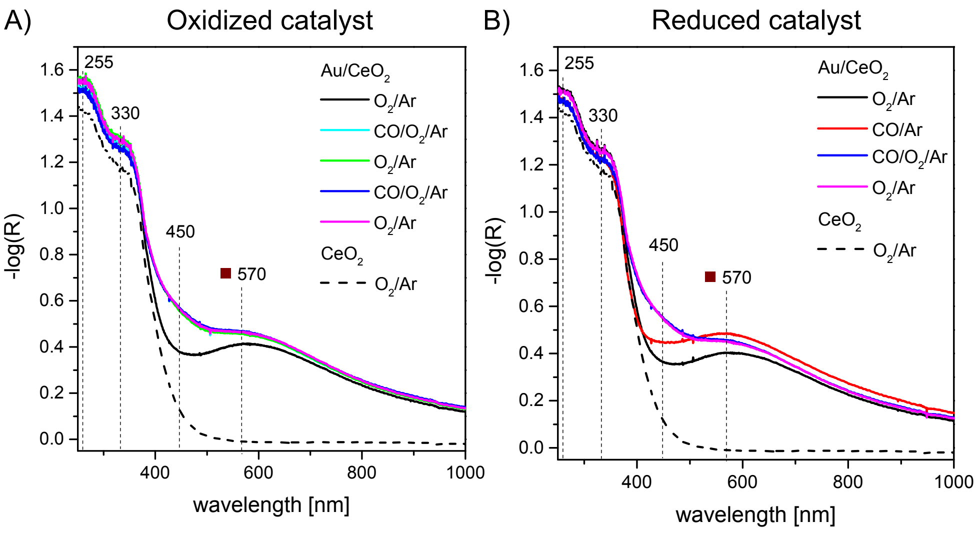

Figure 7.6.: *Operando* UV-Vis spectra of 0.5 wt% Au/CeO_2 at 21°C during A) equilibration (black, 25 % O_2), activation in reaction conditions (light blue, 2 % CO and 10 % O_2), treatment in oxidizing conditions (green, 25 % O_2), a second exposure to reaction conditions (blue), and oxidizing treatment (magenta). And during B) equilibration (black, 25 % O_2), pretreatment and activation in reducing conditions (red, 2 % CO), reaction conditions (blue), and oxidizing treatment (magenta). The color code corresponds to Figure 7.5. The UV-Vis spectrum of bare CeO_2 (dashed line) was measured in O_2.

The UV-Vis spectra of the Au/CeO_2 catalyst after equilibration are identical. The two different pretreatments (oxidizing and reducing) result in two different spectra, the green spectrum in figure 7.6 A and the red spectrum in figure 7.6 B. During activation and oxidizing pretreatment only a minor absorption increase at 570 nm is observed but the band at 450 nm strongly increases in intensity. In contrast upon reduction a broad absorption in the visible region is observed. After exposure to reaction conditions for

1 h both spectra are comparable again exhibiting a slight increase in absorption at 570 nm and the band at 450 nm.

7.6 Time-resolved *operando* Raman/UV-Vis spectroscopy

To gain insight into the oxygen defect dynamics during reaction, *operando* Raman and UV-Vis spectra are recorded in a time-resolved manner (every ∼260 s over the course of the experiment). Simultaneously, the gas-phase analysis provides information about the activity of the catalyst. In figures 7.7 and 7.8 each point (colored dots) refers to the spectroscopic information deduced from an *operando* Raman or UV-Vis spectrum at the indicated time point and is correlated to the activity of the catalyst (black dots). First the observations characterizing the subsurface of the ceria support by Raman and UV-Vis spectroscopy are discussed (see figure 7.7). Then the characterization of the ceria surface is discussed (see figure 7.8).

As mentioned above, the F_{2g} band is shifted to 463.5 cm^{-1} for Au/CeO_2 catalysts compared to the bare support (464.0 cm^{-1}). This indicates a reduction of the support upon gold deposition. During reaction the F_{2g} band is further redshifted by 1.5 cm^{-1} in total. The shift occurs in accordance with the increase in the catalyst activity. The redshift corresponds to a stoichiometry change from $CeO_{1.988-x}$ to $CeO_{1.952-x}$. This is reversible and observed for both exposures to reaction conditions (see figure 7.7 A). The reduction of the support is furthermore monitored by the increase of the Raman defect band intensity at 540 cm^{-1} (orange squares) and the absorption increase at 570 nm in the UV-Vis spectra (brown squares). For reducing pretreatment (see figure 7.7 B) a redshift of 3 cm^{-1} of the F_{2g} band is observed (stoichiometry $CeO_{1.916-x}$). This is again in line with an increase of the defect band at 540 cm^{-1} and the absorption at 570 nm.

Exposure of the reduced catalyst to reaction conditions (2 % CO, 10 % O_2) results in an increase of the activity of 100 % (6 % catalytic activity) as described above, followed by a slow decay to 4 % activity. The F_{2g} position, the defect band, and the absorption at 570 nm show a sudden blueshift, an intensity drop, and an absorption drop, respectively. This is followed by a gradual blueshift of the F_{2g} band and a slower decay of intensity of the defect band at 540 cm^{-1}, while the UV-Vis absorption remains stable. This behavior shows that the activity of the catalyst is linked to the subsurface oxidation state of the ceria support. After 1 h in reaction gas mixture the activity is still 30 % increased compared to a prior oxidized support and has not reached a steady-state behavior.

The band at 246 cm^{-1} is assigned to a longitudinal stretch of the O-Ce layer of the CeO_2(111) surface (compare chapter 4 and 5). Surface oxygen vacancy creation (reduction) decreases the intensity of the band and broadens the band (see section 4.5). Figure 7.8 depicts the intensity of the band over time as green dots. For guidance the steady-state intensity of the band during reaction conditions is shown as a green dashed line. After oxidizing pretreatment and during the second exposure to reaction conditions the intensity of the 246 cm^{-1} band can be correlated to the activity, showing a slight decrease during reaction conditions. During reducing pretreatment the intensity decrease of the band at 246 cm^{-1} is much more pronounced, indicating a higher oxygen vacancy concentration at the surface during reduction in 2 % CO. Upon exposure to reaction conditions the steady-state intensity of the band is reached immediately. This resembles the behavior of the UV-Vis absorption band at 570 nm. Therefore the UV-Vis absorption at 570 nm may be attributed mainly to a surface reduction of the ceria support. For

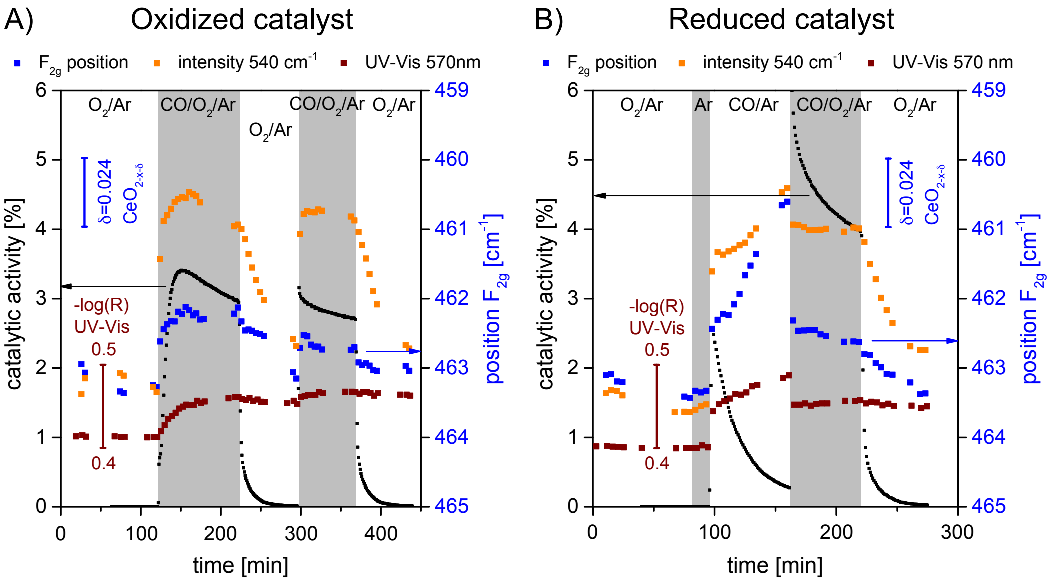

Figure 7.7.: Time-dependent *operando* Raman and UV-Vis spectroscopic information for the ceria sub-surface reduction state of a 0.5 wt% Au/CeO$_2$ catalyst during A) two consecutive exposures to reaction conditions (oxidizing pretreatment). And during B) reaction after reducing pretreatment. Black squares indicate the catalytic activity of the catalyst, blue squares the position of the F$_{2g}$ band, orange squares the absolute intensity of the 540 cm^{-1} defect band in the Raman spectra, and brown squares the UV-Vis reflectivity at 570 nm. The scales are identical for both graphs.

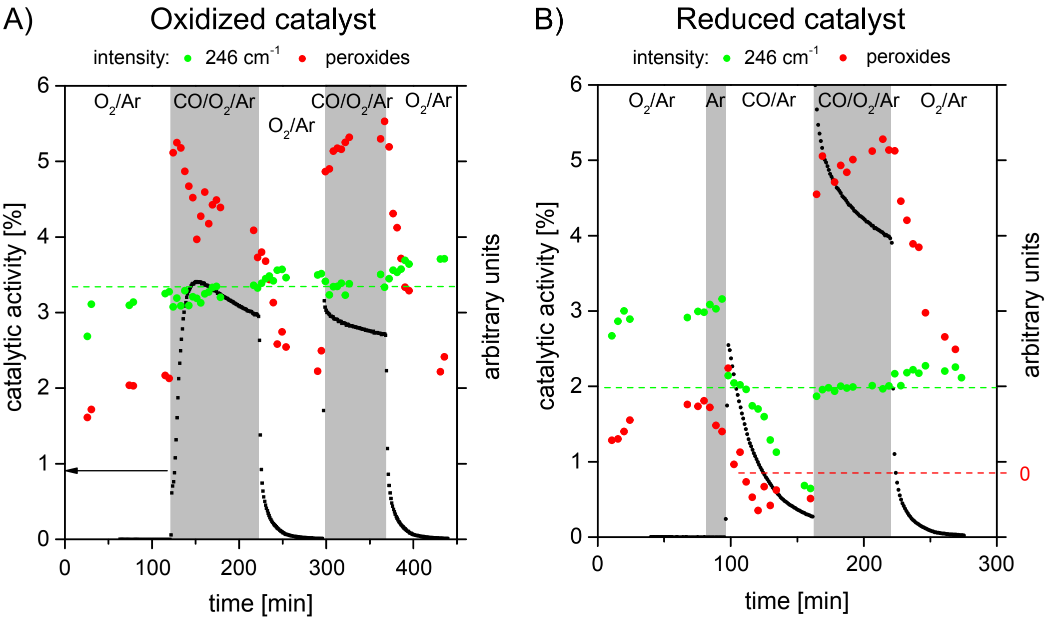

Figure 7.8.: Time-dependent *operando* Raman spectroscopic information for the ceria surface reduction state of a 0.5 wt% Au/CeO$_2$ catalyst during A) two consecutive exposures to reaction conditions (oxidizing pretreatment). And during B) reaction after reducing pretreatment. Black dots indicate the catalytic activity to CO$_2$, red dots the integrated intensity of the peroxide band, and green dots the integrated intensity of the 246 cm^{-1} band. The scales are identical for both graphs. The green dashed line indicates the steady-state intensity level in reaction conditions CO/O$_2$/Ar.

completeness the temporal evolution of the position of the band maximum around 246 cm^{-1} is shown in the appendix in figure C.2. For a lowered intensity a blueshift of the band is observed and vice versa. In the last step the integral intensity of the peroxide band at 828 cm^{-1} in analyzed. The relevance of peroxide species at Au/CeO$_2$ catalysts for CO oxidation has been highlighted before. [190] Red dots in figure 7.8 show an increase of peroxide species under reaction conditions compared to oxidizing conditions. Under reducing conditions no peroxide species are observed, indicating a decomposition of peroxide species in CO atmosphere. Furthermore, the intensity of the peroxide band is identical under reaction conditions regardless of the pretreatment procedure and the catalytic activity. This suggests that the number of oxygen adsorption sites does not increase upon reduction, but rather the reactivity per site.

7.7 Discussion on the *operando* spectroscopy results

The CO oxidation activity of Au/CeO$_2$ catalysts has been reported to increase with reducing pretreatment, [245] being independent of the pretreatment, [39] or being lower after prior reduction of the catalyst. [59] For Au/TiO$_2$ catalysts a strong decrease in activity by prior reduction has been observed. [246] The results reported here reveal a clear increase in activity of a 0.5 wt% Au/CeO$_2$ catalyst upon prior reduction for 1 h in 2 % CO. The catalytic activity is raised by 100 % from 3 % to 6 % and declines to 4 % within 1 h in reaction conditions after reducing pretreatment. Please note that the catalytic activity derived from CO$_2$ production resembles the CO conversion. A similar behavior was reported by Zhang *et al.* [245], who measured an initially doubled activity of a 0.34 wt% Au/CeO$_2$ catalyst prepared by the same synthesis route after reduction in hydrogen at 250°C. A deactivation profile (about 1 h) after pretreatment in CO at 400°C was observed at a 4.5 wt% Au/CeO$_2$ catalyst at 80°C. However, the catalyst reduced in CO was less active compared to the catalyst treated in oxygen or nitrogen atmosphere at the same temperature prior to reaction. Temporal analysis of products (TAP) experiments at Au/CeO$_2$ powder catalysts at 120°C have shown a slow activation of the catalyst after outgassing the sample at 400°C, but a fast activation and adjustment to the steady-state activity after prior CO reduction and reoxidation with O$_2$ at 120°C. For a reduced catalyst (without reoxidation) an increase in CO$_2$ formation accompanied by an increased O$_2$ consumption was observed. In contrast, the CO uptake was decreased. The authors explained this observation by an oxygen-assisted carbonate release as the origin of the CO$_2$ formation in conjunction with a lowered CO uptake. [59] The Raman results in figure 7.5 rather reveal an increased concentration of carbonate species under reaction conditions indicated by the band at 1650 cm^{-1} that is assigned to a hydrogen carbonate species (see also section 4.15).

By *operando* Raman and UV-Vis spectroscopy, a surface and subsurface reduction upon pretreatment in reducing conditions is clearly observed. The surface oxidation state is monitored by the intensity of the Raman band at 246 cm^{-1} assigned to the Ce-O stretching mode of the CeO$_2$(111) surface [183] and the absorption of the sample at 570 nm in the UV-Vis spectra. The band at 402 cm^{-1} is assigned to the transversal stretching mode of the CeO$_2$(111) surface. However, this band was not evaluated quantitatively due to its proximity to the intense F$_{2g}$ band. The subsurface reduction state is monitored by the F$_{2g}$ position and a direct link to the stoichiometry is provided. The band at 540 cm^{-1} in Raman spectra corroborates the observation of a reduction of the subsurface as well and constitutes a semi-quantitative indicator for the oxidation state of the subsurface. The dynamic *operando* spectroscopy results show that the reduction of the subsurface governs the increased activity of the Au/CeO$_2$ catalyst. The descriptors for the oxidation state of the CeO$_2$(111) surface reveal an immediate reoxidation of the prior reduced catalyst support surface under reaction conditions, whereas the descriptors for the ceria subsurface reveal a continuous reoxidation of the prior reduced catalyst (see scheme 7.1)

Recently, an electronic metal-support interaction at Au/TiO$_2$, i.e., transfer of excess charge after reduction to the gold particle, hindering CO adsorption and lowering the activity of the catalyst, was proposed. [246] In contrast, the results for the Au/CeO$_2$ catalyst obtained here strongly suggest a localization of excess charge at the ceria support. This allows a facilitated oxygen adsorption and activation at the oxygen vacancies at the support. This is further supported by the high oxygen mobility in ceria compared to other oxides. [247] In addition, a further increased oxygen mobility was measured for 1 wt% Au/CeO$_2$ compared to a bare CeO$_2$ material. [248]

7.8 Conclusions

In conclusion, the ceria oxygen defect dynamics in Au/CeO$_2$ catalysts could be successfully evaluated by combined *operando* Raman/UV-Vis spectroscopy. The defect dynamics were examined in a time-resolved fashion by following activation and deactivation processes employing dynamic spectroscopic measurements. The data reveal a surface reduction of the CeO$_2$(111) surface in reducing and reaction conditions. The reduction in not only limited to the surface but also the nanoparticle subsurface. By quantitative analysis of the spectroscopic data, the increase of 100 % in activity of the Au/CeO$_2$ catalyst can be linked to a stoichiometry of CeO$_{1.912-x}$ of the ceria support after reduction compared to CeO$_{1.976-x}$ for oxidizing pretreatment. With the dynamic *operando* spectra it was shown that the subsurface reduction state indeed alters the activity increase. This can be rationalized by the high oxygen mobility of Au/CeO$_2$ catalysts.

This study highlights the importance of combined spectroscopy at the catalyst and its correlation with the activity of the catalyst (*operando* approach) to elucidate the mode of operation of metal/ceria catalysts.

8 Spectroscopic Evidence for Single Gold Site Formation at Au/CeO_2 Catalysts during CO Oxidation

Since the work of Haruta *et al.* [16, 17] oxide supported gold catalysts have gained enormous attention. [210, 237] Experimental results suggest that only a minor fraction of adsorbed gold is active for oxidation reaction over Au/CeO_2 catalysts, as the metallic gold was leached from the sample. [19] This is corroborated by the finding of a greatly enhanced activity upon nanosizing of the ceria support, i.e., providing a higher surface area for gold ceria interaction. [13]

On the basis of *ex situ* [51] and *operando* [190] Raman spectroscopy oxygen activation is proposed to proceed at the ceria support. An active fraction of oxygen ions in the proximity of gold was proposed on the basis of temporal evolution of products (TAP) experiments for CeO_2 and TiO_2 supported gold particles. [59] The stability of gold particles at the ceria support was evidenced by atomic resolution environmental TEM proposing interfacial gold atoms to be the adsorption site for the CO molecule during oxidation reactions. [61] Besides, the inverse CeO_{2-x}/Au(111) catalysts exhibited activity for the water-gas shift reaction, if the CeO_2 expose oxygen vacancies which are proposed as the site for water activation. [75]

This brief review summarizes that the reaction proceeds most probably at the perimeter interface between gold and the ceria support, while CO is adsorbed on the gold and the ceria support assists in oxygen activation for the reaction. Although CO adsorption has been studied at Au/CeO_2 catalysts, [249–252] a definite statement on the adsorption of CO onto gold forming the *active site* has not been made.

In an elegant experiment Ding *et al.* employed *in situ* infrared spectroscopy to measure the CO stretch frequency of adsorbed and reactive CO. [253] In combination with TEM measurements single supported Pt atoms were identified as the active site for the water-gas shift reaction over Pt/CeO_2 catalysts and Pt model catalysts. [253] Due to the low contrast of gold and ceria in TEM, single gold atoms have only rarely been identified at a ceria support [254] but gold particles in the range of 2-4 nm [61], 2-3 nm, [190] and up to 10 nm (see chapter 7) were reported more often.

With respect to DFT results gold clusters (Au_1, [131, 239] Au_{13}, [65] and Au_{20} [67]) tend to adsorb at the CeO_2(111) surface and transfer charge to the ceria surface releasing gold in an oxidized state. Also adsorption of Au_n ($n > 5$) clusters adsorbed at an oxygen vacancy site are charged positive. [255] The reaction mechanism for a Au_1/CeO_2(111) structure, i.e., a single Au atom adsorbed to the CeO_2(111) surface, was modeled by Camellone *et al.* [63] The authors found adsorption of CO to a Au^+ ion, reaction with a surface lattice oxygen and diffusion of the Au atom to the surface oxygen vacancy position carrying the negative charge. The barrier for CO_2 desorption was calculated as 0.86 eV with a PBE+U/4.5 eV functional. [63]

Kim *et al.* [65] compared reaction pathways at larger gold particles (Au_{13}) adsorbed at the $CeO_2(111)$ surface and found a Mars-van Krevelen type reaction mechanism to be preferred at higher temperatures. [65] Due to oxygen vacancy formation after CO_2 desorption, the activation energy is strongly altered by the oxygen vacancy formation energy at the ceria surface (see chapter 6). A facilitated CO_2 desorption was found for a $Au_3/CeO_{2-x}(111)$ structure because the Au_3 cluster is very flexible. [64] Furthermore, doping of the $CeO_2(111)$ surface lowered the calculated oxygen vacancy formation energy and therefore the activation energy of the reaction. [235] A Mars-van Krevelen mechanism is also preferred, if stepped sites at the $CeO_2(111)$ surface are considered. At stepped sites the oxygen vacancy formation energy is lowered (see chapter 6). [66] Recently, the dynamic formation of a single Au-CO site from a Au_{20} cluster after CO adsorption was predicted by DFT+U calculations. [67] As for the single gold site before, Au^- is formed at the oxygen vacancy after CO_2 desorption. The activation barrier is small enough to allow CO oxidation to occur at room temperature. [67] However, by STM experiments and DFT calculations a diffusion barrier for gold atoms at the $CeO_2(111)$ surface was found. [256] The results reveal that the formation of Au^- is kinetically hindered although thermodynamically favored. [256]
CO adsorption at the $CeO_2(111)$ surface has been studied before by DFT calculations [121–123] and infrared spectroscopy (IRRAS) at single crystals. [124] Moreover, the formation of carbonates and formates after CO and CO_2 adsorption is well known from experiment [34–36, 257] but only rarely studied from a DFT point of view. [205, 206, 208]

In this chapter *operando* diffuse reflectance infrared Fourier transform spectroscopy (DRIFTS) is employed in a time-resolved fashion together with density functional theory calculations (DFT) to identify the active adsorbed CO species at polycrystalline Au/CeO_2 catalysts spectroscopically. On the basis of DFT calculations these active CO species are characterized as a *single gold site* or a *pseudo single gold site*. The latter is proposed as a single gold site formed after CO adsorption and a slight abstraction of the gold ion from a gold cluster. [64, 67] These two species are shown in the blue boxes in figure 8.1 corresponding to the blue component in the spectrum. Furthermore, inactive CO, i.e., CO adsorbed at the top site of a three dimensional gold particle, is observed (green box in figure 8.1). CO adsorbed at the ceria support is found to inhibit the reaction (black box in figure 8.1), as does readsorbed CO_2 in the form of hydrogen carbonates. [37]

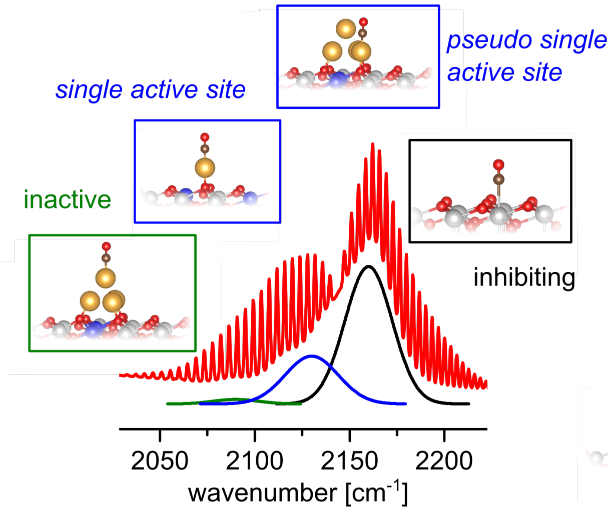

Figure 8.1.: The scheme illustrates the key findings of this chapter. The excerpt of the infrared spectrum of a Au/CeO_2 catalyst during reaction shows the CO stretch frequency region. The CO-Au/CeO_2(111) and CO-Au_4/CeO_2(111) active species are highlighted in blue, CO/CeO_2(111) inhibiting species in black, and inactive CO-Au_4/CeO_2(111) species in green.

8.1 Experimental

A 0.5 wt% Au/CeO_2 sample was employed as catalyst which is prepared by deposition precipitation of gold at the ceria nanosheets (see chapter 2). The bare ceria support was throughly characterized as described in chapter 5. TEM images reveal the presence of a stepped CeO_2(111) surface facet at the support. Additionally, the Au/CeO_2 catalyst was characterized by TEM and XPS (see chapter 7).

For details on the the diffuse reflectance infrared setup the reader is referred to section 2.2. The infrared setup was used in *operando* mode analyzing the effluent gas stream from the Harrick reaction cell by gas-phase infrared spectroscopy as described in section 2.3. Gas-phase analysis and *operando* infrared spectroscopy applied at the catalyst sample in diffuse reflection mode was synchronized, i.e., every minute the spectrum averaging over one minute was saved for gas-phase analysis and infrared characterization of the Au/CeO_2 catalyst. This allows a direct comparison of the activity of the catalyst and spectroscopic information from infrared spectroscopy. In figure 8.2 the course of the experiments is shown, each point refers to a spectrum measured at the respective timepoint. The black dots indicate the activity of the catalyst as derived from gas-phase infrared spectroscopy. For a correlation of spectroscopic information, extracted from diffuse infrared spectra of the catalyst, see figure C.3 and C.4 of the appendix.

The catalyst was pretreated in two ways. For pretreatment A the catalyst was equilibrated in 25 % O_2 balanced with Ar at a total gas flow of 100 ml/min. Afterwards reaction conditions (2 % CO, 10 % O_2) were applied for ∼100 minutes. A regeneration of the catalyst in 25 % O_2 for 1 h follows, before a second exposure to reaction conditions, and a final regeneration was done. The exposure to reaction condition is indicated by the grey background in figures 8.2 A and B. For pretreatment B the catalyst was heated to 200°C for 1 h in 25 % O_2, cooled to room temperature (∼21°C), and was then exposed to the same protocol as before.

The temporal evolution of the catalytic activity is shown in the left panel of figure 8.2 for pretreatment A and in the right panel for pretreatment B. The characteristics are discussed in the following section.

8.2 *Operando* diffuse reflectance infrared spectroscopy results

Figure 8.2 depicts the catalytic activity over time for pretreatment A and pretreatment B. As already discussed in chapter 2 and 7, after equilibration at room temperature the catalyst exhibits an activation period (20 minutes), reaches a maximum and then deactivates slowly and exhibits comparable activity during the second exposure to reaction conditions. In comparison, for the catalyst pretreated at 200°C for 1 h in O_2/Ar, the activation period prolongs during the first exposure to reaction conditions (∼120 minutes). After regeneration the activity curve still possesses an activation profile. This behavior can be rationalized by a recent study of Zhang *et al.* [37] The authors reported a longer activation period for dry reaction gas and a very short (<1 min) induction period for humid reaction gas. [37] Adsorbed water is present at oxide nanoparticles as also probed by Raman spectroscopy (see figure 7.5). Therefore, heating the sample to 200°C prior to the experiment drastically decreases the amount of residual water at the sample and causes the prolonged induction period.

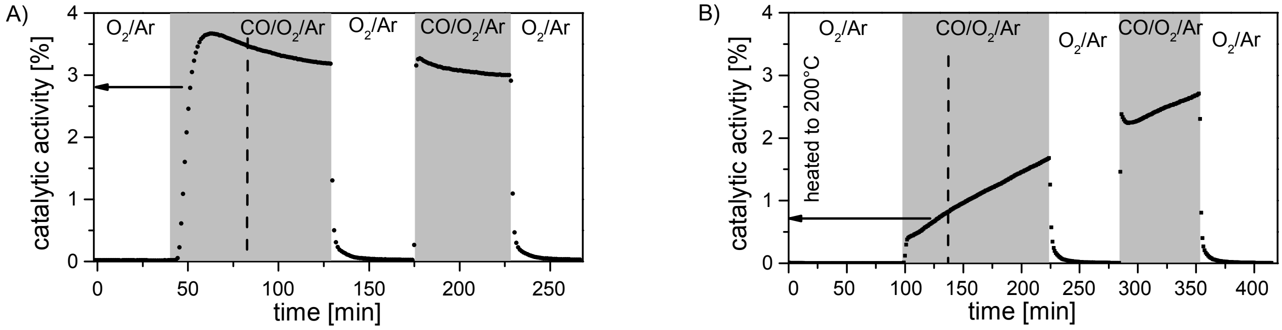

Figure 8.2.: Catalytic activity of a 0.5 wt% Au/CeO_2 catalyst during two cycles of CO oxidation (2 % CO, 10 % O_2) at 21°C after A) equilibration in 25 % O_2 and after B) 1 h at 200°C in 25 % O_2. The dashed line indicates the time of the infrared spectroscopy measurement depicted in figure 8.3.

To gain insight into the origin of the induction period, the *operando* infrared spectra of the catalyst are depicted in figure 8.3. Two spectra are compared, one after pretreatment and one after about 30 minutes in reaction conditions. The dashed line in figure 8.2 indicates the time of the infrared spectroscopy measurement. The analysis of the spectra focuses first on the carbonate region (800 – 1800 cm^{-1}) and then on the carbonyl region (2000 – 2300 cm^{-1}).

Together with the DFT+U calculations on the formation of carbonates and formates at the CeO_2(111) surface discussed in section 4.15, three different adsorbed carbon species are identified. The bands at 1050, 1254, 1358, and 1550 cm^{-1} are assigned to formate species. The observed frequencies coincide well with the calculated frequency regions at 1017 – 1020 cm^{-1}, 1253 – 1283 cm^{-1}, 1338 – 1340 cm^{-1}, and 1580 – 1602 cm^{-1} for formates at the CeO_2(111) surface. A comparison of the experimental spectra with calculated spectra of HCO_2/CeO_{2-x}(111) seems legit as the catalyst exposes the CeO_2(111) surface (see chapter 5). The corresponding vibrational modes of formate are indicated in table 4.2. Formate species are stable as the bands are observed after treatment at 200°C and remain stable also during reaction (compare black and grey spectrum in figure 8.3). Therefore, these species are proposed to be spectator species not participating in the reaction.

The second set of bands at 1023, 1218, 1393, and 1620 cm^{-1} is assigned to hydrogen carbonate species and match the calculated regions of 999 – 1007 cm^{-1}, 1170 – 1178 cm^{-1}, 1336 – 1388 cm^{-1}, and 1608 – 1655 cm^{-1}. This species is neither present at the 200°C treated sample nor at the equilibrated sample. But during reaction a small increase is observed after equilibration and a drastical increase in intensity is observed after 200°C treatment and subsequent exposure to reaction conditions. The frequency of the ν(O-H) mode of hydrogen carbonate is predicted as 3667 cm^{-1} and is experimentally observed at 3619 cm^{-1} in agreement with the literature. [36]

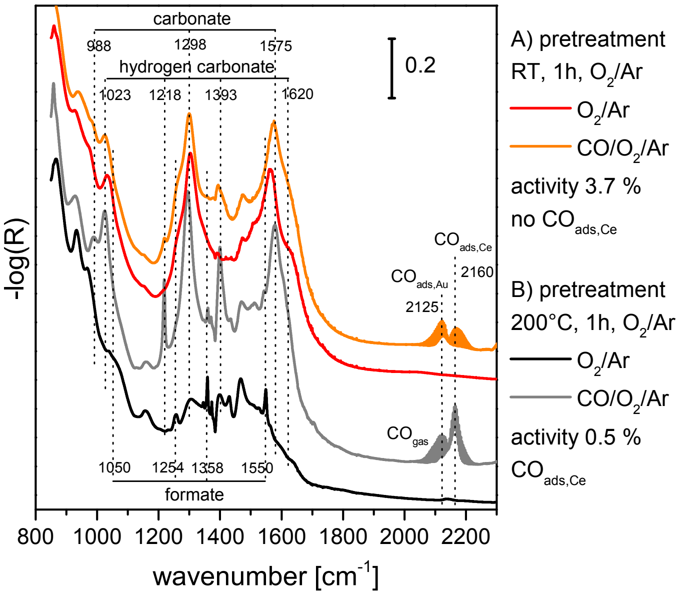

Figure 8.3.: *Operando* DRIFT spectra of a 0.5 wt% Au/CeO_2 catalyst in 25 % O_2 at 21°C recorded directly after equilibration in 25 % O_2 (pretreatment A, red) and after 30 minutes in reaction conditions, 2 % CO, 10 % O_2, (orange) and directly after 1 h at 200°C in 25 % O_2 (pretreatment B, black) and after 30 minutes in reaction conditions (grey). The spectra are offset for clarity.

Three bands at 988, 1298, and 1575 cm^{-1} are assigned to carbonate species based on the predicted frequencies of 949, 1239, and 1592 cm^{-1}. This species is present after equilibration and during reaction but not after treatment at 200°C. The assignments resemble the prior assignments from experiment [34–36] and transfer the theoretical results on a CeO_2 cluster [205] to the extended CeO_2(111) surface while coverage effects, i.e., including the effect of carbonates in direct proximity to each other, are neglected. [208]

These observations indicate that hydrogen carbonate and carbonate are the dominant species formed under reaction conditions of CO oxidation. Most probably these are formed during reaction from readsorption of the product, CO_2. [34, 35]

In a second step the spectral region of the carbonyl stretching mode (2000 – 2300 cm^{-1}) is analyzed. As indicated in figure 8.3, adsorbed CO species at Ce and Au are proposed at 2160 and 2125 cm^{-1} respectively, which are overlayed by the rotational vibrational spectrum of gas-phase CO. This spectral region is enlarged in figures 8.4 and 8.5 for pretreatment A and B, respectively. The spectra clearly show the spectral fine structure of gas-phase CO due to vibrational rotational transitions. However, CO adsorbed to the catalyst does not a exhibit rotational fine structure. For comparison the spectrum of the corresponding bare CeO_2 support in reaction conditions is shown in dark blue. No adsorption of CO can be identified at the bare support, while the center of the P- and R-*Zweig* is located at 2143 cm^{-1}.

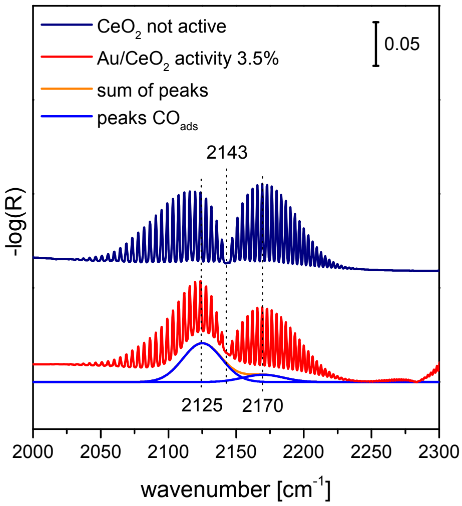

Figure 8.4.: CO stretch frequency region of the infrared spectrum of a 0.5 wt% Au/CeO_2 catalyst under reaction conditions (red) after pretreatment A, i.e., equilibration in 25 % O_2. The spectrum of gas-phase CO over a bare CeO_2 sample (dark blue) can be subtracted and the residual spectrum (orange) can be deconvolved in two components at 2170 cm^{-1} and 2125 cm^{-1}.

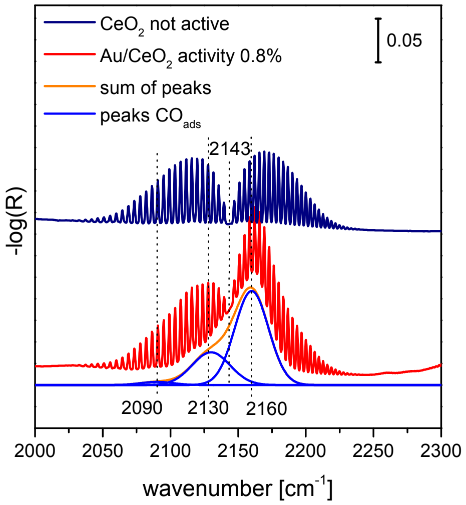

Figure 8.5.: CO stretch frequency region of the infrared spectrum of a 0.5 wt% Au/CeO_2 catalyst under reaction conditions (red) after pretreatment B, i.e., 1 h at 200°C. The spectrum of gas-phase CO over a bare CeO_2 sample (dark blue) can be subtracted and the residual spectrum (orange) can be deconvolved in three components at 2160 cm^{-1}, 2125 cm^{-1}, and 2090 cm^{-1}.

For an analysis of the adsorbed species the gas-phase CO spectrum over the bare support (dark blue) is subtracted from the spectrum of the catalyst under reaction conditions (red spectrum) and the residual spectrum (orange) is deconvolved by three components (Gauss functions). The deconvolution revealed two components for pretreatment A at 2125 cm^{-1} and 2170 cm^{-1}. After pretreatment B the high wavenumber component shifts to 2160 cm^{-1} and increases strongly and in addition to a component at 2130 cm^{-1}, a third component at 2090 cm^{-1} is observed as shown in figures 8.4 and 8.5.

So from experiment three distinct CO frequencies are observed at 2090, 2125 – 2130, and 2160 – 2170 cm^{-1}. To provide a basis for the assignment of the observed bands to a distinct CO adsorption site, a thorough DFT study was done and is discussed in the following section. The study focuses on single Au_1 and pyramidal Au_4 adsorption at the $CeO_2(111)$ surface. Afterwards the vibrational frequency of CO adsorbed to the $CeO_2(111)$ and $Au/CeO_2(111)$ model structures is analyzed in detail.

8.3 Modeling of $Au_1/CeO_2(111)$ and $Au_4/CeO_2(111)$ structures

For an assignment of the experimentally observed CO stretch frequencies, the Au/CeO_2 catalyst material is modeled first (Au adsorption at the $CeO_2(111)$ surface). Then the adsorption of CO at the model systems is studied and the CO stretch frequency is derived (see section 8.4).

First the adsorption of a single gold atom (Au_1) at the $CeO_2(111)$ surface was studied at a $CeO_2(111)$ surface slab with (2×2) periodicity. For a direct comparison the calculations were done with the PBE+U/4.5 eV functional, neglecting and including van der Waals (vdW) contributions, and with the HSE06 functional. As k-point mesh, a $(3 \times 3 \times 1)$ and $(2 \times 2 \times 1)$ Monkhorst-Pack grid [153] was employed for PBE+U/4.5 eV and HSE06 calculations, respectively. This is directly comparable to the recent literature on $Au_1/CeO_2(111)$ structures. [130, 131] The considered structures are depicted in figure 8.6 B to G and the corresponding total energies are listed in table B.10. By direct comparison the PBE+U/4.5 eV results neglecting vdW contributions resemble the results including vdW contributions in terms of structure and adsorption energy. In the following the results which neglect vdW contributions are discussed in-depth.

A transfer of the $6s^1$ electron of gold to the $CeO_2(111)$ surface is predicted and the excess charge is localized at a cerium ion forming Ce^{3+}. [131] Two different adsorption structures are identified, the Au^+ adsorption on top of a surface oxygen ion (Au@O, figure 8.6 B and C) and at a bridged position between two surface oxygen ions (O-O bridge, figure 8.6 F and G). For both structures the excess charge can be localized in nearest (NN) or next nearest neighbor position (NNN) to the gold ion. The O-O bridged position is by 100 − 200 meV more stable than the Au@O position. The NNN Ce^{3+} configuration is again by 50 − 150 meV more stable, resulting from the calculated adsorption energies of $E_{\text{ads,Au}} = -0.966$ eV (Au@O, Ce^{3+} NN), −1.017 eV (Au@O, Ce^{3+} NNN), −1.061 eV (O-O bridge, Ce^{3+} NN), and −1.209 eV (O-O bridge, Ce^{3+} NNN). The adsorption energy for Au and Ce^{3+} localization in NNN configuration can be compared to those in the literature (Au@O, $E_{\text{ads,Au}} = -1.04$ eV and O-O bridge, −1.18 eV; [63] Au@O, −1.07 eV and O-O bridge, −1.20 eV [131]) and show excellent consistency.

For comparison and validation the calculations were repeated with the HSE06 functional. With this functional no charge transfer from gold to the surface is predicted for a Au@O adsorption resulting in a $Au_1{}^0/CeO_2(111)$ structure (see figure 8.6 D). The adsorption energy is calculated as $E_{\text{ads,Au}} = -0.483$ eV in full accordance with the literature. [131] Furthermore, with the HSE06 functional a Au@O structure was found, in which gold possesses a Au^+ state and the Ce^{3+} locates in a NNN position (figure 8.6 C). The adsorption energy is calculated as $E_{\text{ads,Au}} = -0.503$ eV, i.e., this structure is more stable than the Au^0 structure. A gold atom adsorbed to the Ce bridge position (figure 8.6 E) was found to not transfer an electron to the surface as well. The adsorption energy for this structure is calculated as $E_{\text{ads,Au}} = -0.531$ eV. However, a charge transfer is predicted for Au adsorbed at the O-O bridge position. The configuration in which Ce^{3+} is located in NN position is less stable ($E_{\text{ads,Au}} = -0.437$) eV [131] than the configuration in which Ce^{3+} is located in NNN position ($E_{\text{ads,Au}} = -0.587$ eV). The adsorption at the O-O bridge position with Ce^{3+} in NNN position is the $Au_1/CeO_2(111)$ structure that is predicted as the most stable one although the others are close in energy. These discussed $Au_1/CeO_2(111)$ structures are considered as the starting points for CO adsorption described in the following section.

Furthermore, it is briefly reported on the Au adsorption at the reduced $CeO_{2-x}(111)$ surface with a surface oxygen vacancy. The location of Au adsorption at the $CeO_{2-x}(111)$ surface with a subsurface

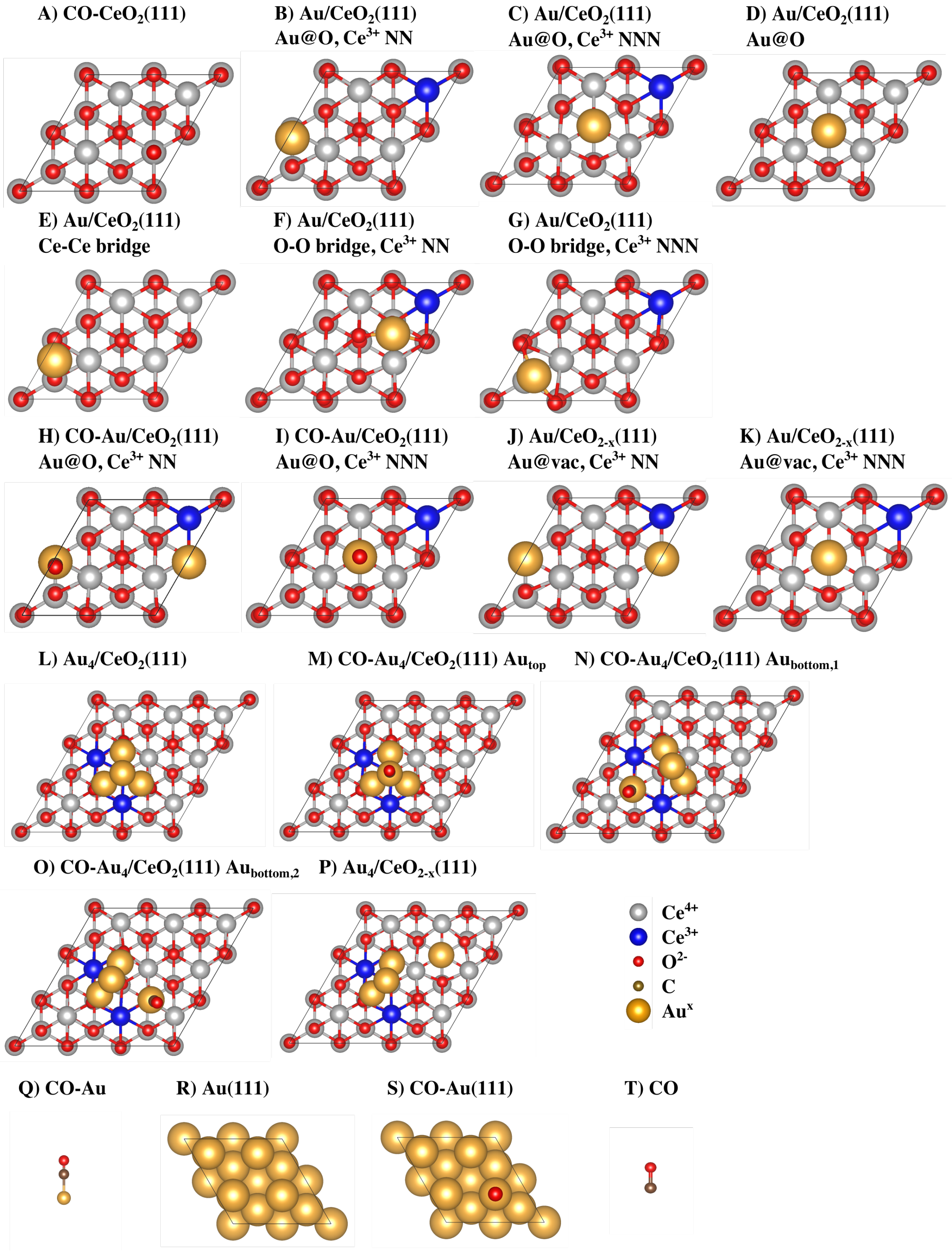

A) CO-CeO_2(111)

B) Au/CeO_2(111) Au@O, Ce^{3+} NN

C) Au/CeO_2(111) Au@O, Ce^{3+} NNN

D) Au/CeO_2(111) Au@O

E) Au/CeO_2(111) Ce-Ce bridge

F) Au/CeO_2(111) O-O bridge, Ce^{3+} NN

G) Au/CeO_2(111) O-O bridge, Ce^{3+} NNN

H) CO-Au/CeO_2(111) Au@O, Ce^{3+} NN

I) CO-Au/CeO_2(111) Au@O, Ce^{3+} NNN

J) Au/CeO_{2-x}(111) Au@vac, Ce^{3+} NN

K) Au/CeO_{2-x}(111) Au@vac, Ce^{3+} NNN

L) Au_4/CeO_2(111)

M) CO-Au_4/CeO_2(111) Au_{top}

N) CO-Au_4/CeO_2(111) $Au_{bottom,1}$

O) CO-Au_4/CeO_2(111) $Au_{bottom,2}$

P) Au_4/CeO_{2-x}(111)

Q) CO-Au

R) Au(111)

S) CO-Au(111)

T) CO

Figure 8.6.: CO adsorbed to CeO_2(111) A), Au adsorbed on top of O (Au^+@O) with Ce^{3+} in NN B) and NNN C) position, Au^0@O D), Au^0 adsorbed in Ce bridged position E), Au^+ in O-O bridged with Ce^{3+} in NN F) and NNN G) position. CO adsorbed to Au/CeO_2(111) structures CO-Au@O with Ce^{3+} in NN H) and NNN I) position. Au^- adsorbed to CeO_{2-x}(111) surface with Ce^{3+} in NN J) and NNN K) position. Stable Au_4/CeO_2(111) structure L), CO adsorbed to Au_4/CeO_2(111) in top M), bottom (1) N) and bottom (2) O) position. Au_4 adsorbed to CeO_{2-x}(111). Au-CO in the gas-phase Q), Au(111) surface R), CO adsorbed to Au(111) in top position S), and gas-phase CO T).

oxygen vacancy is debated [129–131] but for a surface oxygen vacancy only the adsorption into the defect has been reported, [63,67] although a formation of this structure has been found to be kinetically hindered. [256] The considered structures are depicted in figure 8.6 J and K and possess an adsorption energy of $E_{\mathrm{ads,Au}} = -2.196$ eV (PBE+U/4.5 eV) for Ce^{3+} in NN position and −2.439 for Ce^{3+} in NNN position.

With respect to a three-dimensional gold particle adsorbed to the $CeO_2(111)$ surface, a pyramidal configuration of Au_4 is predicted for the $CeO_2(111)$ [64,132] and the reduced $CeO_{2-x}(111)$ surface. [255]. The $CeO_2(111)$ surface slab with (3 × 3) periodicity was modeled with a (2 × 2 × 1) and (1 × 1 × 1) k-points grid for calculations employing the PBE+U/4.5 eV and HSE06 functional, respectively. Both functionals predict a transfer of 2 e^- from the Au_4 cluster to the $CeO_2(111)$ surface. For the excess charge localization and gold adsorption site, 17 Ce^{3+} configurations were tested with the PBE+U/4.5 eV functional of which the structure in figure 8.6 L shows the highest stability (see also table B.11). In this configuration the excess charge localizes in nearest neighbor positions of the Au_4 cluster. The bottom three $Au^{\delta+}$ atoms interact with the oxygen ions of the $CeO_2(111)$ surface, while the gold atom on the top is practically not charged (Au^0). [64]

As for the $Au_1/CeO_2(111)$ structure a reduced $CeO_{2-x}(111)$ surface and adsorption of a Au^- anion in the vacancy was modeled corresponding to a ${Au_3}^{2+}{Au_1}^{-}/CeO_{2-x}(111)$ structure as depicted in figure 8.6 P. The remaining ${Au_3}^{2+}$ cluster stays in upright configuration. This allows the calculation of the energy ΔE_0 for CO oxidation by a lattice oxygen at a Au/CeO_2 model system.

8.4 Modeling of the CO adsorption and stretch frequency at the $CeO_2(111)$, $Au_1/CeO_2(111)$, $Au_4/CeO_2(111)$ and Au(111) structures

At the $Au_1/CeO_2(111)$ structures CO adsorption was studied with the PBE+U/4.5 eV functional, neglecting and including vdW contributions, and with the HSE06 functional. For the $Au_1/CeO_2(111)$ structure CO adsorption at the gold atom and the formation of a Au^+-CO structure is observed, regardless of the starting structure (Au@O, O-O bridge, or Ce bridge) and the charge state of gold $Au^{+/0}$. The CO molecule is adsorbed on top of the Au^+ ion orthogonal to the $CeO_2(111)$ surface forming a linear O_{lattice}-Au^+-CO species. The resulting structures only differ in the Ce^{3+} configuration. In figure 8.6 H the O_{lattice}-Au^+-CO and Ce^{3+} are in NN configuration and in figure 8.6 I in NNN configuration. The adsorption energy is calculated with respect to the most stable $Au_1/CeO_2(111)$ structure, i.e., Au@O-O bridge and Ce^{3+} in NNN position. In the stable configuration the electron localizes at Ce^{3+} in NNN position with an adsorption energy of $E_{\mathrm{ads,CO}} = -2.505$ eV, −2.555 eV, and −2.428 eV compared to the localization in NN position with an adsorption energy of $E_{\mathrm{ads,CO}} = -2.406$ eV, −2.461 eV, and −2.299 eV calculated with PBE+U/4.5 eV, PBE+U/4.5 eV+vdW, and HSE06 functional, respectively.

For CO adsorption at the $Au_4/CeO_2(111)$ cluster three different adsorption sites are possible. The adsorption on the topmost gold atom (Au_{top}) revealed an adsorption energy of $E_{\mathrm{ads,CO}} = -0.922$ eV and −0.768 eV for PBE+U/4.5 eV and HSE06 functional, respectively, and a linear adsorption geometry on top of the gold cluster (structure in figure 8.6 M). Furthermore, CO adsorption to $Au_{\mathrm{bottom,1}}$, i.e., the Au atom with two Ce^{3+} in NN position, is calculated to be more stable than adsorption to Au_{top} with an adsorption energy of $E_{\mathrm{ads,CO}} = -1.366$ eV and −1.257 eV for the PBE+U/4.5 eV and HSE06 functional.

Interestingly, the Au atom at which CO is adsorbed is abstracted from the remaining Au_3 cluster forming a *pseudo single Au site*, i.e., an $O_{lattice}$-Au^+-CO species slightly abstracted from the gold particle (see figure 8.6 N). The second $Au_{bottom,2}$ adsorption site where the Au atom for adsorption is located between Ce^{3+} and Ce^{4+} is predicted to be the most stable adsorption site with $E_{ads,CO} = -1.397$ eV and -1.289 eV. During CO adsorption at one of the bottom Au the remaining Au_3 cluster remains upright.

For a Au_{20} cluster adsorbed at the $CeO_2(111)$ surface, an adsorption energy of $E_{ads,CO} = -1.44$ eV was calculated together with the above mentioned formation of an abstracted $O_{lattice}$-Au^+-CO species in the literature. [67] And the CO adsorption energy to a gold atom of a Au_{13} cluster at the Au/CeO_2 interface was calculated as $E_{ads,CO} = -1.28$ eV. [65] It should be noted that in the latter study the Au-CO species is neither in direct contact with the CeO_2 support nor abstracted from the gold particles. [65] However, the adsorption energy is in good agreement with results obtained here. For comparison with the literature [67] the net difference in the total energy ΔE_0 for the CO oxidation reaction at the Au_4 cluster with a lattice oxygen is calculated from the PBE+U/4.5 eV total energies.

$$\text{CO-Au}_4/\text{CeO}_2(111) \rightarrow \text{Au}_3^{2+}\text{Au}_1^{-}/\text{CeO}_{2-x}(111) + \text{CO}_2 \quad \Delta\text{E}_0 = -0.89 \text{ eV} \tag{8.1}$$

The value of $\Delta E_0 = -0.89$ eV agrees well with the value of -0.95 eV for a Au_{20} cluster adsorbed to the $CeO_2(111)$ surface. [67] This shows that the concept of the "*dynamic formation of single-atom catalytic active sites*" [67] of larger gold particles is transferable to the smaller Au_4 cluster which is capable for vibrational analysis.

Besides the adsorption onto the gold/ceria structures, the adsorption of CO onto the clean $CeO_2(111)$ surface was modeled (see figure 8.6 A). CO adsorbs linearly on top of a Ce^{4+} ion. The adsorption energy is calculated as $E_{ads,CO} = -0.186$ eV, -0.281 eV, and -0.150 eV for PBE+U/4.5 eV, PBE+U/4.5 eV+vdW, and HSE06 functional, in agreement with previous studies. [121, 123]

In addition, the adsorption of CO on top of a Au atom of the Au(111) surface is studied. The adsorption energy is calculated as $E_{ads,CO} = -0.082$ eV with the PBE+U/4.5 eV and -0.873 eV with the HSE06 functional. Experimental results also show adsorption at the top site as illustrated in figure B.11 S with an adsorption energy of $E_{ads,CO} = -0.34$ eV for the Au(111) surface and adsorption to a Au/Au(111) surface of -1.151 eV as calculated by DFT methods without specifying the employed functional. [258] However, this is in good agreement with the adsorption energy of CO at the top site of the $Au_4/CeO_2(111)$ surface of $E_{ads,CO} = -0.922$ eV. The stabilization of low coordinated Au at the Au(111) surface has been observed before. [259] This corresponds to the pyramidal formation of Au_4 cluster in the considered model system.

For a thorough analysis of the vibrational frequency of CO adsorbed at the model systems, an isolated CO molecule is studied as a benchmark first. Therefore the same parameters of Yang *et al.* [124] are used to model isolated CO, including vdW contributions with the PBE+U/4.5 eV functional, employing a finite differences approach, and four displacements for each coordinate (NFREE = 4). The stretch frequency of CO is calculated as 2122.0 cm^{-1}. This compares to the value of 2122.5 cm^{-1} as reported by Yang *et al.* [124] with a difference of only 0.5 cm^{-1}. For the following calculations only two displacements per coordinate were considered (NFREE = 2). This shifts the predicted stretch frequency to 2124.5 cm^{-1} (including vdW contributions) and 2121.9 cm^{-1} (neglecting vdW contributions). With the HSE06 functional the frequency is predicted as 2235.7 cm^{-1}. The values are summarized in table 8.1 and the frequency of gas-phase CO ($\tilde{\nu}_{\text{CO}}$) is considered as the reference frequency to which frequencies of adsorbed CO are compared ($\Delta\tilde{\nu}_{\text{CO,gas}}$). It is proceeded identically for the experimental results in the bottom row of table 8.1. The frequency of the stretching mode of gas-phase CO from experiment is 2143 cm^{-1} as shown in figure 8.4.

First the vibrational properties of the CO-CeO_2(111) structure is discussed. Within PBE+U/4.5 eV framework the stretch frequency of CO adsorbed to the CeO_2(111) surface is predicted as 2126.2 cm^{-1} and 2129.5 cm^{-1}, neglecting and including vdW contributions, respectively. This corresponds to a blueshift of $\Delta\tilde{\nu}_{\text{CO,gas}}$ = +4.3 cm^{-1} and +5.0 cm^{-1} with respect to isolated gas-phase CO. The shift is smaller than the one reported in previous studies. [121,124] With the HSE06 functional the frequency is predicted as 2250.7 cm^{-1} resulting in a blueshift of +15 cm^{-1}.

In table 8.1 the structures are sorted with respect to the CO stretch frequency starting with the highest frequency that was obtained. All structures, in which CO is adsorbed to gold, exhibit a redshifted frequency with respect to the frequency of isolated CO ($\Delta\tilde{\nu}_{\text{CO,gas}} < 0$). For the Au_1/CeO_2(111) structures possessing an isolated Au_1 atom adsorbed at the CeO_2(111) surface, a stretch frequency of 2094.6 cm^{-1} and 2091.5 cm^{-1} is predicted for the configurations with Ce^{3+} in NN and NNN position, respectively. This corresponds to a redshift of $\Delta\tilde{\nu}_{\text{CO,gas}}$ = −27.3 cm^{-1} and −30.4 cm^{-1}. In general the PBE+U/4.5 eV functional including vdW contributions resemble the frequencies calculated with the same functional neglecting vdW contributions by ±3 cm^{-1}. Therefore vdW contributions are neglected in the following and only the results obtained with the PBE+U/4.5 eV and HSE06 functional are discussed. The CO-Au_1/CeO_2(111) structures reveal a stretch frequency of 2219.4 cm^{-1} and 2217.2 cm^{-1} with the HSE06 functional corresponding to a redshift with respect to the frequency of isolated CO of $\Delta\tilde{\nu}_{\text{CO,gas}}$ = −16.3 cm^{-1} and −18.5 cm^{-1}.

In the CO-Au_4/CeO_2(111) structure an $\text{O}_{\text{lattice}}$-$\text{Au}^{+}$-CO species is formed when CO is adsorbed to one of the Au atoms interacting with the CeO_2(111) surface (bottom). The CO stretch frequency is calculated as 2086.3 cm^{-1} and 2085.5 cm^{-1} for $\text{O}_{\text{lattice}}$-$\text{Au}^{+}$-CO with two Ce^{3+} in NN ($\text{Au}_{\text{bottom,1}}$) and one Ce^{3+} in NN ($\text{Au}_{\text{bottom,2}}$) position, respectively. This is only slightly redshifted (5 − 8 cm^{-1}) compared to the isolated CO-Au_1/CeO_2(111) structures. With the hybrid functional the difference in frequencies is slightly smaller amounting to only 2.5 − 6.5 cm^{-1}. In contrast, adsorption to the top Au atom of the Au_4 cluster (Au_{top}) revealed a stretch frequency of 2069.2 cm^{-1} (PBE+U/4.5 eV) and 2199.4 cm^{-1} (HSE06). This relates to $\Delta\tilde{\nu}_{\text{CO,gas}}$ = −52.4 cm^{-1} (PBE+U/4.5 eV) or −36.3 cm^{-1} (HSE06).

For comparison the stretch frequency of CO adsorbed to a single isolated Au and onto the Au(111) surface was calculated. While the frequency of the isolated Au-CO resembles the frequency of CO adsorbed to the Au_4 top site, adsorption to the Au(111) reveals a frequency of 2045.3 cm^{-1} (PBE+U/4.5 eV) and 2141 cm^{-1} (HSE06). The redshift with respect to isolated CO is considerably larger with the HSE06 functional ($\Delta\tilde{\nu}_{\text{CO,gas}}$ = −95 cm^{-1}) than with the PBE+U/4.5 eV functional ($\Delta\tilde{\nu}_{\text{CO,gas}}$ = −76.6 cm^{-1}). This might be due to the known shortcoming of semi-local functionals for calculations of metal surfaces. [260] However, for CO adsorbed to a gold surface a frequency of 2060 cm^{-1} was observed by reflection absorption infrared spectroscopy (RAIRS) and assigned to low coordinated Au atoms at the surface. [258]

Table 8.1.: Summary of CO stretch frequency $\tilde{\nu}_{CO}$ with respect to CO in the gas-phase ($\Delta\tilde{\nu}_{CO_{gas}}$) with PBE+U/4.5 eV, PBE+U/4.5 eV including vdW contributions and HSE06 functional. CO adsorbed to $CeO_2(111)$, to $Au_1/CeO_2(111)$, to $Au_4/CeO_2(111)$, to isolated Au_1 and to the Au(111) surface. For $Au_1/CeO_2(111)$ two Ce^{3+} configurations and for $Au_4/CeO_2(111)$ the three non equivalent adsorption sites (top, bottom and bottom,2) are considered. For [a] and [b] see table B.11.

Structure	CO/ $CeO_2(111)$	CO isolated	CO-Au^+/ $CeO_2(111)$ Ce^{3+} NN	CO-Au^+/ $CeO_2(111)$ Ce^{3+} NNN	CO-$Au_4{}^{2+}$/ $CeO_2(111)$ 2 Ce^{3+} NN	CO-$Au_4{}^{2+}$/ $CeO_2(111)$ 1 Ce^{3+} NN	CO-$Au_4{}^{2+}$/ $CeO_2(111)$	CO-Au isolated	CO Au(111)
	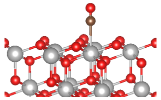		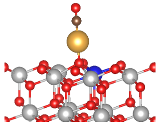	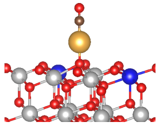	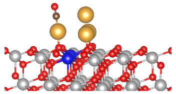	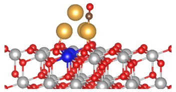	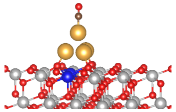	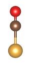	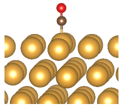
PBE+U/4.5 eV									
$E_{ads,CO}$ [eV]	−0.185		−2.406	−2.505	−1.366	−1.397	−0.922	−0.812	−0.082
$\tilde{\nu}_{CO}$ [cm^{-1}]	2126.2	2121.9	2094.6	2091.5	2086.3	2085.5	2069.5	2068.8	2045.3
$\Delta\tilde{\nu}_{CO,gas}$ [cm^{-1}]	+4.3	0	−27.3	−30.4	−35.6	−35.4	−52.4	−53.1	−76.6
PBE+U/4.5 eV+vdW contributions									
$E_{ads,CO}$ [eV]	−0.281		−2.461	−2.555					
$\tilde{\nu}_{CO}$ [cm^{-1}]	2129.5	2124.5	2094.5	2094.2					
$\Delta\tilde{\nu}_{CO,gas}$ [cm^{-1}]	+5.0	0	−30.0	−30.3					
HSE06									
$E_{ads,CO}$ [eV]	−0.150		−2.299	−1.428	−1.257	−1.289	−0.768	−0.407	−0.873
$\tilde{\nu}_{CO}$ [cm^{-1}]	2250.7	2235.7	2219.4	2217.2	2214.7	2213.9	2199.4	2197.5 [a]	~2141 [b]
$\Delta\tilde{\nu}_{CO,gas}$ [cm^{-1}]	+15.0	0	−16.3	−18.5	−21.0	−21.8	−36.3	−38.2	−95
Experimental									
$\tilde{\nu}_{CO}$ [cm^{-1}]	2160	2143	~2130		-	~2125	~2090		2060 [258]
$\Delta\tilde{\nu}_{CO,gas}$ [cm^{-1}]	+17	0	−13		-	−18	−53		−83

8.5 Discussion

The analysis of the CO stretch frequency at various adsorption sites of the Au/CeO_2 model catalysts by DFT calculations provide the basis for the assignment of the components in the carbonyl region of the *operando* infrared spectra measured at a 0.5 wt% Au/CeO_2 catalyst (see figures 8.4 and 8.5).

The assumption of a $CeO_2(111)$ surface for the DFT calculations is justified as by TEM and Raman spectroscopy a $CeO_2(111)$ surface facet of the support is evidenced (see ceria sheets in chapter 5). Furthermore, it is shown by continuous *operando* Raman spectroscopy that the surface is only slightly reduced under reaction conditions (see the minor change in intensity of the longitudinal surface mode at 246 cm^{-1} under reaction conditions in chapter 7). The existence of three-dimensional gold particles is shown by TEM images in chapter 7.

Therefore, the three components in the carbonyl region are assigned to the CO-$CeO_2(111)$, the CO-$Au_{x,\mathrm{bottom}}{}^{+}/CeO_2(111)$, and the CO-$Au_{\mathrm{top}}{}^{0}/CeO_2(111)$ structure. These refer to CO adsorbed at the ceria support, the formation of the O_{lattice}-Au^{+}-CO species, and CO adsorbed to a three-dimensional particle on the top site of the Au_4 cluster, respectively. The corresponding experimental frequencies are $2160 - 2170$ cm^{-1} for CO-$CeO_2(111)$, $2125 - 2130$ cm^{-1} for CO-$Au_{x,\mathrm{bottom}}{}^{+}/CeO_2(111)$, and 2090 cm^{-1} for CO-$Au^{0}/CeO_2(111)$ structure. The experimentally observed frequencies are blueshifted by $\Delta\tilde{\nu}_{\mathrm{CO,gas}} = +17$ cm^{-1} and redshifted by -18 cm^{-1} and -53 cm^{-1} with respect to gas-phase CO. These shifts compare extraordinarily well to the calculated frequency shifts of the calculations with the HSE06 functional of $+15.0$ cm^{-1}, -16.3 to -21.8 cm^{-1} and -36.3 cm^{-1} and the PBE+U/4.5 eV functional (see table 8.1). So the experimental bands are assigned to model structures based on the red or blueshift of the measured and predicted frequency with respect to that of gas-phase CO.

The intensity of the components at $2160 - 2170$ cm^{-1}, $2125 - 2130$ cm^{-1}, and 2090 cm^{-1} was followed over time for the two pretreatment procedures discussed in section 8.2 (see figures C.3 and C.4). The intensity is shown together with the catalytic activity of the Au/CeO_2 sample. As the activity and the intensity of the components were measured every minute the activity can be directly correlated to the components of the deconvolution analysis (dynamic *operando* spectroscopy).

In figure 8.7 the activity of the catalyst (y-axis) is plotted against the integrated intensity of the component at $2125 - 2130$ cm^{-1} (x-axis). Thus, correlating the catalytic activity directly to the spectroscopic information (band intensity). From this graph the temporal evolution can not be drawn and for clarity the temporal evolution is indicated by the arrows, showing a fast activation for the non-preheated sample (pretreatment A) and slow activation for the preheated sample (pretreatment B). Based on the assumption of a proportionality between the band intensity and the concentration of the corresponding species a direct relation between the O_{lattice}-Au^{+}-CO species and the activity is proposed (see dashed line in figure 8.7). This behavior can be rationalized as the O_{lattice}-Au^{+}-CO species has been proposed as the intermediate species, formed after CO adsorption to a gold particle at the $CeO_2(111)$ surface in several DFT+U studies. [63, 64, 67] In these studies the adsorption is followed by the oxidation of adsorbed CO with lattice oxygen. However, this is an endothermic process because an oxygen vacancy needs to be created (compare calculated vacancy formation energy $E_{\mathrm{vac,O}}$ in section 4.5). In general the endothermic reaction step associated with the highest energy barrier in a reaction mechanism is called the rate determining step (RDS). The intermediate species created before the RDS, in this case the $O_{lattice}$-Au-CO species, can be agglomerated. Therefore a direct correlation of the species with the activity is reasonable.

Please note that this is the first spectroscopic evidence for this species to form the active species for the CO oxidation over Au/CeO_2 catalysts on the basis of dynamic infrared spectroscopy and a thorough DFT study on the CO stretching frequency of adsorbed CO at the Au/CeO_2 catalyst surface.

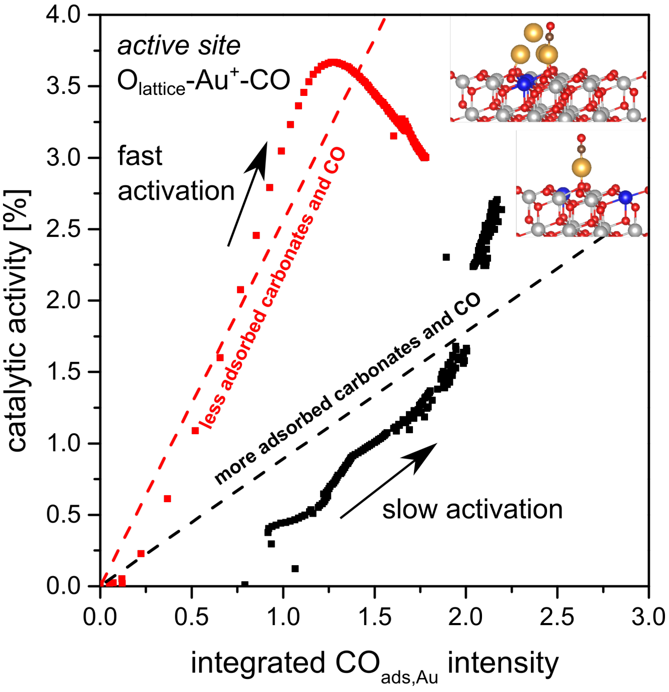

Figure 8.7.: The intensity of CO adsorbed to Au^+/CeO_2 (2125 — 2130 cm^{-1}) is correlated with the corresponding activity of the Au/CeO_2 catalyst for pretreatment A (equilibration in 25 % O_2, red) and B (1 h at 200°C in 25 % O_2, black) The dashed lines are a rough interpolation indicating the direct correlation of the adsorbed species and catalytic activity (*active species*). The black line refers to an increased carbonate and CO concentration and the red line to a lowered carbonate and CO concentration. For details see text.

The fact that depending on the pretreatment the slope of the dashed lines in figure 8.7 is different shows that the activity is not solely governed by the concentration of the $O_{lattice}$-Au^+-CO species. In the same manner as before the activity is plotted against the intensity of the components at 2160 — 2170 cm^{-1} (see figure 8.8). Clearly this relation is antiproportional as visualized by the dashed line. For the non-preheated sample hardly any intensity is observed at 2160 — 2170 cm^{-1}, whereas for a preheated catalyst the intensity of the species slowly decreases during activation of the catalyst. Obviously the species assigned to this frequency range (CO adsorbed to the $CeO_2(111)$ surface) has an inhibiting effect on the catalytic activity. Till now, the observation of adsorbed CO to the $CeO_2(111)$ catalyst surface as an inhibiting species has not been reported in the literature.

A comparable behavior is observed for hydrogen carbonate species by evaluating the intensity of the band at 1218 cm^{-1} and correlating it to the activity (see figure 8.9). This band is assigned to the bending mode δ(COOH) of hydrogen carbonate (see section 4.15). Initially only a small intensity is observed for the non-preheated sample which increases slowly upon deactivation of the catalyst. For the preheated sample initially the highest intensity of the band is observed corresponding to the highest concentration

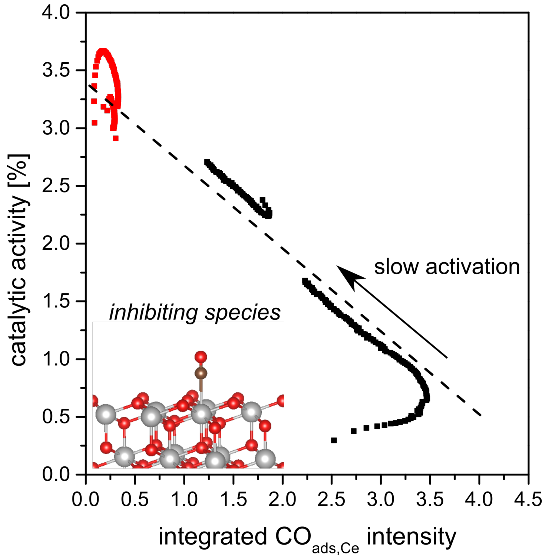

Figure 8.8.: The intensity of the band assigned to an adsorbed CO species at Ce of the $CeO_2(111)$ surface (2160 − 2170 cm^{-1}) is correlated to the corresponding activity of the Au/CeO_2 catalyst for pretreatment A (equilibration in 25 % O_2, red) and B (1 h at 200°C in 25 % O_2, black). The dashed line indicates an inverse correlation of this species with the catalytic activity (*inhibiting species*).

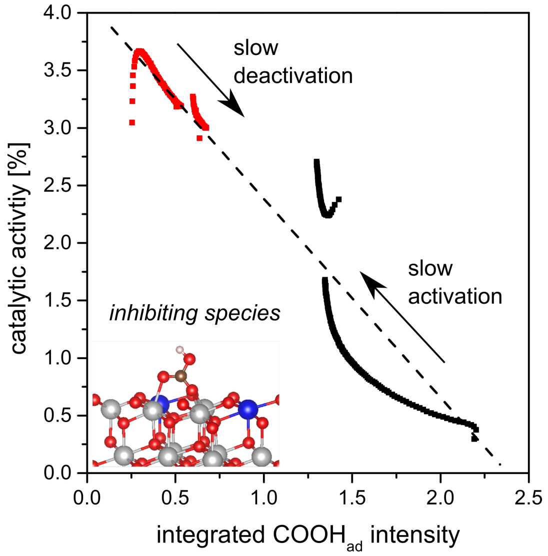

Figure 8.9.: The intensity of the band assigned to hydrogen carbonate (1218 cm^{-1}) is correlated to the corresponding activity of the Au/CeO_2 catalyst for pretreatment A (equilibration in 25 % O_2, red) and B (1 h at 200°C in 25 % O_2, black). Dashed line indicates an inverse correlation of this species with the catalytic activity (*inhibiting species*).

of hydrogen carbonate at the catalyst. Please note that the highest concentration of hydrogen carbonate is observed at the least CO_2 gas-phase concentration. This clearly shows that readsorption of CO_2 from the gas-phase is rather governed by the accessible adsorption sites, than by the gas-phase concentration of CO_2. The concentration of hydrogen carbonate reduces, while the catalyst becomes active. An inhibiting effect by hydrogen carbonate [37] and carbonate species [38] at the surface has been proposed before, although this was not concluded from *operando* infrared spectroscopy in a time-resolved manner.

8.6 Conclusions

Summarizing, a linear $O_{lattice}$-Au^+-CO species is shown to directly correlate with the catalytic activity of a 0.5 wt% Au/CeO_2 catalyst. This provides the first spectroscopic evidence for the existence of an isolated $O_{lattice}$-Au^+-CO species that either results from adsorption at a single Au site or the Au is abstracted from a three dimensional gold particle. The assignment of the corresponding CO stretch frequency at 2125 − 2130 cm^{-1} is based on DFT calculations which provide a robust picture of CO adsorption sites and the CO stretch frequency employing a PBE+U/4.5 eV and HSE06 functional.

In addition, two regimes of catalytic activity can be observed. One in which adsorbed hydrogen carbonate and CO is rare at the surface (red dashed line in figure 8.7) with a higher catalytic activity and one in which hydrogen carbonate and CO is present at the surface (black dashed in figure 8.7). Therefore, adsorbed CO and hydrogen carbonate are proposed as inhibiting species for the CO oxidation over Au/CeO_2 catalysts.

9 Water-gas Shift Reaction over Au/CeO$_2$ Catalysts: The Perspective of *Operando* Raman Spectroscopy

The water-gas shift reaction (see reaction equation 9.1) is important for the production of hydrogen that is used for ammonia or methanol synthesis or that needs to be purified for the use in fuel cells. [26] Technically iron-chromia catalysts at temperatures up to ~720 K (high temperature shift, HTS) and copper-zinc catalysts at temperatures below ~520 K (low temperature shift, LTS) are employed for the water-gas shift reaction. For a detailed review on the technical details the reader is referred to reference [26]. Gold/ceria is a robust alternative catalyst. [19] It was shown that small amounts (<0.5 wt%) of gold supported on a ceria containing support catalyze the reaction at temperatures as low as 473 K with a slightly lower rate than copper-zinc catalysts. [19] For review articles on gold catalysis refer to [210, 237, 261].

$$CO + H_2O \rightleftharpoons CO_2 + H_2 \quad \Delta H^0 = -41.2\ \mathrm{kJ\ mol^{-1}} \tag{9.1}$$

For the water-gas shift reaction over metal/oxide catalysts a formate mechanism has been proposed for Rh/CeO$_2$ catalysts. This means that a formate intermediate is formed during reaction. [41,42,69] On the basis of infrared spectroscopy the formate mechanism has been proposed for Au/CeO$_2$ catalysts as well. [43, 44] The formation of formates was rationalized by CO insertion into terminal hydroxyl (OH) groups under reaction conditions. However, decomposition of formate adsorbed at a Au/CeO$_2$ catalyst could only account for <10 % of the CO$_2$ evolution and therefore the formate mechanism was questioned. [70] Burch *et al.* critically reviewed the studies proposing a formate mechanism and concluded that the experimental results "*cannot be used to provide any mechanistic information either for or against a formate model*" [71]. A redox type mechanism, i.e., the dynamic formation of oxygen vacancies in the presence of oxidized gold particles has been proposed by Fu *et al.* [19]

DFT+U studies have been briefly reviewed by Paier *et al.* [100] and the formate and redox mechanisms were analyzed in detail by density functional theory before. [72] The authors found that the barrier for OH-bond breaking in the redox mechanism is too high for a catalytic reaction. And in the formate mechanism the step of OH-bond cleavage has a barrier of >1eV. Therefore the key step was proposed to be the surface oxygen regeneration from terminal hydroxyl groups. This corresponds to the formation of lattice oxygen ions (O^{2-}) from hydroxyl groups. A more recent DFT study by the same author proposed a carboxyl mechanism. It is described, that during reaction of CO at the Au cluster with a surface hydroxyl group a carboxyl molecule is formed. This carboxyl molecule reacts with a hydroxyl group to form CO$_2$, while H$_2$ combines and desorbs from the gold particles. [73] Near ambient pressure X-ray photoelectron spectra show a carboxyl species at CeO$_{2-x}$/Au(111) inverse catalysts. [74] The reactions proceeding via formate or carboxylate intermediates are called associate mechanisms, opposite to redox type mechanisms. [74, 262, 263]

Metal (Au) free ceria, more precisely ceria exposing the $CeO_2(100)$ surface facet, was found to be active in the water-gas shift reaction above 500 K. The reactivity was ascribed to the reduced ceria sites. [264] Recently, nanoparticle cubes were found to perform with doubled activity compared to particles and rods in the reverse water-gas shift reaction. [233]

In the literature no *operando* Raman study of Au/CeO_2 catalysts under water-gas shift reaction conditions has been reported. Therefore *operando* Raman spectroscopy was applied to a 0.5 wt% Au/CeO_2 catalyst and the corresponding bare ceria support. Idealized water-gas shift reaction conditions of 2 % CO and 8 % or 10 % H_2O with argon as carrier gas were employed. The aim is to gain insight into the reaction mechanism of the water-gas shift reaction at Au/CeO_2 catalysts. Thus, the $H_2{}^{18}O$ isotope was employed as reactant because ^{18}O exchange alters the vibrational properties of ceria which can be probed by *operando* Raman spectroscopy. Therefore *dynamic operando* Raman spectra during the initial exposure of a $Au/Ce^{16}O_2$ catalyst to water-gas shift reaction conditions of 2 % and 8 % $H_2{}^{18}O$ are reported.

Please note that besides the incorporation of the ^{18}O isotope in the CO_2 product ($C^{16}O^{18}$) explicitly the incorporation into the ceria lattice is probed by *operando* Raman spectroscopy due to the altered vibrational properties of an ^{18}O doped ceria lattice (see figure 4.7 for the calculated properties of a $Ce^{18}O_2(111)$ surface slab).

9.1 Experimental

As catalyst material the 0.5 wt% Au/CeO_2 catalyst was employed, that is throughly characterized in chapter 7. The ceria support exposes the $CeO_2(111)$ surface facet as evident from combined TEM and Raman spectroscopy analysis in chapter 5. For the *operando* experiments the gas-phase composition was mixed by digital mass flow controllers and the controlled liquid evaporation unit as schematically shown in figure A.1 of the appendix. The gas-phase concentration of CO was 2 vol% (abbreviated as % in the following). The gas stream was always balanced with argon to yield a total flow of 100 ml/min. For 8 % or 10 % H_2O concentration in the gas-phase 0.384 or 0.480 g/h deionized water (electric conductivity $< 3\ \mu S\ m^{-1}$) was dosed through the liquid mass flow meter and evaporated into the (CO)/Ar stream by a controlled evaporation mixer. To dose 8 % $H_2{}^{18}O$ into the gas stream 0.422 g/h $H_2{}^{18}O$ (97 %+ ^{18}O, euriso-top®) were evaporated.

The gas-phase was analyzed by infrared spectroscopy as described in section 2.1 and figure 9.1 depicts the gas-phase composition over time. An infrared spectrum was measured every minute and the gas-phase composition was determined.

For an *operando* experiment, the catalyst was first transferred to the reaction chamber and an *ex situ* Raman spectrum was recorded. During the measurement the bypass (see figure A.1) and the infrared gas cell was cleaned with 100 ml/min argon. Then the background spectrum $I_{\lambda,0}$ for the gas-phase analysis was recorded assuming no residual CO_2, CO, and H_2O in the gas cell. This was confirmed as this spectrum (baseline, no absorption) did not change over time (5 minutes, 5 spectra). The argon stream was applied to the reaction chamber and the sample was heated to 120°C. Residual CO_2 and H_2O were cleaned from the cell and desorbed from the sample during heating (see increased CO_2 and H_2O concentration at ~80 minutes). Two Raman spectra (80 s exposure 5 accumulations, ~26 min)

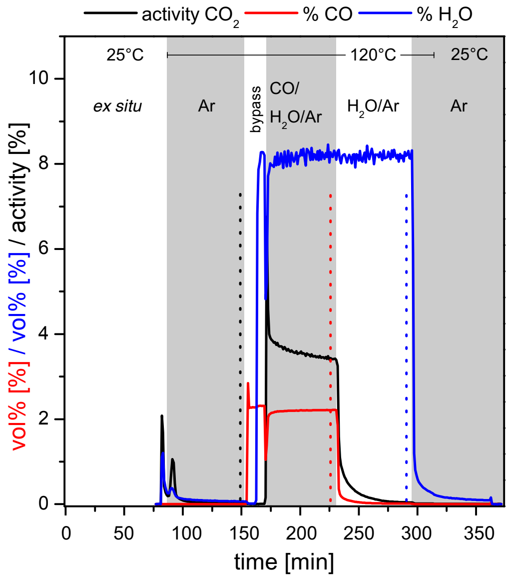

Figure 9.1.: Gas-phase composition analysis over a 0.5 wt% Au/CeO_2 catalyst at 120°C in the *operando* Raman/UV-Vis setup. The catalytic activity (CO_2 evolution) is shown in black, the CO concentration (%) in red and the H_2O concentration (%) in blue. The catalyst is heated to 120°C in Ar. Then the reaction gas mixture (2 % CO, 8 % H_2O) is equilibrated in the bypass and subsequently applied to the reaction chamber. The catalyst is regenerated in 8 % H_2O and cooled down to room temperature in Ar. The dashed lines indicate the end of the Raman measurements that are shown in figures 9.3 and 9.4.

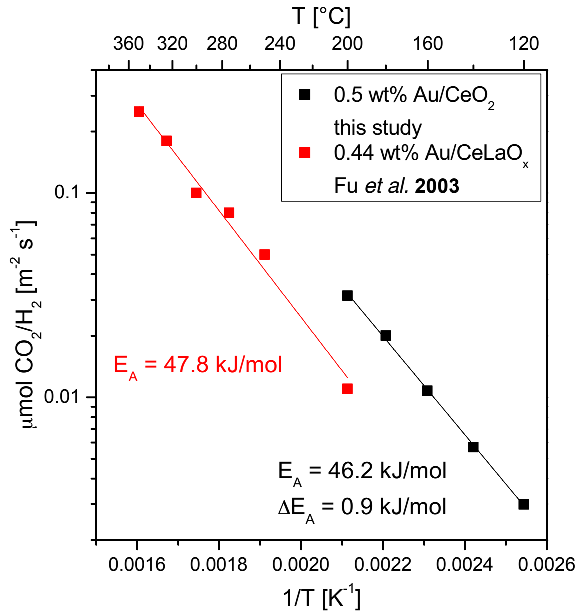

Figure 9.2.: Arrhenius plot [265] for the water-gas shift reaction (2 % CO, 10 % H_2O) over a 0.5 wt% Au/CeO_2 catalyst in a quartz tubular reactor with an online mass spectrometer described before. [266] For comparison the results of a cyanide leached 0.44 wt% Au/$CeLaO_x$ (deposition precipitation) sample are shown. [19]

followed by UV-Vis spectra (300 ms, 200 averages, ~1 min) were recorded, while the catalyst was kept in the argon stream at 120°C. Then the gas stream was switched again to the bypass and the sample was kept in a stable inert, argon atmosphere. In the bypass first 2 % CO and second 8 % or 10 % water was added to the stream and the mixture is equilibrated for at least 5 minutes, before it was applied to the reaction chamber for 1 h. *Dynamic operando* Raman/UV-Vis spectra were taken immediately afterwards and steady-state *operando* spectra were measured after the catalyst reached a steady-state conversion at ~200 minutes in figure 9.1. The catalyst exhibited a steady-state activity of 3.5 % as determined by the CO_2 content in the gas stream. After the steady-state *operando* spectra, CO was switched off and the catalyst was regenerated in H_2O. Finally the cell was cleaned from water with a pure argon stream.

For comparison the cell and the empty sample holder did not exhibit any CO_2 evolution in CO/H_2O up to a temperature of 175°C.

To evidence H_2 evolution, which is not possible by gas-phase infrared spectroscopy, 36.7 mg of the catalyst was filled in a heatable quartz tubular reactor attached to an online mass spectrometer for gas-phase analysis. [266, 267] At 50 ml/min total flow and 2 % CO, 10 % H_2O in He the measured

H_2 concentration is identical to the CO_2 concentration in the product stream for sample temperatures between 120°C and 200°C. The production rate of CO_2 and H_2 as a function of temperature is plotted in figure 9.2 in an Arrhenius type plot. The activation energy is determined as $E_A = 46.2 \pm 0.9$ kJ/mol, which is in line with the reported value of 47.8 ± 1.5 kJ/mol for 0.44 wt% Au/CeLaO_x (8 % La) catalyst where metallic gold was leached from the samples with cyanide. In the prior study the activation energy and reaction rate of a 0.44 wt% Au/CeLaO_x catalyst resembled that of a 4.4 wt% Au/CeLaO_x catalyst, that was yielded by deposition precipitation of gold and metallic gold was not leached from the catalyst. [19] In the quartz tubular reactor the corresponding bare ceria support was inactive at temperatures between 120°C and 200°C.

Concerning the *operando* Raman spectroscopy, due to the strong absorption at the Raman excitation energy $\lambda_{ex} = 532$ nm and the increased absorption of the Au/CeO_2 samples under water-gas shift reaction conditions (see UV-Vis spectrum in figure 9.5) the Raman spectra are corrected by the reflectivity $\mathrm{R}_{\infty,532\ \mathrm{nm}}$ of the sample at this energy as derived from the UV-Vis spectrum. Please note that a UV-Vis spectrum was measured after each Raman spectrum. Equation 9.2 is employed to calculate $G(R_{\infty,532\ \mathrm{nm}})$ and the spectrum is scaled by $1/G(R_{\infty,532\ \mathrm{nm}})$. The values of the correction factor are in the range $0.4 \leq G(R_{\infty,532\ \mathrm{nm}}) \leq 1.5$. For details refer to references [85, 134, 268, 269]. Raman spectra of the bare ceria support are reported as measured.

$$G(R_{\infty,532\ \mathrm{nm}}) = \frac{R_{\infty,532\ \mathrm{nm}}(1 + R_{\infty,532\ \mathrm{nm}})}{(1 - R_{\infty,532\ \mathrm{nm}})} \tag{9.2}$$

The rather low Raman cross section of water vapor allows for Raman spectra, which are not superimposed by gas-phase H_2O signals. Therefore, the spectral region from 150 to 2000 cm^{-1} can be evaluated in a straightforward manner. However, the technique suffers from fluorescence, caused by the strong absorption of the Au/CeO_2 catalyst at the Raman excitation energy. Therefore, the spectra of Au/CeO_2 catalysts are not evaluated in the spectral region between 2000 and 4000 cm^{-1} where $\tilde{\nu}$(O-H) and $\tilde{\nu}$(C-H) stretching modes are expected at 3500 − 3800 cm^{-1} and at ∼3000 cm^{-1}, respectively.

9.2 Water-gas shift reaction in CO/$H_2{}^{16}O$: *Operando* spectroscopy

In figures 9.3 and 9.4 *operando* Raman spectra of a 0.5 wt% Au/CeO_2 catalyst at 120°C in argon, under water-gas shift reaction conditions (2 % CO, 8 % H_2O), and in H_2O (8 %) are depicted showing the phonon region (0 − 1000 cm^{-1}) and the adsorbate region (800 − 2300 cm^{-1}), respectively. The end of each measurement is indicated by the dashed lines in figure 9.1. The position of the most intense band (F_{2g} mode) is given in the top left of figure 9.3. In argon the F_{2g} band is located at 459.5 cm^{-1} representing a considerable redshift as compared to the spectra measured at room temperature in chapter 7. For comparison the position of the F_{2g} band at the bare ceria support in argon at 120°C is 461.7 cm^{-1} (see figure C.5 of the appendix). The latter F_{2g} band position is taken as a reference state for CeO_{2-x}, where the x accounts for intrinsic defects in ceria. With respect to this F_{2g} band position the stoichiometry of Au/CeO_2 in argon is determined as $CeO_{1.947-x}$ and under water-gas shift reaction conditions as $CeO_{1.873-x}$ (F_{2g} position 456.4 cm^{-1}), based on the shift of the F_{2g} band. For details about the derivation of the relationship between the redshift of the F_{2g} band position and the stoichiometry of ceria from

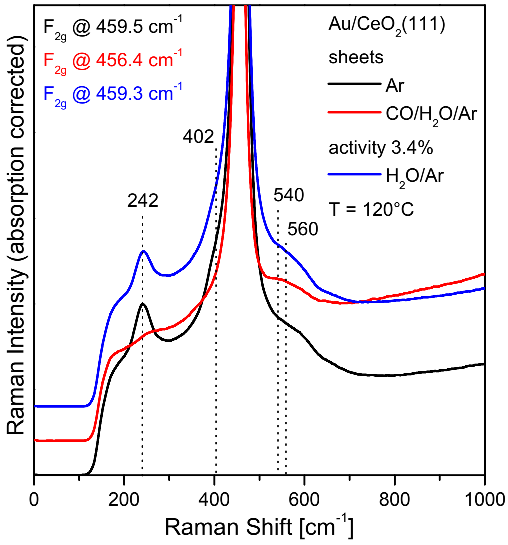

Figure 9.3.: *Operando* Raman spectra (phonon region) of a 0.5 wt% Au/CeO_2 catalyst at 120°C during water-gas shift reaction (2 % CO, 8 % H_2O, red). For comparison spectra in Ar prior reaction (black) and in 8 % H_2O after reaction (blue) are shown. The F_{2g} band is cut and the position of the F_{2g} band is given at the top left. The spectra are offset for clarity.

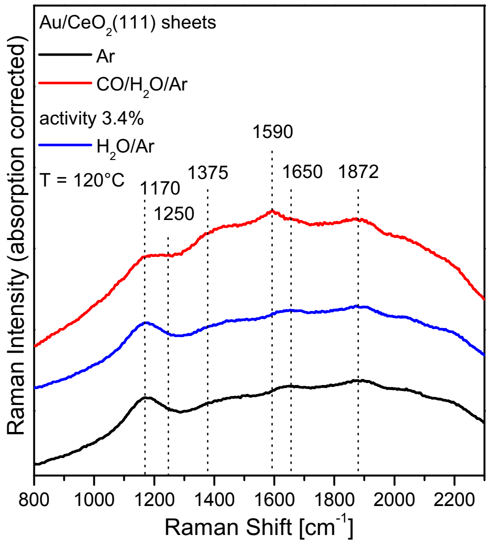

Figure 9.4.: *Operando* Raman spectra (carbonate region) of a 0.5 wt% Au/CeO_2 catalyst at 120°C during water-gas shift reaction (2 % CO, 8 % H_2O, red). For comparison spectra in Ar prior reaction (black) and in 8 % H_2O after reaction (blue) are shown. The spectra are offset for clarity.

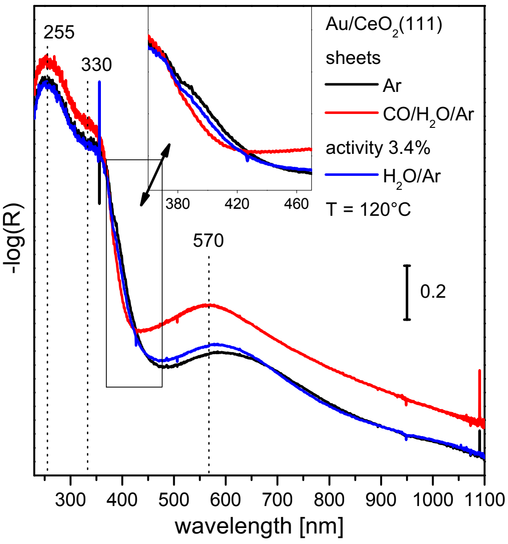

Figure 9.5.: *Operando* UV-Vis spectra of a 0.5 wt% Au/CeO_2 catalyst at 120°C during water-gas shift reaction (2 % CO, 8 % H_2O, red). For comparison spectra in Ar prior reaction (black) and in 8 % H_2O after reaction (dark blue) are shown. The inset gives an enlarged view of the band gap region.

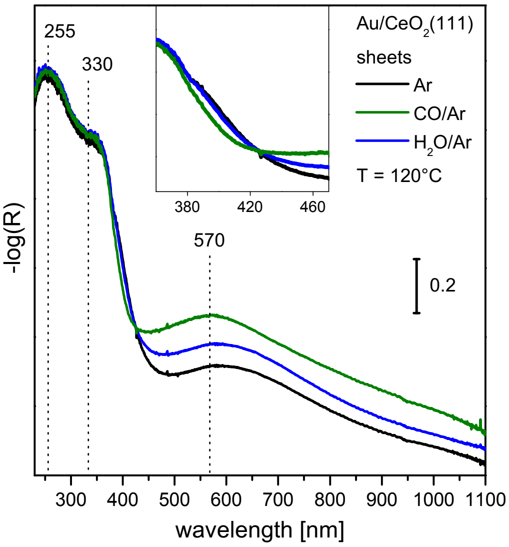

Figure 9.6.: *In situ* UV-Vis spectra of a 0.5 wt% Au/CeO_2 catalyst at 120°C exposed to argon (black), 2 % CO (green) and 10 % H_2O (blue). The inset gives an enlarged view of the band gap region.

DFT+U results see section 4.3. Almost the same position of the F_{2g} band as in argon atmosphere is observed in water atmosphere after exposure to reaction conditions (459.3 cm^{-1}). Obviously the reduction of the Au/CeO_2 catalyst under reaction conditions is reversible.

An increased concentration of oxygen vacancies in the subsurface under reaction conditions is also indicated by the broad increase of the defect bands at 540 and 560 cm^{-1}. These bands are assigned to a $Ce^{3+}O_8$ coordination cube (oxygen vacancy in the second coordination sphere of Ce^{3+}) and to a $Ce^{3+}O_7V_O^{\bullet\bullet}$ coordination cube (oxygen vacancy and Ce^{3+} in direct proximity), respectively. For a detailed discussion and assignment of the bands based on DFT+U results the reader is referred to sections 4.3 and 4.4. Qualitatively, the increased intensity of the band at 560 cm^{-1} indicates a higher concentration of oxygen vacancies, while the concentration is quantified by the F_{2g} position with the aid of DFT+U calculations.

The longitudinal and transversal stretching modes of the CeO_2(111) surface are observed at 242 and 402 cm^{-1} (see section 4.5 and reference [183]). The longitudinal surface mode is by 4 cm^{-1} redshifted at 120°C compared to room temperature measurements (see chapter 7). Both bands disappear under water-gas shift reaction conditions, while the intensity in water atmosphere almost resembles the intensity measured in argon. Obviously also the surface processes at the Au/CeO_2 catalyst are reversible in H_2O.

In the adsorbate region of the spectrum in figure 9.4 the 2LO overtone is observed at 1170 cm^{-1} and residual adsorbed water at 1872 cm^{-1}. The band at 1650 cm^{-1} is assigned to carbonate and hydrogen carbonate species and the bands at 1590, 1375, and 1250 cm^{-1} to formate species adsorbed at the ceria surface (for an assignment to corresponding vibrational modes on the basis of DFT+U results see table 4.2). Qualitatively, the bands assigned to formate species increase under reaction conditions and the bands assigned to carbonate and water remain stable.

For comparison at the bare ceria support neither a shift of the F_{2g} band position, nor a defect band increase or bands assigned to formate species are observed under water-gas shift reaction conditions (not shown). Additionally, the surface modes at 246 and 402 cm^{-1} remain stable in intensity as well.

The *operando* UV-Vis spectra during reaction are shown in figure 9.5 and compared to *in situ* Raman spectra in pure CO (2 %) and H_2O (10 %) in figure 9.6. The spectrum recorded under reaction conditions resembles that obtained in CO showing a strongly increased absorption in the region between 450 – 1100 nm. Following the assignment from section 7.5 this is attributed to reduced cerium ions of the ceria support rather than a gold plasmon as proposed before. [22] However, a contribution from the plasmon can not be excluded here, but an assignment to a support reduction of the sample is corroborated by the *operando* Raman spectra discussed above. The spectrum after reaction in 8 % H_2O resembles the spectrum of the Au/CeO_2 catalyst that was only exposed to 8 % water. A decrease of the absorption at the band gap at ~350 nm is observed in reaction conditions and in pure CO that is regained in water atmosphere. This behavior can not be explained in this study, as a detailed interpretation of UV-Vis spectra of Au/CeO_2 catalyst is lacking in the literature and is not the focus of this work.

9.3 Water-gas shift reaction in CO/$H_2{}^{18}O$: *Operando* spectroscopy

To gain insight into the mechanism of the water-gas shift reaction over Au/CeO_2 catalysts, *operando* Raman and UV-Vis spectra are measured during exposure of the catalyst to 2 % CO and 8 % $H_2{}^{18}O$.

As water activation and O-H bond cleavage is proposed as the rate determining step for the water-gas shift reaction, the exchange of ^{16}O by ^{18}O will provide fundamental insight into the reaction mechanism over Au/CeO_2 catalysts, especially as the vibrational properties of the ceria support are altered by ^{18}O incorporation and this can be probed by *operando* Raman spectroscopy.

Analysis of the gas-phase infrared spectra during $CO/H_2{}^{18}O$ water-gas shift reaction and comparison with literature data for rotational vibrational spectra of $C^{16}O_2$, $C^{18}O_2$, and $C^{16}O^{18}O$ [270] revealed that the product gas stream consists only of $C^{16}O^{18}O$ after a short initial period where $C^{16}O_2$ and $C^{16}O^{18}O$ are both observed with a decreasing amount of $C^{16}O_2$. As no calibration for the $C^{16}O^{18}O$ concentration from the infrared signal was done, the activity of the catalyst can only be estimated as $3-4$ %. This is comparable to the experiments with $H_2{}^{16}O$. It is expected that the ^{18}O isotope has only minor influence on the activity (negligible kinetic isotope effect).

The *operando* Raman spectra in figure 9.7 (orange for $CO/H_2{}^{18}O$ water-gas shift reaction and dark blue for $H_2{}^{18}O$) revealed a comparable behavior as with the $H_2{}^{16}O$ isotope on the first sight, i.e., the longitudinal and transversal modes of the $CeO_2(111)$ surface disappears and the defect bands at 540 and 560 cm^{-1} increase in intensity. Interestingly, the F_{2g} band maximum is located at 440.4 cm^{-1}, compared to 456.4 cm^{-1} for the reaction with $H_2{}^{16}O$. This can only be rationalized by the band made up of two components representing a F_{2g} in $Ce^{18}O_2$ and in $Ce^{16}O_2$. This shows that ^{16}O of the gold/ceria catalyst is exchanged with ^{18}O from $H_2{}^{18}O$.

In section 4.5 the Raman spectrum of the $Ce^{18}O_2(111)$ surface was calculated by DFT+U and it was shown that the surface and bulk phonons can likewise be treated as isolated vibrations of ^{140}Ce-$^{16/18}O$ oscillators. The shift attributed to the isotope exchange is calculated from its reduced masses as $\tilde{\nu}_{^{140}Ce^{18}O} = 0.949 \cdot \tilde{\nu}_{^{140}Ce^{16}O}$. This corresponds to a 24 cm^{-1} redshift of the F_{2g} band for a $Ce^{18}O_2$ lattice. A deconvolution of the $^{16/18}O$ composite band is done in the following section, revealing components at 456 cm^{-1} and 436 cm^{-1}. This 20 cm^{-1} difference of the components is consistent with the estimated difference derived for an F_{2g} band of a $Ce^{16}O_2$ and $Ce^{18}O_2$ lattice abbreviated as ^{16}O F_{2g} and ^{18}O F_{2g} in the following. The deconvolution reveals that the majority of the probed sample is oxygen of type ^{18}O. The position of the F_{2g} band maximum of the compound band is almost maintained in 8 % $H_2{}^{18}O$ atmosphere at 441.9 cm^{-1} (dark blue in figure 9.7).

Another interesting fact is that the longitudinal and transversal mode are located at 231 cm^{-1} and 385 cm^{-1} in 8 % $H_2{}^{18}O$ atmosphere after the reaction, respectively. This corresponds to a 11 cm^{-1} and 17 cm^{-1} redshift compared to the position in argon atmosphere before the reaction. Again this is in accordance with the redshifts calculated by DFT+U for the $Ce^{18}O_2(111)$ surface of 11 and 17 cm^{-1} and the estimated shifts on the basis of an isolated Ce-^{18}O oscillator model. To this end, a complete exchange of the surface oxygen from ^{16}O to ^{18}O is concluded during reaction with $H_2{}^{18}O$ as a reactant. Additionally, a major fraction of the subsurface oxygen is ^{18}O as evident from presence of the ^{18}O F_{2g} band.

In comparison, *operando* Raman spectra of the bare ceria support exhibit neither a shift of the F_{2g} band nor of the bands assigned to the longitudinal or transversal ceria surface modes (see figure C.5). Furthermore, no bands at 1590 cm^{-1} or 1375 cm^{-1} that are assigned to formate species, are observed at the bare ceria support (see figure C.8). In contrast, the bands assigned to hydroxyl groups at 3653 cm^{-1} and 3682 cm^{-1} in argon atmosphere (see figure C.7) shift by 10 and 12 cm^{-1} to 3643 and 3670 cm^{-1}, respectively. This coincides well with an estimated ^{18}O-H isotope factor of $\sqrt{\frac{19/18}{17/16}} = 0.9967$, that accounts for ^{16}O isotope exchange to ^{18}O, assuming an isolated $^{16/18}$O-^{1}H oscillator. In the Raman spectrum obtained for the bare ceria support exposed to CO/$H_2{}^{16}O$, no shift of the hydroxyl bands is observed. This indicates that terminal hydroxyl groups (OH) are indeed exchanged at the bare ceria support but surface and subsurface oxygen ions (O^{2-}), that are part of the ceria lattice, are not liable to isotope exchange.

The *operando* Raman spectra of the Au/CeO_2 catalyst are compared to *in situ* Raman spectra in various gas atmospheres in figure 9.8. The black spectrum corresponds to the spectrum of a Au/CeO_2 catalyst equilibrated in Argon as in the figures 9.3 and 9.7. Prior to all *in situ* measurements the catalyst is equilibrated in Ar at 120°C. The red and orange spectrum measured in CO/$H_2{}^{16}O$ and CO/$H_2{}^{18}O$, are discussed before. The spectrum in $H_2{}^{16}O$ (blue) resembles the spectrum in $H_2{}^{16}O$ after reaction. Interestingly, upon exposure of the Au/CeO_2 catalyst only to $H_2{}^{18}O$ the bands assigned to the longitudinal and transversal surface modes shift to 231 and 385 cm^{-1}, respectively. As discussed above this indicates that all ^{16}O atoms of the CeO_2(111) surface are exchanged by ^{18}O atoms. Obviously for a complete isotope exchange of the surface oxygen ions, exposure to pure $H_2{}^{18}O$ is sufficient. Please note that the F_{2g} band position is not shifted indicating that ^{18}O is only exchanged at the surface oxygen layer.

The Raman spectrum in pure CO resembles the spectrum in CO/$H_2{}^{16}O$ as it is the case for the UV-Vis spectrum (see figure 9.5 for UV-Vis spectra and figure 9.8 for Raman spectra). Briefly, the bands assigned to surface modes at 242 and 402 cm^{-1} are absent and the F_{2g} position and defect band profile are identical. This is in agreement with the corresponding UV-Vis spectra, as discussed above.

For CO oxidation conditions (2 % CO and 10 % O_2) at 120°C bands assigned to the surface modes of the CeO_2(111) surface are observed with the same intensity as before, the F_{2g} band is observed at 459.9 cm^{-1} (compare to argon atmosphere, 459.6 cm^{-1}) and the defect band profile mirrors also the profile in pure argon atmosphere. Obviously surface and subsurface oxygen at the Au/CeO_2 catalyst is replenished at 120°C if O_2 is accessible in the gas-phase.

The corresponding adsorbate region of the *in situ* Raman spectra is depicted in figure 9.9. The assignment of the bands is discussed above. The band assigned to adsorbed water at 1872 cm^{-1} is stable under all conditions. Although the catalyst is exposed to $H_2{}^{18}O$ (orange and dark blue spectra) the bending mode of adsorbed water is hardly affected by the isotope exchange. This can be rationalized by the small shift of the bending mode in $H_2{}^{18}O$ compared to $H_2{}^{16}O$ and the rather broad band ($\Delta\tilde{\nu}$ = 6.4 cm^{-1}, $H_2{}^{16}O$: $\tilde{\nu}$ = 1594.7 cm^{-1} [271], $H_2{}^{18}O$: $\tilde{\nu}$ = 1588.3 cm^{-1} [272]). A small and broad band due to hydrogen carbonate is observed at 1650 cm^{-1} most clearly in argon atmosphere. Under reaction conditions (CO, $H_2{}^{16}O$) formate species (HCO_2) are formed indicated by the bands at 1590, 1375, and 1250 cm^{-1}. The first band is assigned to an asymmetric stretching mode ν(OCO, asym, O_{outer}) involving the outer oxygen O_{outer}, the second is assigned to the symmetric stretching mode ν(OCO, sym), and the latter to an asymmetric stretching mode ν(OCO, asym, $O_{lattice}$) involving the lattice oxygen ($O_{lattice}$). For details see section 4.15. Only the latter band is shifted to 1220 cm^{-1} upon exposure to (CO, $H_2{}^{18}O$). This suggests that the outer oxygen is ^{16}O while the oxygen at the lattice position ($O_{lattice}$) in $HCO^{18}O_{lattice}$ is indeed ^{18}O (compare table 4.2). Only this formate configuration allows the band at 1590 and 1375 cm^{-1} to remain almost stable and the band at 1250 to shifts to 1220 cm^{-1} in CO/$H_2{}^{18}O$ atmosphere (see table 4.2). As the majority component of the F_{2g} phonon redshifts by a factor of 0.949 due to ^{18}O exchange, this rationalizes the shift of the 2LO overtone from 1170 to 1118 cm^{-1}.

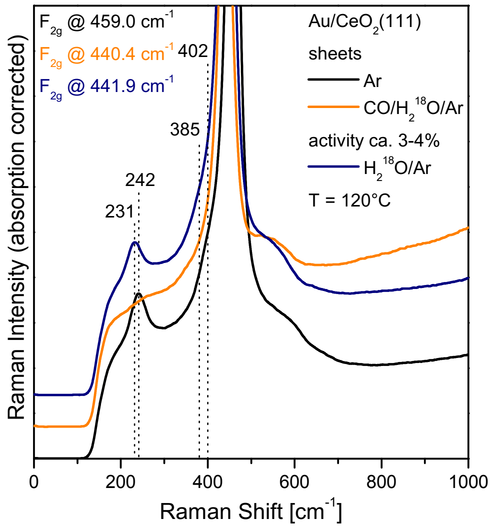

Figure 9.7.: *Operando* Raman spectra (phonon region) of a 0.5 wt% Au/CeO_2 catalyst at 120°C during water-gas shift reaction (2 % CO, 8 % $H_2{}^{18}O$). For comparison spectra in Ar prior reaction (black) and in 8 % $H_2{}^{18}O$ after reaction (dark blue) are shown The F_{2g} band is cut and the position of the F_{2g} band given at the top left. The spectra are offset for clarity.

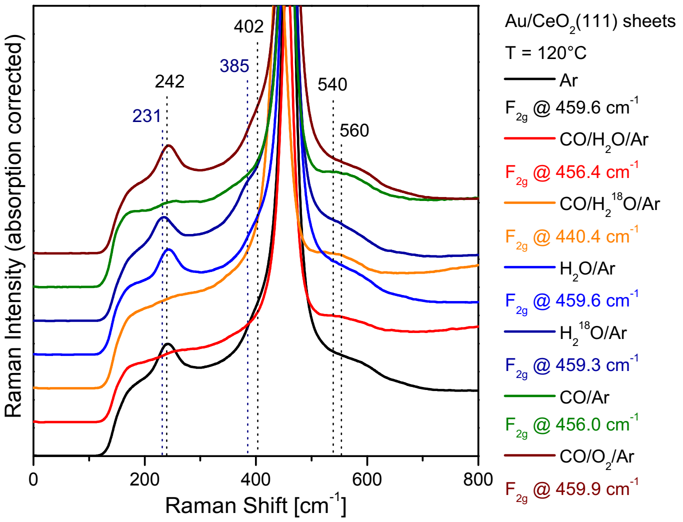

Figure 9.8.: *In situ* Raman spectra (phonon region) of a 0.5 wt% Au/CeO_2 catalyst at 120°C exposed to argon (black), water-gas shift reaction conditions (2 % CO, 8 % H_2O, red), water gas shift conditions with $H_2{}^{18}O$ (orange), 10 % H_2O (blue), 8 % $H_2{}^{18}O$ (dark blue), 2 % CO (green), and CO oxidation conditions (2 % CO, 10 % O_2, brown). In each case the F_{2g} band position is given in the legend. The spectra are offset for clarity.

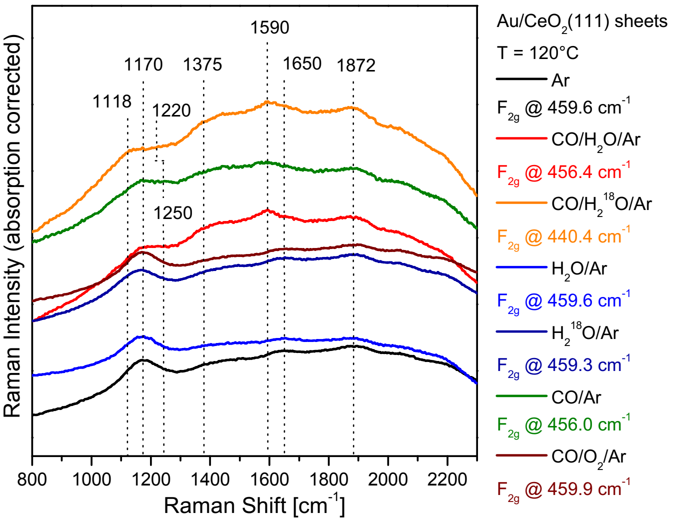

Figure 9.9.: *In situ* Raman spectra (carbonate region) of a 0.5 wt% Au/CeO_2 catalyst at 120°C exposed argon (black), water-gas shift reaction conditions (2 % CO, 8 % H_2O, red), water-gas shift reaction conditions with $H_2{}^{18}O$ (orange), 10 % H_2O (blue), 8 % $H_2{}^{18}O$ (dark blue), 2 % CO (green), and CO oxidation conditions (2 % CO, 10 % O_2, brown). The spectra are offset for clarity.

As mentioned above *dynamic operando* Raman spectra were measured during the initial exposure (∼60 minutes) of a Au/Ce^{16}O$_2$ catalyst to CO/H$_2$^{18}O water-gas shift reaction conditions. The Raman spectrum in argon and after 3, 10, and 30 minutes under reaction conditions are depicted in figure 9.10 as black, orange, yellow, and red spectrum, respectively. A gradual redshift of the maximum of the band from 460 cm^{-1} to 440 cm^{-1} is observed. From experiments with pure CO and CO/H$_2$^{16}O a redshift of the F$_{2g}$ band to 456 cm^{-1} is assigned to an increased concentration of oxygen vacancies in the ceria subsurface. [50, 183] However, this can not explain the redshift of ∼20 cm^{-1} upon exposure to CO/H$_2$^{18}O. This can only be rationalized by a composite band originating from a ^{16}O F$_{2g}$ at 456 cm^{-1} and a ^{18}O F$_{2g}$ mode while the latter is redshifted compared to the prior.

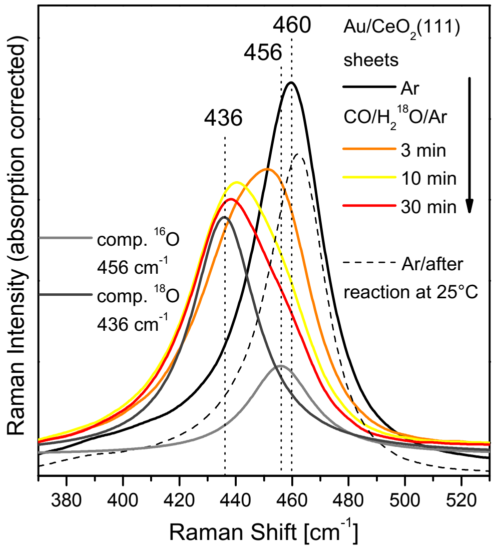

Figure 9.10.: *Dynamic operando* Raman spectra of a 0.5 wt% Au/CeO$_2$ catalyst at 120°C during water-gas shift reaction conditions (2 % CO, 8 % H$_2$^{18}O) and deconvolution of the F$_{2g}$ mode into a component accounting for a ^{16}O F$_{2g}$ mode at 456 cm^{-1} (grey) and for a ^{18}O F$_{2g}$ mode at 436 cm^{-1} (dark grey). The black dashed line shows a spectrum after reaction.

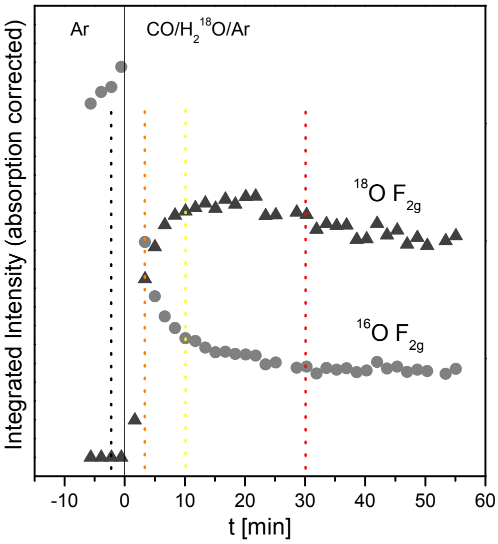

Figure 9.11.: Temporal evolution of the intensity of the ^{16}O F$_{2g}$ (light grey circles) and the ^{18}O F$_{2g}$ (dark grey triangles) mode under water-gas shift reaction conditions (2 % CO and 8 % H$_2$^{18}O.) Dashed lines indicate the time point of the spectra depicted in figure 9.10.

In this contribution the measured band is deconvolved by two Lorentz functions both with a full width at half maximum (fwhm) of 28 cm^{-1}. One component is fixed at 456 cm^{-1}, while the second component locates at 436 cm^{-1} after a least squares fit. This corresponds to a difference of the ^{16}O F$_{2g}$ and the ^{18}O F$_{2g}$ of 20 cm^{-1} which is in agreement with the difference of 24 cm^{-1} derived from DFT calculations and the estimates from isolated ^{140}Ce-$^{16/18}$O oscillators (compare section 9.3). Exemplarily the two components of the red spectrum are shown in figure 9.10 as a grey and a dark grey line accounting for the ^{16}O F$_{2g}$ and the ^{18}O F$_{2g}$, respectively.

The integrated intensity of the two components over time is shown in figure 9.11. The intensity of the ^{16}O F_{2g} gradually decreases within ~30 minutes in the same manner as the ^{18}O F_{2g} increases to its steady-state intensity.

Analysis of the longitudinal surface mode at 242 cm^{-1} over the same time span reveals that the intensity initially drops to its steady-state intensity (not shown). So the descriptors for surface and the subsurface oxygen species change at two different time scales. While the descriptor for the surface (242 cm^{-1} band) changes fast the descriptor for the subsurface F_{2g} position is slower. This resembles the surface and subsurface oxygen dynamics obtained during room temperature CO oxidation at the same material.

9.5 Discussion

Summarizing the results, Raman spectroscopy provides the possibility to probe three different type of oxygen species of ceria supported catalysts relevant for water-gas shift reaction conditions, besides the known superoxide ($O_2{}^{-}$) and peroxide ($O_2{}^{2-}$) species (see chapter 4 and 5 for detailed analysis of these species). First, the terminal hydroxyl groups are mentioned, which are probed by the O-H stretching mode with frequencies in the range of $3643 - 3704$ cm^{-1}. These bands were assigned on the basis of infrared experiments [36, 141, 273] and are not further discussed here. Second, the longitudinal and transversal stretching modes of the surface oxygen ions against the adjacent cerium ions allow to probe these oxygen species of the $CeO_2(111)$ surface. It is proposed that either vacancy formation or hydroxyl formation lead to a decrease of the band assinged to the longitudinal stretching mode at 242 cm^{-1} (see section 4.5 and 4.14). [137] And third, the F_{2g} mode provides insight into subsurface oxygen defects. [50, 128] With the aid of DFT calculations also a quantification of the oxygen vacancy concentration in the ceria subsurface can be drawn, while the defect bands at 540 and 560 cm^{-1} provide a qualitative interpretation. [183] Besides oxygen, formate species are observed by the characteristic bands at 1590, 1375, and 1250 cm^{-1}. The formate vibrations were also observed in infrared experiments before [36, 44] and the Raman cross sections of the modes are calculated in section 4.15.

As the vibrational modes are altered by isotope exchange all the vibrational modes above show a shift if ^{18}O is incorporated at the respective ^{16}O position (exchange). The shift of solid state and surface phonons was calculated by DFT+U and it was shown that an isolated ^{140}Ce-$^{16/18}O$ oscillator model provides a profound estimate of the shift as for isolated terminal hydroxyl groups. In addition, the specific vibrational frequencies were calculated for the $^{16/18}O$ isotopic analogs of the formate species in section 4.15.

To gain insight into the reaction mechanism of the water-gas shift reaction the *operando* Raman spectra upon exposure to $CO/H_2{}^{16}O$ and $CO/H_2{}^{18}O$ are studied in detail. First, the bare ceria support is characterized. Upon exposure to reaction conditions CO/H_2O neither a catalytic activity (CO_2 evolution) nor formate species are observed in *operando* Raman spectra. Moreover, terminal hydroxyl groups and the bulk and surface phonons remain stable in intensity. Only minor formation of formate species at the bare ceria support was proposed on the basis of infrared experiments before. [44] Interestingly, upon exposure of the ceria support to $CO/H_2{}^{18}O$ the terminal hydroxyl groups shift, which indicates an exchange of ^{16}OH by ^{18}OH. Obviously the hydroxyl groups at the bare ceria support are liable to oxygen exchange while the lattice oxygen ions are not at a temperature of 120°C. For comparison, a partial oxygen exchange by gas-phase O_2 at polycrystalline ceria was observed at 400°C temperature in a previous study. [248]

Upon 0.5 wt% deposition of gold at the ceria support this situation changes drastically. As mentioned above due to strong fluorescence the spectral region of the terminal hydroxyl groups can not be analyzed anymore. But upon exposure to pure $H_2{}^{18}O$ a complete exchange of surface ^{16}O ions with ^{18}O ions is evidenced by the 11 and 17 cm^{-1} shifts of the two bands assigned the longitudinal and transversal surface mode of the $CeO_2(111)$ surface. Assuming that water adsorbs dissociatively at the Au/CeO_2 catalyst to two hydroxyl groups, a backward reaction must be possible to restore $^{18}O^{2-}$ ($O_O{}^x$ in Kröger Vink notation) ions at the surface, which are not part of a terminal hydroxyl group and can build a longitudinal and transversal stretching mode at the surface as shown in equation 9.3. In the equation $*$ refers to a possible adsorption site for hydroxyl at the ceria surface, e.g., a surface oxygen vacancy.

The O-H bond cleavage is indeed proposed as the rate determining step of the water-gas shift reaction over Au/CeO_2 catalysts (see introduction to chapter 9). But it is shown here, that there is a channel for OH bond cleavage in the presence of gold as the whole surface is covered by $^{18}O_O^x$ ions in $H_2{}^{18}O$ atmosphere at 120°C (shift of 11 and 17 cm^{-1} for the longitudinal and transversal mode). Furthermore it is concluded here, that this reaction channel is opened in the absence of CO which means that no format or carboxylate species can be formed as intermediate as proposed in prior experimental [44, 74] and theoretical [72, 73] studies. This is confirmed by *in situ* Raman spectra revealing no bands assigned to formate and no increase of bands assigned to carbonate species in figure 9.9 upon exposure to pure H_2O.

$$H_2{}^{18}O + {}^{16}O_O + * \xrightleftharpoons{Au/CeO_2} H\text{-}{}^{18}O + H\text{-}{}^{16}O \xrightleftharpoons{Au/CeO_2} H_2{}^{16}O + {}^{18}O_O + * \tag{9.3}$$

Finally, upon exposure of a Au/CeO_2 catalyst to reaction conditions the longitudinal and transversal surface modes are absent. This can be attributed to oxygen vacancy creation (section 4.5) or hydroxyl formation (section 4.14) at the surface. As the dissociative water adsorption into an oxygen vacancy is proposed as strongly exothermic process ($E_{ads,H_2O} = -2.024$ eV), [203] it is assumed here that the surface is hydroxylated rather than populated with oxygen vacancies. In contrast, the F_{2g} band position strongly suggests an increase in subsurface oxygen vacancy concentration in $CO/H_2{}^{16}O$ by a redshift of the F_{2g} band to 456.4 cm^{-1}. In argon atmosphere the F_{2g} band is located at 459.5 cm^{-1}. The corresponding stoichiometry of the ceria support is $CeO_{1.947-x}$ in argon and $CeO_{1.873-x}$ in reaction atmosphere, indicating a strongly reduced ceria subsurface. The observation of large amounts of ^{18}O in the subsurface probed by the ^{18}O F_{2g} band at 436 cm^{-1} in $CO/H_2{}^{18}O$ highlights the oxygen dynamics of the ceria support and can only be rationalized by a fraction of oxygen vacancies in the subsurface allowing for oxygen ion mobility and transfer of ^{18}O from the surface, i.e., from the adsorption site to the ceria subsurface.

Due to this observation and the fact that formate species remain stable in its configurations at the ceria support, these are tentatively assigned to spectator species during water-gas shift reaction over Au/CeO_2 catalysts. Furthermore, no increase of carbonate species are observed in *operando* Raman spectra. To this end, it is proposed that the reaction indeed rather proceeds via a redox mechanism [19] with a channel for replenishment of surface oxygen ions from terminal hydroxyl groups as shown in equation 9.3. It needs to be highlighted that this channel is also open if CO is absent in the gas-phase.

In conclusion, this proposal was only possible by the combination of the isotopic labelling in combination with *operando* Raman spectra, while DFT+U calculations allowed an assignment of bands to the vibrational modes of phonons, surface phonons, and adsorbates.

9.6 Critical discussion of the probe depth of Raman spectroscopy

Up to now it is assumed that Raman spectroscopy probes the whole ceria nanoparticle of a Au/CeO_2 catalyst. This needs to be questioned based on the evaluation of the isotopic exchange experiments presented in this chapter. Upon exposure of the Au/CeO_2 catalyst to CO/$H_2{}^{18}O$ a more intense ^{18}O F_{2g} phonon is observed. After cooling the catalyst in argon stream the black dashed spectrum in figure 9.10 is observed which possesses an F_{2g} band at the original ^{16}O position. It needs to be mentioned that the catalyst was not exposed to $^{16}O_2$ or $H_2{}^{16}O$ and was rather kept in inert argon atmosphere. This allows the conclusion that Raman spectroscopy probes only the subsurface layers of the ceria particle where ^{18}O agglomerates during exposure to CO/$H_2{}^{18}O$, while a fraction of oxygen in the ceria particle remains ^{16}O. After the exposure to $H_2{}^{18}O$ ^{18}O equilibrates in the whole particle and a dominant ^{16}O F_{2g} phonon is measured by Raman spectroscopy in the probed region of the sample.

The conclusions derived from Raman spectroscopy by the F_{2g} phonon are assigned to the subsurface region of the particle rather than the whole ceria particle or the *bulk*. This wording is used here and in the study described in chapter 7. Most probably the ceria subsurface layers are indeed part of the reaction and govern the activity of the catalyst as shown in chapter 7 for the room temperature CO oxidation and in this chapter for the low temperature water-gas shift reaction at 120°C. However, a fraction of the particle is proposed to remain stable and is not probed by Raman spectroscopy. Therefore, the probe depth of Raman spectroscopy at Au/CeO_2 catalysts is limited to the subsurface layers of the ceria particle.

10 Summary

In this work a combined spectroscopic setup was established to characterize active catalysts under working conditions (CO oxidation and water-gas shift reaction, *operando* approach) by Raman, UV-Vis, and infrared spectroscopy. The approach allows to correlate the activity of ceria catalysts and the information on the catalyst structure from spectroscopy directly to each other and to follow activation and deactivation processes of the catalyst material on a timescale of less than four minutes. [52] The structural information are deduced from density functional theory (DFT+U) calculations in conjunction with the applied spectroscopy. The DFT+U calculations provide a prediction of Raman and infrared active solid-state phonons and adsorbate vibrations of model structures to interpret the experimental results on a molecular scale. The results of the combined experimental and theoretical approach are summarized in the following, starting with a description of the vibrational properties of bulk ceria (CeO_2), oxygen defective or reduced bulk ceria (CeO_{2-x}), and the $CeO_2(111)$ and $CeO_2(100)$ surface facets. [183] Second, the study on the vibrational properties of peroxide (${O_2}^{2-}$) and superoxide species (${O_2}^{-}$), formed at nanoparticles exposing the $CeO_2(111)$ and $CeO_2(100)$ surface facets, by *in situ* Raman spectroscopy and their comparison with DFT+U model systems is summarized. This is of relevance for ceria containing catalysts as oxygen vacancies at the surface and activated oxygen species (peroxide and superoxide) play a major role in oxidation reactions over ceria containing catalysts. [190] For example, the relevance of oxygen defects at the ceria surface and in the subsurface on the activity of gold/ceria catalysts during CO oxidation is highlighted by *operando* Raman spectroscopy. [137] Additionally, the same method revealed similar defect dynamics in the ceria support during the water-gas shift reaction over gold/ceria catalysts. Finally, the active site for oxidation reactions is found as CO adsorbed to an isolated gold ion (Au^+) in direct contact with the ceria surface ($O_{lattice}$-Au^+-CO species) using *operando* infrared spectroscopy, which represents the first spectroscopic observation and characterization of such a species at gold/ceria catalysts.

In the following, a detailed description of the results is given. Based on the experimental observation of an intense Raman band, that is assigned to the first-order Raman mode (F_{2g}) at 464 cm^{-1}, and the calculated frequency of this mode as 437 cm^{-1} with the PBE+U/4.5 eV functional, a scaling factor between experimental and calculated frequencies of $\tilde{\nu}_{exp.} = 1.06\ \tilde{\nu}_{PBE+U/4.5\ eV}$ is proposed for solid-state phonons of ceria. On this basis the vibrational properties of reduced ceria were studied at $Ce_{32}O_{63}$ and $Ce_{32}O_{62}$ supercells and can explain the experimental redshift (shift to lower frequencies) of the F_{2g} band quantitatively. Precisely, the redshift is caused by an expansion of the ceria lattice due oxygen vacancy creation and Ce^{3+} formation. For the relation between the stoichiometry ($CeO_{2-\delta}$) of ceria nanoparticles and the redshift ($\Delta\omega$) of the F_{2g} band, the following equation is proposed on the basis of DFT+U calculations: $\delta = (0.024 \pm 0.05)\Delta\omega/cm^{-1}$. Furthermore, after oxygen vacancy creation two bands in the defect band region at 480 cm^{-1} (experiment: ~540 cm^{-1}) and 500 cm^{-1} (experiment: ~560 cm^{-1}) can be explained within a simple coordination model by a $Ce^{3+}O_8$ and a $Ce^{3+}O_7V_O^{\bullet\bullet}$ cube, that correspond to the presence of an oxygen vacancy either in the second coordination sphere or in direct proximity to Ce^{3+}, respectively. [183]

To take the surface termination of ceria nanoparticles into account, the vibrational properties of the $CeO_2(111)$ and $CeO_2(100)$ surfaces were modeled. For the $CeO_2(111)$ surface a longitudinal surface phonon (parallel stretching mode along the surface of the topmost cerium against the oxygen ions) is predicted with a frequency of 225 cm^{-1}. The corresponding transversal phonon (stretching mode orthogonal to the surface) is predicted with a frequency of 364 cm^{-1}. This coincides well with the experimentally observed Raman bands at 242 cm^{-1} and 402 cm^{-1} for hydrothermally synthesized ceria nanocrystals exposing selectively the $CeO_2(111)$ surface facet. The surface faceting was confirmed by the lattice plane spacing of ceria in TEM images. For polycrystalline ceria these bands are observed as well. Therefore, it is concluded that polycrystalline ceria nanoparticles terminate with a (111) surface facet. Upon introduction of a surface oxygen vacancy the intensity of the band at 225 cm^{-1} is predicted to strongly decrease. Therefore, it is proposed that this band allows a quantification of the $CeO_2(111)$ surface oxidation state of ceria nanoparticles.

The two Raman bands at 242 and 402 cm^{-1} are not observed at hydrothermally synthesized ceria nanocubes exposing the $CeO_2(100)$ surface (confirmed by TEM). For these samples two Raman bands at 350 and 600 cm^{-1} are observed. These compare well with the predicted bands at 331 and 563 cm^{-1} for the $CeO_2(100)$ surface termination based on a checkerboard type of arrangement of the surface oxygen layer. Opposite to the $CeO_2(111)$ surface, these vibrations are not confined at the surface but are rather located in the subsurface below the $CeO_2(100)$ surface. However, the vibrational modes are caused by the termination of the nanocrystals in (100) direction.

The DFT+U study on the vibrational properties of CeO_2, oxygen defective CeO_{2-x}, and the surface facets is the first DFT+U study with a distinct focus on Raman active vibrations of ceria nanoparticles. The assignment of the experimentally observed Raman bands to modes at the (111) and (100) surface facet has not been accomplished in the literature before. [183]

At the uniformly faceted ceria nanoparticles oxygen adsorption as peroxide ($O_2{}^{2-}$) and superoxide ($O_2{}^{-}$) anions, i.e., as activated oxygen species, is studied by *in situ* Raman spectroscopy and by DFT+U calculations. The calculations consider a coverage-dependence of adsorbed peroxide ($x = 2$) and superoxide ($x = 1$ in $O_2{}^{x-}/CeO_{2-x}(111)$ and $O_2{}^{x-}/CeO_{2-x}(100)$ structures). Experimentally the O-O stretch frequencies are observed at $830 - 880$ cm^{-1} (peroxide) and $1100 - 1140$ cm^{-1} (superoxide) in Raman spectra. Together with the DFT+U calculations, which provide information on the adsorption geometry, the stability, and the prediction of vibrational properties of these oxygen species, this approach allows a thorough characterization of these species.

In detail, DFT+U calculations predict two stable peroxide structures (outer oxygen is *a* tilted towards Ce^{4+} and *b* tilted between two Ce^{4+}) for coverages $\leq$0.25 ML at the $CeO_2(111)$ surface that differ by 20 meV in total energy for 0.25 ML coverage. The difference of the O-O stretch frequency is predicted as 38 cm^{-1}, whereas in experiment a difference between the two bands (832 and 860 cm^{-1}) of 28 cm^{-1} is observed. On top of that, experiments suggest a blueshift of ∼20 cm^{-1} of the O-O stretch frequency for agglomerated peroxides (∼877 cm^{-1}). [32] This can be rationalized by the DFT calculations, as a blueshift of 35 cm^{-1} is predicted for the stable configuration *b* (outer oxygen ion is tilted between two surface Ce^{4+}) at 1 ML coverage (coverage effect). [183] Furthermore, a shift of the stretch frequency of configuration *b* of 30 cm^{-1} is observed, if two Ce^{3+} are located in proximity of the peroxide molecule (chemical shift). This can explain the prior observation of a peroxide band at 847 cm^{-1} at Au/CeO_2 catalysts and is rationalized by a charge transfer from adsorbed gold particles to the ceria lattice creating Ce^{3+} (compare below). [190]

With respect to the superoxide species at the $CeO_2(111)$ surface, DFT+U calculations predict only a spectral region of 2 cm^{-1} between 1132 and 1134 cm^{-1} (not scaled) for the superoxide stretch frequency irrespective of $Ce^{3+/4+}$ ions in direct proximity. This resembles the experimental results of a very narrow band at ∼1127 cm^{-1} in Raman [32] or infrared [196] spectra in the literature.

At the $CeO_2(100)$ surface (ceria nanocubes) a strongly different oxygen adsorption behavior is observed highlighting the effect of surface faceting on the properties of ceria in catalysis. [57] The Raman bands at 832 and 862 cm^{-1} are assigned to peroxide species and the Raman bands at 1103 and 1137 cm^{-1} to superoxide species. However, comparing absolute intensities the overall peroxide band is strongly enhanced at the nanocubes exposing the $CeO_2(100)$ facet compared to the $CeO_2(111)$ faceted samples. This observation is corroborated by the exalted stability of adsorbed oxygen species at the $CeO_2(100)$ surface compared to the $CeO_2(111)$ surface predicted by DFT+U calculations (compare $E_{\mathrm{ads,O_2^{2-}}} = -1.92$ eV and $E_{\mathrm{ads,O_2^{-}}} = -1.42$ eV for $CeO_{2-x}(111)$ surface with (2×2) periodicity and $E_{\mathrm{ads,O_2^{2-}}} = -2.141$ eV and $E_{\mathrm{ads,O_2^{-}}} = -1.625$ eV for a $CeO_{2-x}(100)$ surface with $p(2 \times 2)$ periodicity, each 0.25 ML coverage). For peroxides at the $CeO_2(100)$ surface a comparable coverage effect as for the $CeO_2(111)$ surface was found. The predicted blueshift amounts to 39 cm^{-1} for a coverage increase from 0.125 ML to 1 ML and compares well to the 30 cm^{-1} blueshift observed in Raman spectra of ceria nanocubes. However, for low coverages only a single flat lying configuration is predicted by the DFT calculations.

The two distinct Raman bands in the superoxide region provide the first observation of a superoxide species at (100) faceted ceria nanoparticles. On the basis of DFT+U calculations these bands are assigned to superoxide anions in the direct proximity of Ce^{3+} (1137 cm^{-1}) and in the second coordination sphere of Ce^{3+} (1103 cm^{-1}). The prior is dynamically formed in CO/O_2 atmosphere at 35°C, whereas the latter can be explained by an electron hopping to a cerium ion in a next nearest neighbor position at elevated temperatures (>60°C), as this is an activated process with a barrier of 0.5 eV in bulk ceria. [231]

To study the effect of ceria surface facets on the activity of gold/ceria catalysts such catalysts were prepared by deposition precipitation of $HAuCl_4$ at the ceria nanoparticles exposing the $CeO_2(111)$ or $CeO_2(100)$ facet. Indeed, an effect of the surface facet on the activity was observed. A 0.5 wt% $Au/CeO_2(111)$ catalyst with a flat $CeO_2(111)$ support surface exhibited the lowest evolution rate of CO_2 per Au^+ (Au^+ content determined by XPS) during CO oxidation. For comparison, a $Au/CeO_2(100)$ catalyst with a flat $CeO_2(100)$ surface exhibited a threefold evolution rate compared to the $Au/CeO_2(111)$ catalyst. This highlights that the surface faceting of the ceria support is directly relevant for catalysis. Interestingly, a $Au/CeO_2(111)$-stepped catalyst with a polycrystalline ceria support terminating with a stepped (111) facet revealed a fivefold evolution rate compared to the $Au/CeO_2(100)$ catalyst. This can only be rationalized by the stepped surface sites (evident from TEM images), which possess a decreased oxygen vacancy formation energy (see [66]: $E_{\mathrm{vac,O}} = 1.52$ eV) compared to $E_{\mathrm{vac,O}} = 2.27$ eV for the flat $CeO_2(111)$ and $E_{\mathrm{vac,O}} = 1.824$ eV for the flat $CeO_2(100)$ facet as derived here. Therefore, the observed activity follows the order Au/CeO_2(111)-stepped > Au/CeO_2(100) > Au/CeO_2(111) for the CO oxidation and this is explained by the increase in oxygen vacancy formation energy in opposite direction. These results demonstrate that not only the surface facet has an influence on the activity but also the surface structuring of the support can greatly influence the activity of the catalyst.

For insight into the oxygen defect dynamics in the ceria support *operando* Raman and UV-Vis spectroscopy is applied at the 0.5 wt% Au/CeO_2 catalyst with a stepped CeO_2(111) surface facet during CO oxidation. As outlined above by Raman spectroscopy the oxidation state of the ceria surface (longitudinal surface mode at 246 cm^{-1}) can be monitored. Additionally, the oxygen defect concentration in the ceria subsurface can be quantified by the position of the F_{2g} band. Under reaction conditions (2 % CO, 10 % O_2) the surface is slightly reduced, indicated by a decrease of the band intensity at 246 cm^{-1}. Additionally, the subsurface stoichiometry is determined as $CeO_{1.952-x}$ under reaction conditions compared to $CeO_{1.976-x}$ in oxidizing environment (25 % O_2). Under reducing condition (2 % CO) a reduction of the subsurface is indicated by a strong redshift of the F_{2g} band position corresponding to a stoichiometry of $CeO_{1.916-x}$. In addition, the reduction of CeO_2(111) support surface is indicated by an intensity drop of the longitudinal surface phonon at 246 cm^{-1}. Exposing this reduced catalyst to reaction conditions resulted in a 100 % increased activity compared to a pretreatment under oxidizing conditions. Dynamic *operando* Raman spectra reveal that the surface is reoxidized much faster than the ceria subsurface. The reoxidation of the subsurface proceeds on the same timescale as the activity decreases to its steady-state activity. Hence, it is concluded that the subsurface reduction state of the support alters the activity of the Au/CeO_2 catalyst showing the participation of the ceria support in the reaction mechanism. Therefore, it is strongly suggested that active oxygen for oxidation reactions is delivered from the lattice forming an oxygen vacancy (Mars-van Krevelen type of mechanism). At these sites oxygen can be activated in the form of peroxides or superoxides (see above) for reoxidation of the ceria support.

Similar defect dynamics are observed at the 0.5 wt% Au/CeO_2 catalyst with a stepped CeO_2(111) surface by *operando* Raman and UV-Vis spectroscopy during the water-gas shift reaction (2 % CO, 8 % H_2O). The Raman data reveal the disappearance of the band assigned to the longitudinal surface mode (246 cm^{-1}) under reaction conditions. The band reversibly reappears upon exposure of the catalyst to H_2O. This suggests that the CeO_2(111) surface is hydroxylated under reaction conditions (terminal OH groups). Besides that, the formation of formate species (HCO) during reaction is indicated by a band at 1590 cm^{-1} in the *operando* Raman spectra. $H_2{}^{18}O$ isotope experiments show that the hydroxyl groups (OH), which are omnipresent at the bare ceria support surface (no gold deposition), are exchanged by ^{18}O forming ^{18}OH groups, whereas the surface and subsurface oxygen ions of the lattice remain ^{16}O. In the presence of 0.5 wt% gold the oxygen ions at the CeO_2(111) support surface are exchanged by ^{18}O ions upon exposure to $H_2{}^{18}O$ only. This is concluded from a shift of the longitudinal and transversal surface phonon from 242 cm^{-1} and 402 cm^{-1} to 231 cm^{-1} and 385 cm^{-1}, respectively. Interestingly, this exchange and the formation of $^{18}O^{2-}$ ions does not require the presence of CO and the formation of formate or carboxylate as proposed in the literature. [44,72,74] This indicates that a redox type mechanism for the oxidation of CO by lattice oxygen is possible. However, lattice oxygen can be replenished from hydroxyl groups without the formation of format or carboxylate intermediate species. Upon exposure of the Au/CeO_2 catalyst to CO/$H_2{}^{18}O$ a thorough exchange of the surface and subsurface oxygen ions by ^{18}O is observed. This is unequivocally shown by the presence of F_{2g} phonon bands at 456 cm^{-1} and 436 cm^{-1} assigned to ^{16}O F_{2g} and ^{18}O F_{2g} phonons, respectively. Obviously, during reaction lattice oxygen O^{2-} is consumed to form CO_2 and replenished by water forming hydroxyl groups (OH) first, but there has to be a reaction channel for the formation for surface oxygen ions from hydroxyl groups even in the absence of CO (redox mechanism).

Concerning the state of gold in gold/ceria catalysts DFT+U calculations predict that adsorbed gold at the CeO_2(111) surface transfers an electron to the support forming oxidized Au^+ that interacts preferably with surface oxygen ions. By X-ray photoelectron spectroscopy (XPS) Au^+ formation at nanoparticle Au/CeO_2 catalyst can be confirmed. Furthermore, *operando* infrared spectroscopy at the Au/CeO_2 catalyst provides evidence for CO adsorption at these Au^+ sites forming $O_{lattice}$-Au^+-CO species, as detected by the CO stretch frequency of $2125 - 2130$ cm^{-1}. In addition, the intensity of this band can be directly correlated to the activity of the catalyst. The assignment of the CO stretch frequency to the distinct species is based on DFT calculations employing the PBE+U/4.5 eV or the HSE06 functional for model structures with CO adsorbed to CeO_2(111), Au_1/CeO_2(111), Au_4/CeO_2(111), Au_1, and Au(111). The results reveal that the stretch frequency, which is observed in the experiment, can only be assigned to CO adsorbed to an oxidized Au^+ ion in direct contact with the CeO_2(111) surface, i.e., an $O_{lattice}$-Au^+-CO species. This species has been predicted by prior theoretical studies, [67] but a spectroscopic observation has not been reported in the literature yet. In this work such an isolated gold species is evidenced by the combined *operando* spectroscopic and DFT approach revealing the active site of gold/ceria catalysts for CO oxidation reactions.

The results of this work demonstrate the relevance and influence of the ceria support properties on the activity of oxidation reactions over Au/CeO_2 catalysts. Furthermore, the potential of infrared and Raman spectroscopy for the characterization of catalysts under working conditions and the interplay with DFT calculations for an interpretation of the results on a molecular scale are highlighted. The strong dynamics in the oxide support caused by the change of the gas-phase environment points out the necessity for characterization of catalysts under working conditions (*operando* approach).

11 Outlook

In this work ceria (CeO_2) is studied as a prototype oxide material because of its high oxygen mobility and the facile exchange of oxygen with the gas-phase (oxygen storage capacity). Therefore, it is able to deliver reactive oxygen for oxidation reactions over ceria containing catalysts (active support material). The oxygen dynamics in gold/ceria catalysts as an example for oxide supported precious metal particles (metal/oxide) in catalysis are highlighted. For example, the reduced catalyst exhibits initially a 100 % higher activity for CO oxidation than the oxidized catalyst.

Besides that for the gold/ceria system an active species characterized as a single Au^+-CO species in direct contact with the ceria support was unraveled by infrared spectroscopy in conjunction with DFT modeling. It is suggested that the single gold species is formed dynamically under reaction conditions at the CeO_2(111) surface. The adsorption of gold to the CeO_2(100) surface and the adsorption of CO to the Au/CeO_2(100) model systems can be studied by DFT in future projects. In combination the synthesis of ceria nanocubes which selectively expose the CeO_2(100) surface facet, provides a platform structure to transfer the *operando* spectroscopy results obtained for polycrystalline ceria, to (100) faceted samples.

For the water-gas shift reaction a redox type mechanism (Mars-van Krevelen mechanism) is proposed for gold/ceria catalysts. Nevertheless, the water-gas shift reaction was only studied at a Au/CeO_2 sample with a polycrystalline ceria support. Employing also the ceria nanocubes allows to extend this study for the CeO_2(100) surface facet. Most probably a facet-dependent acceleration in activity can also be deduced for the water-gas shift reaction over Au/CeO_2 catalysts.

The backward reaction, i.e., the reverse water-gas shift over metal/ceria catalysts allows for the utilization of CO_2 with hydrogen. [25] This reaction provides the first reaction step for the creation of hydrocarbons from CO_2. These hydrocarbons can be synthesized independent of fossile sources and can by sustainably produced, if the H_2 is yielded from electrolyses employing a renewable energy source.

Besides employing gold/ceria catalysts in heterogeneous catalysis these material has been studied as a photocatalyst for water splitting and yielded a promising performance. [274] However, the properties of ceria are comparable to the properties of the most studied photocatalyst titania (TiO_2) in terms of oxygen dynamics and oxygen defect formation.

The transferability of the obtained results to other metal/oxide materials is of interest for a general understanding of the mode of operation of polycrystalline oxide catalyst materials. The goal is to unravel the mechanism of a reaction aiming at a molecular design of the catalyst. That means to selectively synthesize the active site at the catalyst, thus, increase the performance of a material. Concerning catalysts the performance is directly related to the conversion, selectivity, and durability of the catalyst. This concept is referred to as knowledge based design of materials and can also be applied to other functional materials, such as oxide materials employed in cathodes of batteries [275] or oxide gas sensors. [276]

In this work the potential of vibrational spectroscopy and especially Raman spectroscopy for the characterization of oxide materials under working conditions is elaborated. In combination with other spectroscopic methods and in conjunction with DFT calculations of model systems a better understanding of complex active oxide materials can be gained.

Bibliography

[1] M. Baerns, A. Behr, A. Brehm, J. Gmehling, H. Hofmann, U. Onken, A. Renken, K. Hinrichsen, R. Palkovits, *Technische Chemie*, Wiley VCH Verlag GmbH, **2013**.

[2] F. Schüth, *Chem. Unserer Zeit* **2006**, *40*(2), 92–103.

[3] *Organisation Internationale des Constructeurs d'Automobile*, http://www.oica.net, **2017**.

[4] M. Sugiura, *Catal. Surv. Asia* **2003**, *7*(1), 77–87.

[5] H. C. Yao, Y. F. Y. Yao, *J. Catal.* **1984**, *86*(2), 254–265.

[6] R. J. Gorte, *AlChE J.* **2010**, *56*(5), 1126–1135.

[7] H. S. Gandhi, G. W. Graham, R. W. McCabe, *J. Catal.* **2003**, *216*(1), 433–442.

[8] G. Ertl, H. Knözinger, F. Schüth, J. E. Weitkamp, *Handbook of Heterogeneous Catalysis, 8 Volumes*, Wiley, **2008**.

[9] S. Park, J. M. Vohs, R. J. Gorte, *Nature* **2000**, *404*, 265.

[10] A. Trovarelli, P. Fornasiero, *Catalysis by Ceria and Related Materials*, Imperial College Press, **2013**.

[11] R. W. McCabe, A. Trovarelli, *Appl. Catal., B* **2016**, *197*.

[12] T. Montini, M. Melchionna, M. Monai, P. Fornasiero, *Chem. Rev.* **2016**, *116*(10), 5987–6041.

[13] S. Carrettin, P. Concepción, A. Corma, J. M. López Nieto, V. F. Puntes, *Angew. Chem. Int. Ed.* **2004**, *43*(19), 2538–2540.

[14] M. M. Schubert, S. Hackenberg, A. C. van Veen, M. Muhler, V. Plzak, R. J. Behm, *J. Catal.* **2001**, *197*(1), 113–122.

[15] G. N. Vayssilov, Y. Lykhach, A. Migani, T. Staudt, G. P. Petrova, N. Tsud, T. Skála, A. Bruix, F. Illas, K. C. Prince, V. Matolín, K. M. Neyman, J. Libuda, *Nat. Mater.* **2011**, *10*(4), 310–315.

[16] M. Haruta, T. Kobayashi, H. Sano, N. Yamada, *Chem. Lett.* **1987**, (2), 405–408.

[17] M. Haruta, S. Tsubota, T. Kobayashi, H. Kageyama, M. J. Genet, B. Delmon, *J. Catal.* **1993**, *144*(1), 175–192.

[18] A. S. K. Hashmi, G. J. Hutchings, *Angew. Chem. Int. Ed.* **2006**, *45*(47), 7896–7936.

[19] Q. Fu, H. Saltsburg, M. Flytzani-Stephanopoulos, *Science* **2003**, *301*(5635), 935–938.

[20] W. Deng, M. Flytzani-Stephanopoulos, *Angew. Chem. Int. Ed.* **2006**, *45*(14), 2285–2289.

[21] G. A. Deluga, J. R. Salge, L. D. Schmidt, X. E. Verykios, *Science* **2004**, *303*(5660), 993.

[22] J. A. Hernández, S. A. Gómez, T. A. Zepeda, J. C. Fierro-González, G. A. Fuentes, *ACS Catal.* **2015**, *5*(7), 4003–4012.

[23] T. Engel, G. Ertl, *J. Chem. Phys.* **1978**, *69*(3), 1267–1281.

[24] G. Ertl, *J. Vac. Sci. Technol., A* **1983**, *1*(2), 1247–1253.

[25] H.-J. Freund, G. Meijer, M. Scheffler, R. Schlögl, M. Wolf, *Angew. Chem. Int. Ed.* **2011**, *50*(43), 10064–10094.

[26] C. Ratnasamy, J. P. Wagner, *Catal. Rev.* **2009**, *51*(3), 325–440.

[27] A. Goguet, S. O. Shekhtman, R. Burch, C. Hardacre, E. Meunier, G. S. Yablonsky, *J. Catal.* **2006**, *237*(1), 102–110.

[28] C. Hess, *Top. Catal.* **2013**, *56*(15-17), 1593–1600.

[29] W. H. Weber, R. Merlin (Eds.), *Raman Scattering in Materials Science*, Springer, **2013**.

[30] W. Weber, K. Hass, J. McBride, *Phys. Rev. B: Condens. Matter* **1993**, *48*(1), 178–185.

[31] J. E. Spanier, R. D. Robinson, F. Zhang, S.-W. Chan, I. P. Herman, *Phys. Rev. B: Condens. Matter* **2001**, *64*(24), 245407.

[32] V. V. Pushkarev, V. I. Kovalchuk, J. L. d'Itri, *J. Phys. Chem. B* **2004**, *108*(17), 5341–5348.

[33] Z. Wu, M. Li, J. Howe, H. M. Meyer, S. H. Overbury, *Langmuir* **2010**, *26*(21), 16595–16606.

[34] C. Li, Y. Sakata, T. Arai, K. Domen, K.-I. Maruya, T. Onishi, *J. Chem. Soc., Faraday Trans. 1* **1989**, *85*(4), 929–943.

[35] C. Li, Y. Sakata, T. Arai, K. Domen, K.-I. Maruya, T. Onishi, *J. Chem. Soc., Faraday Trans. 1* **1989**, *85*(6), 1451–1461.

[36] C. Binet, M. Daturi, J.-C. Lavalley, *Catal. Today* **1999**, *50*(2), 207–225.

[37] S. Zhang, X.-S. Li, B. Chen, X. Zhu, C. Shi, A.-M. Zhu, *ACS Catal.* **2014**, *4*(10), 3481–3489.

[38] S. Chen, L. Luo, Z. Jiang, W. Huang, *ACS Catal.* **2015**, *5*(3), 1653–1662.

[39] A. Abd El-Moemen, A. M. Abdel-Mageed, J. Bansmann, M. Parlinska-Wojtan, R. J. Behm, G. Kučerová, *J. Catal.* **2016**, *341*, 160–179.

[40] P. Fornasiero, M. Cargnello (Eds.), *Morphological, Compositional, and Shape Control of Materials for Catalysis*, Bd. 177 von *Studies in Surface Science and Catalysis*, Elsevier, **2017**.

[41] T. Shido, Y. Iwasawa, *J. Catal.* **1992**, *136*(2), 493–503.

[42] T. Shido, Y. Iwasawa, *J. Catal.* **1993**, *141*(1), 71–81.

[43] A. Karpenko, R. Leppelt, V. Plzak, J. Cai, A. Chuvilin, B. Schumacher, U. Kaiser, R. J. Behm, *Top. Catal.* **2007**, *44*(1-2), 183–198.

[44] R. Leppelt, B. Schumacher, V. Plzak, M. Kinne, R. J. Behm, *J. Catal.* **2006**, *244*(2), 137–152.

[45] H.-X. Mai, L.-D. Sun, Y.-W. Zhang, R. Si, W. Feng, H.-P. Zhang, H.-C. Liu, C.-H. Yan, *J. Phys. Chem. B* **2005**, *109*(51), 24380–24385.

[46] K. Wu, L.-D. Sun, C.-H. Yan, *Adv. Energy Mater.* **2016**, *6*(17), 1600501.

[47] D. R. Mullins, *Surf. Sci. Rep.* **2015**, *70*(1), 42–85.

[48] A. Trovarelli, J. Llorca, *ACS Catal.* **2017**, *7*(7), 4716–4735.

[49] A. Filtschew, K. Hofmann, C. Hess, *J. Phys. Chem. C* **2016**, *120*(12), 6694–6703.

[50] Y. Lee, G. He, A. J. Akey, R. Si, M. Flytzani-Stephanopoulos, I. P. Herman, *J. Am. Chem. Soc.* **2011**, *133*(33), 12952–12955.

[51] J. Guzman, S. Carrettin, A. Corma, *J. Am. Chem. Soc.* **2005**, *127*(10), 3286–3287.

[52] C. Schilling, C. Hess, *Top. Catal.* **2017**, *60*(1), 131–140.

[53] R. Kopelent, J. A. van Bokhoven, J. Szlachetka, J. Edebeli, C. Paun, M. Nachtegaal, O. V. Safonova, *Angew. Chem. Int. Ed.* **2015**, *54*(30), 8728–8731.

[54] M. Huang, S. Fabris, *Phys. Rev. B: Condens. Matter* **2007**, *75*(8), 081404.

[55] Y. Zhao, B.-T. Teng, X.-D. Wen, Y. Zhao, Q.-P. Chen, L.-H. Zhao, M.-F. Luo, *J. Phys. Chem. C* **2012**, *116*(30), 15986–15991.

[56] Y. M. Choi, H. Abernathy, H.-T. Chen, M. C. Linã, M. Liu, *ChemPhysChem* **2006**, *7*(9), 1957–1963.

[57] C. Yang, X. Yu, S. Heiß ler, P. G. Weidler, A. Nefedov, Y. Wang, C. Wöll, T. Kropp, J. Paier, J. Sauer, *Angew. Chem. Int. Ed.* **2017**, *56*(51), 16399–16404.

[58] M. Tinoco, S. Fernandez-Garcia, M. Lopez-Haro, A. B. Hungria, X. Chen, G. Blanco, J. A. Perez-Omil, S. E. Collins, H. Okuno, J. J. Calvino, *ACS Catal.* **2015**, *5*(6), 3504–3513.

[59] D. Widmann, R. Leppelt, R. J. Behm, *J. Catal.* **2007**, *251*(2), 437–442.

[60] J. Wang, H. Tan, S. Yu, K. Zhou, *ACS Catal.* **2015**, *5*(5), 2873–2881.

[61] N. Ta, J. Liu, S. Chenna, P. A. Crozier, Y. Li, A. Chen, W. Shen, *J. Am. Chem. Soc.* **2012**, *134*(51), 20585–20588.

[62] M. Valden, X. Lai, D. W. Goodman, *Science* **1998**, *281*(5383), 1647.

[63] M. F. Camellone, S. Fabris, *J. Am. Chem. Soc.* **2009**, *131*(30), 10473–10483.

[64] P. Ghosh, M. Farnesi Camellone, S. Fabris, *J. Phys. Chem. Lett.* **2013**, *4*(14), 2256–2263.

[65] H. Y. Kim, H. M. Lee, G. Henkelman, *J. Am. Chem. Soc.* **2012**, *134*(3), 1560–1570.

[66] H. Y. Kim, G. Henkelman, *J. Phys. Chem. Lett.* **2013**, *4*(1), 216–221.

[67] Y.-G. Wang, D. Mei, V.-A. Glezakou, J. Li, R. Rousseau, *Nat. Commun.* **2015**, *6*.

[68] J. Rodriguez, P. Liu, J. Hrbek, J. Evans, M. Pérez, *Angew. Chem. Int. Ed.* **2007**, *46*(8), 1329–1332.

[69] G. Jacobs, A. C. Crawford, B. H. Davis, *Catal. Lett.* **2005**, *100*(3-4), 147–152.

[70] F. C. Meunier, A. Goguet, C. Hardacre, R. Burch, D. Thompsett, *J. Catal.* **2007**, *252*(1), 18–22.

[71] R. Burch, A. Goguet, F. C. Meunier, *Appl. Catal., A* **2011**, *409-410*, 3–12.

[72] Y. Chen, J. Cheng, P. Hu, H. Wang, *Surf. Sci.* **2008**, *602*(17), 2828–2834.

[73] Y. Chen, H. Wang, R. Burch, C. Hardacre, P. Hu, *Faraday Discuss.* **2011**, *152*(0), 121–133.

[74] K. Mudiyanselage, S. D. Senanayake, L. Feria, S. Kundu, A. E. Baber, J. Graciani, A. B. Vidal, S. Agnoli, J. Evans, R. Chang, S. Axnanda, Z. Liu, J. F. Sanz, P. Liu, J. A. Rodriguez, D. J. Stacchiola, *Angew. Chem. Int. Ed.* **2013**, *52*(19), 5101–5105.

[75] J. A. Rodriguez, S. Ma, P. Liu, J. Hrbek, J. Evans, M. Pérez, *Science* **2007**, *318*(5857), 1757.

[76] M. A. Bañares, *Catal. Today* **2005**, *100*(1-2), 71–77.

[77] A. Chakrabarti, M. E. Ford, D. Gregory, R. Hu, C. J. Keturakis, S. Lwin, Y. Tang, Z. Yang, M. Zhu, M. A. Bañares, I. E. Wachs, *Catal. Today* **2017**, *283*, 27–53.

[78] B. M. Weckhuysen, *Chem. Soc. Rev.* **2010**, *39*(12), 4557–4559.

[79] U. Bentrup, *Chem. Soc. Rev.* **2010**, *39*(12), 4718–4730.

[80] A. Brückner, *Catal. Rev.* **2003**, *45*(1), 97–150.

[81] S. J. Tinnemans, J. G. Mesu, K. Kervinen, T. Visser, T. A. Nijhuis, A. M. Beale, D. E. Keller, A. M. J. van der Eerden, B. M. Weckhuysen, *Catal. Today* **2006**, *113*(1-2), 3–15.

[82] M. A. Bañares, M. O. Guerrero-Perez, J. L. G. Fierro, G. G. Cortez, *J. Mater. Chem.* **2002**, *12*(11), 3337–3342.

[83] M. A. Bañares, I. E. Wachs, *J. Raman Spectrosc.* **2002**, *33*(5), 359–380.

[84] M. O. Guerrero-Perez, M. A. Bañares, *Chem. Commun.* **2002**, (12), 1292–1293.

[85] S. J. Tinnemans, M. H. F. Kox, T. A. Nijhuis, T. Visser, B. M. Weckhuysen, *Phys. Chem. Chem. Phys.* **2005**, *7*(1), 211–216.

[86] M. O Brien, A. Beale, S. M. Jacques, M. Di Michel, B. Weckhuysen, *ChemCatChem* **2009**, *1*(1), 99–102.

[87] U. Bentrup, J. Radnik, U. Armbruster, A. Martin, J. Leiterer, F. Emmerling, A. Brückner, *Top. Catal.* **2009**, *52*(10), 1350–1359.

[88] C. Kongmark, V. Martis, A. Rubbens, C. Pirovano, A. Lofberg, G. Sankar, E. Bordes-Richard, R.-N. Vannier, W. Van Beek, *Chem. Commun.* **2009**, (32), 4850–4852.

[89] G. Le Bourdon, F. Adar, M. Moreau, S. Morel, J. Reffner, A. S. Mamede, C. Dujardin, E. Payen, *Phys. Chem. Chem. Phys.* **2003**, *5*(20), 4441–4444.

[90] M. Brandhorst, S. Cristol, M. Capron, C. Dujardin, H. Vezin, G. Le bourdon, E. Payen, *Catal. Today* **2006**, *113*(1-2), 34–39.

[91] P. Vandenabeele, *Practical Raman Spectroscopy: An Introduction*, Wiley, **2013**.

[92] E. Smith, G. Dent, *Modern Raman Spectroscopy: A Practical Approach*, Wiley, **2013**.

[93] D. Nitsche, C. Hess, *J. Raman Spectrosc.* **2013**, *44*(12), 1733–1738.

[94] J. Hollas, *Modern Spectroscopy*, Wiley, **2004**.

[95] M. V. Ganduglia-Pirovano, A. Hofmann, J. Sauer, *Surf. Sci. Rep.* **2007**, *62*(6), 219–270.

[96] E. Wilson, J. Decius, P. Cross, *Molecular Vibrations: The Theory of Infrared and Raman Vibrational Spectra*, Dover Publications, **2012**.

[97] S. Baroni, S. de Gironcoli, A. Dal Corso, P. Giannozzi, *Rev. Mod. Phys.* **2001**, *73*(2), 515–562.

[98] M. Gajdoš, K. Hummer, G. Kresse, J. Furthmüller, F. Bechstedt, *Phys. Rev. B: Condens. Matter* **2006**, *73*(4), 045112.

[99] D. Bishop, *Group Theory and Chemistry*, Dover Publications, **2012**.

[100] J. Paier, C. Penschke, J. Sauer, *Chem. Rev.* **2013**, *113*(6), 3949–3985.

[101] M. V. Ganduglia-Pirovano, *Catal. Today* **2015**, *253*, 20–32.

[102] M. V. Ganduglia-Pirovano, J. L. F. Da Silva, J. Sauer, *Phys. Rev. Lett.* **2009**, *102*(2), 026101.

[103] G. E. Murgida, M. V. Ganduglia-Pirovano, *Phys. Rev. Lett.* **2013**, *110*(24), 246101.

[104] J. E. Sutton, A. Beste, S. H. Overbury, *Phys. Rev. B: Condens. Matter* **2015**, *92*(14), 144105.

[105] A. V. Krukau, O. A. Vydrov, A. F. Izmaylov, G. E. Scuseria, *J. Chem. Phys.* **2006**, *125*(22), 224106.

[106] J. L. F. Da Silva, M. V. Ganduglia-Pirovano, J. Sauer, V. Bayer, G. Kresse, *Phys. Rev. B: Condens. Matter* **2007**, *75*(4), 045121.

[107] S. L. Dudarev, G. A. Botton, S. Y. Savrasov, C. J. Humphreys, A. P. Sutton, *Phys. Rev. B: Condens. Matter* **1998**, *57*(3), 1505–1509.

[108] S. Fabris, S. de Gironcoli, S. Baroni, G. Vicario, G. Balducci, *Phys. Rev. B: Condens. Matter* **2005**, *71*(4), 041102.

[109] J. P. Perdew, K. Burke, M. Ernzerhof, *Phys. Rev. Lett.* **1996**, *77*(18), 3865–3868.

[110] P. G. Lustemberg, P. J. Ramírez, Z. Liu, R. A. Gutiérrez, D. G. Grinter, J. Carrasco, S. D. Senanayake, J. A. Rodriguez, M. V. Ganduglia-Pirovano, *ACS Catal.* **2016**, *6*(12), 8184–8191.

[111] F. Esch, S. Fabris, L. Zhou, T. Montini, C. Africh, P. Fornasiero, G. Comelli, R. Rosei, *Science* **2005**, *309*(5735), 752.

[112] D. C. Grinter, R. Ithnin, C. L. Pang, G. Thornton, *J. Phys. Chem. C* **2010**, *114*(40), 17036–17041.

[113] S. Torbrügge, M. Reichling, A. Ishiyama, S. Morita, O. Custance, *Phys. Rev. Lett.* **2007**, *99*(5), 056101.

[114] Z.-K. Han, Y.-Z. Yang, B. Zhu, M. V. Ganduglia-Pirovano, Y. Gao, *Phys. Rev. Mat.* **2018**, *2*(3), 035802.

[115] R. Olbrich, G. E. Murgida, V. Ferrari, C. Barth, A. M. Llois, M. Reichling, M. V. Ganduglia-Pirovano, *J. Phys. Chem. C* **2017**.

[116] T. Duchoň, F. Dvořák, M. Aulickáą, V. Stetsovych, M. Vorokhta, D. Mazur, K. Veltruskáą, T. Skála, J. Mysliveček, I. Matolínová, V. Matolín, *J. Phys. Chem. C* **2014**, *118*(1), 357–365.

[117] Y. Pan, N. Nilius, C. Stiehler, H. Freund, J. Goniakowski, C. Noguera, *Adv. Mater. Interfaces* **2014**, *1*(9), 1400404.

[118] C. Penschke, J. Paier, J. Sauer, *J. Phys. Chem. C* **2013**, *117*(10), 5274–5285.

[119] N. V. Skorodumova, M. Baudin, K. Hermansson, *Phys. Rev. B: Condens. Matter* **2004**, *69*(7), 075401.

[120] M. Nolan, S. Grigoleit, D. C. Sayle, S. C. Parker, G. W. Watson, *Surf. Sci.* **2005**, *576*(1âĂŞ3), 217–229.

[121] M. Nolan, S. C. Parker, G. W. Watson, *Surf. Sci.* **2006**, *600*(14), 175–178.

[122] Z. Yang, T. K. Woo, K. Hermansson, *Chem. Phys. Lett.* **2004**, *396*(4-6), 384–392.

[123] M. Huang, S. Fabris, *J. Phys. Chem. C* **2008**, *112*(23), 8643–8648.

[124] C. Yang, L.-L. Yin, F. Bebensee, M. Buchholz, H. Sezen, S. Heissler, J. Chen, A. Nefedov, H. Idriss, X.-Q. Gong, C. Woll, *Phys. Chem. Chem. Phys.* **2014**, *16*(44), 24165–24168.

[125] M. Fronzi, S. Piccinin, B. Delley, E. Traversa, C. Stampfl, *Phys. Chem. Chem. Phys.* **2009**, *11*(40), 9188–9199.

[126] D. Fernández-Torre, K. Kośmider, J. Carrasco, M. V. Ganduglia-Pirovano, R. Pérez, *J. Phys. Chem. C* **2012**, *116*(25), 13584–13593.

[127] T. Kropp, J. Paier, *J. Phys. Chem. C* **2015**, *119*(40), 23021–23031.

[128] J. R. McBride, K. C. Hass, B. D. Poindexter, W. H. Weber, *J. Appl. Phys.* **1994**, *76*(4), 2435–2441.

[129] Y. Pan, N. Nilius, H.-J. Freund, J. Paier, C. Penschke, J. Sauer, *Phys. Rev. Lett.* **2013**, *111*(20), 206101.

[130] K. Kośmider, V. Brázdováą, M. V. Ganduglia-Pirovano, R. Pérez, *J. Phys. Chem. C* **2016**, *120*(2), 927–933.

[131] C. Penschke, J. Paier, *Phys. Chem. Chem. Phys.* **2017**, *19*(19), 12546–12558.

[132] B.-T. Teng, F.-M. Wu, W.-X. Huang, X.-D. Wen, L.-H. Zhao, M.-F. Luo, *ChemPhysChem* **2012**, *13*(5), 1261–1271.

[133] G. Mills, H. Jónsson, G. K. Schenter, *Surf. Sci.* **1995**, *324*(2), 305–337.

[134] C. Schilling, *CO oxidation on ceria supported gold catalysts studied by combined operando Raman/UV-Vis and IR spectroscopy*, Master Thesis, TU Darmstadt, **2016**.

[135] C. T. Nottbohm, C. Hess, *Catal. Commun.* **2012**, *22*, 39–42.

[136] C. Wang, X.-K. Gu, H. Yan, Y. Lin, J. Li, D. Liu, W.-X. Li, J. Lu, *ACS Catal.* **2017**, *7*(1), 887–891.

[137] C. Schilling, C. Hess, *J. Phys. Chem. C* **2018**, *122*(5), 2909–2917.

[138] M. Haruta, *Catal. Today* **1997**, *36*(1), 153–166.

[139] U. R. Pillai, S. Deevi, *Appl. Catal., A* **2006**, *299*(0), 266–273.

[140] J. F. Moulder, W. F. Stickle, P. E. Sobol, K. D. Bomben, *Handbook of X-ray photoelectron spectroscopy*, Bd. 40, Perkin Elmer Eden Prairie, MN, **1992**.

[141] A. Laachir, V. Perrichon, A. Badri, J. Lamotte, E. Catherine, J. C. Lavalley, J. El Fallah, L. Hilaire, F. Le Normand, E. Quemere, G. N. Sauvion, O. Touret, *J. Chem. Soc., Faraday Trans.* **1991**, *87*(10), 1601–1609.

[142] S. Brunauer, P. H. Emmett, E. Teller, *J. Am. Chem. Soc.* **1938**, *60*(2), 309–319.

[143] P. S. Waleska, C. Hess, *J. Phys. Chem. C* **2016**, *120*(33), 18510–18519.

[144] W. Koch, M. Holthausen, *A Chemist's Guide to Density Functional Theory*, Wiley-VCH, **2001**.

[145] J. Kohanoff, *Electronic Structure Calculations for Solids and Molecules: Theory and Computational Methods*, Cambridge University Press, **2006**.

[146] A. Szabo, N. Ostlund, *Modern Quantum Chemistry: Introduction to Advanced Electronic Structure Theory*, Dover Publications, **2012**.

[147] D. M. Ceperley, B. J. Alder, *Phys. Rev. Lett.* **1980**, *45*(7), 566–569.

[148] P. Hohenberg, W. Kohn, *Phys. Rev.* **1964**, *136*(3B), B864–B871.

[149] J. Rohrer, *Density Functional Theory: A Practical Introduction*, Lecture notes, **2014**.

[150] R. Parr, Y. Weitao, *Density-Functional Theory of Atoms and Molecules*, Oxford University Press, **1989**.

[151] P. E. Blöchl, *Phys. Rev. B: Condens. Matter* **1994**, *50*(24), 17953–17979.

[152] G. Kresse, D. Joubert, *Phys. Rev. B: Condens. Matter* **1999**, *59*(3), 1758–1775.

[153] H. J. Monkhorst, J. D. Pack, *Phys. Rev. B: Condens. Matter* **1976**, *13*(12), 5188–5192.

[154] J. Heyd, G. E. Scuseria, M. Ernzerhof, *J. Chem. Phys.* **2003**, *118*(18), 8207–8215.

[155] J. Heyd, G. E. Scuseria, M. Ernzerhof, *J. Chem. Phys.* **2006**, *124*(21), 219906.

[156] G. Kresse, J. Hafner, *Phys. Rev. B: Condens. Matter* **1993**, *47*(1), 558–561.

[157] G. Kresse, J. Hafner, *Phys. Rev. B: Condens. Matter* **1994**, *49*(20), 14251–14269.

[158] G. Kresse, J. Furthmüller, *Comput. Mater. Sci.* **1996**, *6*(1), 15–50.

[159] G. Kresse, J. Furthmüller, *Phys. Rev. B: Condens. Matter* **1996**, *54*(16), 11169–11186.

[160] F. D. Murnaghan, *PNAS* **1944**, *30*(9), 244.

[161] G. E. Murgida, V. Ferrari, M. V. Ganduglia-Pirovano, A. M. Llois, *Phys. Rev. B: Condens. Matter* **2014**, *90*(11), 115120.

[162] P. W. Tasker, *J. Phys. C: Solid State Phys.* **1979**, *12*(22), 4977.

[163] S. Grimme, *J. Comput. Chem.* **2004**, *25*(12), 1463–1473.

[164] S. Grimme, *J. Comput. Chem.* **2006**, *27*(15), 1787–1799.

[165] S. Tosoni, A. D. Boese, J. Sauer, *J. Phys. Chem. C* **2011**, *115*, 24871–24879.

[166] X. Gonze, C. Lee, *Phys. Rev. B: Condens. Matter* **1997**, *55*(16), 10355–10368.

[167] D. Karhánek, *Calculation of vibrational (IR) intensities in VASP 5.**, http://homepage.univie.ac.at/david.karhanek/downloads.html#Entry02, **2012**.

[168] D. Porezag, M. R. Pederson, *Phys. Rev. B: Condens. Matter* **1996**, *54*(11), 7830–7836.

[169] M. Lazzeri, F. Mauri, *Phys. Rev. Lett.* **2003**, *90*(3), 036401.

[170] A. Fonari, S. Stauffer, *vasp_raman.py*, https://github.com/raman-sc/VASP/, **2013**.

[171] A. Togo, I. Tanaka, *Scr. Mater.* **2015**, *108*, 1–5.

[172] J. Buckeridge, D. O. Scanlon, A. Walsh, C. R. A. Catlow, A. A. Sokol, *Phys. Rev. B: Condens. Matter* **2013**, *87*(21), 214304.

[173] S. Mochizuki, *Phys. Status Solidi B* **1982**, *114*(1), 189–199.

[174] D. A. Andersson, S. I. Simak, B. Johansson, I. A. Abrikosov, N. V. Skorodumova, *Phys. Rev. B: Condens. Matter* **2007**, *75*(3), 035109.

[175] C. Loschen, J. Carrasco, K. M. Neyman, F. Illas, *Phys. Rev. B: Condens. Matter* **2007**, *75*(3), 035115.

[176] H. Bärnighausen, G. Schiller, *J. Less Common Met.* **1985**, *110*(1), 385–390.

[177] J. L. F. Da Silva, *Phys. Rev. B: Condens. Matter* **2007**, *76*(19), 193108.

[178] G. A. Kourouklis, A. Jayaraman, G. P. Espinosa, *Phys. Rev. B: Condens. Matter* **1988**, *37*(8), 4250–4253.

[179] A. Nakajima, A. Yoshihara, M. Ishigame, *Phys. Rev. B: Condens. Matter* **1994**, *50*(18), 13297–13307.

[180] F. Marabelli, P. Wachter, *Phys. Rev. B: Condens. Matter* **1987**, *36*(2), 1238–1243.

[181] K. Clausen, W. Hayes, J. E. Macdonald, R. Osborn, P. G. Schnabel, M. T. Hutchings, A. Magerl, *J. Chem. Soc., Faraday Trans. 2* **1987**, *83*(7), 1109–1112.

[182] D. Avisar, T. Livneh, *Vib. Spectrosc.* **2016**, *86*, 14–16.

[183] C. Schilling, A. Hofmann, C. Hess, M. Ganduglia-Pirovano, *J. Phys. Chem. C* **2017**, *121*(38), 20834–20849.

[184] C. M. Hamm, L. Alff, B. Albert, *ZAAC* **2014**, *640*(6), 1050–1053.

[185] I. Kosacki, T. Suzuki, H. U. Anderson, P. Colomban, *Solid State Ion.* **2002**, *149*(1-2), 99–105.

[186] A. Migani, G. N. Vayssilov, S. T. Bromley, F. Illas, K. M. Neyman, *Chem. Commun.* **2010**, *46*(32), 5936–5938.

[187] T. Sato, S. Tateyama, *Phys. Rev. B: Condens. Matter* **1982**, *26*(4), 2257–2260.

[188] T. Taniguchi, T. Watanabe, N. Sugiyama, A. K. Subramani, H. Wagata, N. Matsushita, M. Yoshimura, *J. Phys. Chem. C* **2009**, *113*(46), 19789–19793.

[189] S. Agarwal, X. Zhu, E. J. M. Hensen, B. L. Mojet, L. Lefferts, *J. Phys. Chem. C* **2015**, *119*(22), 12423–12433.

[190] M. Lohrenscheit, C. Hess, *ChemCatChem* **2015**, *8*(3), 523–526.

[191] W. R. Busing, H. A. Levy, *J. Chem. Phys.* **1965**, *42*(9), 3054–3059.

[192] M. Fronzi, A. Soon, B. Delley, E. Traversa, C. Stampfl, *J. Chem. Phys.* **2009**, *131*(10), 104701.

[193] W. Tang, E. Sanville, G. Henkelman, *J. Phys.: Condens. Matter* **2009**, *21*(8), 084204.

[194] M. Daniel, S. Loridant, *J. Raman Spectrosc.* **2012**, *43*(9), 1312–1319.

[195] J. Kullgren, K. Hermansson, P. Broqvist, *Phys. Status Solidi RRL* **2014**, *8*(6), 600–604.

[196] C. Li, K. Domen, K. Maruya, T. Onishi, *J. Am. Chem. Soc.* **1989**, *111*(20), 7683–7687.

[197] Z. Wu, Y. Cheng, F. Tao, L. Daemen, G. S. Foo, L. Nguyen, X. Zhang, A. Beste, A. J. Ramirez-Cuesta, *J. Am. Chem. Soc.* **2017**.

[198] J. Xu, J. Harmer, G. Li, T. Chapman, P. Collier, S. Longworth, S. C. Tsang, *Chem. Commun.* **2010**, *46*(11), 1887–1889.

[199] A. Filtschew, D. Stranz, C. Hess, *Phys. Chem. Chem. Phys.* **2013**, *15*(23), 9066–9069.

[200] M. Haneda, T. Mizushima, N. Kakuta, *J. Chem. Soc., Faraday Trans.* **1995**, *91*(24), 4459–4465.

[201] Y. Zhang, Z. Kang, J. Dong, H. Abernathy, M. Liu, *J. Solid State Chem.* **2006**, *179*(6), 1733–1738.

[202] M. Molinari, S. C. Parker, D. C. Sayle, M. S. Islam, *J. Phys. Chem. C* **2012**, *116*(12), 7073–7082.

[203] J. Carrasco, D. López-Durán, Z. Liu, T. Duchoň, J. Evans, S. D. Senanayake, E. J. Crumlin, V. Matolín, J. A. Rodríguez, M. V. Ganduglia-Pirovano, *Angew. Chem. Int. Ed.* **2015**, *54*(13), 3917–3921.

[204] T. Kropp, J. Paier, J. Sauer, *J. Phys. Chem. C* **2017**, *121*(39), 21571–21578.

[205] G. N. Vayssilov, M. Mihaylov, P. S. Petkov, K. I. Hadjiivanov, K. M. Neyman, *J. Phys. Chem. C* **2011**, *115*(47), 23435–23454.

[206] P. G. Lustemberg, M. V. Bosco, A. Bonivardi, H. F. Busnengo, M. V. Ganduglia-Pirovano, *J. Phys. Chem. C* **2015**, *119*(37), 21452–21464.

[207] Z. L. Wu, M. J. Li, S. H. Overbury, *J. Catal.* **2012**, *285*(1), 61–73.

[208] K. R. Hahn, M. Iannuzzi, A. P. Seitsonen, J. Hutter, *J. Phys. Chem. C* **2013**, *117*(4), 1701–1711.

[209] D. Zhang, X. Du, L. Shi, R. Gao, *Dalton Trans.* **2012**, *41*(48), 14455–14475.

[210] Z. Wu, S. Overbury (Eds.), *Catalysis by Materials with Well-Defined Structures*, Elsevier Science, **2015**.

[211] C. S. Pan, D. S. Zhang, L. Y. Shi, J. H. Fang, *Eur. J. Inorg. Chem.* **2008**, (15), 2429–2436.

[212] K. Zhou, X. Wang, X. Sun, Q. Peng, Y. Li, *J. Catal.* **2005**, *229*(1), 206–212.

[213] J. Zhang, H. Kumagai, K. Yamamura, S. Ohara, S. Takami, A. Morikawa, H. Shinjoh, K. Kaneko, T. Adschiri, A. Suda, *Nano Lett.* **2011**, *11*(2), 361–364.

[214] X. Liu, K. Zhou, L. Wang, B. Wang, Y. Li, *J. Am. Chem. Soc.* **2009**, *131*(9), 3140–3141.

[215] P. X. Huang, F. Wu, B. L. Zhu, X. P. Gao, H. Y. Zhu, T. Y. Yan, W. P. Huang, S. H. Wu, D. Y. Song, *J. Phys. Chem. B* **2005**, *109*(41), 19169–19174.

[216] S. Agarwal, L. Lefferts, B. L. Mojet, *ChemCatChem* **2013**, *5*(2), 479–489.

[217] C. Yang, X. Yu, S. Heiß §ler, A. Nefedov, S. Colussi, J. Llorca, A. Trovarelli, Y. Wang, C. Wöll, *Angew. Chem. Int. Ed.* **2017**, *56*(1), 375–379.

[218] M. Nolan, *J. Chem. Phys.* **2009**, *130*(14), 144702.

[219] X. Huang, M. J. Beck, *Chem. Mater.* **2015**, *27*(17), 5840–5844.

[220] G. Preda, A. Migani, K. M. Neyman, S. T. Bromley, F. Illas, G. Pacchioni, *J. Phys. Chem. C* **2011**, *115*(13), 5817–5822.

[221] Y. J. Kim, Y. Gao, G. S. Herman, S. Thevuthasan, W. Jiang, D. E. McCready, S. A. Chambers, *J. Vac. Sci. Technol. A* **1999**, *17*(3), 926–935.

[222] G. S. Herman, *Phys. Rev. B: Condens. Matter* **1999**, *59*(23), 14899–14902.

[223] H. Nörenberg, J. H. Harding, *Surf. Sci.* **2001**, *477*(1), 17–24.

[224] Y. Lin, Z. Wu, J. Wen, K. R. Poeppelmeier, L. D. Marks, *Nano Lett.* **2014**, *14*(1), 191–196.

[225] J. Huang, Y. Yu, J. Zhu, R. Yu, *Sci. Chin. Mater.* **2017**, *60*(9), 903–908.

[226] S.-H. Zhong, G. Lu, X.-Q. Gong, *Chin. J. Catal.* **2017**, *38*(7), 1138–1147.

[227] U. Mueller, *Anorganische Strukturchemie*, Vieweg+Teubner Verlag, **2008**.

[228] P. H. Krupenie, *J. Phys. Chem. Ref. Data* **1972**, *1*(2), 423–534.

[229] N. Sergent, M. Epifani, T. Pagnier, *J. Raman Spectrosc.* **2006**, *37*(11), 1272–1277.

[230] C. Hess, J. H. Lunsford, *J. Phys. Chem. B* **2002**, *106*(25), 6358–6360.

[231] H. L. Tuller, A. S. Nowick, *J. Phys. Chem. Solids* **1977**, *38*(8), 859–867.

[232] Tana, M. Zhang, J. Li, H. Li, Y. Li, W. Shen, *Catal. Today* **2009**, *148*(1), 179–183.

[233] M. Kovacevic, B. L. Mojet, J. G. van Ommen, L. Lefferts, *Catal. Lett.* **2016**, *146*(4), 770–777.

[234] Z. Hu, X. Liu, D. Meng, Y. Guo, Y. Guo, G. Lu, *ACS Catal.* **2016**, *6*(4), 2265–2279.

[235] H. Y. Kim, G. Henkelman, *J. Phys. Chem. Lett.* **2012**, *3*(16), 2194–2199.

[236] D. Briggs, P. Seah, *Practical Surface Analysis, Auger and X-ray Photoelectron Spectroscopy*, Wiley, **1990**.

[237] G. Bond, C. Louis, D. Thompson, *Catalysis by Gold*, Imperial College Press, **2006**.

[238] D. Widmann, R. J. Behm, *Angew. Chem. Int. Ed.* **2011**, *50*(43), 10241–10245.

[239] C. Zhang, A. Michaelides, D. A. King, S. J. Jenkins, *J. Chem. Phys.* **2008**, *129*(19), 194708.

[240] C. Chai, S. Yang, Z. Liu, M. Liao, N. Chen, *Chin. Sci. Bull.* **2003**, *48*(12), 1198–1200.

[241] M. A. Henderson, C. L. Perkins, M. H. Engelhard, S. Thevuthasan, C. H. F. Peden, *Surf. Sci.* **2003**, *526*(1), 1–18.

[242] D. R. Mullins, S. H. Overbury, D. R. Huntley, *Surf. Sci.* **1998**, *409*(2), 307–319.

[243] A. Pfau, K. D. Schierbaum, *Surf. Sci.* **1994**, *321*(1), 71–80.

[244] E. Wuilloud, B. Delley, W. D. Schneider, Y. Baer, *Phys. Rev. Lett.* **1984**, *53*(2), 202–205.

[245] R.-R. Zhang, L.-H. Ren, A.-H. Lu, W.-C. Li, *Catal. Commun.* **2011**, *13*(1), 18–21.

[246] Y. Wang, D. Widmann, R. J. Behm, *ACS Catal.* **2017**, 2339–2345.

[247] D. Martin, D. Duprez, *J. Phys. Chem.* **1996**, *100*(22), 9429–9438.

[248] P. Lakshmanan, F. Averseng, N. Bion, L. Delannoy, J.-M. Tatibouët, C. Louis, *Gold Bull.* **2013**, *46*(4), 233–242.

[249] M. Manzoli, F. Boccuzzi, A. Chiorino, F. Vindigni, W. L. Deng, M. Flytzani-Stephanopoulos, *J. Catal.* **2007**, *245*(2), 308–315.

[250] A. Chiorino, M. Manzoli, F. Menegazzo, M. Signoretto, F. Vindigni, F. Pinna, F. Boccuzzi, *J. Catal.* **2009**, *262*(1), 169–176.

[251] F. Vindigni, M. Manzoli, A. Chiorino, F. Boccuzzi, *Gold Bull.* **2009**, *42*(2), 106–112.

[252] Y. Guan, D. A. J. Michel Ligthart, O. Pirgon-Galin, J. A. Z. Pieterse, R. A. van Santen, E. J. M. Hensen, *Top. Catal.* **2011**, *54*(5-7), 424–438.

[253] K. Ding, A. Gulec, A. M. Johnson, N. M. Schweitzer, G. D. Stucky, L. D. Marks, P. C. Stair, *Science* **2015**, *350*(6257), 189–192.

[254] B. Qiao, J. Liu, Y.-G. Wang, Q. Lin, X. Liu, A. Wang, J. Li, T. Zhang, J. Liu, *ACS Catal.* **2015**, *5*(11), 6249–6254.

[255] C. Zhang, A. Michaelides, D. A. King, S. J. Jenkins, *J. Am. Chem. Soc.* **2010**, *132*(7), 2175–2182.

[256] P. G. Lustemberg, Y. Pan, B. J. Shaw, D. Grinter, C. Pang, G. Thornton, R. Pérez, M. V. Ganduglia-Pirovano, N. Nilius, *Phys. Rev. Lett.* **2016**, *116*(23), 236101.

[257] F. C. Meunier, D. Tibiletti, A. Goguet, D. Reid, R. Burch, *Appl. Catal., A* **2005**, *289*(1), 104–112.

[258] L. Piccolo, D. Loffreda, F. J. Cadete Santos Aires, C. Deranlot, Y. Jugnet, P. Sautet, J. C. Bertolini, *Surf. Sci.* **2004**, *566*, 995–1000.

[259] W.-L. Yim, T. Nowitzki, M. Necke, H. Schnars, P. Nickut, J. Biener, M. M. Biener, V. Zielasek, K. Al-Shamery, T. Klüner, M. Bäumer, *J. Phys. Chem. C* **2007**, *111*(1), 445–451.

[260] L. Schimka, J. Harl, A. Stroppa, A. Grüneis, M. Marsman, F. Mittendorfer, G. Kresse, *Nat. Mater.* **2010**, *9*(9), 741–744.

[261] R. Coquet, K. L. Howard, D. J. Willock, *Chem. Soc. Rev.* **2008**, *37*(9), 2046–2076.

[262] C. M. Kalamaras, D. D. Dionysiou, A. M. Efstathiou, *ACS Catal.* **2012**, *2*(12), 2729–2742.

[263] J. Vecchietti, A. Bonivardi, W. Xu, D. Stacchiola, J. J. Delgado, M. Calatayud, S. E. Collins, *ACS Catal.* **2014**, *4*(6), 2088–2096.

[264] C. J. Guild, D. Vovchok, D. A. Kriz, A. Bruix, B. Hammer, J. Llorca, W. Xu, A. El-Sawy, S. Biswas, J. A. Rodriguez, S. D. Senanayake, S. L. Suib, *ChemCatChem* **2017**, *9*(8), 1373–1377.

[265] P. Atkins, J. De Paula, M. Bär, *Physikalische Chemie: 4. Auflage*, Wiley-VCH Verlag GmbH, **2006**.

[266] N. Dürr, *Partialoxidation von Methacrolein zu Methacrylsäure an Heteropolysäurekatalysatoren*, PhD Thesis, TU Darmstadt, **2014**.

[267] A. Drochner, D. Ohlig, S. Knoche, N. Gora, M. Heid, N. Menning, T. Petzold, H. Vogel, *Top. Catal.* **2016**, *59*(17), 1518–1532.

[268] S. Kuba, H. Knözinger, *J. Raman Spectrosc.* **2002**, *33*(5), 325–332.

[269] A. Filtschew, C. Hess, *J. Phys. Chem. C* **2017**, *121*(35), 19280–19287.

[270] B. M. Elliott, K. Sung, C. E. Miller, *J. Mol. Spectrosc.* **2015**, *312*, 78–86.

[271] N. F. Zobov, O. L. Polyansky, C. R. Le Sueur, J. Tennyson, *Chem. Phys. Lett.* **1996**, *260*(3), 381–387.

[272] J. Tennyson, P. F. Bernath, L. R. Brown, A. Campargue, M. R. Carleer, A. G. Császár, R. R. Gamache, J. T. Hodges, A. Jenouvrier, O. V. Naumenko, O. L. Polyansky, L. S. Rothman, R. A. Toth, A. C. Vandaele, N. F. Zobov, L. Daumont, A. Z. Fazliev, T. Furtenbacher, I. E. Gordon, S. N. Mikhailenko, S. V. Shirin, *J. Quant. Spectrosc. Radiat. Transfer* **2009**, *110*(9), 573–596.

[273] A. Badri, C. Binet, J.-C. Lavalley, *J. Chem. Soc., Faraday Trans.* **1996**, *92*(23), 4669–4673.

[274] A. Primo, T. Marino, A. Corma, R. Molinari, H. García, *J. Am. Chem. Soc.* **2011**, *133*(18), 6930–6933.

[275] M. Heber, C. Schilling, T. Gross, C. Hess, *Mater. Res. Soc. Symp. Proc.* **2015**, *1773*, 33–40.

[276] S. Sänze, A. Gurlo, C. Hess, *Angew. Chem. Int. Ed.* **2013**, *52*(13), 3607–3610.

Symbols and Abbreviations

Symbols

a_0, c_0	lattice constant of cubic and hexagonal crystal structures	Å	
$c_{\mu i}$	plane wave coefficient		
ΔR_k	displacement along the normal mode vector, here always 0.01 Å	Å	
$\boldsymbol{E}$	electric field vector		
E	total DFT energy of structure indicated by subscript	eV	
E^{el}	electronic energy		see equation 3.18
$E_{\mathrm{ads,O_2^{2-}}}$	adsorption energy for peroxide molecule	eV	def. in sec. 4.8
$E_{\mathrm{ads,O}}$	adsorption energy of a single O atom	eV	def. in sec.4.8
E_{cut}	total energy after the surface is cut from the bulk	eV	
$E_{\mathrm{surf,cut}}$	surface energy to cut the CeO$_2$(100) surface from the bulk	eV nm^{-2}	see equation 4.3
$E_{\mathrm{surf,relax}}$	surface relaxation energy of the CeO$_2$(100) surface	eV nm^{-2}	see equation 4.4
E_{surf}	surface energy of the CeO$_2$(100) surface	eV nm^{-2} / J m^{-2}	see equation 4.5
$E_{\mathrm{vac,O}}$	oxygen vacancy formation energy	eV	
$E_{\mathrm{xc}}[n]$	exchange correlation functional		
E_i	direction i of the electric field		see equation 3.18
$\hat{F}$	Fock operator		
$f_{i,j}$	second derivative of the potential energy with respect to normal mode i and j		
$G(R)$	correction factor for measured Raman intensity due to sample absorption		see equation 9.2
$\Delta\mathrm{H}^0$	standard reaction enthalpy	kJ mol^{-1}	
$\hat{H}$	Hamilton operator		
h, k, l	Miller Indices	-	
I^{Raman}	calculated Raman scattering intensity	Å^2 u$^{\frac{1}{2}}$	see equation 3.15
$J[n]$	Coulomb energy functional		
J_i	Coulomb operator		
K_j	exchange operator		
M	number of electrons		
M_A	mass of nuclei A	u	
m_e	mass of an electron		
N	number of nuclei		
$n(\vec{r})$	electron density		
nN	n th nearest neighbor		in (nN-mN, lN)
$N_{\mathrm{ncl}}[n]$	Coulomb energy functional		
q_i	mass weighted normal coordinate		

$\boldsymbol{R}_v$	transition moment		
R_∞	reflectivity		
r_{AB}	distance between nuclei A and nuclei B		
r_{iA}	distance between electron i and nuclei A		
r_{ij}	distance between electron i and j		
T	kinetic energy		
t_1	decay time for CO in the cell.	min	
$T_s[n]$	kinetic energy functional		
U_eff	effective Hubbard parameter	eV	
$U_s(\nu)$	displacement vector for frequency ν		
V	potential energy		
v	vibrational quantum number	-	
V_ext	external Potential		
x	charge of oxygen molecule in $O_2{}^{x-}$		see sec. 5.5
x	deviation from stoichiometry in CeO_{2-x}		
x, y, z	cartesian coordinates		
Z_A	charge of nuclei A	e	
Z_s^*	Born effective charge as calculated by DFPT approach		

Greek Symbols

$\boldsymbol{\alpha}$	polarizability tensor		
$\delta(COO)$	bending mode of e.g. COO structure		
δ_{ij}	Kronecker delta		
ϵ^∞	dielectric matrix		
ϵ_0	dielectric constant	$F\,m^{-1}$	
ϵ_i	eigenvalue i		
η^PW	plane wave η		
λ	eigenvalue of the Hessian matrix		
λ_ex	Raman excitation wavelength	nm	
μ	screening factor		in HSE06 Funct.
μ_ind	induced dipole moment	C m	
μ	dipole moment	C m	
$\nu(C{=}O)$	stretching mode of e.g. CO structure		
ν_ex	Raman excitation frequency	s^{-1}	
ν_vib	vibrational frequency	s^{-1}	
$\tilde{\nu}$	vibrational frequency / wavenumber expressed as reciprocal e.m. wavelength	cm^{-1}	
Ω	solid angle		
ω	angular frequency	s^{-1}	
Ω_cell	cell volume of the calculated model structure	$Å^3$	
ϕ	angle between superoxide molecule and surface normal, orthogonal to direction of θ at the $CeO_2(100)$ surface	°	see sec. 4.12
$\phi_i(\vec{r})$	Kohn-Sham orbitals		

Ψ	electronic wavefunction		
θ	angle between superoxide molecule and surface normal towards surface Ce^{4+} at the $CeO_2(100)$ surface	°	see sec. 4.12

Abbreviations

AFM	atomic force microscopy
CEM	controlled evaporation mixer
DFPT	density functional perturbation theory
DFT	density functional theory
DRIFTS	diffuse reflectance infrared Fourier transform spectroscopy
EDX	energy dispersive X-ray spectroscopy
EPR	electron paramagnetic resonance
FTIR	Fourier transform infrared
fwhm	full width at half maximum of a spectral band
GGA	generalized gradient approximation
HSE06	exchange correlation functional parameterized by Heyd, Scuseria and Ernzerhof
IR	infrared
KSE	Kohn-Sham equations
KSO	Kohn-Sham orbitals
LDA	local density approximation
LFM	liquid flow meter
MCT	mercury cadmium telluride
MFC	mass flow controller
NEB	nudge elastic band method
NN	nearest neighbor
NNN	next nearest neighbor
PAW	projector augmented wave
PBE	exchange correlation functional parameterized by Perdew, Burke and Ernzerhof
PES	potential energy surface
STM	scanning tunneling microscopy
TAP	temporal analysis of products
TEM	transmission electron microscopy
TPSR-IR	temperature-programmed surface reaction infrared
VASP	Vienna *ab initio* simulation package
vdW	van der Waals contributions/interactions
XPS	X-ray photoelectron spectroscopy

List of Figures

List of Tables

A Supporting Information for the Experimental Setup

In this work an independent fluid evaporation system was planned and realized to allow for a controlled evaporation of any fluid into a gas stream. In this setup the gas stream consists of $CO/O_2/Ar$, that is mixed by digital mass flow controllers (see scheme A.1). The setup was employed for the evaporation of water (H_2O and $H_2{}^{18}O$) to study the water-gas shift reaction in the *operando* Raman/UV-Vis spectroscopy setup. The red colored gas pipes and the reaction chamber can be heated externally to 100°C to avoid condensation of evaporated water.

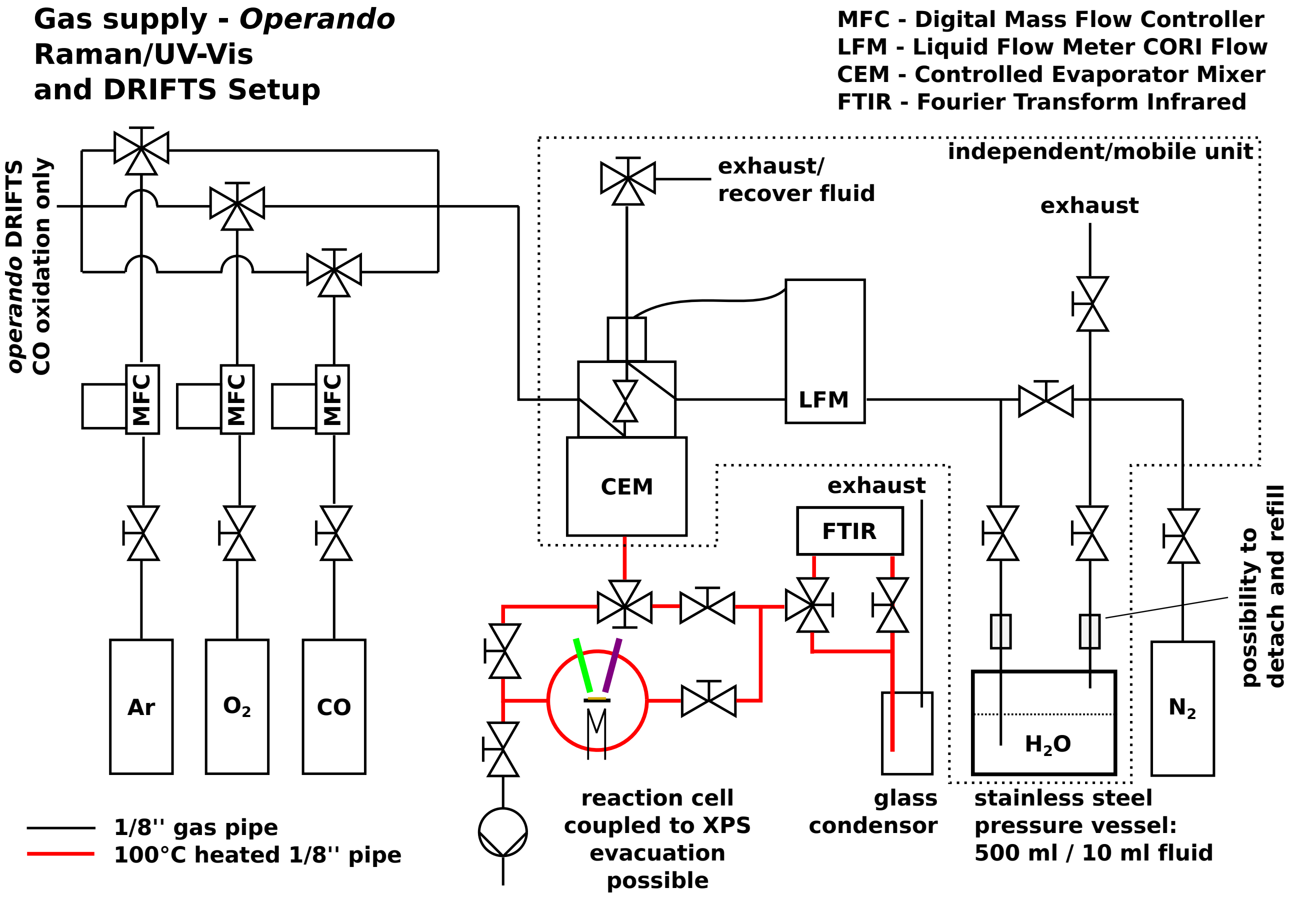

Figure A.1.: Scheme of the gas supply unit and the reaction chamber of the *operando* Raman/UV-Vis spectroscopy setup employed for CO oxidation and the water-gas shift reaction. Additionally the gas supply for *operando* diffuse infrared spectroscopy during CO oxidation is shown in the top left.

B Supporting Information for the DFT Calculations

In this part of the appendix detailed results of the density functional theory (DFT) calculations are given. The DFT total energy E_{tot} and derived energies, such as the vacancy formation energies $E_{\mathrm{vac,O}}$, as well as the model structures are provided as ball-and-stick models.

B.1 Performance and parallelization of VASP

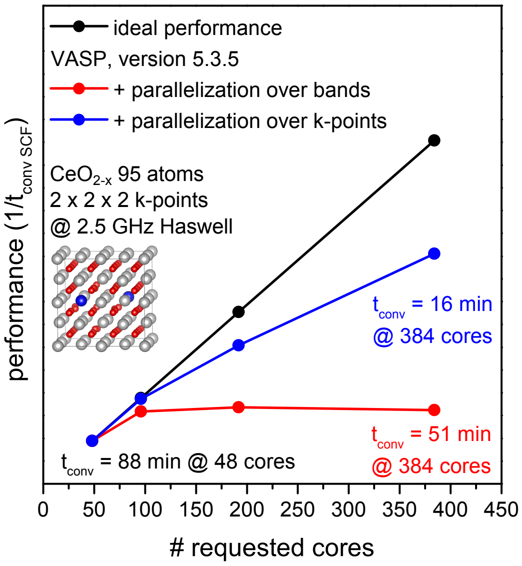

Figure B.1.: Performance (reciprocal of SCF convergence time $1/t_{\mathrm{conv}}$) for a standard PBE+U/4.5 eV calculation of a $Ce_{32}O_{63}$ supercell containing 95 atoms at 48, 96, 192, and 384 2.5 GHz Haswell cores. By proper parallelization over the calculated electron bands VASP is scalable to 96 cores. Employing *k*-point parallelization allows scalability up to 384 cores.

B.2 CeO_2 and CeO_{2-x} structures

Table B.1 lists the total energy E_{tot} and oxygen vacancy formation energies $E_{vac,O}$ for the oxygen defective ceria bulk structures (CeO_{2-x}). For the corresponding calculated Raman spectra see figure 4.4.

Table B.1.: Total energy E_{tot} and oxygen vacancy formation energy $E_{vac,O}$ for the reduced bulk structures without lattice relaxation. The vacancy formation energy is calculated with respect to $\frac{1}{2}E_{O_2}$ = 4.939 eV.

Structure	E_{tot} [eV]	$E_{vac,O}$ [eV]
$Ce_{32}O_{64}$	−789.379	
$Ce_{32}O_{63}$ (1N-1N, 1N)	−781.532	2.91
$Ce_{32}O_{63}$ (2N-2N, 4N)	−781.585	2.86
$Ce_{32}O_{63}$ (1N-2N, 3N)	−781.585	2.85
$Ce_{32}O_{62}$ (3x1N-1N, 1N)	−773.946	2.78 per O atom

B.3 $CeO_2(111)$ and $CeO_{2-x}(111)$ structures

Table B.2 lists the total energy E_{tot} and the vacancy formation energy $E_{vac,O}$ for the $CeO_2(111)$ and the reduced $CeO_{2-x}(111)$ surface structures. In table B.3 the Raman active vibrations of the oxidized $CeO_2(111)$ surface are summarized together with the assignments of the vibrational modes. The calculated spectra are depicted in figure 4.6.

Table B.2.: Total energy E_{tot} and oxygen vacancy formation energy $E_{vac,O}$ for the reduced $CeO_{2-x}(111)$ surface structures with (2 × 2) periodicity. The vacancy formation energy is calculated with respect to $\frac{1}{2}E_{O_2}$ = 4.939 eV.

Structure	E_{tot} [eV]	$E_{vac,O}$ [eV]
$CeO_2(111)$	−291.330	
$CeO_{2-x}(111)$ surface O vacancy	−284.126	2.27
$CeO_{2-x}(111)$ subsurface O vacancy	−284.499	1.89

Table B.3.: Calculated Raman active vibrations for the oxidized $CeO_2(111)$ surface in comparison with experimental Raman spectra. *d* indicates two degenerated longitudinal vibrations in *x* and *y* direction. The transversal vibrations in the *z* direction are non-degenerated. Note the comparable intensities of the modes at ~225 cm^{-1} and ~363 cm^{-1} (printed bold) for calculations with three and five O-Ce-O trilayers. The Raman intensities of structures with (1 × 1) periodicity are multiplied by a factor of four to be comparable to the structures with (2 × 2) periodicity.

$CeO_2(111)$ 3 TL (2 × 2) PBE+U/4.5 eV DFPT		$CeO_2(111)$ 5 TL (1 × 1) PBE+U/4.5 eV DFPT		$CeO_2(111)$ 3 TL (1 × 1) HSE06 finite diff.	Exp.	Assignment
Raman shift [cm^{-1}]	Intensity [$\mathring{A}^2$ $u^{\frac{1}{2}}$]	Raman shift [cm^{-1}]	Intensity [$\mathring{A}^2$ $u^{\frac{1}{2}}$]	Raman shift [cm^{-1}]	Raman shift [cm^{-1}]	
224.9	236 *d*	**225.1**	240 *d*	216.2 *d*	**246**	**topmost O-Ce longitudinal mode**
305.1	133 *d*	323.8	76 *d*	321.1 *d*	-	middle O-Ce-O trilayer
363.3	97 *d*	**364.6**	102 *d*	407.2 *d*	**402**	**topmost O-Ce transversal mode**
375.0	131 *d*	370.2	156 *d*	397.0 *d*	-	all O-Ce-O middle long.
		397.2	280 *d*		-	all O-Ce-O middle long.
422.8	376 *d*	432.0	1306 *d*	454.8 *d*	464	F_{2g} like
423.0	1600 *d*	432.3	2946 *d*	448.0 *d*	464	F_{2g} like
475.2	249 *d*	476.8	232 *d*	516.4 *d*		transversal mode of bottom O vs fixed Ce (model artifact)

B.4 Peroxide $O_2{}^{2-}/CeO_2(111)$ and superoxide $O_2{}^{-}/CeO_2(111)$ structures

Figures B.2 to B.5 show the peroxide $O_2{}^{2-}/CeO_{2-x}(111)$, reduced $CeO_{2-x}(111)$ surface and superoxide $O_2{}^{-}/CeO_{2-x}(111)$ structures, respectively. Table B.4 lists the results of the PBE+U/4.5 eV calculations such as total energy E_{tot}, peroxide Raman shift and peroxide bond length.

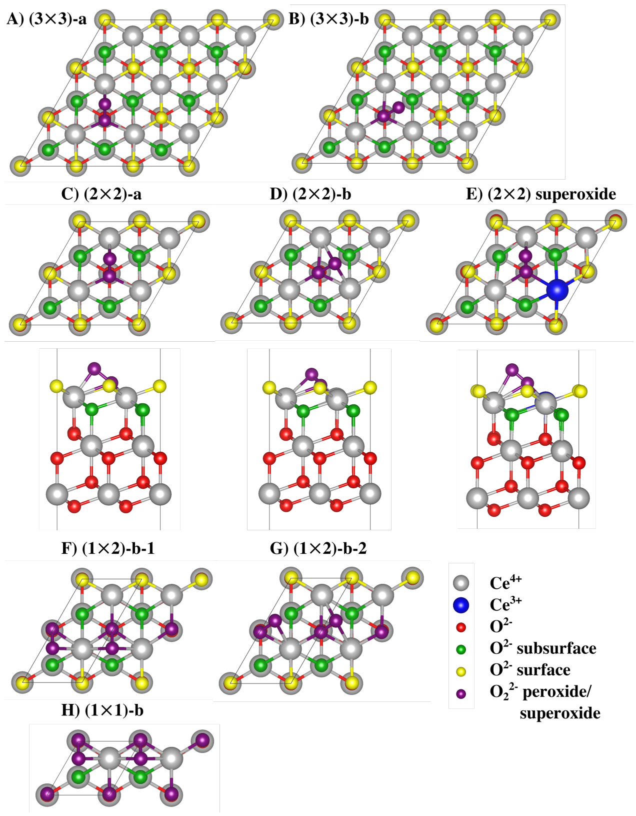

Figure B.2.: Peroxide $O_2{}^{2-}/CeO_{2-x}(111)$ structures with various periodicities. Top view of A) peroxide species leaning toward Ce^{4+} (configuration *a*) with (3 × 3) periodicity and B) peroxide species leaning toward O_{sub} (configuration *b*). Top and side views of C) configuration *a* with (2 × 2) periodicity, D) configuration *b* with (2 × 2) periodicity, and E) superoxide structure with (2 × 2) periodicity. Top view of F) configuration *b*-1 (rectangle) and G) configuration *b*-2, (parallelogram) with (1 × 2) periodicity. H) Top view of configuration *b* with (1 × 1) periodicity. The unit cell is indicated by black lines and doubled for the (1 × 2) and (1 × 1) structures for clarity. Violet balls indicate absorbed peroxide/superoxide species.

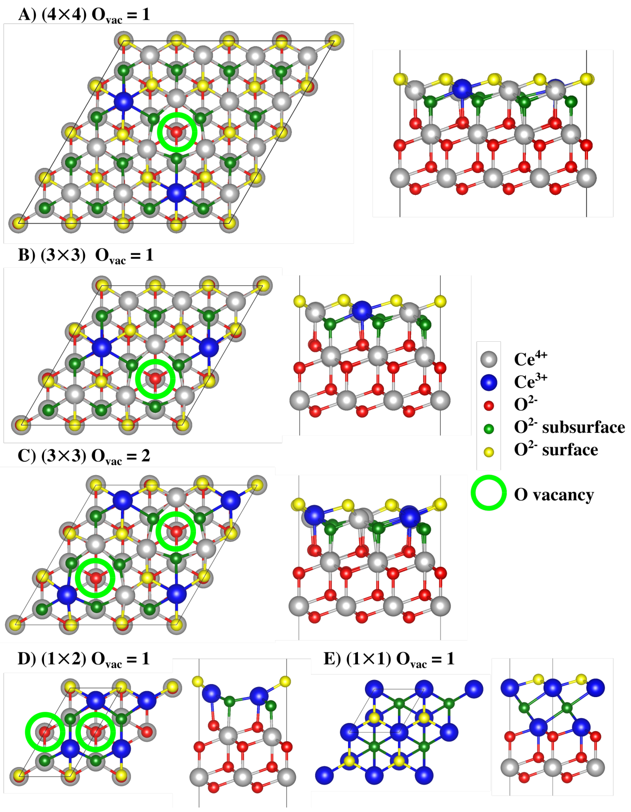

Figure B.3.: Top and side view of reduced $CeO_{2-x}(111)$ surfaces with A) (4 × 4) periodicity and an oxygen vacancy $O_{vac} = 1$, B) (3 × 3) periodicity and $O_{vac} = 1$, C) (3 × 3) periodicity and $O_{vac} = 2$, D) (1 × 2) periodicity and $O_{vac} = 1$ (doubled for clarity), and E) (1 × 1) periodicity (quadrupled for clarity, Ce_2O_3 quintuple overlayer). Grey balls indicate Ce^{4+}, blue balls Ce^{3+}, red balls bulk oxygen, green balls subsurface oxygen, and yellow balls surface oxygen.

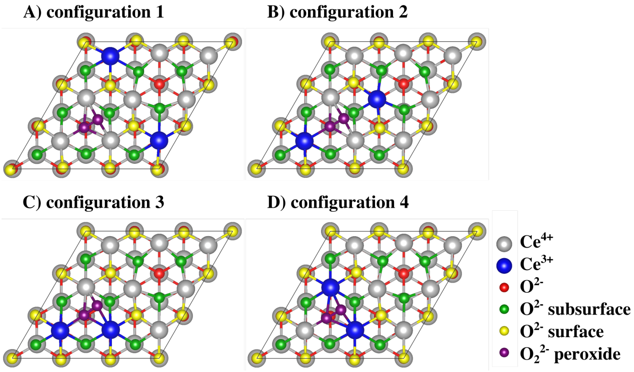

Figure B.4.: Top view of the peroxide $O_2{}^{2-}/CeO_{2-x}(111)$ configurations with $O_2{}^{2-}/O_{vac} = 0.5$ and (3×3) periodicity, i.e., surface oxygen vacancy plus an adsorbed peroxide molecule. Blue balls indicate the positions of the excess charge located at Ce^{3+} ions.

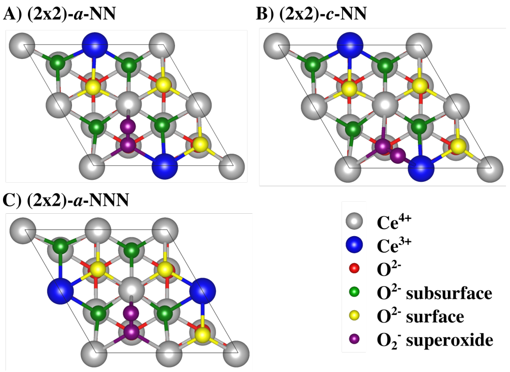

Figure B.5.: Top view of the superoxide $O_2{}^{-}/CeO_2(111)$ configurations with (2×2) periodicity and $O_{vac} = 1$. Configuration *a*-NN resembles the $O_2{}^{-}$ configuration for peroxide structures, in configuration *c*-NN $O_2{}^{-}$ leans towards a nearest neighbor Ce^{3+}, and in configuration *a*-NNN the Ce^{3+} is in next nearest neighbor (NNN) position.

Table B.4.: Total energy E_{tot}, oxygen vacancy formation energy $E_{vac,O}$ for the $CeO_2(111)$ surface with (4×4), (3×3), (2×2), (1×2) and (1×1) periodicity and $O_{vac} = 1$ and 2 with respect to $\frac{1}{2}E_{O_2} = 4.939$ eV. Molecular $E_{ads,O_2^{x-}}$ $(x = 1,2)$ and atomic $E_{ads,O}$ oxygen adsorption energies, for peroxide $O_2{}^{2-}$ and superoxide $O_2{}^{-}$ species at the $CeO_{2-x}(111)$ surface with respect to $E_{O_2} = 9.879$ eV, and at the $CeO_2(111)$ surface with respect to $\frac{1}{2}E_{O_2} = 4.939$ eV. Raman shift and Raman intensity for the stretching mode of the adsorbed oxygen species ($O_2{}^{x-}$, $x = 1,2$) and corresponding bond length. The calculated oxygen vacancy formation energy $E_{vac,O}$ is in accordance with literature values. [103, 110, 113]

Structure	Cov. [ML]	E_{tot} [eV]	$E_{vac,O}$ [eV]	$E_{ads,O_2^{x-}}$ [eV]	$E_{ads,O}$ [eV]	Raman shift [cm^{-1}]	Intensity [Å^2 u$^{\frac{1}{2}}$]	Bond length [Å]
(4×4) $O_{vac} = 0$		-1165.322						
(4×4) $O_{vac} = 1$		-1158.496	1.89					
(3×3) $O_{vac} = 0$		-655.506						
(3×3) $O_{vac} = 1$		-648.556	2.01					
(3×3) $O_{vac} = 2$		-641.045	2.57					
(2×2) $O_{vac} = 0$		-291.330						
(2×2) $O_{vac} = 1$		-284.125	2.27					
(1×2) $O_{vac} = 0$		-145.667						
(1×2) $O_{vac} = 1$		-138.029	2.70					
(1×1) $O_{vac} = 0$		-72.833						
(1×1) $O_{vac} = 1$		-65.623	2.27					

the table continues on the next page

Structure	Cov. [ML]	E_{tot} [eV]	$E_{\text{vac,O}}$ [eV]	$E_{\text{ads,O}_2^{x-}}$ [eV]	$E_{\text{ads,O}}$ [eV]	Raman shift [cm^{-1}]	Intensity [$\text{Å}^2\ \text{u}^{\frac{1}{2}}$]	Bond length [Å]
Peroxide $O_2{}^{2-}/CeO_{2-x}(111)$ $O_2{}^{2-}/O_{\text{vac}} = 1$								
(4 × 4) *a*	0.06	−1169.977		−1.60	0.28	893	3263	1.444
(4 × 4) *b*	0.06	−1169.952		−1.58	0.31	932	858	1.445
(3 × 3) *a*	0.11	−660.134		−1.70	0.30	894	2875	1.444
(3 × 3) *b*	0.11	−660.119		−1.68	0.32	933	920	1.445
(2 × 2) *a*	0.25	−295.905		−1.90	0.37	900	2160	1.443
(2 × 2) *b*	0.25	−295.924		−1.92	0.35	938	855	1.446
(1 × 2) *b*-1	0.50	−150.249		−2.34	0.36	940	1280	1.446
(1 × 2) *b*-2	0.50	−150.192		−2.28	0.41	952	680	1.436
(1 × 1) *b*	1.00	−77.275		−1.72	0.50	973	605	1.433
Peroxide $O_2{}^{2-}/CeO_{2-x}(111)$ $O_2{}^{2-}/O_{\text{vac}} = 0.5$								
(3 × 3) 1	0.11	−653.099		−2.18		941	650	1.443
(3 × 3) 2	0.11	−653.013		−2.09		930	1200	1.448
(3 × 3) 3	0.11	−652.993		−2.07		921	350	1.458
(3 × 3) 4	0.11	−652.924		−2.00		911	3000	1.461
Superoxide $O_2{}^{-}/CeO_{2-x}(111)$								
(2 × 2)-a	0.25	−295.294		−1.29	0.98	1134	11800	1.350
(2 × 2)-c	0.25	−295.214		−1.28	0.97	1132	2900	1.351
(2 × 2)-a-NNN	0.25	−295.427		−1.42	0.85	1134	3300	1.346
Molecular O_2								
O_2	gas	-9.879				1561		1.234

B.5 Peroxide $O_2^{2-}/CeO_{2-x}(100)$ and superoxide $O_2^{-}/CeO_{2-x}(100)$ structures

Figures B.6 to B.10 show the peroxide $O_2^{2-}/CeO_{2-x}(100)$, the oxygen defective $CeO_{2-x}(100)$ surface, the superoxide $O_2^{-}/CeO_{2-x}(100)$, and adsorbed oxygen $O_2/CeO_2(100)$ structures. Table B.5 and B.6 list the results of the calculations neglecting and including vdW contributions, respectively. Table B.7 lists the results for the adsorbed oxygen $O_2/CeO_2(100)$ structures.

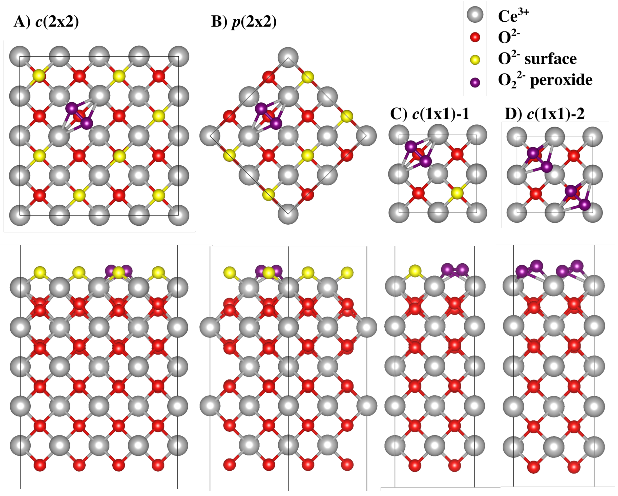

Figure B.6.: Top and side view of the peroxide $O_2^{2-}/CeO_{2-x}(100)$ structures with A) $c(2 \times 2)$, B) $p(2 \times 2)$, and C) $c(1 \times 1)$. periodicity. Violet balls indicate peroxide species.

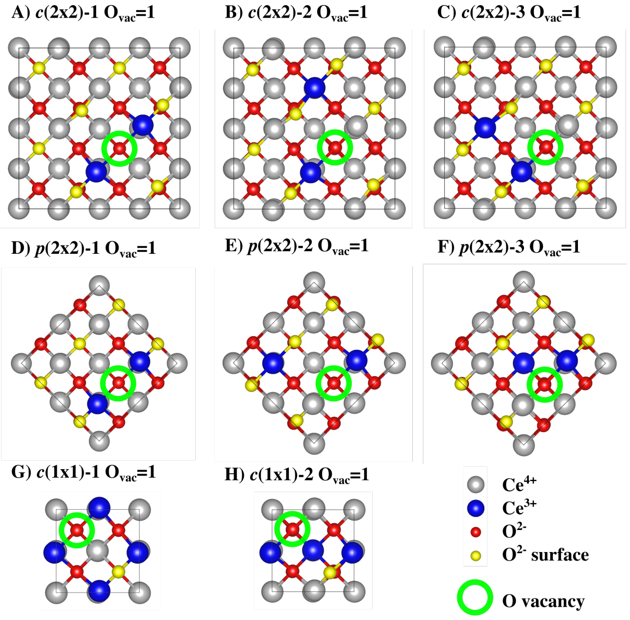

Figure B.7.: Top view of the oxygen defective $CeO_{2-x}(100)$ structures with A-C) $c(2\times2)$ periodicity, D-F) $p(2\times2)$ periodicity, and G-H) $c(1\times1)$ periodicity with $O_{vac} = 1$ and different localization of the excess charge. Grey balls indicate Ce^{4+}, blue balls Ce^{3+}, red balls bulk oxygen and yellow balls surface oxygen

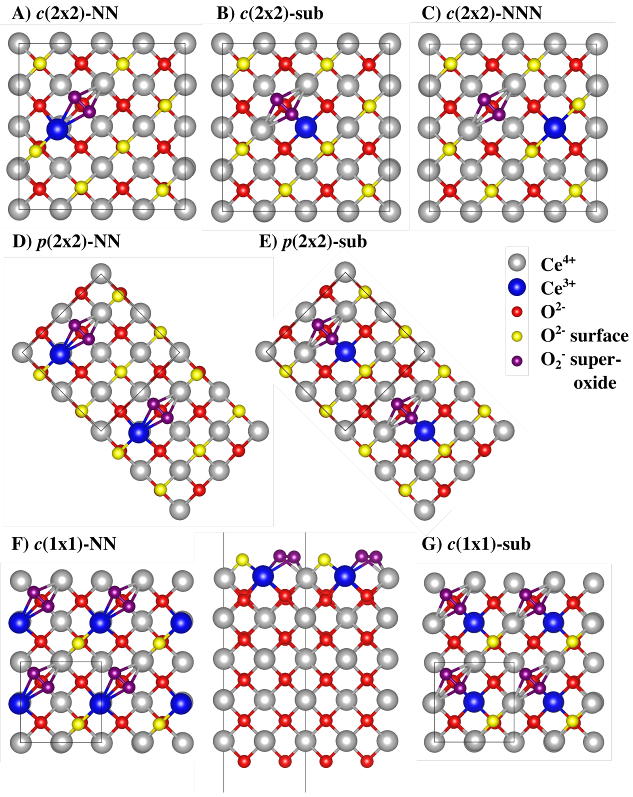

Figure B.8.: Superoxide O_2^-/CeO_{2-x} (100) structures with side on adsorption and $c(2 \times 2)$ periodicity with Ce^{3+} in A) nearest neighbor (NN), B) subsurface, and C) next nearest neighbor (NNN) position. Doubled $p(2 \times 2)$ periodicity with Ce^{3+} in D) (NN) and E) subsurface position. F) Top and side view of quadrupled $c(1 \times 1)$ periodicity and Ce^{3+} in NN position and G) $c(1 \times 1)$ with Ce^{3+} in subsurface position.

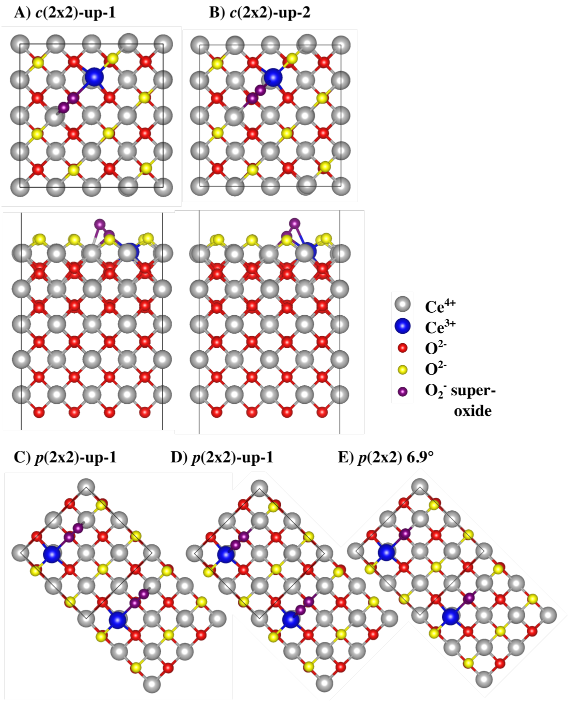

Figure B.9.: Superoxide O_2^-/CeO_{2-x} (100) structures with upright adsorption and A-B) $c(2 \times 2)$ and C-D) $p(2 \times 2)$ periodicity. The excess charge is localized in nearest neighbor (NN) position. In structures A) and C) superoxide leans towards Ce^{4+} and in B) and D) towards Ce^{3+}.

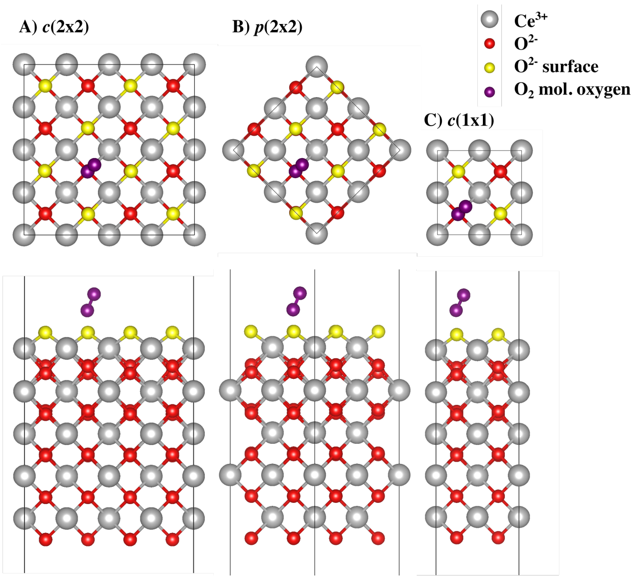

Figure B.10.: Top and side view of adsorbed oxygen $O_2/CeO_2(100)$ structures with A) $c(2 \times 2)$, B) $p(2 \times 2)$, and C) $c(1 \times 1)$ periodicity.

Table B.5.: Total energy E_{tot} and oxygen vacancy formation energy $E_{\text{vac,O}}$ for the $CeO_2(100)$ surface with $c(2\times2)$, $p(2\times2)$ and $c(1\times1)$ periodicity with respect to $\frac{1}{2}E_{O_2} = 4.939$ eV neglecting vdW contributions. Molecular $E_{\text{ads},O_2^{x-}}$ $(x = 1,2)$ and average atomic $E_{\text{ads,O}}$ oxygen adsorption energy of peroxide ($O_2{}^{2-}$) and superoxide ($O_2{}^{-}$) species at the $CeO_{2-x}(100)$ surface with respect to $E_{O_2} = 9.879$ eV, and at the $CeO_2(100)$ surface with respect to $\frac{1}{2}E_{O_2} = 4.939$ eV. Raman shift and Raman intensity for the $O_2{}^{x-}$ stretching mode and $O_2{}^{x-}$ $(x = 1,2)$ bond length. The calculated oxygen vacancy formation energy $E_{\text{vac,O}}$ is in accordance with literature values for $c(2\times2)$ periodicity. [57, 127] The calculations were done at 400 eV cutoff energy and neglecting vdW interactions. [a] one imaginary frequency.

Structure	Cov. [ML]	E_{tot} [eV]	$E_{\text{vac,O}}$ [eV]	$E_{\text{ads},O_2^{x-}}$ [eV]	$E_{\text{ads,O}}$ [eV]	Raman shift [cm^{-1}]	Intensity [$\text{Å}^2\ \text{u}^{\frac{1}{2}}$]	Bond length [Å]
$c(2\times2)$ $O_{\text{vac}} = 0$		−959.603						
$c(2\times2)$-1 $O_{\text{vac}} = 1$		−953.203	1.392					
$c(2\times2)$-2 $O_{\text{vac}} = 1$		−953.218	1.446					
$c(2\times2)$-3 $O_{\text{vac}} = 1$		−953.190	1.473					
$p(2\times2)$ $O_{\text{vac}} = 0$		−479.802						
$p(2\times2)$-1 $O_{\text{vac}} = 1$		−472.892	1.970					
$p(2\times2)$-2 $O_{\text{vac}} = 1$		−472.987	1.875					
$p(2\times2)$-3 $O_{\text{vac}} = 1$		−473.038	1.824					
$c(1\times1)$ $O_{\text{vac}} = 0$		−239.898						
$c(1\times1)$-1 $O_{\text{vac}} = 1$		−232.915	2.044					
$c(1\times1)$-2 $O_{\text{vac}} = 1$		−232.904	2.055					
Peroxide $O_2{}^{2-}/CeO_{2-x}(100)$								
$c(2\times2)$	0.125	−964.882		−1.732	−0.340	868	1407	1.468
$p(2\times2)$	0.25	−485.058		−2.141	−0.317	868	1075	1.468
$c(1\times1)$-1	0.5	−245.160		−2.367	−0.323	873	985	1.467
$c(1\times1)$-2	1.0	−250.066			−0.145	907	2637	1.455
Superoxide $O_2{}^{-}/CeO_{2-x}(100)$								
$c(2\times2)$ NN	0.125	−964.494		−1.344	0.048	1050	435	1.364
$c(2\times2)$ sub	0.125	−964.211		−1.061	0.331	1024	1120	1.374
$c(2\times2)$ NNN	0.125	−964.326		−1.176	0.216	1025		1.374
$c(2\times2)$ up-1 [a]	0.125	−964.148		−0.996	0.394	1174	233	1.334
$c(2\times2)$ up-2 [a]	0.125	−964.072		−0.922	0.471	1179	640	1.340
$p(2\times2)$ NN	0.25	−484.542		−1.625	0.199	1046	4514	1.371
$p(2\times2)$ sub	0.25	−484.296		−1.379	0.445	1014		1.382
$p(2\times2)$ up-1 [a]	0.25	−484.113		−1.196	0.628	1192	140	1.334
$p(2\times2)$ up-2 [a]	0.25	−484.141		−1.224	0.600	1188	35	1.339
$c(1\times1)$ NN	0.5	−244.626		−1.833	0.212	1070	1232	1.366
$c(1\times1)$ sub	0.5	−244.310		−1.517	0.528	1045		1.376

Table B.6.: Total energy E_{tot} and oxygen vacancy formation energy $E_{\mathrm{vac,O}}$ for the $CeO_2(100)$ surface with $p(2 \times 2)$ and $c(1 \times 1)$ periodicity with respect to $\frac{1}{2}E_{O_2} = 4.933$ eV including vdW contributions. Molecular $E_{\mathrm{ads},O_2^{x-}}$ $(x = 1, 2)$ and average atomic $E_{\mathrm{ads,O}}$ oxygen adsorption energy of peroxide ($O_2{}^{2-}$) and superoxide ($O_2{}^{-}$) species at the $CeO_{2-x}(100)$ surface with respect to $E_{O_2} = 9.866$ eV and at the $CeO_2(100)$ surface with respect to $\frac{1}{2}E_{O_2} = 4.933$ eV. Raman shift (finite differences approach at 10^{-8} eV energy convergence) for the $O_2{}^{x-}$ stretching mode and $O_2{}^{x-}$ $(x = 1, 2)$ bond length. [a] calculated at 600 eV cutoff energy [57]. [b] one imaginary frequency. [c] two imaginary frequencies.

Structure	Cov. [ML]	E_{tot} [eV]	$E_{\mathrm{vac,O}}$ [eV]	$E_{\mathrm{ads},O_2^{x-}}$ [eV]	$E_{\mathrm{ads,O}}$ [eV]	Raman shift [cm^{-1}]	Intensity [$\mathrm{Å}^2\ \mathrm{u}^{\frac{1}{2}}$]	Bond length [Å]
$p(2 \times 2)$ $O_{\mathrm{vac}} = 0$		−487.197						
$p(2 \times 2)$ $O_{\mathrm{vac}} = 0$ [a]		−486.557						
$p(2 \times 2)$-3 $O_{\mathrm{vac}} = 1$		−480.336	1.928					
$p(2 \times 2)$-3 $O_{\mathrm{vac}} = 1$ [a]		−479.711	1.901					
$c(1 \times 1)$ $O_{\mathrm{vac}} = 0$		−243.596						
$c(1 \times 1)$ $O_{\mathrm{vac}} = 1$		−236.529	2.134					
Peroxide $O_2{}^{2-}/CeO_{2-x}(100)$								
$p(2 \times 2)$ flat	0.25	−492.540		−2.338	−0.410	868	-	1.470
$p(2 \times 2)$ flat [a]	0.25	−491.893		−2.29	−0.403	857.2	-	1.472
$c(1 \times 1)$-1	0.5	−248.945		−2.550	−0.410	870	-	1.469
$c(1 \times 1)$-2	1	−253.951			−0.238	908	-	1.455
Superoxide $O_2{}^{-}/CeO_{2-x}(100)$								
$p(2 \times 2)$ flat NN	0.25	−491.997		−1.795	0.133	1043	-	1.373
$p(2 \times 2)$ flat sub	0.25	−491.742		−1.540	0.387	1026	-	1.384
$p(2 \times 2)$ up-1 [b]	0.25	−491.538		−1.336	0.592	1194	-	1.325
$p(2 \times 2)$ up-2 [b]	0.25	−491.562		−1.360	0.567	1189	-	1.338
$p(2 \times 2)$ 6.9° [a,c]	0.25	−490.713		−1.112	0.778	1125	-	1.342
Molecular O_2								
O_2	gas	−9.866				1563	-	1.235
O_2 [c]	gas	−9.890					-	1.233

Table B.7.: Total energy E_{tot} and molecular adsorption energy E_{ads,O_2} of oxygen at the $CeO_2(100)$ surface with respect to $E_{O_2} = 9.879$ eV. Raman shift and Raman intensity of the O_2 stretching mode and O_2 bond length.

Structure	Cov. [ML]	E_{tot} [eV]	$E_{\text{vac},O}$ [eV]	$E_{\text{ads},O_2^{x-}}$ [eV]	$E_{\text{ads},O}$ [eV]	Raman shift [cm^{-1}]	Intensity [$\text{Å}^2\ u^{\frac{1}{2}}$]	Bond length [Å]
$c(2 \times 2)$ $O_{\text{vac}} = 0$		−959.603						
$p(2 \times 2)$ $O_{\text{vac}} = 0$		−479.802						
$c(1 \times 1)$ $O_{\text{vac}} = 0$		−239.898						
Molecular $O_2/CeO_2(100)$								
$c(2 \times 2)$	0.125	−969.550		−0.069		1544	3270	1.233
$p(2 \times 2)$	0.25	−489.746		−0.066		1545	4103	1.233
$c(1 \times 1)$	0.5	−249.837		−0.060		1550	1742	1.233
Molecular O_2								
O_2	gas	−9.866				1561		1.235

B.6 Water adsorption at the $CeO_2(111)$ and the $CeO_2(100)$ surface

Figures B.11 and B.12 depict the stable of adsorbed water at the $CeO_2(111)$ and $CeO_2(100)$ surface, respectively. In table B.8 the total energy E_{tot} and adsorption energy E_{ads,H_2O} are summarized. For the calculated Raman spectra of the structures, refer to figures 4.22 and 4.23.

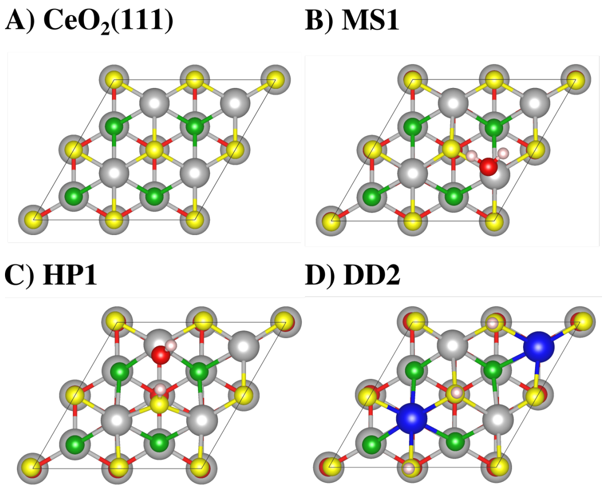

Figure B.11.: Top view of the A) oxidized CeO$_2$(111) surface, B) molecular, and C) hydroxyl pair type adsorption of H_2O at the CeO$_2$(111) surface and D) dissociative adsorption at the reduced CeO$_{2-x}$(111) surface.

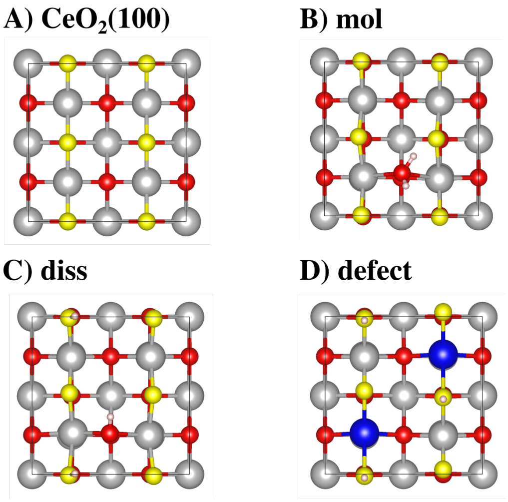

Figure B.12.: Top view of the A) oxidized CeO$_2$(100) surface, B) molecular, and C) dissociative adsorption of H_2O at the CeO$_2$(100) surface and D) dissociative adsorption at the reduced CeO$_{2-x}$(100) surface.

Table B.8.: Total energy E_{tot} and adsorption energy of H_2O at CeO$_2$(111) and CeO$_2$(100) surface $E_{\mathrm{ads,H_2O}}$ with respect to $E_{\mathrm{H_2O}}$ = 14.229 eV. For the structures with $p(2 \times 2)$ periodicity refer to figures B.11 and B.12.

Structure	$p(2 \times 2)$		$c(2 \times 2)$	
	E_{tot} [eV]	$E_{\mathrm{ads,H_2O}}$ [eV]	E_{tot} [eV]	$E_{\mathrm{ads,H_2O}}$ [eV]
CeO$_2$(111)	−291.330			
CeO$_2$(111) + H_2O (MS1)	−306.094	−0.535		
CeO$_2$(111) + H_2O (HP1)	−306.072	−0.512		
CeO$_{2-x}$(111)	−284.126			
CeO$_{2-x}$(111) + H_2O (DD2)	−300.445	−2.024		
CeO$_2$(100)	−479.802		−959.603	
CeO$_2$(100) + H_2O (mol)	−495.006	−0.975	−974.817	−0.986
CeO$_2$(100) + H_2O (diss)	−495.558	−1.549	−975.511	−1.679
CeO$_{2-x}$(100)	−472.988			
CeO$_{2-x}$(100) + H_2O	−489.953	−2.736		

B.7 Carbonate and formate formation at the CeO$_2$(111) surface

Figure B.13 depicts the most stable structures for carbonate, hydrogen carbonate, and formate formation at the CeO$_2$(111) surface. Table 8.6 lists the corresponding total energies E_{tot} and adsorption energies $E_{\mathrm{ads,CO_2}}$.

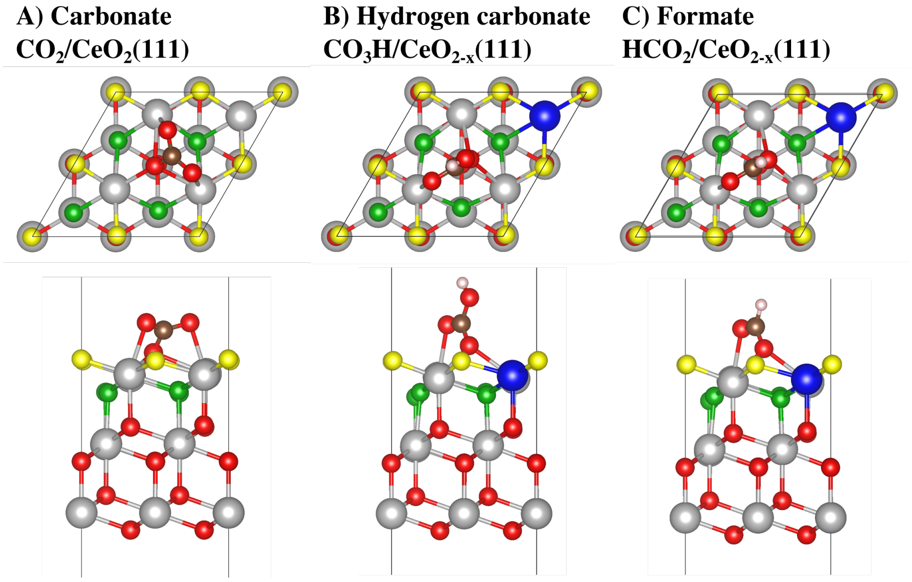

Figure B.13.: Top and side view of the most stable A) carbonate CO$_2$/CeO$_2$(111), B) hydrogen carbonate CO$_3$H/CeO$_{2-x}$(111), and C) formate HCO$_2$/CeO$_{2-x}$(111) structure.

Table B.9.: Total energy E_{tot} of the most stable carbonate, hydrogen carbonate, and formate species and adsorption energy of CO_2, $E_{\mathrm{ads,CO_2}}$ for the carbonate structure calculated with respect to the gas-phase molecule. NNN refers to the next nearest neighbor position of the Ce^{3+} with respect to the carbonate/formate and NN to the nearest neighbor position. In plane and out of plane refers to Ce^{3+} localization in or out of the plane spanned by the carbonate/formate molecule. -*b* refers to the proton pointing to the surface, no letter refers to the proton pointing away from the surface.

Structure	E_{tot} [eV]	$E_{\mathrm{ads,CO_2}}$ [eV]
$CeO_2(111)$	−291.330	
$CO_2/CeO_2(111)$	−314.833	−0.515
$CO_3H/CeO_{2-x}(111)$ NNN	−319.353	
$CO_3H/CeO_{2-x}(111)$ NN, out plane	−319.196	
$CO_3H/CeO_{2-x}(111)$ NN, in plane	−319.192	
$CO_3H/CeO_{2-x}(111)$ NNN-*b*	−319.316	
$CO_3H/CeO_{2-x}(111)$ NN, in plane-*b*	−319.151	
$HCO_2/CeO_{2-x}(111)$ NNN	−311.994	
$HCO_2/CeO_{2-x}(111)$ NN, out plane	−311.829	
$HCO_2/CeO_{2-x}(111)$ NN, in plane	−311.818	
CO_2 gas	−22.988	
H_2 gas	−6.760	
CO gas	−14.806	

B.8 Au/CeO_2(111) and CO-Au/CeO_2(111) structures

The structures to mimic CO adsorption at Au/CeO_2 model catalysts described in chapter 8 are shown in figure 8.6. The corresponding total energies E_{tot}, Au and CO adsorption energies, $E_{\mathrm{ads,Au}}$ and $E_{\mathrm{ads,CO}}$, and CO stretch frequencies for the structures are given in table B.10 and B.11. For a detailed discussion the reader is referred to sections 8.3 and 8.4.

Table B.10.: Total energy E_{tot} (PBE+U/4.5 eV or HSE06 functional), gold (Au) oxidation state, Au adsorption energy $E_{\mathrm{ads,Au}}$ at the $CeO_2(111)$ surface, CO adsorption energy $E_{\mathrm{ads,CO}}$, and CO stretch frequency. All structures possess (2 × 2) periodicity. For the first two structures the cell is 31 Å in hight and for the rest 43 Å in hight, corresponding to 24 Å and 36 Å vacuum between the ceria surface slabs.

Structure	Funct.	$Au_1{}^x$	E_{tot} [eV]	$E_{\mathrm{ads,Au}}$ [eV]	$E_{\mathrm{ads,CO}}$ [eV]	$\tilde{\nu}_{\mathrm{CO}}$ [cm^{-1}]
$CeO_2(111)$ cell height 31 Å	PBE		−291.330			
	PBE+vdW		−295.480			
	HSE		−382.006			
$CO/CeO_2(111)$	PBE		−306.321		−0.185	2126.2
	PBE+vdW		−310.567		−0.281	2129.5
	HSE		−400.382		−0.150	2250.7
$CeO_2(111)$ cell height 44 Å	PBE		−291.318			
	PBE+vdW		−295.467			
	HSE		−381.990			
$Au/CeO_2(111)$ Au@O, Ce^{3+} NN	PBE	$Au_1{}^+$	−292.469	−0.966		
	PBE+vdW	$Au_1{}^+$	−296.822	−1.170		
	HSE	$Au_1{}^0$	−382.994	−0.483		
$Au/CeO_2(111)$ Au@O Ce^{3+} NNN	PBE	$Au_1{}^+$	−292.520	−1.017		
	PBE+vdW	$Au_1{}^+$	−296.882	−1.230		
	HSE	$Au_1{}^+$	−383.014	−0.503		
$Au/CeO_2(111)$ Au@Ce bridged	PBE	$Au_1{}^0$	instable			
	PBE+vdW	$Au_1{}^0$	instable			
	HSE	$Au_1{}^0$	−383.042	−0.531		
$Au/CeO_2(111)$ O-O bridge, Ce^{3+} NN	PBE	$Au_1{}^+$	−292.564	−1.061		
	PBE+vdW	$Au_1{}^+$	−296.903	−1.251		
	HSE	$Au_1{}^+$	−382.948	−0.437		
$Au/CeO_2(111)$ O-O bridge, Ce^{3+} NNN	PBE	$Au_1{}^+$	−292.712	−1.209		
	PBE+vdW	$Au_1{}^+$	−297.038	−1.386		
	HSE	$Au_1{}^+$	−383.098	−0.587		
$CO\text{-}Au/CeO_2(111)$ Au@O, Ce^{3+} NN	PBE	$Au_1{}^+$	−309.924		−2.406	2094.6
	PBE+vdW	$Au_1{}^+$	−314.305		−2.461	2094.5
	HSE	$Au_1{}^+$	−403.623		−2.299	2219.4
$CO\text{-}Au/CeO_2(111)$ Au@O, Ce^{3+} NNN	PBE	$Au_1{}^+$	−310.023		−2.505	2091.5
	PBE+vdW	$Au_1{}^+$	−314.399		−2.555	2094.2
	HSE	$Au_1{}^+$	−403.752		−2.428	2217.2
$CeO_{2-x}(111)$	PBE		−284.126			
$Au/CeO_{2-x}(111)$ $Au@O_{\mathrm{vac}}$, Ce^{3+} NN	PBE	$Au_1{}^-$	−286.507	−2.196		
$Au/CeO_{2-x}(111)$ $Au@O_{\mathrm{vac}}$, Ce^{3+} NNN	PBE	$Au_1{}^-$	−286.750	−2.439		

Table B.11.: Total energy E_{tot} (PBE+U/4.5 eV or HSE06 functional), gold (Au) oxidation state, Au adsorption energy $E_{\text{ads,Au}}$, CO adsorption energy $E_{\text{ads,CO}}$, and CO stretch frequency. The $CeO_2(111)$ surface structures possess (3 × 3) periodicity. [a] During finite differences calculations the energy convergence criterion was 10^{-6} eV. [b] The lattice constant of fcc gold is determined as a_0 = 4.153 Å (PBE+U/4.5 eV) and 4.124 Å (HSE06). Calculations of the CO-Au(111) structure with the HSE06 functional were carried out at a_0 = 4.140 Å.

Structure	Funct.	$Au_y{}^x$	E_{tot} [eV]	$E_{\text{ads,Au}}$ [eV]	$E_{\text{ads,CO}}$ [eV]	$\tilde{\nu}_{\text{CO}}$ [cm^{-1}]
$Au_4/CeO_2(111)$	PBE	$Au_4{}^{2+}$	−665.390			
	HSE	$Au_4{}^{2+}$	−869.467			
$CO\text{-}Au_4/CeO_2(111)$	PBE	$Au_4{}^{2+}$	−681.118		−0.922	2069.5
$CO@Au_{\text{top}}$	HSE	$Au_4{}^{2+}$	−888.461		−0.768	2199.4
$CO\text{-}Au_4/CeO_2(111)$	PBE	$Au_4{}^{2+}$	−681.562		−1.366	2086.3
$CO@Au_{\text{bottom},1}$	HSE	$Au_4{}^{2+}$	−888.950		−1.257	2214.7
$CO\text{-}Au_4/CeO_2(111)$	PBE	$Au_4{}^{2+}$	−681.593		−1.397	2085.5
$CO@Au_{\text{bottom},2}$	HSE	$Au_4{}^{2+}$	−888.982		−1.289	2213.9
$Au_4/CeO_{2-x}(111)$	PBE	$Au_3{}^{2+}/Au_1{}^{-}$	−658.092			
Au_1	PBE	$Au_1{}^0$	−0.185			
	PBE+vdW	$Au_1{}^0$	−0.185			
	HSE	$Au_1{}^0$	−0.521			
$CO\text{-}Au_1$	PBE	$Au_1{}^0$	−15.803		−0.812	2068.8
	HSE [a]	$Au_1{}^0$	−18.700		−0.407	2197.5
Au(111)	PBE		−35.642			
	HSE		−18.611			
CO-Au(111)	PBE	Au^0	−50.530		−0.082	2045.3
$CO@Au_{\text{top}}$	HSE [b]	Au^0	−37.710		−0.873	2140.9
CO	PBE		−14.806			2121.9
	PBE+vdW		−14.806			2124.5
	HSE		−18.226			2235.7
CO_2	PBE		−22.989			section 4.15

C Supporting Information for the Experimental Results

In this chapter supporting information for the experimental studies are given. The data in section C.1 corresponds to the study on the oxygen defect dynamics during CO oxidation over a Au/CeO$_2$ catalyst in chapter 7, the data in section C.2 to the study on CO adsorption at the Au/CeO$_2$ catalyst studied by infrared spectroscopy in chapter 8, and the data in section C.3 to the study on the water-gas shift reaction over Au/CeO$_2$ catalysts in chapter 9.

C.1 Support dynamics in ceria supported gold catalysts

Figure C.1 depicts the Ce3d photoemission of a 0.5 wt% Au/CeO$_2$ catalyst and figure C.2 shows the position of the Raman band around 246 cm^{-1} during the dynamic *operando* experiments.

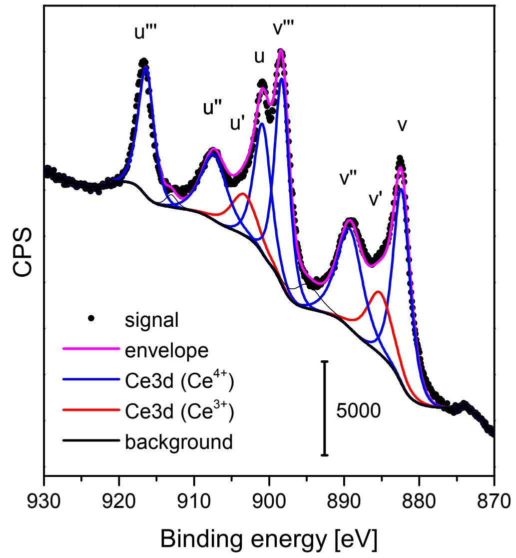

Figure C.1.: Ce3d emission of the X-ray photoelectron spectrum of a 0.5 wt% Au/CeO$_2$ catalyst. Spin orbit splitting into a d$_{5/2}$ and a d$_{3/2}$ component is indicated by u and v. Final states of Ce^{4+} are indicated as v, u, v″, u″, v‴, and u‴ and final states of Ce^{3+} are indicated as v′ and u′. For deconvolution 10 Gauss-Lorentz components (70/30) were employed with the following constraints: The energy difference due to spin orbit splitting was set to 18.1 eV [140], the intensity (area) of the component was set to I(d$_{5/3}$) = 1.5 I(d$_{3/2}$) and the corresponding u and v components possessed an identical line width (fwhm <4.1 eV).

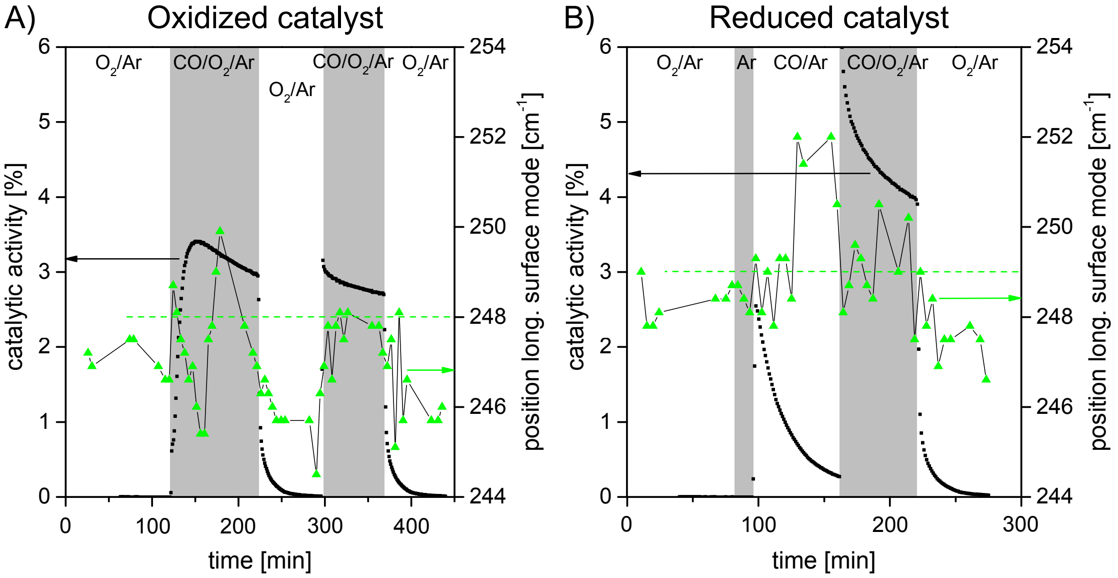

Figure C.2.: Time-dependent Raman spectroscopic information for the position of the $CeO_2(111)$ longitudinal surface mode of a 0.5 wt% Au/CeO_2 catalyst during A) two consecutive exposures to reaction conditions and during B) reaction after reducing pretreatment. Dashed lines indicate the steady-state position during exposure to reaction conditions (2 % CO, 10 % O_2, 100 ml/min).

C.2 Spectroscopic evidence for single gold site formation at Au/CeO$_2$ catalysts during CO oxidation

Figures C.3 and C.4 show the temporal evolution of the catalytic activity of a 0.5 wt% Au/CeO$_2$ catalyst (black dots) and the results obtained from *dynamic operando* infrared spectra. These data provide the basis for the evaluation discussed in chapter 8.

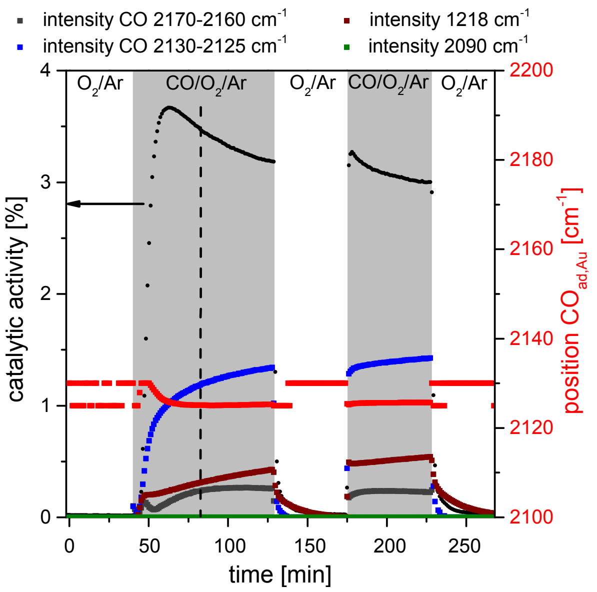

Figure C.3.: Catalytic activity (black) of a 0.5 wt% Au/CeO$_2$ catalyst equilibrated in 25 % O$_2$ (100 ml/min) and then exposed to reaction conditions (grey background, 2 % CO and 10 % O$_2$). Grey dots indicate the intensity of the component at 2160 – 2170 cm^{-1}, blue dots indicate the intensity of the component at 2125 – 2130 cm^{-1}, and green dots indicate the intensity of the component at 2090 cm^{-1} from deconvolution analysis. Red dots refer to the precise position of the band between 2125 and 2130 cm^{-1}. Brown dots indicate the integrated intensity of the band at 1218 cm^{-1}, which is assigned to hydrogen carbonate.

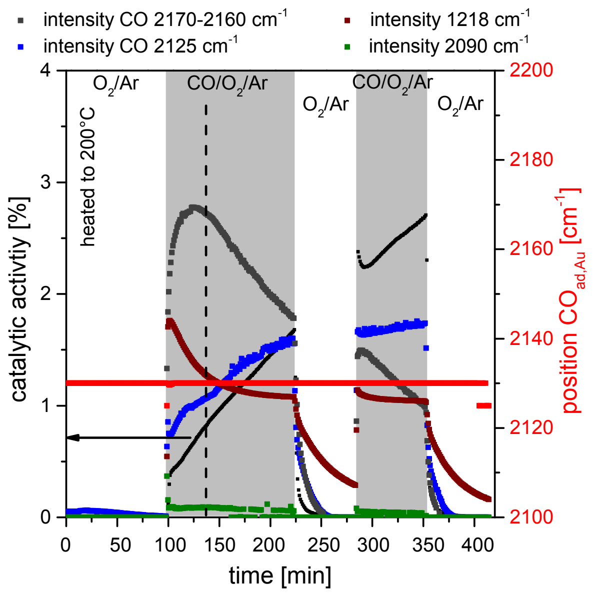

Figure C.4.: Catalytic activity (black) of a 0.5 wt% Au/CeO$_2$ catalyst heated *in situ* to 200°C in 25 % O$_2$ (100 ml/min) prior to the experiment at room temperature and then exposed to reaction conditions (grey background, 2 % CO and 10 % O$_2$). Grey dots indicate the intensity of the component at 2160 – 2170 cm^{-1}, blue dot indicate the intensity of the component at 2125 – 2130 cm^{-1}, and green dots indicate the intensity of the component at 2090 cm^{-1} from deconvolution analysis. Red dots refer to the precise position of the band between 2125 and 2130 cm^{-1}. Brown dots indicate the integrated intensity of the band at 1218 cm^{-1}, which is assigned to hydrogen carbonate.

C.3 Water-gas shift reaction over Au/CeO$_2$ catalysts: *Operando* Raman spectroscopy

Figures C.5 to C.7 show the phonon, adsorbate, and hydroxyl region of *operando* Raman spectra of the bare ceria support in CO/H$_2$^{18}O atmosphere. Figure C.8 shows the hydroxyl region of the support in CO/H$_2$^{16}O.

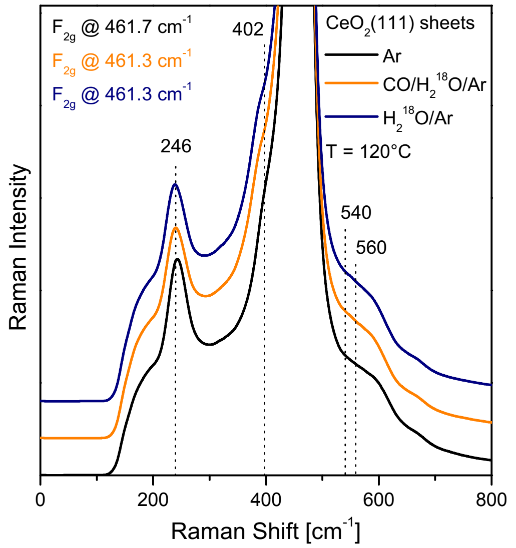

Figure C.5.: *Operando* Raman spectra (phonon region) of a the CeO_2 support during water-gas shift reaction conditions (2 % CO, 8 % $H_2{}^{18}O$, orange). For comparison spectra in Ar prior reaction (black) and in 8 % $H_2{}^{18}O$ after reaction (dark blue) are shown. The F_{2g} band is cut and the position of the F_{2g} band given at the top left. The spectra are offset for clarity.

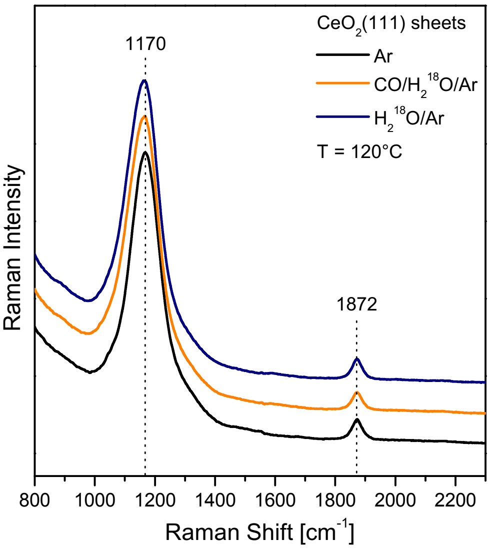

Figure C.6.: *Operando* Raman spectra (carbonate region) of the CeO_2 support during water-gas shift reaction conditions (2 % CO, 8 % $H_2{}^{18}O$, orange). For comparison spectra in Ar prior reaction (black) and in 8 % $H_2{}^{18}O$ after reaction (dark blue) are shown. The spectra are offset for clarity.

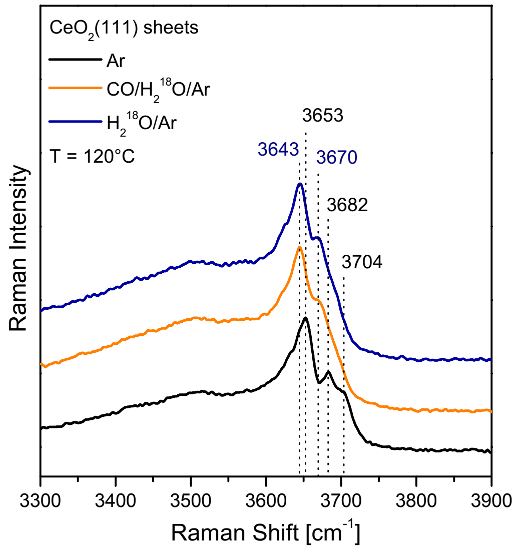

Figure C.7.: *Operando* Raman spectra (hydroxyl region) of the CeO_2 support during water-gas shift reaction conditions (2 % CO, 8 % $H_2{}^{18}O$, orange). For comparison spectra in Ar prior reaction (black) and in 8 % $H_2{}^{18}O$ after reaction (dark blue) are shown. The spectra are offset for clarity.

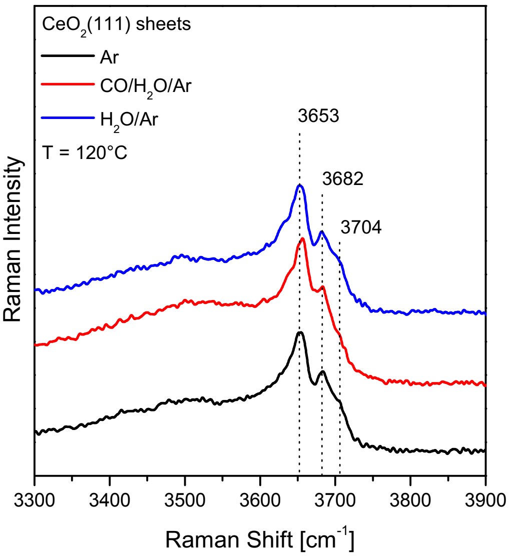

Figure C.8.: *Operando* Raman spectra (hydroxyl region) of the CeO_2 support during water-gas shift reaction conditions (2 % CO, 8 % $H_2{}^{16}O$ red). For comparison spectra in Ar prior reaction (black) and in 8 % $H_2{}^{16}O$ after reaction (blue) are shown. The spectra are offset for clarity.

Christian Michael Schilling - Curriculum Vitae

Neckarstraße 5
64283 Darmstadt
born 20.02.1991 in Gelnhausen
married

Professional Experience

since 01/2017	**Research Assistant**, Technische Universität Darmstadt, Eduard-Zintl-Institut, Group of Prof. Dr. C. Hess

Education

since 10/2014	**Doctoral Student**, Technische Universität Darmstadt, Eduard-Zintl-Institut, Group of Prof. Dr. C. Hess Topic: *Operando* spectroscopy and DFT modeling of gold/ceria catalysts
01/2015 - 12/2016	**Scholarship for Doctoral Studies** from the Merck'sche Gesellschaft für Kunst und Wissenschaft e.V.
06/2016 - 08/2016	**Research Stay** at the Institute for Catalysis and Petrochemistry, Madrid, Spain with Dr. M. V. Ganduglia-Pirovano
04/2016	**Master of Science in Chemistry**, Technische Universität Darmstadt, Grade 1.0 **with honors**. Equivalent to **Dipl. Ing.** (see certificate)
01/2015	**Research Visit** at the Inorganic Chemistry Department of the Fritz-Haber-Institut, Berlin
10/2013 - 10/2014	**Preliminary Studies for Doctoral Thesis**, TU Darmstadt Program: **Master of Science Chemistry for Excellent Students** Specialization: Physical Chemistry and Chemical Engineering Further Subjects: Inorganic and Theoretical Chemistry
10/2010 - 10/2013	**Bachelor of Science in Chemistry**, Technische Universität Darmstadt, Grade 1.4
06/2010	**Abitur** Kopernikusschule Freigereicht, Grade 1.4

Teaching and Research Experience

11/2013 - 07/2014	**Student Research Assistant**, Project: *In situ* Spectroscopy TU Darmstadt, Group of Prof. Dr. C. Hess
05/2013 - 06/2013	**Teaching**, Physical Chemistry Lab Course, TU Darmstadt
11/2012 - 03/2013	**Teaching**, Exercises on Quantum Mechanics, TU Darmstadt

Awards

01/2015 - 12/2016	**Scholarship for Doctoral Studies** from the Merck'sche Gesellschaft für Kunst und Wissenschaft e.V.
12/2014	**Dr. Anton Keller prize** for outstanding Bachelor Thesis
10/2013 - 09/2014	**Deutschlandstipendium** from Merck KGaA
06/2010	**Gesellschaft Deutscher Chemiker (GDCh) Abiturpreis / Deutsche Mathematiker-Vereinigung (DMV) Abiturpreis**

Additional Qualifications

02/2018	**Introduction to Business Administration for Chemists** (Gesellschaft deutscher Chemiker, GDCh)
08/2017	**Seminar on Agile Project Management (Scrum)**, TU Darmstadt
07/2017	**Test of Englisch for International Communication - Level C1**
11/2015	**Certificate of Competence on Laser Safety**

Christian Schilling